Imperial College London
Department of Aeronautics

On the use of spectral element methods for under-resolved simulations of transitional and turbulent flows

Rodrigo Costa Moura

supervised by

Prof. Spencer Sherwin and Dr. Joaquim Peiró

Submitted in part fulfilment of the requirements for the degree of
PhD in Aeronautics Engineering of Imperial College London, July 2017

COPYRIGHT

DECLARATION OF ORIGINALITY

I hereby declare that the material presented in this thesis is my own, except where otherwise acknowledged and appropriately referenced.

Rodrigo Costa Moura

London, July 2017

ACKNOWLEDGEMENTS

First and foremost, I would like to thank my supervisors, Prof. Spencer Sherwin and Dr. Joaquim Peiró for their constant guidance and advice. I am deeply grateful for their trust in my capabilities and for the freedom of research I had during these four years. I must thank Spencer for his patience in kindly pointing out whenever my argumentation needed refinement, despite my (often stubborn) defensiveness. I need also to thank Joaquim for his thoroughness in reviewing all my works and for being (originally) very reticent about implicit LES approaches. This fuelled long discussions over this topic, which trained me to answer tough questions others might have. I am thankful for everything they shared with me, professionally or otherwise, and for the unique opportunities I had under their wings, including the chance to collaborate with Dr. Andrew Winters and Prof. Gregor Gassner from the University of Cologne.

In addition, I want to acknowledge the many good colleagues and friends I made at Imperial, namely Andrea Cassinelli, Daniele de Grazia, David Moxey, Dirk Ekelschot, Jean-Eloi Lombard and finally Gianmarco Mengaldo, which took interest in my research and actively contributed to it. I must also include here my Brazilian colleagues and good friends David Kurka and Douglas Serson. I am very grateful for their friendship and feel honoured to be part of such a distinguished academic family.

Outside Imperial, I owe a big first thanks to my wife Isabela for being such a wonderful helper and infinitely more. She lifted my spirit whenever I was discouraged and stood strong by my side in many difficult moments. She taught me perseverance when I was overwhelmed or tired and discipline when I was lazy or disorganised, always in a kind manner. She is a constant source of joy and inspiration for me. I look forward to keep her by my side for the rest of my days.

I am deeply grateful for my parents and aunts that raised me with notorious love and allowed for me to attend good schools and to study the English language from an early age. This proved essential to the pursuit of doctoral studies in London. I also need to acknowledge my wife's original family (from her mother's side), which has always treated me as one of their own. I feel privileged for having such a lovely extended family.

Finally, I ought to thank Jesus Christ, my Lord and personal friend, who gave me the capabilities and motivation to pursue my doctoral studies to the end. In addition, I thank my church family for providing my wife and I with loving friendship and spiritual fellowship during our time in the UK, while also upholding us in prayer many times.

DEDICATION

To the Brazilian taxpayers, who supported my living expenses and tuition fees during the four years of my PhD studies. I hope to meet their expectations in returning to my home country and contributing to its development in my areas of expertise.

ABSTRACT

On the use of spectral element methods for under-resolved simulations of transitional and turbulent flows

by

Rodrigo Costa Moura

The present thesis comprises a sequence of studies that investigate the suitability of spectral element methods for model-free under-resolved computations of transitional and turbulent flows. More specifically, the continuous and the discontinuous Galerkin (i.e. CG and DG) methods have their performance assessed for under-resolved direct numerical simulations (uDNS) / implicit large-eddy simulations (iLES). In these approaches, the governing equations of fluid motion are solved in unfiltered form, as in a typical direct numerical simulation, but the degrees of freedom employed are insufficient to capture all the turbulent scales. Numerical dissipation introduced by appropriate stabilisation techniques complements molecular viscosity in providing small-scale regularisation at very large Reynolds numbers. Added spectral vanishing viscosity (SVV) is considered for CG, while upwind dissipation is relied upon for DG-based computations. In both cases, the use of polynomial dealiasing strategies is assumed.

Focus is given to the so-called eigensolution analysis framework, where numerical dispersion and diffusion errors are appraised in wavenumber / frequency space for simplified model problems, such as the one-dimensional linear advection equation. In the assessment of CG and DG, both temporal and spatial eigenanalyses are considered. While the former assumes periodic boundary conditions and is better suited for temporally evolving problems, the latter considers inflow / outflow type boundaries and should be favoured for spatially developing flows. Despite the simplicity of linear eigensolution analyses, surprisingly useful insights can be obtained from them and verified in actual turbulence problems. In fact, one of the most important contributions of this thesis is to highlight how linear eigenanalysis can be helpful in explaining why and how to use spectral element methods (particularly CG and DG) in uDNS / iLES approaches. Various aspects of solution quality and numerical stability are discussed by connecting observations from eigensolution analyses and under-resolved turbulence computations.

First, DG's temporal eigenanalysis is revisited and a simple criterion named "the 1% rule" is devised to estimate DG's effective resolution power in spectral space. This criterion is shown to pinpoint the wavenumber beyond which a numerically induced dissipation range appears in the energy spectra of Burgers turbulence simulations in one dimension. Next, the temporal eigenanalysis of CG is discussed with and without SVV. A modified SVV operator based on DG's upwind dissipation is proposed to enhance CG's accuracy and robustness for uDNS / iLES. In the sequence, an extensive set of DG computations of the inviscid Taylor-Green vortex model problem is considered. These are used for the validation of the 1% rule in actual three-dimensional transitional / turbulent flows. The performance of various Riemann solvers is also discussed in this infinite Reynolds number scenario, with high quality solutions being achieved. Subsequently, the capabilities of CG for uDNS / iLES are tested through a complex turbulent boundary layer (periodic) test problem. While LES results of this test case are known to require sophisticated modelling and relatively fine grids, high-order CG approaches are shown to deliver surprisingly good quality with significantly less degrees of freedom, even without SVV. Finally, spatial eigenanalyses are conducted for DG and CG. Differences caused by upwinding levels and Riemann solvers are explored in the DG case, while robust SVV design is considered for CG, again by reference to DG's upwind dissipation. These aspects are then tested in a two-dimensional test problem that mimics spatially developing grid turbulence.

In summary, a point is made that uDNS / iLES approaches based on high-order spectral element methods, when properly stabilised, are very powerful tools for the computation of practically all types of transitional and turbulent flows. This capability is argued to stem essentially from their superior resolution power per degree of freedom and the absence of (often restrictive) modelling assumptions. Conscientious usage is however necessary as solution quality and numerical robustness may depend strongly on discretisation variables such as polynomial order, appropriate mesh spacing, Riemann solver, SVV parameters, dealiasing strategy and alternative stabilisation techniques.

Contents

List of Tables

List of Figures

Preface

This thesis presents a systematic study on the suitability of under-resolved DNS (uDNS) — more often called implicit LES (iLES) — approaches based on spectral element methods (SEM), with emphasis on high-order continuous and discontinuous Galerkin (i.e. CG and DG) schemes. Broadly speaking, these are model-free eddy-resolving approaches to turbulence which solve the governing equations in unfiltered form and rely on numerical stabilization techniques for small-scale regularization. While spectral vanishing viscosity (SVV) is considered as the main stabilisation technique for CG at large Reynolds numbers, the upwind dissipation introduced by Riemann solvers is considered in the DG case. Model problems in 1D, 2D and 3D are used in the assessment of solution quality and numerical stability. A rationale for the excellent potential of these methods for transitional and turbulent flows is offered on the basis of linear dispersion-diffusion (eigensolution) analysis.

SEM-based uDNS / iLES approaches have received considerable attention over recent years. In some cases, these have been shown to outperform traditional LES approaches (even with sophisticated modelling) and provide superior results for the same number of degrees of freedom. However, very few studies have investigated the question of why these methods are able perform so well. It is also important to explore under which conditions the approaches in question can fail to produce usefully accurate solutions or even "crash" due to under-resolution. As SEM approaches vary considerably depending on discretisation variables such as polynomial order, Riemann solver, SVV design, dealiasing strategy and other stabilization techniques, it is crucial to analyse the effect of these variables on solution quality and numerical stability / robustness. It is the author's expectation that this research might contribute to a broader and more conscientious usage of SEM-based uDNS / iLES.

The present thesis is written in manuscript format. As such, each chapter is a self-contained study that has either been published or is being prepared for submission (in which case chapters are based on research reports). However, the thesis is structured in a seamless way so as to make evident the unity of the work as a whole, with the initial chapters being complemented by the subsequent ones. The material is organised as follows.

Chapter 1 revisits DG's eigensolution analysis under the assumption of periodic boundary conditions. A criterion is proposed to estimate DG's effective resolution power in spectral space, which is verified against (one-dimensional) Burgers turbulence simulations. This chapter is based on:

> R. C. Moura, S. J. Sherwin, J. Peiró (2015) *Linear dispersion–diffusion analysis and its application to under-resolved turbulence simulations using discontinuous Galerkin spectral/hp methods*, **Journal of Computational Physics** 298:695–710 (doi:10.1016/j.jcp.2015.06.020).

Chapter 2 discusses the eigenanalysis of CG with and without SVV assuming periodic boundary conditions. A modified SVV operator based on DG's dissipation characteristics is proposed in order to enhance CG's accuracy and robustness for uDNS / iLES. This chapter is based on:

> R. C. Moura, S. J. Sherwin, J. Peiró (2016) *Eigensolution analysis of spectral/hp continuous Galerkin approximations to advection-diffusion problems: insights into spectral vanishing viscosity*, **Journal of Computational Physics** 307:401–422 (doi:10.1016/j.jcp.2015.12.009).

Chapter 3 covers an extensive set of DG-based computations of the inviscid Taylor-Green vortex problem. These are used to validate the resolution criterion discussed in Chapter 1 in actual turbulent flows. Aspects of solution quality and numerical stability are also appraised in this infinite Reynolds number scenario. This chapter is based on:

> R. C. Moura, G. Mengaldo, J. Peiró, S. J. Sherwin (2017) *On the eddy-resolving capability of high-order discontinuous Galerkin approaches to implicit LES / under-resolved DNS of Euler turbulence*, **Journal of Computational Physics** 330:615–623 (doi:10.1016/j.jcp.2016.10.056).

Chapter 4 investigates the suitability of CG for wall-bounded turbulent flows through a complex boundary layer test problem. Despite the preliminary character of the investigation, high-order CG is shown to outperform sophisticated LES approaches even without SVV and with fewer degrees of freedom. This chapter is based on:

> R. C. Moura, S. J. Sherwin, J. Peiró (2017) *On the suitability of CG for non-trivial wall-bounded turbulent flows*, **Research Report** (doi:10.13140/RG.2.2.30744.70407).

Chapter 5 considers the eigenanalysis of DG while assuming inflow / outflow boundary conditions. Effects of different upwinding levels are discussed and tested in a two-dimensional model problem that mimics spatially developing grid turbulence. This chapter is based on:

> G. Mengaldo, R. C. Moura, B. Giralda, J. Peiró, S. J. Sherwin (2017) *Spatial eigensolution analysis of discontinuous Galerkin schemes with practical insights for under-resolved computations and implicit LES*, **Computers & Fluids** (accepted for publication).

Chapter 6 addresses CG's eigensolution analysis with and without SVV, again assuming inflow / outflow type boundaries. A strategy is devised to make the dissipation levels of SVV match those of DG at appropriate polynomial orders. The adapted SVV operator is demonstrated to improve CG's accuracy and robustness for under-resolved spatially developing flows. This chapter is based on:

> R. C. Moura, S. J. Sherwin, J. Peiró (2017) *Spatial eigenanalysis of CG and DG methods with insights on solution quality and numerical stability*, **Research Report** (doi:10.13140/RG.2.2.33310.13129).

Additional publications

The publications below have also been authored (or co-authored) during the course of this PhD, but are either too preliminary or focus on topics somewhat beyond those of interest here. However, certain pieces of them can be found into the thesis as well, in which case they are duly cited.

- R. C. Moura, S. J. Sherwin, J. Peiró (2014) *Modified equation analysis for the discontinuous Galerkin formulation*, **Proceedings of the 10th International Conference on Spectral and High Order Methods**, Salt Lake City, USA (doi:10.1007/978-3-319-19800-2_34).

- R. C. Moura, G. Mengaldo, J. Peiró, S. J. Sherwin (2016) *An LES setting for DG-based implicit LES with insights on dissipation and robustness*, **Proceedings of the 11th International Conference on Spectral and High Order Methods**, Rio de Janeiro, Brazil (doi available soon).

- A. R. Winters, R. C. Moura, G. Mengaldo, G. J. Gassner, S. Walch, J. Peiró, S. J. Sherwin (2018) *A comparative study on polynomial dealiasing and split form discontinuous Galerkin schemes for under-resolved turbulence computations*, **Journal of Computational Physics** (under preparation).

Chapter 1

Temporal eigenanalysis of discontinuous Galerkin methods and its relevance to under-resolved turbulence simulations

Summary [†]

This chapter investigates the potential of linear dispersion-diffusion analysis in providing direct guidelines for turbulence simulations based on under-resolved DNS (often called implicit LES) approaches via spectral/*hp* methods. The discontinuous Galerkin (DG) scheme is assessed in particular as a representative of these methods. The temporal eigenanalysis as applied to linear advection is revisited and a new perspective on the role of multiple numerical modes, peculiar to spectral/*hp* methods, is suggested. From this new perspective, "secondary" eigenmodes are seen to replicate the propagation behaviour of a "primary" mode, so that DG's propagation characteristics can be obtained directly from the dispersion-diffusion curves of the primary mode. Numerical dissipation is then appraised from these primary eigencurves and its effect over poorly-resolved scales is quantified. Within this scenario, a simple criterion is proposed to estimate DG's effective resolution in terms of the largest wavenumber it can accurately resolve in a given *hp* approximation space, allowing for the evaluation of points per wavelength estimates typically used in spectral and finite difference methods. Although strictly valid for linear advection, the devised criterion is tested against (1D) Burgers turbulence and found to predict with good accuracy the beginning of the dissipation range on the energy spectra of under-resolved simulations. The analysis of these test cases through the proposed methodology clarifies why and how the DG formulation can be used for under-resolved turbulence simulations without explicit subgrid-scale modelling. In particular, when dealing with communication limited hardware which forces one to consider the performance for a fixed number of degrees of freedom, the use of higher polynomial orders along with moderately coarser meshes is shown to be the best way to translate available degrees of freedom into resolution power.

[†] This chapter is based on "R. C. Moura, S. J. Sherwin, J. Peiró (2015) *Linear dispersion–diffusion analysis and its application to under-resolved turbulence simulations using discontinuous Galerkin spectral/hp methods*, **Journal of Computational Physics** 298:695–710".

1.1 Introduction

No-model under-resolved turbulence computations based on spectral/hp methods have been growing in popularity in recent years. In this approach, the goal is to resolve only the largest scales of motion, as in classical LES (Large Eddy Simulation), but no explicit modelling is used for the smallest scales. Accordingly, the unfiltered Navier-Stokes are simulated in a manner similar to DNS (Direct Numerical Simulation), except that an insufficient number of degrees of freedom is employed to resolve the flow. Hence, the terms under-resolved DNS (uDNS) and implicit LES (iLES) have been used to describe this approach. It can be argued, however, that the term iLES should be reserved for schemes whose truncation terms implicitly mimic LES-like models [1]. Note that for traditional low-order schemes, where the leading truncation error usually takes the form of a second-order diffusion operator, some kind of eddy-viscosity modelling can normally be recognized. On the other hand, since no direct correspondence between numerical errors and standard subgrid-scale (SGS) models is anticipated for high-order spectral/hp methods, the term uDNS is preferred in the present work.

Bypassing the need for explicit SGS models makes both iLES and uDNS approaches attractive since most of the theoretical and implementation complexities of traditional LES are avoided. It is argued that the former approaches are also advantageous because, even if implicit turbulence models lack physics, the absence of modelling terms in the computations makes it possible to use a finer mesh than the one that would be used in classic LES (for the same cost). As emphasized by Pope in [2], LES models must be appraised not only by their physical accuracy, but also by their related computational cost, which together define a kind of effective performance for a given model. In a similar line of thought, Spalart points out that most works advocating sophisticated modelling "fail to show a clear advantage over the *same-cost* LES with a simplistic model" [3].

High-order spectral/hp methods [4] have been successfully used in under-resolved turbulence simulations with different discretisations, such as: the continuous Galerkin (CG) method [5, 6]; the discontinuous Galerkin (DG) formulation [7, 8]; the spectral difference (SD) method [9, 10]; as well as with the correction procedure via reconstruction (CPR) scheme [11, 12]. Apart from the CG discretisation, where stability is usually enforced by added SVV (Spectral Vanishing Viscosity) [13], all these methods incorporate in their formulation some form of stabilization by means of upwind Riemann fluxes. It is recognized that these (either SVV or upwind fluxes) are the techniques responsible for providing dissipation at the under-resolved scales. It is worth noting that truncation error is also expected to contribute to the numerical dissipation. Other than that and regardless of the aforementioned ongoing applications, there is still little knowledge on *why* and *how* one can use spectral/hp methods for under-resolved turbulence simulations. This study aims to clarify these points while focusing on the discontinuous Galerkin formulation.

An early discussion on the suitability of DG for turbulence simulations was reported in [14, 15], where the scheme was found to successfully predict low-order statistics with fewer degrees of freedom (DOFs) than traditional numerical methods. More extensive assessments [16, 17] in the DNS of turbulent channel flows revealed that DG can predict high-order statistics with accuracy comparable to that of spectral methods for an equivalent number of DOFs. Regarding under-resolved simulations, a detailed study conducted in [18] showed that, for a given number of DOFs, increasing the polynomial order can be more effective than refining the mesh in order to improve the accuracy. This study considered discretisations up to 16th-order in the solution of the Taylor-Green vortex [19] test case and demonstrated that DG-based uDNS computations can outperform sophisticated LES methods in terms of accuracy (on a DOF basis) as long as the polynomial order is sufficiently high. This result was further confirmed by an extensive investigation reported in [8] where practical engineering test cases were considered. The effect of different types of mesh elements was assessed in [20] again through the Taylor-Green vortex problem and these were found to impact flow resolution mainly at small scales. The latter study however only considered discretisations up to 4th-order.

In the context of iLES, the modified equation analysis technique is usually employed [21] to justify why certain numerical schemes are particularly suited for implicit large eddy simulations. By resorting to Taylor series to rewrite discrete derivative expressions, modified equation analysis can reveal which PDE is actually governing a numerical solution. Due to the presence of truncation terms, the resulting PDE (referred to as the modified equation) differs from the physical PDE being discretised. In the analysis of low-order schemes for the discretisation of the Navier-Stokes equations, a non-linear form of eddy-viscosity can sometimes be recognized in the first truncation terms [1].

An exploratory study on modified equation analysis for linear advection with DG has recently been conducted [22]. Unfortunately, comparisons between modified equations and DG's dispersion-diffusion errors known from eigensolution analysis [23, 24] were not encouraging. The representation of DG's numerical errors was found to be misleading when just the first few truncation terms were considered. In some cases, up to ten truncation terms were needed for an accurate representation. Moreover, the correspondence was verified to fail sometimes for the poorly-resolved wavenumbers, in which case truncation terms were not even representative of the numerical errors. Since these issues are unlikely to disappear for non-linear problems, a different approach is followed here.

In this chapter, DG's numerical errors are assessed directly through the eigensolution analysis, with particular focus on how numerical dissipation affects the under-resolved scales. While revisiting the temporal eigenanalysis technique, the role of multiple numerical modes (peculiar to spectral/*hp* methods) is discussed and a new perspective on the subjected is advocated, from which "secondary" eigenmodes are considered to replicate the propagation behaviour of a "primary" mode. As a result, DG's propagation characteristics are obtained directly from the dispersion-diffusion curves of this primary mode. Then, from the primary diffusion eigencurves, a simple criterion (named the 1% rule) is proposed to estimate the effective resolution of the DG scheme for a given *hp* approximation space. More specifically, this rule estimates the maximum wavenumber that can be resolved accurately given the mesh spacing and polynomial order employed. The criterion is tested against one-dimensional Burgers turbulence and found to reliably predict the beginning of the dissipation range on turbulent energy spectra. This highlights the potential of linear dispersion-diffusion analysis in providing direct guidelines for the simulation of turbulence through the uDNS approach via spectral/*hp* methods.

Although the temporal eigenanalysis technique adopted here assumes periodic boundary conditions, it is usually regarded as valid for waves propagating far away from boundaries. The temporal analysis is to be differentiated from the (less common) spatial eigenanalysis, where semi-infinite domains are considered and the effect of boundary conditions are taken into account. Currently, only a few studies have considered the spatial eigenanalysis of DG schemes, see e.g. [24].

This chapter is organized as follows. The DG formulation for linear advection in one dimension is briefly summarized in Sec. 1.2. The eigensolution analysis technique is then revisited in Sec. 1.3, where the role of secondary modes is discussed and the 1% rule is introduced. In Sec. 1.4, this rule is tested against Burgers turbulence and the results are appraised in order to clarify *why* and *how* one can use spectral/*hp* methods (DG in particular) for turbulence simulations via uDNS.

1.2 The semi-discrete DG formulation

Assuming suitable initial and boundary conditions are given, the following scalar hyperbolic equation over the one-dimensional domain Ω is considered:

$$\frac{\partial u}{\partial t} + \frac{\partial f}{\partial x} = 0 \ , \tag{1.1}$$

where $f = f(u)$ is the flux function, solely dependent on the solution $u = u(x,t)$. In DG's framework, the solution domain is divided among non-overlapping elements Ω_e such that $\Omega = \bigcup_e \Omega_e$. Within these elements, the solution is then approximated by a weighted sum of basis functions ϕ_j, namely

$$u|_{\Omega_e} \cong \sum_{j=0}^{P} c_j(t)\, \phi_j(\xi) \ , \tag{1.2}$$

where ϕ_j is chosen to be the orthonormal Legendre polynomial of degree j, defined in the standard domain $\Omega_{st} = [-1,1]$, see [4, 25] for details. In order to obtain the coefficients c_j, the projection of Eq. (1.1) is required to vanish locally, i.e.

$$\int_{\Omega_e} \phi_i \left(\frac{\partial u}{\partial t} + \frac{\partial f}{\partial x} \right) dx = 0 \ , \ \text{for } i \in \{0, \ldots, P\} \ . \tag{1.3}$$

Using Eq. (1.2) into Eq. (1.3) and given that the chosen basis functions are orthonormal, yields

$$\frac{h}{2}\frac{\partial c_i}{\partial t} = \int_{\Omega_{st}} \frac{\partial \phi_i}{\partial \xi} f \, d\xi - \int_{\Omega_{st}} \frac{\partial(\phi_i f)}{\partial \xi} \, d\xi \ , \tag{1.4}$$

where h is the size (length) of element Ω_e. Inter-element communication is allowed by the introduction of the numerical flux, $\tilde{f}$, in the second integral on the right-hand side of Eq. (1.4) leading to

$$\frac{h}{2}\frac{\partial c_i}{\partial t} = \int_{\Omega_{st}} f\, \phi_i' \, d\xi - (\tilde{f}\phi_i)|_{\Omega_e^R} + (\tilde{f}\phi_i)|_{\Omega_e^L} \ , \tag{1.5}$$

where Ω_e^L and Ω_e^R denote the left and right boundaries of element Ω_e, respectively. The numerical flux $\tilde{f} = \tilde{f}(u_\ominus, u_\oplus)$ is a function of the values at the left ($u_\ominus$) and right ($u_\oplus$) sides of each interface considered. The standard upwind flux is considered here, namely

$$\tilde{f}(u_\ominus, u_\oplus) = \frac{f(u_\ominus) + f(u_\oplus)}{2} + \left| \frac{\partial f}{\partial u} \right| \frac{u_\ominus - u_\oplus}{2} \ , \text{with } \left| \frac{\partial f}{\partial u} \right| = \frac{u_\ominus + u_\oplus}{2} \ . \tag{1.6}$$

The dispersion-diffusion analysis performed in Sec. 1.3 will focus on the advection equation, namely Eq. (1.1) with $f = au$, where a is the constant advection speed. Hence, Eq. (1.5) becomes

$$\frac{h}{2a}\frac{\partial c_i}{\partial t} = \sum_{j=0}^{P} \mu_{ij}\, c_j - (\tilde{u}\phi_i)|_{\Omega_e^R} + (\tilde{u}\phi_i)|_{\Omega_e^L} \ , \tag{1.7}$$

where the constants μ_{ij} and the (normalized) numerical flux $\tilde{u} = \tilde{f}/a$ are given by

$$\mu_{ij} = \int_{\Omega_{st}} \phi_j \, \frac{\partial \phi_i}{\partial \xi}\, d\xi \quad \text{and} \quad \tilde{u}(u_\ominus, u_\oplus) = \frac{u_\ominus + u_\oplus}{2} + S_a \frac{u_\ominus - u_\oplus}{2} \ , \tag{1.8}$$

where $S_a = |a|/a$ is the sign of a. Using Eqs. (1.7–1.8) and assuming an equispaced mesh, the semi-discrete linear advection problem can be expressed in vector form for each mesh element as

$$\frac{h}{2a}\frac{\partial \vec{c}}{\partial t} = \boldsymbol{\mathcal{L}}\, \vec{c}_L + \boldsymbol{\mathcal{C}}\, \vec{c} + \boldsymbol{\mathcal{R}}\, \vec{c}_R \ , \tag{1.9}$$

where $\vec{c} = \{c_0, \ldots, c_P\}^T$ and the indices L and R refer to the neighbour elements respectively at the left and right sides of the (central) element considered. The matrices in Eq. (1.9) are given by

$$\boldsymbol{\mathcal{C}}_{i,j} = \mu_{ij} \ + \ \frac{1}{2}(1 - S_a)\, \phi_i(-1)\, \phi_j(-1) \ - \ \frac{1}{2}(1 + S_a)\, \phi_i(+1)\, \phi_j(+1) \ , \tag{1.10}$$

$$\boldsymbol{\mathcal{L}}_{i,j} = \frac{1}{2}(1 + S_a)\, \phi_i(-1)\, \phi_j(+1) \ \ , \ \ \boldsymbol{\mathcal{R}}_{i,j} = -\frac{1}{2}(1 - S_a)\, \phi_i(+1)\, \phi_j(-1) \ . \tag{1.11}$$

1.3 Dispersion-diffusion analysis for DG

This section is devoted to the eigensolution analysis DG-based linear advection and investigates in particular the effect of numerical errors for under-resolved simulations. The eigensolution technique has been applied to DG in different ways [23, 26, 24, 27, 28]. The so-called temporal approach is followed here, where a real wavenumber k is considered for the initial condition and a complex wave frequency w is assumed to govern the numerical solution. When this technique is applied to spectral/*hp* methods, several numerical modes are found in connection to each single Fourier mode prescribed for the initial condition. As noted in [29], this fact is interpreted in different ways in the literature, but it is frequently assumed that only one numerical mode is important while all the others should be simply dismissed for being spurious. This question is also discussed in this section and a new perspective on the matter is offered, from which all the eigenmodes are seen to complement the propagation characteristics of a particular mode, here referred to as the primary one.

The temporal eigenanalysis of DG is reviewed in Sec. 1.3.1. Dispersion and diffusion curves are addressed in Sec. 1.3.2, where the role of multiple eigenmodes is also discussed. Sec. 1.3.3 focuses on the effect of numerical errors on the under-resolved scales and proposes a simple criterion to estimate the largest wavenumber that can be accurately resolved by DG's *hp* setting.

1.3.1 Wave-like solutions and eigenmodes

Following the eigensolution analysis framework, one seeks for numerical solutions consistent with the analytic eigenfunctions of the linear advection equation in the form (hereafter, $i = \sqrt{-1}$)

$$u = \exp[i(kx - wt)] \ , \tag{1.12}$$

or, more specifically, solutions in which the element-wise approximating coefficients are related to the above wave-like solution through projection. Using orthonormal polynomials ϕ_j as basis functions, the coefficients associated to element Ω_e are given by

$$c_j(t) = \int_{\Omega_{st}} u\,(x_e + \xi h/2, t)\, \phi_j(\xi)\, d\xi \ , \tag{1.13}$$

where x_e denotes the centre (midpoint) of element Ω_e. Simple substitution yields

$$\vec{c}\,(t) = \vec{\alpha}\, \exp[i(kx_e - wt)] \ , \tag{1.14}$$

in which $\vec{\alpha} = \{\alpha_0, \ldots, \alpha_P\}^T$ and

$$\alpha_j = \int_{\Omega_{st}} \exp\,(ikh\xi/2)\, \phi_j(\xi)\, d\xi \ . \tag{1.15}$$

It is worth noting that for orthonormal Legendre basis functions ϕ_j, one can analytically obtain $\alpha_j = \alpha_j(z)$, with $z = kh/2$, from the relations

$$\alpha_0 = \sqrt{2}\, \frac{\sin z}{z} \ , \ \ \alpha_1 = \frac{i\sqrt{6}}{z} \left(\frac{\sin z}{z} - \cos z \right) \ , \tag{1.16}$$

and, for $n \geq 1$,

$$\alpha_{n+1} = \frac{\sqrt{4n+6}}{z} \left[M_n \sin z + i \left(\frac{\sin z}{z} - \cos z \right) M_{n+1} + i \sum_{m=1}^{n} \sqrt{m + 1/2}\, M_{m+n+1}\, \alpha_m \right] \ , \tag{1.17}$$

where $M_j = \text{mod}(j, 2)$ is the modulus of j after division by two.

One should note that a single Fourier eigenmode can energize several numerical eigenmodes (not to mention element-wise polynomial modes). This is because there is no one-to-one correspondence between the employed polynomials and complex exponential functions which represent the eigenfunctions of the partial differential equation. Hence, a wave of single wavenumber k will be represented numerically by eigenmodes of different frequencies $w_m \neq ak$ and respective eigenvectors $\vec{\zeta}_m \neq \vec{\alpha}$. The role of these multiple modes will be discussed in detail in Sec. 1.3.2.

From Eqs. (1.9) and (1.14), one can anticipate that valid numerical eigenmodes must follow the relation

$$\frac{h}{2a}(-iw)\, \vec{\zeta} = \left[\boldsymbol{\mathcal{L}}\, e^{-ikh} + \boldsymbol{\mathcal{C}} + \boldsymbol{\mathcal{R}}\, e^{+ikh} \right] \vec{\zeta} \ , \tag{1.18}$$

in which, according to the temporal eigenanalysis, k is assumed real and w is allowed to be complex.

By defining $\boldsymbol{\mathcal{M}} = 2\left[\boldsymbol{\mathcal{L}}e^{-ikh} + \boldsymbol{\mathcal{C}} + \boldsymbol{\mathcal{R}}e^{+ikh}\right]$, the above relation becomes

$$-i\frac{wh}{a}\,\vec{\zeta} = \boldsymbol{\mathcal{M}}(kh)\,\vec{\zeta}\ , \tag{1.19}$$

which is clearly an eigenvalue problem with potentially $P+1$ solutions. Therefore, for each given k, the relation above holds for $P+1$ frequencies w_m and eigenvectors $\vec{\zeta}_m$.

The eigenvalue/vector pairs $(\lambda_m, \vec{\zeta}_m)$ of $\boldsymbol{\mathcal{M}}$ relate to the variables in the discrete problem as

$$w_m = \frac{ia}{h}\lambda_m \ \text{ and }\ \vec{v}_m \propto \vec{\zeta}_m\ , \tag{1.20}$$

where, without loss of generality, one can define $\vec{v}_m = \vec{\zeta}_m/s_m$, s_m being the sum of the entries of $\vec{\zeta}_m$. As a result, the general numerical solution (for element Ω_e) can be written as

$$\vec{c}(t) = \sum_{m=0}^{P} A_m\,\vec{v}_m\,\exp[i(kx_e - w_m t)] \quad \text{or} \quad c_j(t) = \sum_{m=0}^{P} A_m\,\boldsymbol{\mathcal{V}}_{j,m}\,\exp[i(kx_e - w_m t)]\ , \tag{1.21}$$

where $\boldsymbol{\mathcal{V}} = \{\vec{v}_0, \dots, \vec{v}_P\}$ and the constants A_m can be obtained from the initial condition. Specifically, when $u(x,0) = \exp(ikx)$ is used via projection at the initial condition, one has

$$\sum_{m=0}^{P} A_m\,\vec{v}_m\,\exp(ikx_e) = \vec{\alpha}\,\exp(ikx_e)\ , \tag{1.22}$$

in which Eqs. (1.14) and (1.21) have been used with $t = 0$. Accordingly, $\vec{A} = \{A_0, \dots, A_P\}^T$ is given by $\vec{A} = \boldsymbol{\mathcal{V}}^{-1}\vec{\alpha}$.

Using the rightmost relation in Eq. (1.21), the element-wise numerical solution within Ω_e reads

$$u_e(\xi, t) = \sum_{j=0}^{P} c_j(t)\,\phi_j(\xi) = \sum_{j=0}^{P}\sum_{m=0}^{P} A_m\,\boldsymbol{\mathcal{V}}_{j,m}\,\phi_j(\xi)\,\exp[i(kx_e - w_m t)]\ , \tag{1.23}$$

which can be rewritten as

$$u_e(\xi, t) = \sum_{m=0}^{P} A_m\,\sigma_m(\xi)\,\exp[i(kx_e - w_m t)] = \exp(ikx_e)\sum_{m=0}^{P} A_m\,\sigma_m(\xi)\,\exp(-iw_m t)\ , \tag{1.24}$$

where the element-wise eigenfunctions $\sigma_m(\xi)$ of the discrete problem were introduced, namely

$$\sigma_m(\xi) = \sum_{j=0}^{P} \boldsymbol{\mathcal{V}}_{j,m}\,\phi_j(\xi)\ . \tag{1.25}$$

Each σ_m can be interpreted as the transformation of the associated $\vec{v}_m$ into physical space. Note from Eq. (1.24) that while the factor $\exp(ikx_e)$ accounts for wave-like variations from one element to another, the discrete eigenfunctions $\sigma_m(\xi)$ account for wave-like variations *inside the elements.* The effect of the latter will be more significant in high-order simulations with coarse meshes.

In summary, Eqs. (1.21–1.24) indicate that the numerical solution is composed by $P+1$ eigenmodes which, through their respective values of w_m, propagate with different dispersion and diffusion characteristics. The eigenvalues λ_m of the discrete problem are related to these characteristics of the numerical approximation to the original advection problem and so are discussed in the next section.

1.3.2 Dispersion/diffusion curves and secondary modes

From the exact dispersion relation for the linear advection equation, $w = ak$, it is possible to define a modified wavenumber k^* as the ratio between the (numerical) angular frequency and the advection speed. One modified wavenumber can therefore be obtained from each angular frequency w_m, such that $w_m = ak^*_m$. The natural interpretation is that each eigenmode (m) of the numerical solution will behave as if related to k^*_m instead of k. Note from Eq. (1.19) that $\boldsymbol{\mathcal{M}}$ is a function of k and so both w_m and k^*_m are also functions of the "baseline" wavenumber k.

Employing the relation between w_m and λ_m given in Eq. (1.20) yields

$$\text{Real}(k^*_m) = \frac{\text{Real}(w_m)}{a} = -\frac{\text{Imag}(\lambda_m)}{h} \ , \quad \text{Imag}(k^*_m) = \frac{\text{Imag}(w_m)}{a} = \frac{\text{Real}(\lambda_m)}{h} \ . \tag{1.26}$$

For pure advection, deviations of Real(k^*) from k are related to dispersion (lead or lag phase errors) while deviations of Imag(k^*) from zero correspond to numerical dissipation, assuming Imag(k^*) < 0.

Case $P = 2$ is considered in Fig. 1.1(a), in which the real and imaginary parts of the modified wavenumbers k^*_m are displayed against the baseline wavenumber k, each curve corresponding to a different eigenmode (m). As in previous works, the axes are normalized by the number of degrees of freedom employed, $N_{DOF} \propto (P+1)/h$. Note that in a DG discretisation, $h/(P+1)$ can be regarded as the measure of one DOF. The mode in the centre of these plots, i.e. the one that recovers $k^* = k$ as $k \to 0$, will be identified as the "primary" mode, while the remaining branches are simply called "secondary" modes. The role played by different numerical modes is discussed in what follows.

Since each $\overline{k^*_m} = k^*_m h/(P+1)$ is a periodic function of $\overline{k} = kh/(P+1)$, with period 2π, it is sufficient to analyse $\overline{k^*_m}$ for $-\pi \le \overline{k} \le \pi$, as shown in Fig. 1.1(a), which displays this periodicity for the real and imaginary parts of $\overline{k^*_m}$. Note that all the eigencurves of secondary modes appearing in Fig. 1.1(a) are just replicas of the primary mode's eigencurve translated of $2\pi/(P+1)$ in the normalized $\overline{k}$-axis, both for dispersion and diffusion. This symmetry can easily be verified for higher values of P and holds both for the eigenvalues λ_m and eigenvectors $\vec{v}_m$. The eigenvectors' symmetry is illustrated in Fig. 1.1(b) for the eigenmatrix's entries $\boldsymbol{\mathcal{V}}_{1,m}$ again for the case $P = 2$.

As eigencurves of secondary modes are simply (equispaced) replicas of the primary mode's eigencurves, one can conclude that all the propagation properties of the secondary modes are essentially contained in the eigencurves of the primary mode. In fact, given $\overline{k}$, the eigenvalues and eigenvectors of the numerical solution can be found either on the different $(P+1)$ eigencurves at a fixed value of $\overline{k}$ or, alternatively, on the values along the primary mode's eigencurves at the equivalent equispaced $(P+1)$ values of $\overline{k}$. Thanks to the symmetries, these equivalent values of $\overline{k}$ are simply replicas of the baseline $\overline{k}$ separated by $2\pi/(P+1)$ in the normalized $\overline{k}$-axis. Both ways of obtaining the eigenvalues are illustrated in Fig. 1.2(a) for $P = 2$ and $\overline{k} = \pi/6 \approx 0.52$. Note that, in Fig. 1.2(a), bullets relate to the first interpretation, whereas circles illustrate the alternative one. The procedure for the eigenvectors is similarly straightforward, but has to be performed in a component-wise manner.

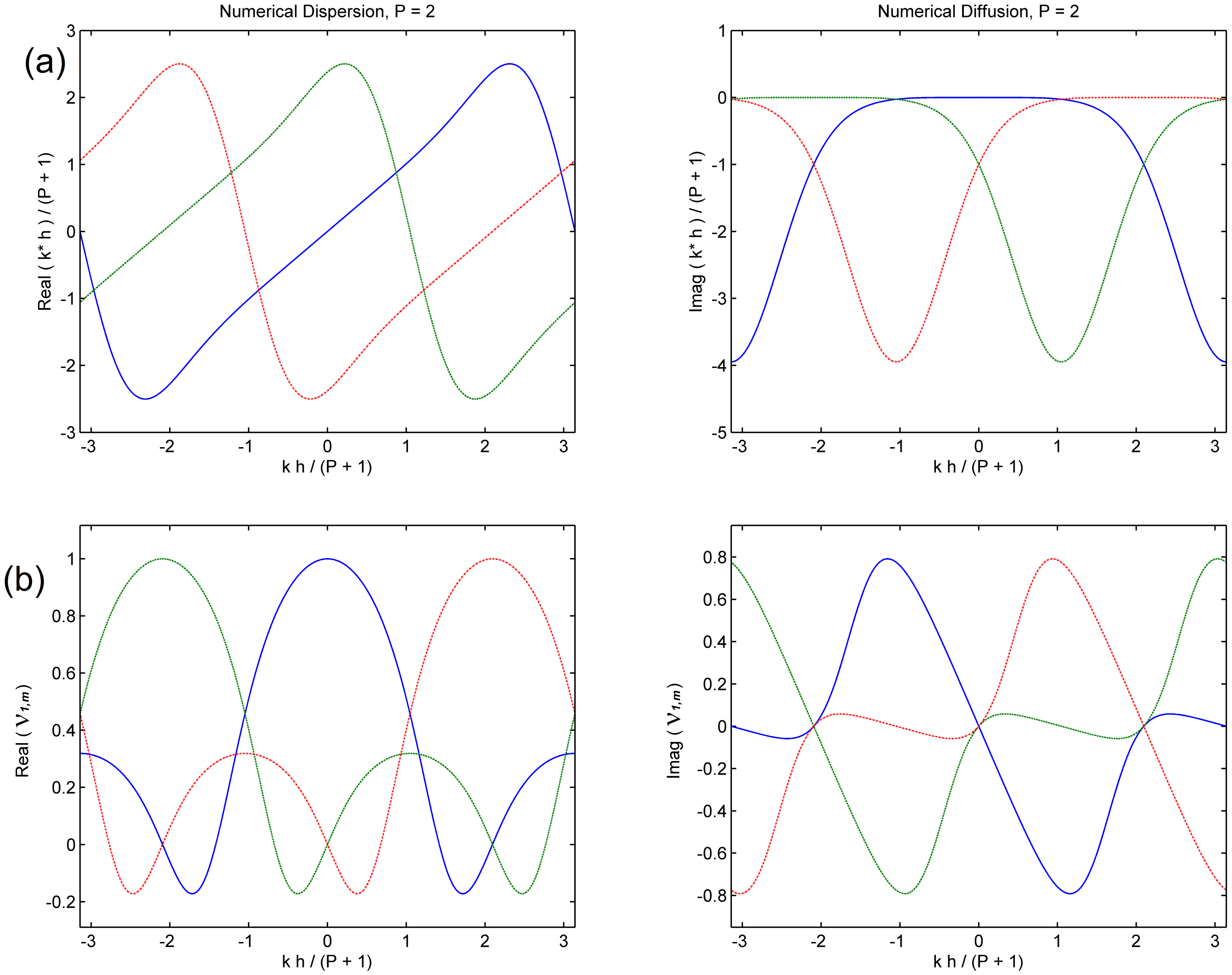

Figure 1.1: Standard upwind DG discretisation with $P = 2$: (a) real (left) and imaginary (right) parts of the modified wavenumbers k^*_m vs. the baseline wavenumber k and (b) real (left) and imaginary (right) parts of an eigenmatrix's entries $\boldsymbol{\mathcal{V}}_{1,m}$ vs. the baseline wavenumber k.

The nature of the secondary modes can be interpreted as follows. If a single Fourier component is prescribed as initial condition through a projection, the *hp* discretisation space will perceive it as several numerical eigenfunctions, instead of just one (as also previously recognized in [30]). Still, such representation corresponds to the optimal approximation (in the L^2 norm) assuming that a Galerkin projection is used. The proposed interpretation is illustrated in Fig. 1.2(b), where one observes the approximation of $u(x,0) = \cos(\pi x)$ with a $P = 2$ discretisation and 8 equispaced elements over the interval $0 \leq x \leq 4$. The discrete approximation to the cosine function is decomposed into three numerical modes (ev_1, ev_2 and ev_3) such that, from Eq. (1.24),

$$ev_m(x,0) = A_m \, \exp(ikx_e) \, \sigma_m(\xi) \ , \ \text{for } m = 1,2,3, \tag{1.27}$$

where the values of A_m are indicated by the scale of the vertical axis of each numerical eigenmode in

Fig. 1.2(b). The projection of $\cos(\pi x)$ leads to a primary contribution from ev_1 which corresponds to the primary mode and captures most of the cosine function. Still, the two other numerical eigenmodes (ev_2 and ev_3) also contribute to the optimal approximation. Although each of the eigenmodes oscillates in time as prescribed by different w_m values, they all vary in space according to a single k. Spatial variations are however also modulated by $\sigma_m(\xi)$, as previously shown in Eqs. (1.23) to (1.25).

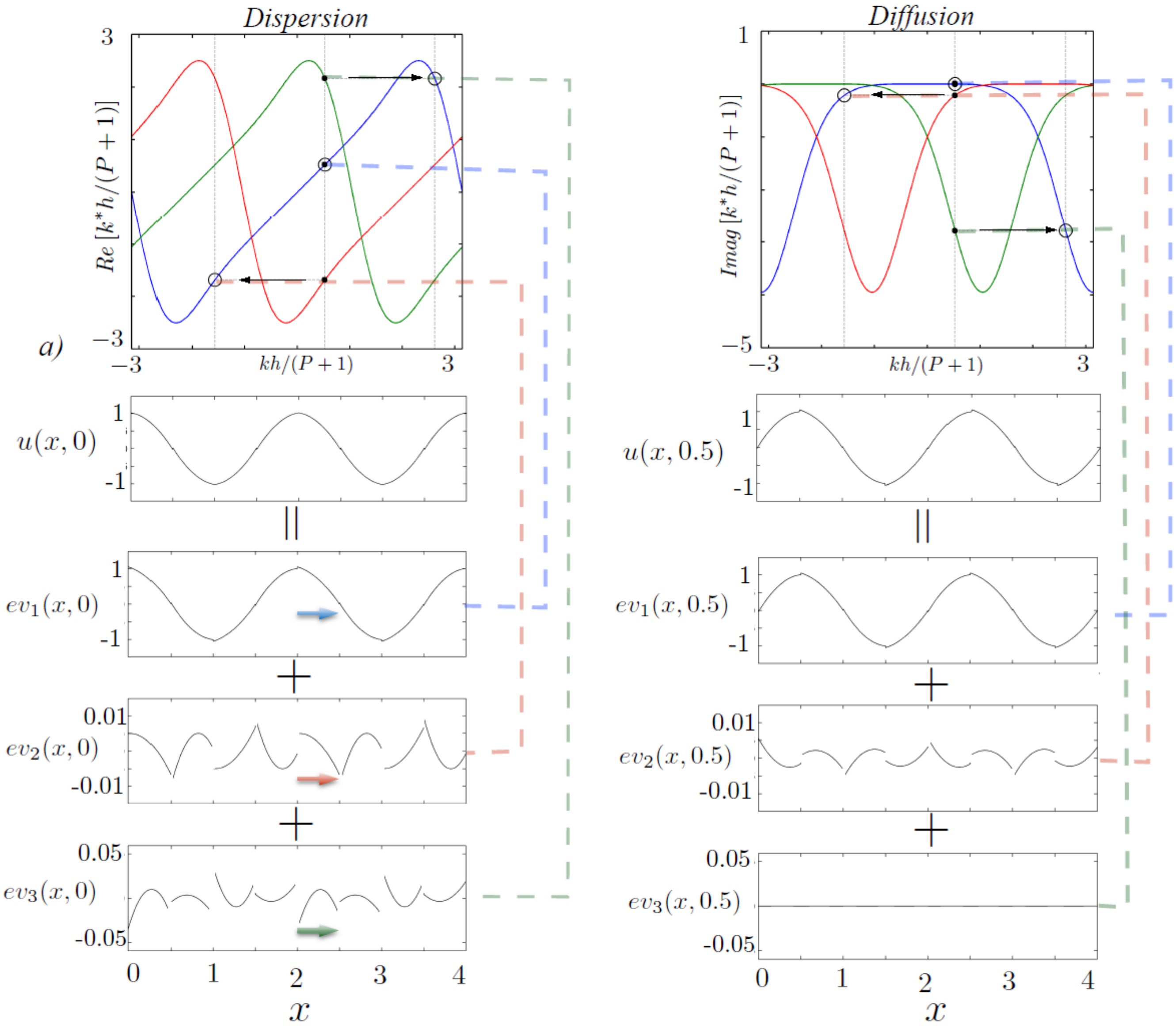

b) Initial condition

c) Solution at t=0.5

Figure 1.2: Understanding multiple eigencurves: (a) For a fixed value of $kh/(P+1) = \pi/6 \approx 0.52$, one obtains three eigenvalues. Two secondary eigenvalues can be considered as replicas of the primary eigenvalue separated by $2\pi/(P+1) = 2\pi/3$. (b) A cosine wave initial condition is perceived through a Galerkin projection as a primary mode ev_1 and two secondary modes, ev_2 and ev_3. (c) All three eigenmodes contribute to the numerical advection of the initial condition but decay at different rates.

As secondary w_m values can be interpreted as distributed along the primary eigencurve, cf. the circles in Fig. 1.2(a), it is natural to think that they relate to secondary wavenumbers k_m. The latter are such that $\overline{k_m} = \overline{k} + 2\pi m/(P+1)$, with k_0 corresponding to the baseline/primary wavenumber. Not surprisingly, the initial condition can be seen as a superposition of $P+1$ spatial eigenmodes which visually relate to different wavenumbers, as shown in Fig. 1.2(b). Hence, secondary eigenmodes can perhaps be regarded as "intrusive", as they relate to wavenumbers not present in the analytical initial condition, but should not be considered spurious as they can indeed improve the numerical approximation. As it is demonstrated below, these can work together via superposition to accurately propagate the numerical initial condition (projection). However, as they propagate forwards in time, numerical dissipation also acts on the secondary modes.

Once the projected initial condition is perceived by the numerical setting as multiple eigenmodes, cf. the dotted lines between plots (a) and (b) in Fig. 1.2, they evolve according to their own wavenumbers / frequencies as prescribed by the primary dispersion-diffusion curve. In Fig. 1.2(c) the considered test case is shown at $t = 1/2$, after being advected a distance of one mesh element with a unit velocity. The solution still consists of three eigenmodes, but with reduced amplitudes since they were subjected to different amounts of dissipation during the propagation. The primary mode ev_1 has its eigenvalue within the linear regions of dispersion-diffusion curves and thus propagates without significant numerical damping. Mode ev_2 has the smallest diffusion of the two secondary modes and so maintains some of its original shape, whereas ev_3 has a large numerical dissipation and by $t = 1/2$ has already decayed to a negligible amplitude.

Fig. 1.3 illustrates the distribution of secondary modes when a higher value of P is considered. This represents an example with $P = 8$ again for $\overline{k} = \pi/6 \approx 0.52$. One can see that each secondary mode acts as the primary mode at a different $\overline{k}$. As in Fig. 1.2(a), the eigenvalues shown as circles are associated with values of $\overline{k}$ separated of $2\pi/(P+1)$ from each other. The primary eigenvalue, i.e. the one directly related to the baseline wavenumber $\overline{k}$, is shown as a solid circle. Note also that the primary solution mode is not necessarily the one subjected to the lowest numerical errors. In particular, there might be an eigenmode that decays slower than the primary one. This will happen if the baseline wavenumber is large enough so that a secondary wavenumber is closer to the origin of the diffusion plots when compared to the primary wavenumber (as is the case in Fig. 1.3). Finally, note that if one of the secondary wavenumbers had been chosen for the initial condition, exactly the same eigenmodes would have been energised, although their relative magnitudes would be different.

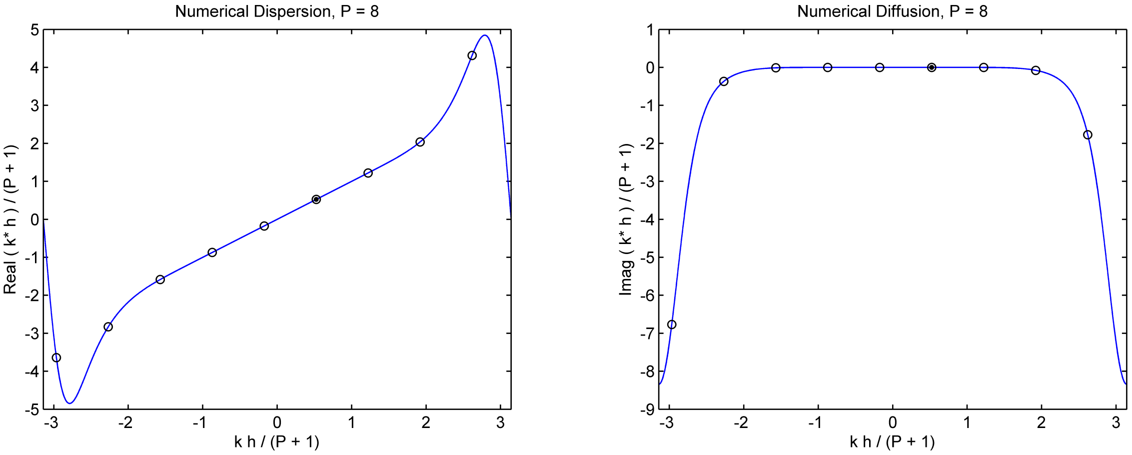

Figure 1.3: Real (left) and imaginary (right) parts of the numerical eigenvalues for all solution modes, shown along the primary mode's eigencurve, for standard upwind DG with $P = 8$ and $\overline{k} = \pi/6 \approx 0.52$.

To further understand the role of the secondary modes one can consider the following analysis. Let $\mathbb{W}$ be the set of values of m whose associated modes (or whose apparent wavenumbers) lie on the linear regions of dispersion/diffusion curves. More precisely, for $m \in \mathbb{W}$, the relations

$$\overline{k_m^*} = \overline{k} + 2\pi m/(P+1) \quad \text{or} \quad k_m^* h = kh + 2\pi m \tag{1.28}$$

are very good approximations, for some $m \in \mathbb{Z}$. A larger portion of the eigenmodes will follow the relations above as P increases, cf. Fig. 1.3. These modes ($m \in \mathbb{W}$) clearly represent the well-resolved part of the numerical solution. It is now shown that the well-resolved part of the solution within Ω_e at time t will match the well-resolved part of the solution within Ω_{e+1} at time $t+\tau_h$, where $\tau_h = h/a$. From Eqs. (1.23–1.25), one has that the well-resolved part of the solution, u^W, is given by

$$u_{e+1}^W(\xi, t+\tau_h) = \sum_{m\in\mathbb{W}} A_m\, \sigma_m(\xi)\, \exp[i(kx_{e+1} - w_m t)]\, \exp(-iw_m\tau_h) \ , \tag{1.29}$$

and since $w_m = ak_m^*$ and $\tau_h = h/a$, one has through Eq. (1.28) that

$$\exp(-iw_m\tau_h) = \exp(-ik_m^* h) = \exp(-ikh)\exp(-2\pi i m) = \exp(-ikh) \ , \tag{1.30}$$

provided that $m \in \mathbb{Z}$, and therefore

$$u_{e+1}^W(\xi, t+\tau_h) = \sum_{m\in\mathbb{W}} A_m\, \sigma_m(\xi)\, \exp[i(kx_{e+1} - w_m t)]\, \exp(-ikh) = u_e^W(\xi, t) \ , \tag{1.31}$$

since by definition $x_{e+1} - x_e = h$.

This shows that the numerical modes related to well-resolved wavenumbers, i.e. those within the linear regions of the eigencurves, will propagate correctly the components of the numerical solution associated to their wavenumbers. In this sense, all these modes can be considered to be physical. The remaining numerical eigenmodes will be detrimental to the solution accuracy as they introduce significant dispersion and diffusion errors. However, since the apparent wavenumbers remain equispaced along the primary mode's eigencurve as P increases, a larger portion of the eigenmodes will contribute to the overall accuracy of the formulation for higher order discretisations, since the regions of negligible numerical error become larger for higher orders.

Finally, another insightful way of looking at multiple eigenmodes is the following. By resorting to the previous interpretation of apparent wavenumbers k_m linked to primary/secondary modes, one can express the solution vector of element-wise polynomial coefficients from Eq. (1.21) as

$$\vec{c} \ = \sum_{m=0}^{P} A_m\, \vec{v}_m\, \exp[i(k_m x_e - w_m^* t)] \ , \tag{1.32}$$

in which the different k_m are now used, whereas variables A_m, $\vec{v}_m$ and w_m^* are obtained as if a single eigenmode existed, namely the primary one. In particular, the numerical frequencies are defined as $w_m^* = w_0(k_m)$, where $w_0(k) = ak_0^*(k)$ denotes the complex frequency function of the primary mode. Since $k_m h = k_0 h + 2\pi m$ and, for the well-resolved modes ($m \in \mathbb{W}$), $w_m^* \approx ak_m$, one has that the well-resolved part of the solution coefficients, $\vec{c}_{\mathbb{W}}$, is to a very good approximation given by

$$\vec{c}_{\mathbb{W}} = \sum_{m\in\mathbb{W}} A_m \, \vec{v}_m \, \exp[ik_m(x_e - at)] = \exp[ik_0(x_e - at)] \sum_{m\in\mathbb{W}} A_m \, \vec{v}_m \, \exp[ik_m^{\mathrm{NY}}(x_e - at)] \; , \tag{1.33}$$

where $k_m^{\mathrm{NY}} = 2\pi m/h$ is a multiple of the mesh-based Nyquist wavenumber. The numerical solution will therefore behave, in physical space, as partially Fourier (coefficients' evolution) and partially polynomial (basis functions).

The above expression's dependency on $\theta = x_e - at$ clearly shows that the solution's well-resolved part propagates as a single signal, which is consistent with previous demonstrations. This signal is composed by the primary mode for which $m = 0$ (whereby $k_m^{\mathrm{NY}} = 0$) and by secondary ones that are spatially periodic for $\Delta x_e = h$ (within the elements). This periodicity indicates that secondary modes originate from some type of aliasing at the element level. Moreover, whenever $\Delta\theta = \Delta x_e - a\Delta t = nh$, for $n \in \mathbb{Z}$, either due to temporal or spatial (element-to-element) variations, the contributions from secondary modes will match the baseline wavenumber because $\exp(ik_m^{\mathrm{NY}} nh) = \exp(2\pi imn)$. Hence, the evolution of solution coefficients will always be intrinsically governed by the primary eigenmode, so long as only well-resolved modes are taken into account. Nevertheless, for "incomplete" variations in θ, such as when $0 < \mathrm{mod}(\Delta t, h/a) < 1$, secondary modes will manifest as wavenumbers different than the baseline one — as if intrusive frequencies were present (also anticipated previously in this section). In any case, when marginally resolved modes are considered as well, the numerical solution will of course involve significant dispersive/diffusive behaviour and the properties just described will only hold partially. Fortunately, as will be discussed in the next section, under-resolved modes tend to be strongly dissipated in properly stabilised discretisations, especially at higher orders.

1.3.3 Effective resolution according to the "1% rule"

All the information regarding dispersion and diffusion characteristics of a DG simulation (of linear advection) is contained in the eigencurves of the primary mode. Therefore, one can anticipate using these eigencurves to quantify the effective resolution that a given *hp* setting can provide. Here, this resolution is measured in terms of the largest wavenumber that can be accurately resolved to within a tolerance of 1%. Although points per wavelength estimates have already been obtained for DG in previous works, e.g. [28], a more physical interpretation is here explored for the adopted tolerance.

As shown in Sec. 1.3.2, the range of wavenumbers for which wave propagation can be considered accurate corresponds to the linear regions of dispersion/diffusion curves. And since dissipation errors have been found to be stronger than dispersion errors in this well resolved range [23, 27], one can focus on defining the extent of the plateau region of dissipation curves. A physical interpretation for the imaginary part of $\overline{k^*} = k^* h/(P+1)$ is discussed in the following.

When expressing the modified wavenumber in the form $k^* = k_R^* + ik_I^*$, a propagating wave can be represented as

$$u \propto \exp[i(kx - w^* t)] = \exp(ak_I^* t) \, \exp[i(kx - ak_R^* t)] \; , \tag{1.34}$$

where the relation $w^* = ak^*$ has been used, so that regarding the wave's amplitude one has

$$|u| \propto \exp(ak_I^* t) = \exp\left(\overline{k_I^*}\, t/\overline{\Delta t}\right) , \tag{1.35}$$

in which $\overline{\Delta t} = \overline{h}/a$ and $\overline{h} = h/(P+1)$. Since $\overline{h}$ is the length measure of a degree of freedom in DG's *hp* setting, $\overline{\Delta t}$ is the time needed for a signal to cross a single DOF. Hence, according to Eq. (1.35), for each $\Delta t = \overline{\Delta t}$ passed, the magnitude of the propagating wave is scaled by $\exp(\overline{k_I^*})$, which can then be regarded as a *damping factor per DOF crossed*. Particularly, for a damping factor of 99%, the value of $\overline{k_I^*}$ would be $\ln(0.99) \approx -0.01$. As demonstrated further on, this value appears to be an excellent choice to define the extent of the plateau region for each given polynomial order. In summary, the "1% rule" consists in relying on the wavenumber $k = k_{1\%}$ for which $\exp(\overline{k_I^*}) = 0.99$ to differentiate between regions of negligible ($k < k_{1\%}$) and significant ($k > k_{1\%}$) dissipation.

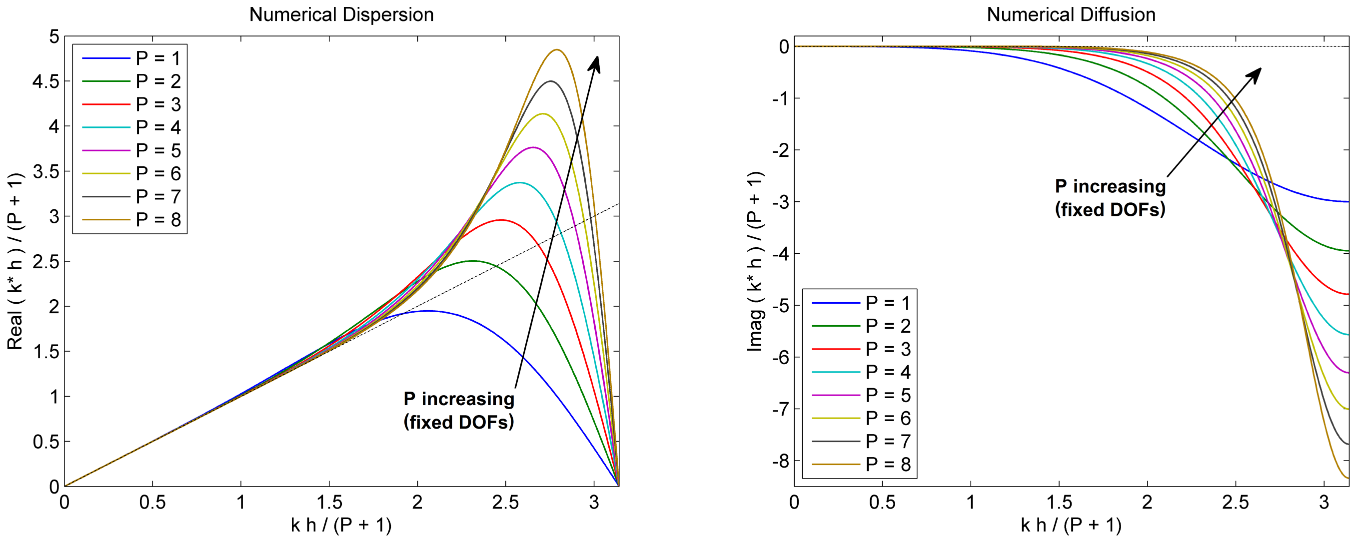

Figure 1.4: Dispersion (left) and diffusion (right) eigencurves of the standard upwind DG formulation for increasing polynomial order P. Note that only positive wavenumbers are shown.

Fig. 1.4 shows dispersion and diffusion characteristics at different polynomial orders P for the standard upwind DG scheme. Particularly, the plateau region in the diffusion curves becomes larger for increasing orders. Given P, it is possible to determine the largest value of $\overline{k}_{1\%}$ within the plateau region through the 1% rule. Then, given h, one can obtain the corresponding value of $k_{1\%}$. Fig. 1.4 also shows that the dissipation affecting wavenumbers outside the plateau region increases with P.

A summary of the relevant quantities obtained from the diffusion curves is given in Table 1.1 for $P = 1, \ldots, 8$. The second and third columns in Table 1.1 show the values of $|\overline{k}|_{1\%}$ and $|kh|_{1\%}$, respectively, achieved within an *hp* setting with standard upwind DG. Through these values, one can also estimate the coarsest mesh spacing that can be used in order to resolve scales up to a given wavenumber. The fourth column shows the associated number of degrees of freedom per wavelength, $\text{DOFpW} = 2\pi/\overline{k}_{1\%}$. This column shows that the DG discretisation becomes more efficient *per degree of freedom* as the polynomial order is increased. In fact, spectral-like resolution [31] is approached for increasing P on a per degree of freedom basis, as shown in Fig. 1.4.

The last two columns in Table 1.1 show respectively the values of $\overline{k_I^*}$ at the Nyquist wavenumber

$\overline{k} = \pi$ and the associated damping factors per DOF, namely $\exp(\overline{k_I^*})_\pi$. These quantities represent the amount of dissipation affecting the smallest captured scales and can be seen to become stronger for increasing P. For $P = 2$, where $\exp(\overline{k_I^*})_\pi \approx 2 \times 10^{-2}$, the smallest scales would propagate more than two DOFs to suffer the same damping provided for a single DOF by the $P = 7$ discretisation, in which $\exp(\overline{k_I^*})_\pi \approx 5 \times 10^{-4}$. This is probably an extra advantage of employing higher order discretisations, since as previously recognised a faster damping of the poorly-resolved scales further precludes them from polluting the numerical solution.

Table 1.1: Relevant diffusion-based quantities of standard upwind DG for increasing P

P	$\lvert\overline{k}\rvert_{1\%}$	$\lvert kh\rvert_{1\%}$	DOFpW	$(\overline{k_I^*})_\pi$	$\exp(\overline{k_I^*})_\pi$
1	0.5635	1.127	11.15	-3.00	4.98×10^{-2}
2	0.8721	2.616	7.20	-3.95	1.93×10^{-2}
3	1.0825	4.330	5.80	-4.79	8.31×10^{-3}
4	1.2327	6.164	5.10	-5.57	3.81×10^{-3}
5	1.3451	8.071	4.67	-6.32	1.80×10^{-3}
6	1.4324	10.027	4.39	-7.01	9.03×10^{-4}
7	1.5022	12.018	4.18	-7.60	5.00×10^{-4}
8	1.5594	14.035	4.03	-8.34	2.39×10^{-4}

1.4 Experiments in Burgers turbulence

In order to assess the methodology proposed in Sec. 1.3.3 for non-linear problems, the forced Burgers turbulence [32] problem is now considered. The adopted forcing approach follows that of [33], where a white-in-time random force $F(x,t)$ is employed with Fourier components

$$F_k(t) = \frac{A\,\sigma_k(t)}{\sqrt{\Delta t}\sqrt{k}} \ , \ \text{for} \ k = \frac{2\pi n}{L} \ \text{and} \ n \in \mathbb{Z} \ , \tag{1.36}$$

where k stands for the wavenumber, A is an amplitude constant, σ_k is a standard Gaussian random function (white-in-time), while Δt and L are the time step and the length of the domain used in the simulation. The forcing function has been used in previous studies [34, 35] as it yields a $-5/3$ slope for the inertial range of the energy spectrum and is therefore more representative of Navier-Stokes turbulence. In what follows, this forcing approach is applied to the inviscid Burgers equation.

The forcing cut-off wavenumber k_c is normally placed inside the dissipation range, but here the effect of the forcing term has been restricted to the inertial range so that it would not counteract the diffusion provided by the DG scheme on the (numerically induced) dissipation range. It is worth noting, however, that once a statistically steady state is reached, the energy transfer by the cascade mechanism is defined by the large scales (forced) and remains constant across the unforced inertial range. The considered Burgers equation with added forcing takes the form

$$\frac{\partial u}{\partial t} + \frac{1}{2}\frac{\partial u^2}{\partial x} = \frac{A_F}{\sqrt{\Delta t}} \sum_{N \in \mathbb{N}_F} \frac{\sigma_N(t)}{\sqrt{|N|}} \exp\left(i\,\frac{2\pi N}{L} x \right) \ , \tag{1.37}$$

where $\mathbb{N}_F = \{\pm 1, \ldots, \pm N_c\}$ and the cut-off wavenumber is $k_c = 2\pi N_c/L$, i.e. $F_k = 0$ if $k > k_c$. The Gaussian variable σ_N is generated from a standard distribution (zero mean and unit variance) for each wavenumber at each new time step.

The standard upwind DG scheme, cf. Eq. (1.6), was used for the simulations with exact integrations to avoid polynomial aliasing. For the non-linear term, Gauss-Legendre quadratures were used with the required number of nodes to ensure exact integration. For the forcing term, the Galerkin projection of the Fourier components was carried out analytically through the relations given in Eqs. (1.15–1.17). These were however numerically stripped from the secondary modes originating from each single Fourier component through a "filtering" procedure based on the system of eigenmodes discussed in Sec. 1.3.1. A detailed description of this procedure is given in this chapter's appendix.

Table 1.2: Summary of test cases (and their shorthand acronyms)

$N_{dof}\backslash P$	1	2	3	4	5	6	7
1024	$a1$	$a2$	$a3$	$a4$	$a5$	$a6$	$a7$
2048	$b1$	$b2$	$b3$	$b4$	$b5$	$b6$	$b7$
4096	$c1$	$c2$	$c3$	$c4$	$c5$	$c6$	$c7$

The test cases addressed here are summarized in Table 1.2, where letters (a, b, c) refer to the total number of DOFs while numbers $(1, \ldots, 7)$ refer to the polynomial order employed in each case. The number of mesh elements can be evaluated as $N_{dof}/(P+1)$. For all the cases, Eq. (1.37) was solved within $\Omega = [-1, 1]$ (and so $L = 2$) with periodic boundary conditions and started from a constant initial condition $u_0 = 1$. Time-stepping relied on an explicit third-order Runge-Kutta TVD algorithm [36] with $\Delta t = 4 \times 10^{-5}$ in all test cases, yielding CFL ≈ 0.1 for the stiffest case ($c7$).

The forcing amplitude constant was set to $A_F = 1/2$ for all test cases. Time integrations were performed over the interval $0 \leq t \leq 600$. A snapshot of the solution at $t = 600$ for the case $c7$ is shown in Fig. 1.5 along with the history of the space-averaged fluctuation $u'_{rms}(t)$. For all test cases addressed, a statistical steady state with an ensemble average of $< u'_{rms} > \approx 0.03$ is reached after approximately $t = 50$. The turnover time of the largest eddies can be estimated as $\tau_0 = L/u'_{rms} \approx 67$.

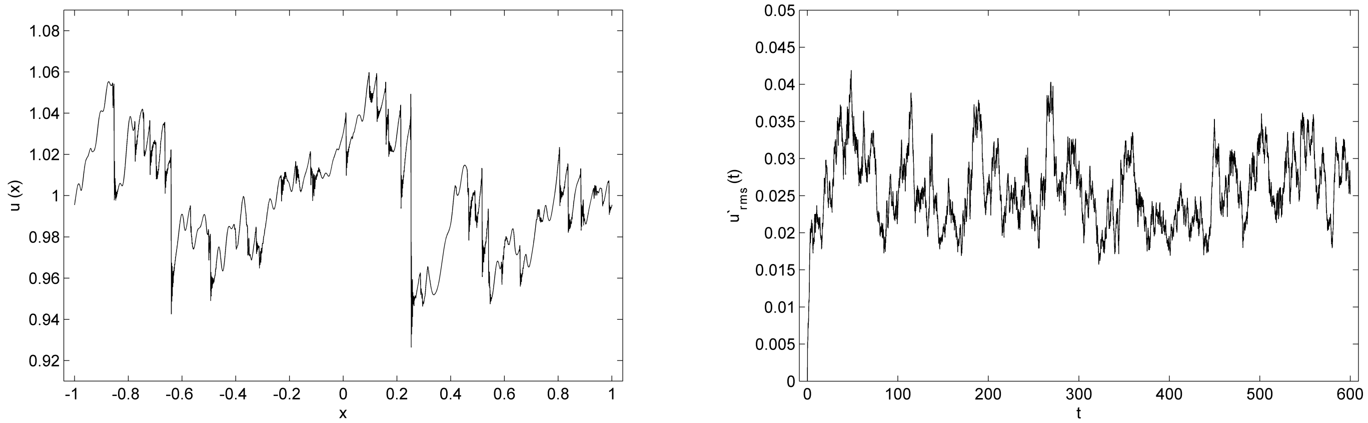

Figure 1.5: Solution snapshot at $t = 600$ (left) and space-averaged fluctuation $u'_{rms}(t)$ history (right), for the test case $c7$.

The time-averaged energy spectrum $ES(k)$ representing the distribution of turbulent kinetic energy in wavenumber space is given in Fig. 1.6 again for the case $c7$. This spectrum corresponds to the average of two hundred spectra obtained from successive applications of Taylor's hypothesis [37, 38] over the interval $200 \leq t \leq 600$. Each of these spectra was evaluated by probing the solution at $x = 0$ over time windows of span $\delta t = L/u_0 = 2$. Note also that $u_0 = 1$ remains the average of u within Ω for all times since neither the forcing nor the non-linear dynamics of the Burgers equation affect the average value (component $k = 0$) of the solution.

For all cases addressed, the forcing in Eq. (1.37) was implemented with $N_c = 80$. As a result, the energy spectrum shown in Fig. 1.6 features the $-5/3 \approx -1.7$ slope up to $\log_{10}(k_c) = \log_{10}(\pi N_c) \approx 2.4$, as expected of the forcing strategy adopted. After that, a slope of -2, typical of unforced Burgers turbulence [32], takes place until numerical diffusion is seen to affect the spectrum. The effective *hp* resolution estimated from the 1% rule for this case is shown as a vertical line in Fig. 1.6. This estimate accurately pinpoints the beginning of the dissipation range. Another effect of the numerical errors is seen in the form of a bump on the energy spectrum around $k_{1\%}$. These "energy bumps" become more noticeable at higher values of P, as will be shown in Fig. 1.8. As this phenomenon is still unclear at this point, the discussion of its causes and effects is left for future studies. Regardless, the accuracy of the 1% rule's estimates is very good for all the cases addressed and is even better for the higher orders, where the impact of numerical errors is more localized (in wavenumber space).

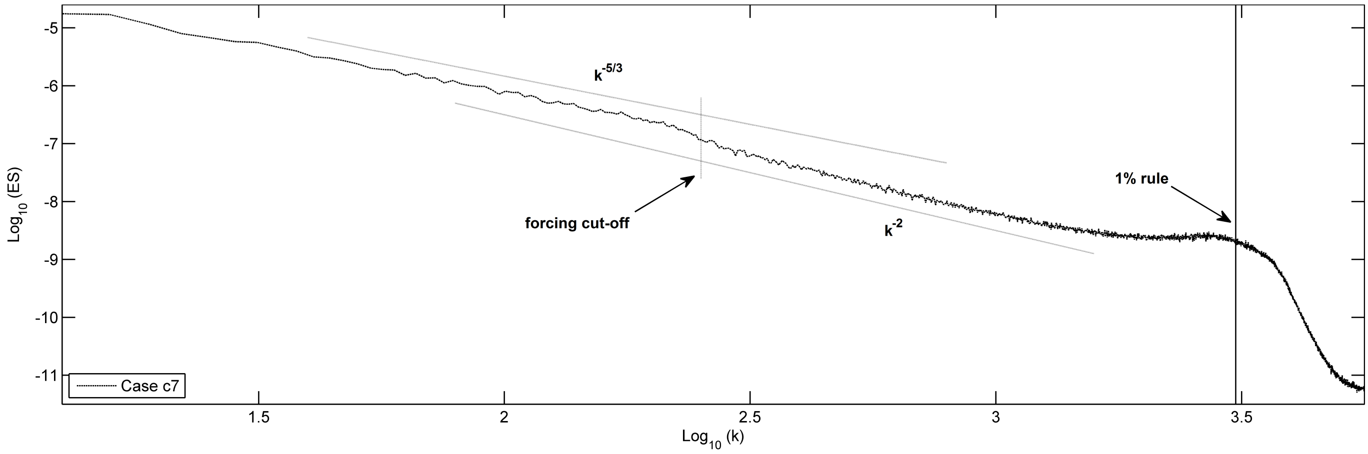

Figure 1.6: Time-averaged energy spectrum for the test case $c7$, featuring slopes of $-5/3$ and -2 respectively on the forced and unforced regions of the inertial range, as well as a numerical dissipation region taking place as predicted by the 1% rule (vertical line).

The effect of mesh refinement is shown in Fig. 1.7, where the energy spectra of cases $a4$, $b4$ and $c4$ are depicted. Once again, the vertical lines mark the values of $k_{1\%}$ obtained from the 1% rule and these match quite well the beginning of the dissipation range for each test case. Fig. 1.7 also helps to clarify *why* the DG formulation can be suitable for under-resolved simulations of turbulence: the numerical discretisation is capable of resolving scales up to $k_{1\%}$ with good accuracy while dissipation is provided at the end of the energy spectrum in the form of numerical diffusion. In this sense, DG-uDNS seems closer to hyperviscosity approaches to turbulence than to LES approaches based on (explicit or implicit) subgrid-scale modelling.

In the application of the 1% rule, although $|kh|_{1\%}$ varies with P (Table 1.1), the resolution gain (in log scale) obtained with a given mesh refinement factor $f = h/h'$ does not depend on P. This is because, for each P,

$$\log(k'_{1\%}) - \log(k_{1\%}) = \log\left(\frac{|kh|_{1\%}}{h'}\right) - \log\left(\frac{|kh|_{1\%}}{h}\right) = \log(h/h') = \log(f) \ . \tag{1.38}$$

In the test cases considered, where a mesh refinement factor of $f = 2$ separates cases *a*-*b* or *b*-*c* for each P, the expected resolution gain is given by $\log_{10}(2) \approx 0.3$, which is also visible in Fig. 1.7.

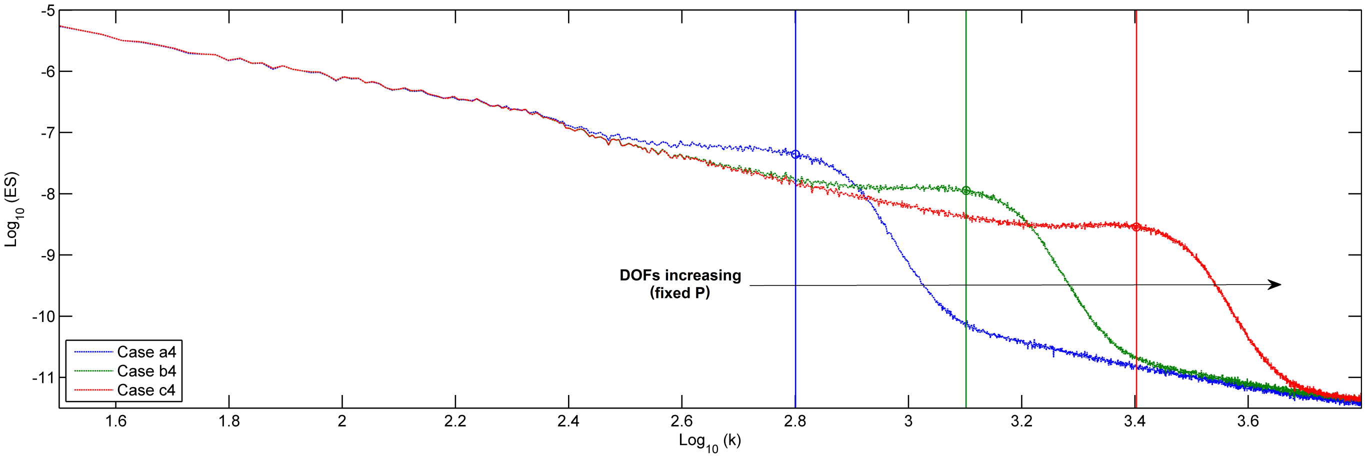

Figure 1.7: Energy spectra of the $P = 4$ test cases ($a4$, $b4$, $c4$) along with the 1% rule estimates for the beginning of the dissipation range (vertical lines). Circles are used pinpoint the intersection between the energy spectra and their respective 1% rule estimates.

On the other hand, the actual value of $k_{1\%}$ is strongly dependent on P. The effect of increasing P is considered in Fig. 1.8, where compensated spectra (for the unforced inertial range) are shown for cases $c1, c2, \ldots, c7$. The horizontal lines correspond exactly to the same value of -2.23, which was defined so as to fit the compensated unforced inertial range of test case $c7$. This value is taken as a reference for all the inertial ranges shown in Fig. 1.8. The estimates for the beginning of the dissipation range obtained from the 1% rule are again depicted as vertical lines at the right end of each horizontal line. The energy spectra in question correspond to a fixed number of DOFs and, as P increases in Fig. 1.8, mesh spacing therefore becomes coarser. The vertical lines corresponding to the 1% rule show that, for a given number of DOFs, employing higher-order discretisations along with coarser meshes yields superior resolution but, as predicted in Table 1.1, the resolution gain per DOF does not increase significantly beyond a sufficiently large order (say, $P > 5$). Furthermore, as much higher polynomial orders would induce stronger energy bumps, it is probably safer to favour moderately high orders so as to avoid potentially undesirable effects related to energy bumps. This point however requires further investigation.

In any event, the 1% rule showed to be, even in a non-linear setting, reliable in predicting the wavenumber $k_{1\%}$ where numerical errors become significant and after which a numerically induced dissipation range takes place. It provides guidelines for designing an *hp* approximation space, thus clarifying *how* the DG formulation can be better used for under-resolved turbulence simulations. In particular, the use of higher-order discretisations along with coarser meshes is expected to be the most efficient way to translate available resources into resolution power. A comparison between test

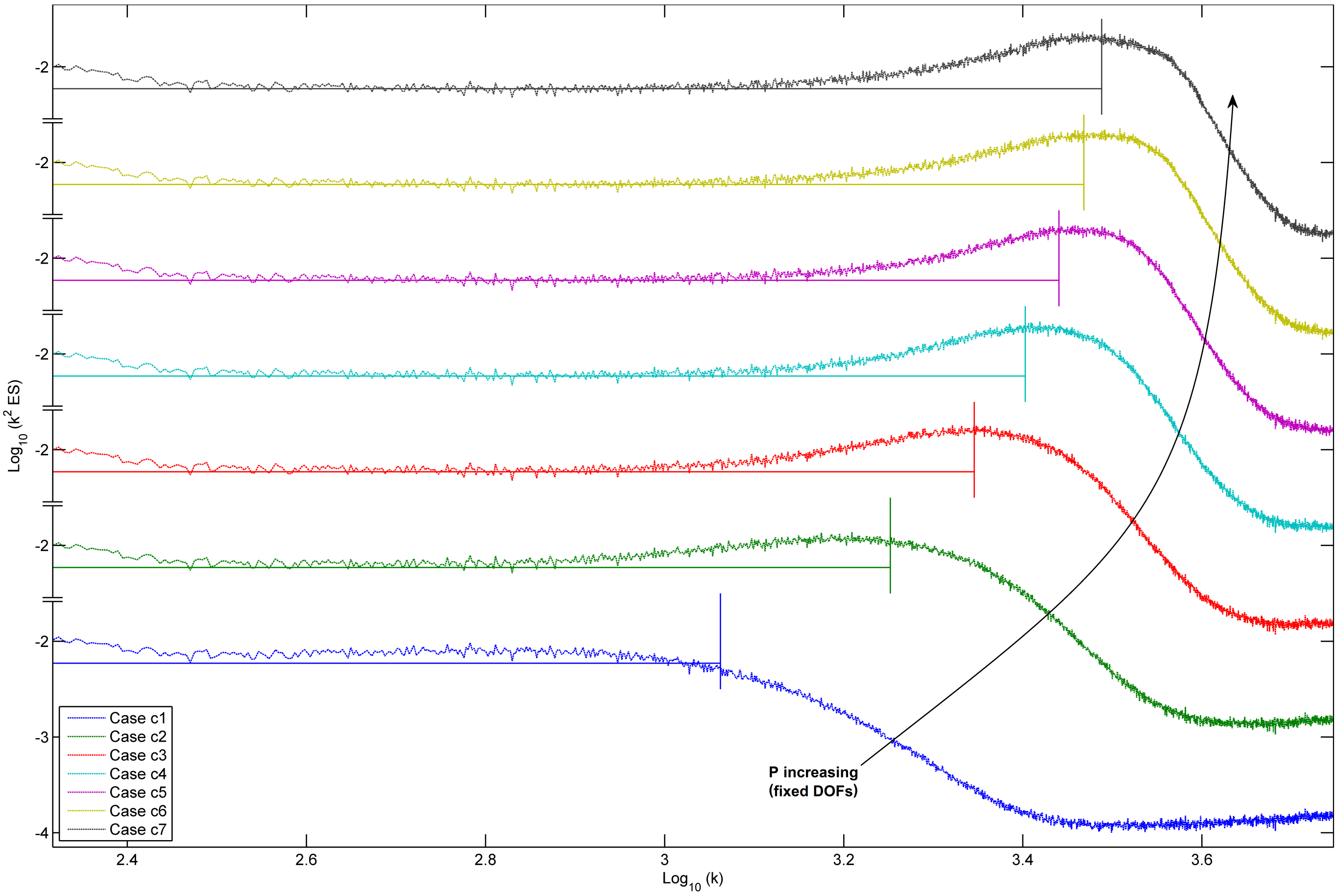

Figure 1.8: Compensated spectra (for the unforced inertial range) of test cases $c1, c2, \ldots, c7$ alongside their respective 1% rule estimates for the beginning of the dissipation range (vertical lines). All horizontal lines correspond to the value -2.23, defined to fit the inertial range of test case $c7$.

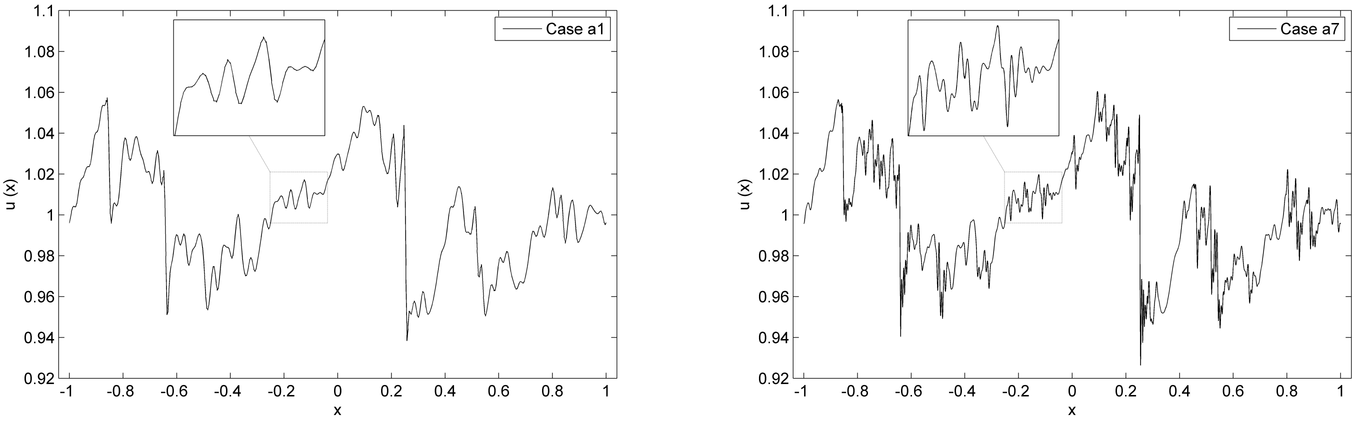

Figure 1.9: Comparison between solution snapshots at $t = 600$ for test cases $a1$ (left) and $a7$ (right). Though having the same number of DOFs, the higher-order simulation is able to capture a much broader range of small structures.

cases $a1$ and $a7$, which have the same number of DOFs, is shown in Fig. 1.9 for $t = 600$. The case with a $(7+1)/(1+1) = 4$ times coarser mesh but $P = 7$ can capture a much broader range of small structures. This feature has also been recognized in previous works [17, 18]. Note that P-type refinement has long been recognized as more efficient than h-type refinement [4, 25] owing to the exponential (also called spectral) convergence property, but this only holds for well-resolved simulations, where all the wavenumbers captured are well within the linear regions of dispersion and diffusion curves, see [27]. Here the advantages of favouring P over h is highlighted for under-resolved turbulence simulations.

The comparison in Fig. 1.9 is relevant because the random number generator employed for the forcing variable $\sigma_k(t)$ is deterministic and therefore the same forcing function was used in both test cases through the whole integration period. Note however that the computational cost of spectral/*hp* methods in terms of floating point operations clearly does not scale linearly with DOFs. Nevertheless, on emerging hardware, large scale computations required for turbulence simulations at high Reynolds number are becoming more communication bandwidth-limited than floating point operation-limited and therefore the total number of DOFs is becoming a more relevant measure of performance.

1.5 Conclusion

In this chapter, a linear dispersion-diffusion analysis was employed to provide direct guidelines for the selection of spatial resolution in simulations of turbulence through the under-resolved DNS (uDNS) approach via high-order discontinuous Galerkin (DG) spectral/*hp* methods. The role of multiple numerical eigenmodes, peculiar to spectral/*hp* methods, was discussed and clarified. Secondary modes have been shown to replicate the behaviour of the primary ones, whereby all of DG's propagation properties (for linear advection) are given in the dispersion/diffusion eigencurves of primary modes. From these curves, numerical errors were assessed (diffusion in particular) and their effect on poorly-resolved scales was quantified. A simple criterion named "the 1% rule" was then proposed to estimate the effective resolution provided by an *hp* setting in terms of the largest wavenumber $k_{1\%}$ that can be accurately resolved by the approximation space.

Though strictly valid for linear advection, the 1% rule was tested against Burgers turbulence and found to predict quite accurately the beginning of the (numerically induced) dissipation range on the energy spectra of under-resolved simulations. The results shed some light on *why* the DG formulation is be able to provide good results for uDNS without sub-grid scale models. Essentially, the numerical discretisation is capable of resolving scales up to $k_{1\%}$ with high accuracy while providing dissipation at the end of the energy spectrum in the form of numerical diffusion. In this sense, DG-uDNS seems closer to hyperviscosity approaches than to LES (or iLES) approaches based on explicit (or implicit) SGS modelling. Also, the 1% rule provides useful guidelines on *how* to better use DG for uDNS. In particular it was shown that, given a limited number of degrees of freedom, the use of higher-order polynomials along with coarser meshes is the best way to translate available resources into resolution power. The advantages of this strategy (as compared to mesh refinement) were first pointed out in [18], but on a more qualitative basis.

It should be stressed that the 1% rule is not expected to be directly applicable (in its present form) to all kinds of turbulence, including Navier-Stokes turbulence. And it does not indicate whether DG-based under-resolved simulations might diverge numerically due to insufficient resolution. Still, should the proposed methodology (with due adaptations) be valid for real turbulent flows, the concept of effective resolution (embodied in $k_{1\%}$) would play in the uDNS context the role played by the filter width in classical LES. While the SGS model in LES (ideally) begins to act on scales smaller than the filter width, in uDNS a strong numerical dissipation provides a sink for the energy cascade at wavenumbers greater than $k_{1\%}$. For the Navier-Stokes equations in three dimensions, the smallest captured scales should be affected, amongst other factors, by the numerical (inviscid and viscous) fluxes employed, the mesh topology and type of elements used. Subsequent studies on the applicability of the 1% rule for real three-dimensional turbulent flows are planned for the near future.

Appendix

This section is devoted to the description of how the source term in Eq. (1.37) was taken into account in the discretisation of the forced Burgers turbulence problem considered in Sec. 1.4.

It is useful to start with Eq. (1.37) in the form

$$\frac{\partial u}{\partial t} + \frac{\partial f}{\partial x} = S \ , \tag{1.39}$$

where $f = u^2/2$ and the source term is given by

$$S = \frac{A_F}{\sqrt{\Delta t}} \sum_{N \in \mathbb{N}_F} \frac{\sigma_N(t)}{\sqrt{|N|}} \exp\left(i k_N x\right) \ , \tag{1.40}$$

in which $k_N = 2\pi N/L$. The remaining variables are defined as in Sec. 1.4.

After the customary steps, cf. Sec. 1.2, the semi-discrete evolution equation for the element-wise coefficients of Ω_e can be found, namely

$$\frac{h}{2}\frac{\partial c_j}{\partial t} = \int_{\Omega_{st}} f\,\phi_j'\,d\xi \,-\, (\tilde{f}\phi_j)|_{\Omega_e^R} \,+\, (\tilde{f}\phi_j)|_{\Omega_e^L} \,+\, \frac{h}{2}\int_{\Omega_{st}} S\,\phi_j\,d\xi \ , \tag{1.41}$$

where Ω_e^L and Ω_e^R denote the left and right boundaries of element Ω_e, respectively, while $\tilde{f}$ is the (standard upwind) numerical flux evaluated at the respective interfaces. Unpacking the last integral above leads to the term

$$\int_{\Omega_{st}} \exp\left[i k_N \left(x_e + \xi h/2\right)\right] \phi_j(\xi)\,d\xi \,=\, \exp\left(i k_N x_e\right) \int_{\Omega_{st}} \exp\left(i k_N h \xi/2\right) \phi_j(\xi)\,d\xi \,=\, \exp\left(i k_N x_e\right) \alpha_j\left(k_N h\right) \ , \tag{1.42}$$

where x_e denotes the centre (midpoint) of Ω_e and α_j is given analytically in Eqs. (1.15–1.17).

In vector form, Eq. (1.41) is given by

$$\frac{h}{2}\frac{\partial \vec{c}}{\partial t} = \int_{\Omega_{st}} f\,\vec{\phi}'\,d\xi \;-\; (\tilde{f}\vec{\phi})|_{\Omega_e^R} \;+\; (\tilde{f}\vec{\phi})|_{\Omega_e^L} \;+\; \frac{h}{2}\,\vec{S}_\alpha \;, \tag{1.43}$$

in which $\vec{c} = \{c_0, \ldots, c_P\}^T$ and

$$\vec{S}_\alpha = \frac{A_F}{\sqrt{\Delta t}} \sum_{N\in\mathbb{N}_F} \frac{\sigma_N(t)}{\sqrt{|N|}} \exp\left(i k_N x_e\right) \vec{\alpha}(k_N h) \tag{1.44}$$

where $\vec{\alpha} = \{\alpha_0, \ldots, \alpha_P\}^T$. As discussed in Sec. 1.3.1, the projection of each single Fourier mode is expected to energize several $(P+1)$ numerical modes with only one of them corresponding to the actual (baseline) wavenumber of the underlying Fourier component. To avoid this, $\vec{S}_\alpha$ is replaced with $\vec{S}_\beta$ in Eq. (1.43), where $\vec{\beta}$ can be regarded as a filtered version of $\vec{\alpha}$ which energizes only the primary eigenmode originating from each Fourier component of the forcing term.

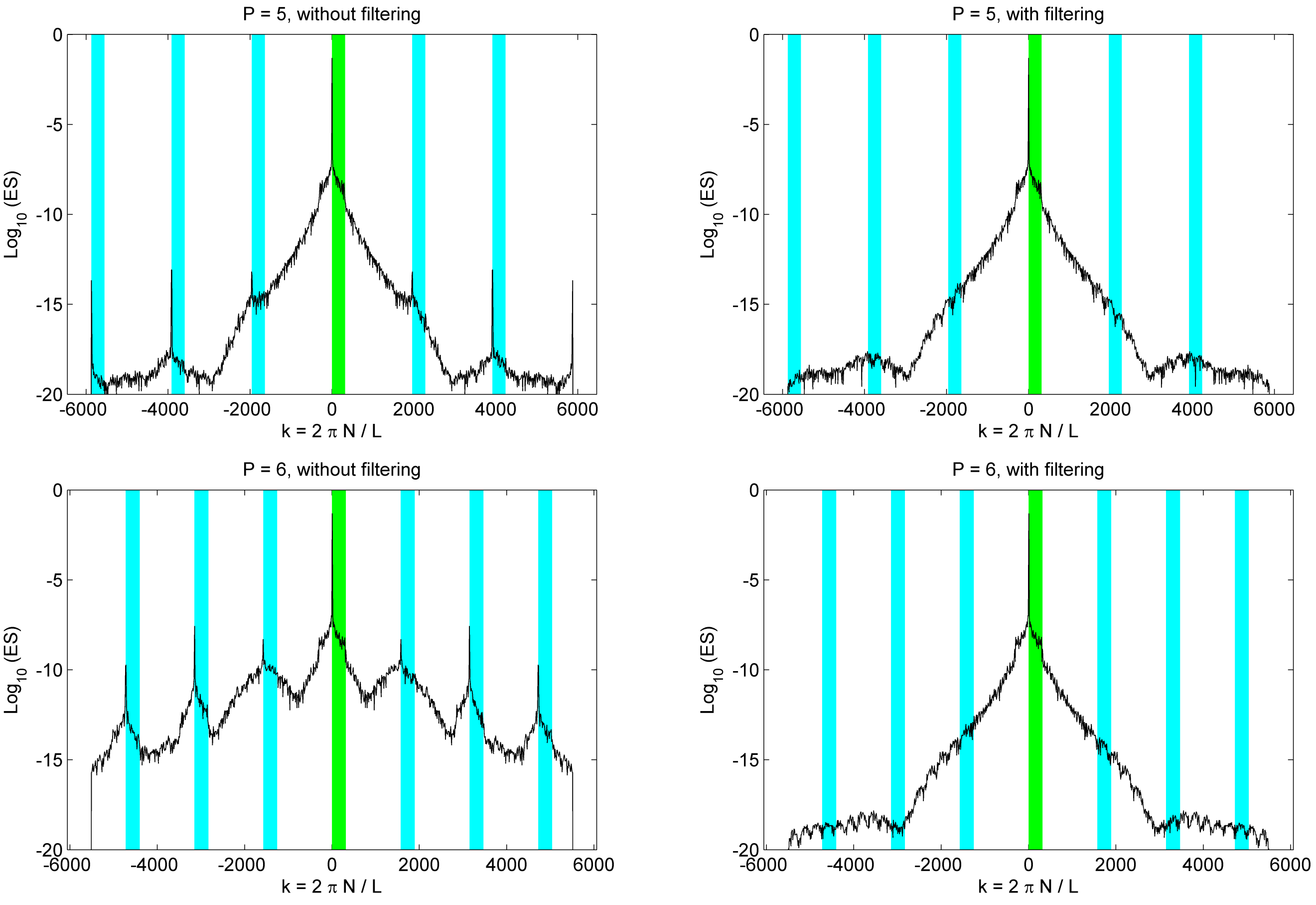

Figure 1.10: Comparison between unfolded energy spectra of simulations carried without (left) and with (right) filtering, exemplified for $P = 5$ (top) and $P = 6$ (bottom). The highlighted wavenumbers near $k = 0$ correspond to the positive Fourier components of the forcing term. The other highlighted wavenumbers are their respective secondary components, avoided through the proposed filtering.

From Eqs. (1.21–1.22), the amplitude A_m of a numerical eigenmode energized by a given Fourier component can be obtained from the projection array $\vec{\alpha}$ of such Fourier mode through the relation $\vec{A} = \boldsymbol{\mathcal{V}}^{-1}\vec{\alpha}$, where $\vec{A} = \{A_0, \ldots, A_P\}^T$ and $\boldsymbol{\mathcal{V}} = \{\vec{v}_0, \ldots, \vec{v}_P\}$ is the matrix whose columns are the eigenvectors related to the projection operator as defined in Eqs. (1.19–1.20). Let M be the index of the primary eigenmode according to the sorting adopted for the entries of $\vec{A}$. One seeks $\vec{\beta}$ such that $\vec{B} = \boldsymbol{\mathcal{V}}^{-1}\vec{\beta}$ with $\vec{B} = \{0, \ldots, 0, A_M, 0, \ldots, 0\}^T$, which can be expressed as $\vec{B} = \boldsymbol{\mathcal{F}}_M \vec{A}$, where $\boldsymbol{\mathcal{F}}_M$ is employed to filter out from $\vec{A}$ all the secondary eigenmodes and retain only the primary one (of index M). Hence, $(\boldsymbol{\mathcal{F}}_M)_{i,j} = \delta_{i,M}\,\delta_{M,j}$ in which $\delta_{i,j}$ is the Kronecker delta. The resulting expression for $\vec{\beta}$ is

$$\vec{\beta} = \boldsymbol{\mathcal{V}}\,\vec{B} = \boldsymbol{\mathcal{V}}\,\boldsymbol{\mathcal{F}}_M\,\vec{A} = \boldsymbol{\mathcal{V}}\,\boldsymbol{\mathcal{F}}_M \boldsymbol{\mathcal{V}}^{-1}\vec{\alpha}\ . \tag{1.45}$$

Note that index M can be identified from the one-to-one correspondence between eigenvalues and eigenvectors in Eqs. (1.19–1.20), since a primary eigenvalue can be more easily distinguished from the secondary ones when compared along dispersion-diffusion curves.

To illustrate the filtering technique, four test cases are considered, for $P = 5$ and $P = 6$, with and without filtering. Simulations carried with no filtering led to early numerical divergence, especially for the highest polynomial orders. To obtain some results before divergence, simulations were integrated in time until $t = 1$ and compared. The energy spectra evaluated through a discrete Fourier transform (in space) are given in Fig. 1.10. Note that “unfolded” energy spectra are shown in Fig. 1.10, where positive and negative wavenumbers are distinguished. Symmetrical plots are obtained due to the conjugate symmetry of the forcing term, which is required to guarantee a real solution at all times. The highlighted wavenumbers close to $k = 0$ correspond to the positive Fourier components of the forcing term. The remaining highlighted wavenumbers are their respective secondary components (recall Fig. 1.3) which can be avoided through the proposed filtering. If these secondary components are not avoided, they will grow in time and eventually lead to numerical divergence. Also, note that non-linear interactions rapidly energize wavenumbers in between the highlighted ranges.

References

[1] F. F. Grinstein, L. G. Margolin, and W. J. Rider. *Implicit large eddy simulation: computing turbulent fluid dynamics.* Cambridge University Press, 2007.

[2] S. B. Pope. Ten questions concerning the large-eddy simulation of turbulent flows. *New Journal of Physics*, 6(1):35, 2004.

[3] P. R. Spalart. Strategies for turbulence modelling and simulations. *International Journal of Heat and Fluid Flow*, 21(3):252–263, 2000.

[4] G. E. Karniadakis and S. J. Sherwin. *Spectral/hp element methods for computational fluid dynamics.* Oxford University Press, 2nd edition, 2005.

[5] G. S. Karamanos and G. E. Karniadakis. A spectral vanishing viscosity method for large-eddy simulations. *Journal of Computational Physics*, 163(1):22–50, 2000.

[6] R. M. Kirby and G. E. Karniadakis. De-aliasing on non-uniform grids: algorithms and applications. *Journal of Computational Physics*, 191(1):249–264, 2003.

[7] A. Uranga, P. O. Persson, M. Drela, and J. Peraire. Implicit large eddy simulation of transition to turbulence at low Reynolds numbers using a discontinuous Galerkin method. *International Journal for Numerical Methods in Engineering*, 87(1-5):232–261, 2011.

[8] A. D. Beck, T. Bolemann, D. Flad, H. Frank, G. J. Gassner, F. Hindenlang, and C. D. Munz. High-order discontinuous Galerkin spectral element methods for transitional and turbulent flow simulations. *International Journal for Numerical Methods in Fluids*, 76(8):522–548, 2014.

[9] C. Liang, S. Premasuthan, A. Jameson, and Z. J. Wang. Large eddy simulation of compressible turbulent channel flow with spectral difference method. In *Proceedings of the 47th AIAA Aerospace Sciences Meeting (AIAA Paper 2009-402)*, Orlando, USA, 2009.

[10] M. Parsani, G. Ghorbaniasl, C. Lacor, and E. Turkel. An implicit high-order spectral difference approach for large eddy simulation. *Journal of Computational Physics*, 229(14):5373–5393, 2010.

[11] B. C. Vermeire, J. S. Cagnone, and S. Nadarajah. ILES using the correction procedure via reconstruction scheme. In *Proceedings of 51st AIAA Aerospace Sciences Meeting (AIAA Paper 2013-1001)*, Grapevine, USA, 2013.

[12] B. C. Vermeire, S. Nadarajah, and P. G. Tucker. Canonical test cases for high-order unstructured implicit large eddy simulation. In *Proceedings of the 52nd AIAA Aerospace Sciences Meeting (AIAA Paper 2014-0935)*, National Harbour, USA, 2014.

[13] R. M. Kirby and S. J. Sherwin. Stabilisation of spectral/hp element methods through spectral vanishing viscosity: application to fluid mechanics modelling. *Computer Methods in Applied Mechanics and Engineering*, 195(23):3128–3144, 2006.

[14] S. S. Collis. Discontinuous Galerkin methods for turbulence simulation. In *Proceedings of the 2002 Center for Turbulence Research Summer Program*, pages 155–167, 2002.

[15] S. S. Collis and K. Ghayour. Discontinuous Galerkin methods for compressible DNS. In *Proceedings of the 4th ASME/JSME Joint Fluids Summer Engineering Conference*, pages 1777–1786, 2003.

[16] L. Wei and A. Pollard. Direct numerical simulation of compressible turbulent channel flows using the discontinuous Galerkin method. *Computers & Fluids*, 47(1):85–100, 2011.

[17] J. B. Chapelier, M. de la Llave Plata, F. Renac, and E. Lamballais. Evaluation of a high-order discontinuous Galerkin method for the DNS of turbulent flows. *Computers & Fluids*, 95:210–226, 2014.

[18] G. J. Gassner and A. D. Beck. On the accuracy of high-order discretizations for underresolved turbulence simulations. *Theoretical and Computational Fluid Dynamics*, 27(3-4):221–237, 2013.

[19] G. I. Taylor and A. E. Green. Mechanism of the production of small eddies from large ones. *Proceedings of the Royal Society of London (A)*, 158(895):499–521, 1937.

[20] C. Carton de Wiart, K. Hillewaert, M. Duponcheel, and G. Winckelmans. Assessment of a discontinuous Galerkin method for the simulation of vortical flows at high Reynolds number. *International Journal for Numerical Methods in Fluids*, 74(7):469–493, 2014.

[21] L. G. Margolin and W. J. Rider. A rationale for implicit turbulence modelling. *International Journal for Numerical Methods in Fluids*, 39(9):821–841, 2002.

[22] R.C. Moura, S.J. Sherwin, and J. Peiró. Modified equation analysis for the discontinuous Galerkin formulation. In *Proceedings of the 10th International Conference on Spectral and High Order Methods (ICOSAHOM)*, Salt Lake City, USA, 2014.

[23] F. Q. Hu, M. Y. Hussaini, and P. Rasetarinera. An analysis of the discontinuous Galerkin method for wave propagation problems. *Journal of Computational Physics*, 151(2):921–946, 1999.

[24] F. Q. Hu and H. L. Atkins. Eigensolution analysis of the discontinuous Galerkin method with nonuniform grids: I. one space dimension. *Journal of Computational Physics*, 182(2):516–545, 2002.

[25] J. S. Hesthaven and T. Warburton. *Nodal discontinuous Galerkin methods: algorithms, analysis, and applications*. Springer, 2007.

[26] S. J. Sherwin. Dispersion analysis of the continuous and discontinuous Galerkin formulations. In B. Cockburn, G. E. Karniadakis, and C. W. Shu, editors, *Discontinuous Galerkin Methods: Theory, Computation and Applications*, pages 425–431. Springer, 2000.

[27] M. Ainsworth. Dispersive and dissipative behaviour of high order discontinuous Galerkin finite element methods. *Journal of Computational Physics*, 198(1):106–130, 2004.

[28] G. Gassner and D.A. Kopriva. A comparison of the dispersion and dissipation errors of Gauss and Gauss-Lobatto discontinuous Galerkin spectral element methods. *SIAM Journal on Scientific Computing*, 33(5):2560–2579, 2011.

[29] P. E. Vincent, P. Castonguay, and A. Jameson. Insights from von Neumann analysis of high-order flux reconstruction schemes. *Journal of Computational Physics*, 230(22):8134–8154, 2011.

[30] N. Chevaugeon, K. Hillewaert, X. Gallez, P. Ploumhans, and J. Remacle. Optimal numerical parameterization of discontinuous Galerkin method applied to wave propagation problems. *Journal of Computational Physics*, 223(1):188–207, 2007.

[31] S. K. Lele. Compact finite difference schemes with spectral-like resolution. *Journal of Computational Physics*, 103(1):16–42, 1992.

[32] J. Bec and K. Khanin. Burgers turbulence. *Physics Reports*, 447(1):1–66, 2007.

[33] A. Chekhlov and V. Yakhot. Kolmogorov turbulence in a random-force-driven Burgers equation. *Physical Review E*, 51(4):R2739, 1995.

[34] O. Zikanov, A. Thess, and R. Grauer. Statistics of turbulence in a generalized random-force-driven burgers equation. *Physics of Fluids*, 9(5):1362–1367, 1997.

[35] N. A. Adams, S. Hickel, and S. Franz. Implicit subgrid-scale modeling by adaptive deconvolution. *Journal of Computational Physics*, 200(2):412–431, 2004.

[36] S. Gottlieb and C. W. Shu. Total variation diminishing Runge-Kutta schemes. *Mathematics of Computation*, 67(221):73–85, 1998.

[37] G. I. Taylor. The spectrum of turbulence. *Proceedings of the Royal Society of London. Series A-Mathematical and Physical Sciences*, 164(919):476–490, 1938.

[38] A. Bahraminasab, M. D. Niry, J. Davoudi, M. R. R. Tabar, A. A. Masoudi, and K. R. Sreenivasan. Taylor's frozen-flow hypothesis in Burgers turbulence. *Physical Review E*, 77(6):065302, 2008.

Chapter 2

Temporal eigenanalysis of continuous Galerkin solutions to advection-diffusion problems with insights into spectral vanishing viscosity

Summary †

This chapter is devoted to the temporal dispersion-diffusion analysis of the spectral/*hp* continuous Galerkin (CG) formulation in one dimension. First, numerical dispersion and diffusion curves are obtained for the advection-diffusion problem and the role of multiple eigencurves peculiar to spectral/*hp* methods is discussed. From the eigencurves' behaviour, it is observed that CG might feature potentially undesirable non-smooth dispersion/diffusion characteristics for under-resolved simulations of problems strongly dominated by either convection or diffusion. Subsequently, the linear advection equation augmented with spectral vanishing viscosity (SVV) is analysed. Dispersion and diffusion characteristics of CG with SVV-based stabilization are found to display similar non-smooth features in flow regions where convection is much stronger than dissipation or vice-versa, owing to a dependency of the standard SVV operator on a local Péclet number. First, a modification is proposed to the traditional SVV scaling that enforces a globally constant Péclet number so as to avoid the previous issues. In addition, a new SVV kernel function is suggested and shown to provide a more regular behaviour for the eigencurves along with a consistent increase in resolution power for higher-order discretisations, as measured by the extent of the wavenumber range where numerical errors are negligible. The dissipation characteristics of CG with the SVV modifications suggested are then verified to be broadly equivalent to those obtained through upwinding in the discontinuous Galerkin (DG) scheme. Still, for the kernel function proposed, the full upwind DG scheme is found to have a slightly higher resolution power for the same dissipation levels. Improved CG-SVV characteristics can however be pursued via different kernel functions with the aid of optimization algorithms.

---

† This chapter is based on "R. C. Moura, S. J. Sherwin, J. Peiró (2016) *Eigensolution analysis of spectral/hp continuous Galerkin approximations to advection-diffusion problems: insights into spectral vanishing viscosity*, **Journal of Computational Physics** 307:401–422".

2.1 Introduction

The analysis of dispersion and diffusion/dissipation errors is a fundamental step in understanding accuracy and stability characteristics of any numerical scheme. This is of particular importance for high-order spectral element (*hp*) methods [1], where the trade-off between small numerical dissipation and robustness for practical problems is of primary relevance. Not surprisingly, dispersion-diffusion analysis has been applied to several spectral/*hp* methods, such as discontinuous Galerkin [2], spectral volume [3], spectral difference [4] and flux reconstruction [5] schemes. However, the present study seems to be the first systematic application of eigensolution analysis to the spectral/*hp* continuous Galerkin (CG) formulation. Preliminary studies with related purposes can be found in [6] and [7] (see chapter 6 of Ref. [7] and references therein). Dispersion-diffusion analyses of the classical (low-order) CG finite element method have also been carried out before, see e.g. [8] for a discussion of element-wise linear and quadratic discretisations.

The one-dimensional linear advection-diffusion equation is considered initially, where the derivation of the discrete problem is described in detail and the dispersion-diffusion curves are evaluated. The role of multiple eigencurves is discussed according to the perspective proposed in [9], where a so-called primary eigencurve is distinguished from the remaining (secondary) ones, which are then perceived as replications of the primary curve. Unexpected behaviour of the eigencurves is found at moderately high wavenumbers for problems strongly dominated by either advection or diffusion, indicating that CG might feature potentially undesirable non-smooth dispersion/diffusion characteristics for such problems, especially in the context of under-resolved simulations. Due to the formulation's lack of numerical dissipation for convection-dominated problems, the effects of spectral vanishing viscosity (SVV) in stabilizing CG are considered throughout the rest of the paper.

The SVV technique was introduced in [10] in an attempt to stabilize (pure) spectral methods for the simulation of non-linear problems. In a sense, SVV works as a higher-order viscosity because its operator is designed to affect only the highest captured wavenumbers. This feature allows for the exponential (or spectral) convergence property to be preserved for sufficiently resolved simulations. SVV was subsequently adapted for more general spectral methods and applied to the solution of practical engineering problems [11, 12, 13, 14]. Moreover, SVV has been used in large-eddy simulations (LES) of turbulent flows playing the role of a turbulence model [13, 15, 16, 17, 18, 19], even though SVV is not explicitly designed to work as an LES-like subgrid-scale model.

In this chapter, the SVV technique is considered as applied to the CG discretisation of the linear advection equation in one dimension. The discrete formulation augmented with the standard SVV operator is found, again, to display unusual non-smooth dispersion/diffusion characteristics for problems dominated by either advection or (SVV-based) diffusion. This is due to a dependency on a local Péclet number given by $\mathrm{Pe} = ah/\mu$, where a is the advection speed, h is the mesh spacing and μ is the base SVV magnitude. A different approach is then proposed where the Péclet number is held constant simply by making the base (spectral) viscosity locally proportional to both the advection speed and the mesh spacing, i.e. $\mu \propto ah$. Within this scenario, SVV dissipation is verified to be, in dimensional terms, essentially equivalent to that introduced by upwind fluxes in a discontinuous Galerkin (DG) formulation.

However, while in a DG formulation the wavenumber range where numerical errors are negligible increases with the polynomial order [9], such increase in resolution power is not naturally achieved in CG with SVV-based stabilization. In particular, this is shown for the widely used "exponential" kernel function [20]. A new SVV kernel function is then proposed which provides a consistent increase in resolution power for higher-order discretisations. Yet, in comparison to the (standard upwind) DG scheme, the suggested kernel is found to yield a reduced resolution power for the same dissipation levels. Improved CG-SVV characteristics can however be pursued via different kernel functions with the aid of optimization algorithms.

This chapter is organized as follows. Sec. 2.2 focuses on the eigenanalysis of the linear advection-diffusion equation with CG, where unexpected behaviours for either advection or diffusion dominated problems are pointed out. Sec. 2.3 addresses in a similar fashion the advection equation augmented with SVV, discusses the issues with standard SVV operators and proposes a new operator to avoid these issues. In Sec. 2.4, the equivalence between the proposed SVV approach and upwinding in DG is explored and a comparison of these techniques as applied to CG and DG is carried out. Concluding remarks are given in Sec. 2.5.

2.2 Advection-diffusion with CG

This section is devoted to the discretisation of the advection-diffusion equation and to the analysis of dispersion and diffusion eigencurves for different polynomial orders. The spectral/*hp* continuous Galerkin method considered closely resembles the formulation presented in [7]. Sec. 2.2.1 describes in detail the derivation of the semi-discrete advection-diffusion problem as applied to wave-like solutions, from which the relevant eigencurves can be obtained. The inviscid case (pure advection) is addressed in Sec. 2.2.2, where the role of primary and secondary eigencurves is discussed from the perspective introduced in [9]. The viscous case is then considered in Sec. 2.2.3, where eigencurves are shown to feature irregular oscillations for problems strongly dominated by either convection or diffusion.

2.2.1 Spatial discretisation and wave-like solutions

The linear advection-diffusion equation is given by

$$\frac{\partial u}{\partial t} + a\frac{\partial u}{\partial x} = \mu\frac{\partial^2 u}{\partial x^2} \text{ , for } x \in \Omega \subset \mathbb{R} \text{ and } t \geq 0, \tag{2.1}$$

where a is the advection speed and μ is the viscosity. Periodic boundary conditions are assumed, as consistent with the temporal eigenanalysis framework. The left and right boundaries of the domain are denoted by $\partial\Omega_L$ and $\partial\Omega_R$, respectively. Following the spectral/*hp* discretisation, Ω is divided into non-overlapping elements Ω_e such that $\Omega = \bigcup_e \Omega_e$. The numerical solution is then approximated by

$$u(x,t) \approx u^\delta(x,t) = \sum_j g_j(t)\,\Phi_j(x) \ , \tag{2.2}$$

where Φ_j are global basis functions and g_j are their respective weights or coefficients.

In modal CG formulations, the set of global basis functions is usually made of interface and (element-wise) bubble functions. An interface function is non-zero only at the elements shared by the interface to which the function is associated, where is has a unit value, decaying linearly to zero at the two nearest neighbouring interfaces. Bubble functions are of higher order and non-zero only within the element to which they are associated. Bubble functions must become zero at interfaces. This boundary-interior decomposition allows one to span a polynomial space of degree P over Ω. Case $P = 1$ implies only interface functions, while for $P > 1$ a high-order representation can be achieved. By construction, C^0 continuity of the numerical solution is guaranteed. Note that due to the periodicity condition assumed, the interface functions related to the first ($\partial\Omega_L$) and last ($\partial\Omega_R$) interfaces are one and the same, being non-zero only at the first and last mesh elements.

An alternative (weak) form of the model problem considered can be derived by integrating the product between Eq. (2.1) and global basis functions Φ_i, namely

$$\int_\Omega \left(\frac{\partial u}{\partial t} + a\frac{\partial u}{\partial x} - \mu\frac{\partial^2 u}{\partial x^2} \right) \Phi_i \, dx = 0 \ , \quad \text{for } i \in \mathbb{S}_P \ , \tag{2.3}$$

where $\mathbb{S}_P$ is the set of values of i associated with an *hp* approximation space of degree P. Now, since

$$\int_\Omega \frac{\partial^2 u}{\partial x^2}\Phi_i \, dx = -\int_\Omega \frac{\partial u}{\partial x}\frac{\partial \Phi_i}{\partial x} \, dx + \int_\Omega \frac{\partial}{\partial x}\left(\frac{\partial u}{\partial x}\Phi_i\right) dx = -\int_\Omega \frac{\partial u}{\partial x}\frac{\partial \Phi_i}{\partial x} \, dx + \left[\frac{\partial u}{\partial x}\Phi_i\right]_{\partial\Omega_L}^{\partial\Omega_R} \ , \tag{2.4}$$

where the rightmost term above vanishes when periodicity is assumed. Hence, CG approximations u^δ are required to obey

$$\int_\Omega \frac{\partial u^\delta}{\partial t}\Phi_i \, dx + a\int_\Omega \frac{\partial u^\delta}{\partial x}\Phi_i \, dx + \mu\int_\Omega \frac{\partial u^\delta}{\partial x}\frac{\partial \Phi_i}{\partial x} \, dx = 0 \ . \tag{2.5}$$

It is useful to express all the global basis functions Φ_j in terms of local boundary and interior (bubble) functions and to cast the above equation in terms of element-wise integrals. Global C^0 continuity will then have to be enforced through an assembly procedure, but until then the solution can be expressed locally at element Ω_e as

$$u^\delta(x,t)|_{\Omega_e} = \sum_{j=0}^{P} \ell_j(t)\,\phi_j(x) \ , \tag{2.6}$$

where ϕ_j are element-wise basis functions and ℓ_j are their coefficients. More specifically, while the set $\{\phi_1, \ldots, \phi_{P-1}\}$ contains the bubble functions necessary to span the polynomial space of degree P, ϕ_0 and ϕ_P are the linear functions corresponding respectively to the descending and ascending parts of the interface functions (of the global approach) associated to the boundaries of Ω_e. This sorting of the basis functions leads to a simpler correspondence between the coefficients ℓ_j and g_j.

Given that for each set of local basis functions one has $\phi_j = \partial\phi_j/\partial x = 0$ for $x \notin \Omega_e$, the elemental contribution of Eq. (2.5) becomes (superscript δ is hereafter omitted to simplify notation)

$$\int_{\Omega_e} \frac{\partial u}{\partial t}\phi_i \, dx + a\int_{\Omega_e} \frac{\partial u}{\partial x}\phi_i \, dx + \mu\int_{\Omega_e} \frac{\partial u}{\partial x}\frac{\partial \phi_i}{\partial x} \, dx = 0 \ , \tag{2.7}$$

which will be subsequently re-assembled into a C^0 continuous expansion. Integrating in the standard domain $\Omega_{st} = [-1, 1]$ and inserting Eq. (2.6) gives

$$\frac{h}{2}\int_{\Omega_{st}} \phi_i \, \Sigma_j \left(\frac{\partial \ell_j}{\partial t} \phi_j \right) d\xi + a \int_{\Omega_{st}} \phi_i \, \Sigma_j \left(\ell_j \frac{\partial \phi_j}{\partial \xi} \right) d\xi = -\mu \frac{2}{h} \int_{\Omega_{st}} \frac{\partial \phi_i}{\partial \xi} \, \Sigma_j \left(\ell_j \frac{\partial \phi_j}{\partial \xi} \right) d\xi \ , \tag{2.8}$$

or

$$\frac{h}{2} \sum_{j=0}^{P} \frac{\partial \ell_j}{\partial t} \boldsymbol{M}[i,j] + a \sum_{j=0}^{P} \ell_j \, \boldsymbol{A}[i,j] = -\mu \frac{2}{h} \sum_{j=0}^{P} \ell_j \, \boldsymbol{D}[i,j] \ , \tag{2.9}$$

where h is the element size (assumed constant throughout the mesh) and

$$\boldsymbol{M}[i,j] = \int_{\Omega_{st}} \phi_i \, \phi_j \, d\xi \ , \quad \boldsymbol{A}[i,j] = \int_{\Omega_{st}} \phi_i \, \phi_j' \, d\xi \ , \quad \boldsymbol{D}[i,j] = \int_{\Omega_{st}} \phi_i' \, \phi_j' \, d\xi \ , \tag{2.10}$$

in which $\phi_j' = \partial \phi_j / \partial \xi$. In vector form, Eq. (2.9) reads (assuming $a \neq 0$)

$$\frac{h}{2a} \boldsymbol{M} \frac{\partial \vec{\ell}_e}{\partial t} + \boldsymbol{A} \, \vec{\ell}_e = -\frac{2\mu}{ah} \boldsymbol{D} \, \vec{\ell}_e \ , \tag{2.11}$$

where $\vec{\ell}_e = \{\ell_0, \ldots, \ell_P\}^T$ is the vector of local coefficients of element Ω_e, while $\boldsymbol{M}$ is the mass matrix and $\boldsymbol{A}$ and $\boldsymbol{D}$ are matrices representing the advection and diffusion terms, respectively.

Finally, the assembly procedure must be performed to introduce inter-element communication and enforce C^0 continuity. Let $\boldsymbol{\mathcal{A}}$ be the assembly matrix such that $\vec{\ell}_\Omega = \boldsymbol{\mathcal{A}} \vec{g}_\Omega$, see [7] for details. Here, $\vec{g}_\Omega = \{\ldots, g_j, \ldots\}^T$ for $j \in \mathbb{S}_P$ while $\vec{\ell}_\Omega = \{\ldots, \vec{\ell}_e, \ldots\}^T$ for $\Omega_e \subset \Omega$. This way, the global counterpart of Eq. (2.11) can be written as

$$\frac{h}{2a} \boldsymbol{M}_g \frac{\partial \vec{g}_\Omega}{\partial t} = \boldsymbol{X}_g \, \vec{g}_\Omega \ , \quad \boldsymbol{X}_g = -\left(\boldsymbol{A}_g + \frac{2}{\mathrm{Pe}} \boldsymbol{D}_g \right) , \tag{2.12}$$

where $\mathrm{Pe} = ah/\mu$ is the Péclet number and the global matrices $\boldsymbol{M}_g$, $\boldsymbol{A}_g$ and $\boldsymbol{D}_g$ are defined by

$$\boldsymbol{M}_g = \boldsymbol{\mathcal{A}}^T \boldsymbol{M}_\Omega \, \boldsymbol{\mathcal{A}} \ , \quad \boldsymbol{A}_g = \boldsymbol{\mathcal{A}}^T \boldsymbol{A}_\Omega \, \boldsymbol{\mathcal{A}} \ , \quad \boldsymbol{D}_g = \boldsymbol{\mathcal{A}}^T \boldsymbol{D}_\Omega \, \boldsymbol{\mathcal{A}} \ , \tag{2.13}$$

according to the block-diagonal structure illustrated in Fig. 2.1, see [7] for details.

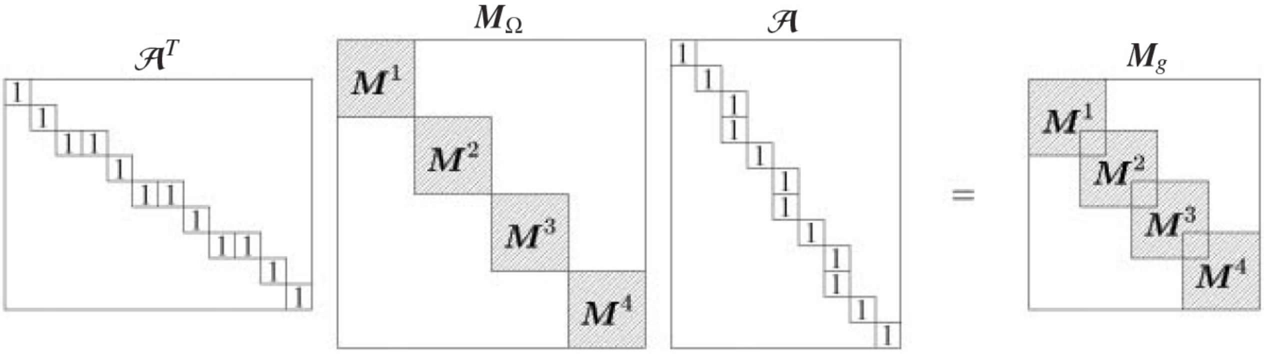

Figure 2.1: Example of the global matrices obtained through the assembly procedure for the case $P = 2$ and four elements.

As pointed out in [6], a pattern can be recognized in these global matrices which allows for the decoupling of individual elements (along with their immediate neighbours) from the global system of equations. This pattern is shown in Fig. 2.2, where the relevant matrices for the central element and its left and right neighbours are highlighted. Note that owing to the assembly structure of the periodic problem considered, the matrices highlighted in Fig. 2.2 are the same for all the elements. Moreover, these matrices have size $P \times P$ because the last coefficient of a given element is now only considered (as the first one) in the expansion of the following mesh element. As a result, the relevant central ($\boldsymbol{\mathcal{C}}$), left ($\boldsymbol{\mathcal{L}}$) and right ($\boldsymbol{\mathcal{R}}$) matrices of Fig. 2.2 are defined directly from the block matrices (generically referred to as $\boldsymbol{\mathcal{B}}$) respectively composing the global matrices $\boldsymbol{M}_g$, $\boldsymbol{A}_g$ and $\boldsymbol{D}_g$ defined in Eq. (2.13). More specifically,

$$\boldsymbol{\mathcal{C}} = \boldsymbol{\mathcal{B}}\,[1\!:\!P, 1\!:\!P] \ , \tag{2.14}$$

$$\boldsymbol{\mathcal{L}}\,[1, 1\!:\!P] = \boldsymbol{\mathcal{B}}\,[P+1, 1\!:\!P] \ , \quad \boldsymbol{\mathcal{L}}\,[2\!:\!P, 1\!:\!P] = \boldsymbol{\mathcal{O}} \ , \tag{2.15}$$

$$\boldsymbol{\mathcal{R}}\,[1\!:\!P, 1] = \boldsymbol{\mathcal{B}}\,[1\!:\!P, P+1] \ , \quad \boldsymbol{\mathcal{R}}\,[1\!:\!P, 2\!:\!P] = \boldsymbol{\mathcal{O}} \ , \tag{2.16}$$

where $\boldsymbol{\mathcal{O}}$ denotes null matrices of the required size. Note that in the above notation, $p : q$ refers to the complete set of integers ranging from p to q.

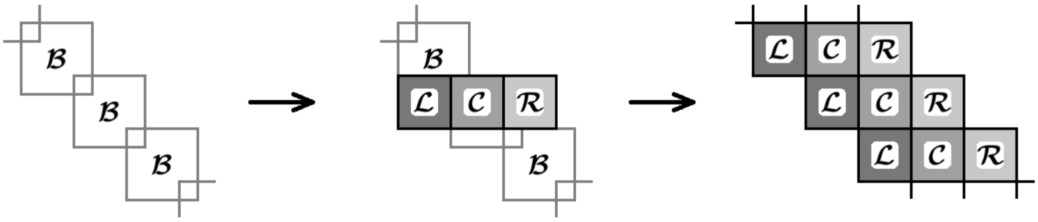

Figure 2.2: Structure of the global matrices, showing the relevant central ($\boldsymbol{\mathcal{C}}$), left ($\boldsymbol{\mathcal{L}}$) and right ($\boldsymbol{\mathcal{R}}$) matrices defined directly from the block matrices ($\boldsymbol{\mathcal{B}}$) which form a given global matrix.

The resulting decoupled semi-discrete advection-diffusion problem is given in vector form by

$$\frac{h}{2a}\left(\boldsymbol{\mathcal{L}}_{\boldsymbol{M}}\,\frac{\partial \vec{c}_L}{\partial t} + \boldsymbol{\mathcal{C}}_{\boldsymbol{M}}\,\frac{\partial \vec{c}}{\partial t} + \boldsymbol{\mathcal{R}}_{\boldsymbol{M}}\,\frac{\partial \vec{c}_R}{\partial t}\right) = \boldsymbol{\mathcal{L}}_{\boldsymbol{X}}\,\vec{c}_L + \boldsymbol{\mathcal{C}}_{\boldsymbol{X}}\,\vec{c} + \boldsymbol{\mathcal{R}}_{\boldsymbol{X}}\,\vec{c}_R \ , \tag{2.17}$$

where subscripts $\boldsymbol{M}$ and $\boldsymbol{X}$ indicate the block matrices ($\boldsymbol{\mathcal{B}}$) from which $\boldsymbol{\mathcal{C}}$, $\boldsymbol{\mathcal{L}}$ and $\boldsymbol{\mathcal{R}}$ were obtained. In addition, $\vec{c} = \{\ell_0, \ldots, \ell_{P-1}\}^T$ is the reduced vector of coefficients associated to the central element, while $\vec{c}_L$ and $\vec{c}_R$ correspond to the reduced vectors of the neighbouring elements from the left and right sides, respectively. It should be stressed that Eq. (2.17) stems directly from Eq. (2.12) without any assumptions, just like individual equations in a system hold independently. Periodicity is used in the assumption that Eq. (2.17) can be applied for all the mesh elements, which is readily justified since the global coupling can then be regarded as cyclic.

For the eigensolution analysis, one seeks for solutions in the form (hereafter, $i = \sqrt{-1}$)

$$u = \exp[i(kx - wt)] \ , \tag{2.18}$$

or, more specifically, solutions in which the element-wise approximating coefficients are related to the above wave-like solution through projection. An element-by-element projection of Eq. (2.18) yields

$$\boldsymbol{M}_\Omega \, \vec{\ell}_\Omega = \vec{I}_\Omega \ , \tag{2.19}$$

where $\vec{I}_\Omega = \{\dots, \vec{I}_e, \dots\}^T$ and $\vec{I}_e = \int_{\Omega_{st}} \{u_e\phi_0 \, , \, \dots \, , \, u_e\phi_P\}^T \, d\xi$, in which $u_e = u(x_e + \xi h/2, t)$ with $\xi \in \Omega_{st}$, x_e being the mid-point of Ω_e. Performing the assembly procedure and the subsequent decoupling of individual elements (with their immediate neighbours) yields

$$\boldsymbol{\mathcal{A}}^T \boldsymbol{M}_\Omega \, \boldsymbol{\mathcal{A}} \vec{g}_\Omega = \boldsymbol{\mathcal{A}}^T \vec{I}_\Omega \ \Rightarrow \ \boldsymbol{M}_g \, \vec{g}_\Omega = \boldsymbol{\mathcal{A}}^T \vec{I}_\Omega \ \Rightarrow \ \boldsymbol{\mathcal{L}_M} \, \vec{c}_{e-1} + \boldsymbol{\mathcal{C}_M} \, \vec{c}_e + \boldsymbol{\mathcal{R}_M} \, \vec{c}_{e+1} = \vec{\mathcal{I}}_e \ , \tag{2.20}$$

where

$$\vec{\mathcal{I}}_e = \int_{\Omega_{st}} \{u_{e-1}\phi_P + u_e\phi_0 \, , \, u_e\phi_1 \, , \, \dots \, , \, u_e\phi_{P-1}\}^T \, d\xi \ = \ \vec{\zeta} \, \exp[i(kx_e - wt)] \ , \tag{2.21}$$

in which $\vec{\zeta} = \{\exp(-ikh) \, \pi_P + \pi_0, \pi_1, \dots, \pi_{P-1}\}^T$ and $\pi_j(kh) = \int_{\Omega_{st}} \exp(ikh\xi/2) \, \phi_j(\xi) \, d\xi$.

In order to extract $\vec{c}_e$ from Eq. (2.20), it should be noted that, owing to the solution periodicity and equispaced mesh employed, $\vec{c}_{e\pm1}\langle u(x)\rangle = \vec{c}_e\langle u(x \pm h)\rangle$, where $\langle\cdot\rangle$ is used to denote a functional dependence on $u(x)$. In addition, since $\vec{\mathcal{I}}_e\langle u(x \pm h)\rangle = \exp(\pm ikh) \, \vec{\mathcal{I}}_e\langle u(x)\rangle$ from Eq. (2.21), one has therefore $\vec{c}_{e\pm1} = \exp(\pm ikh) \, \vec{c}_e$ and thus

$$\vec{c}_e = \left[\boldsymbol{\mathcal{L}_M} \, e^{-ikh} + \boldsymbol{\mathcal{C}_M} + \boldsymbol{\mathcal{R}_M} \, e^{+ikh}\right]^{-1} \vec{\mathcal{I}}_e \ . \tag{2.22}$$

In the temporal eigensolution's approach, one should use Eqs. (2.22) and (2.21) with real k and complex w into the semi-discrete advection problem in Eq. (2.17) to obtain

$$\frac{h}{2a}(-iw) \left[\boldsymbol{\mathcal{L}_M} \, e^{-ikh} + \boldsymbol{\mathcal{C}_M} + \boldsymbol{\mathcal{R}_M} \, e^{+ikh}\right] \vec{c} = \left[\boldsymbol{\mathcal{L}_X} \, e^{-ikh} + \boldsymbol{\mathcal{C}_X} + \boldsymbol{\mathcal{R}_X} \, e^{+ikh}\right] \vec{c} \ , \tag{2.23}$$

which, by defining

$$\boldsymbol{\mathcal{Z}} = 2 \left[\boldsymbol{\mathcal{L}_M} \, e^{-ikh} + \boldsymbol{\mathcal{C}_M} + \boldsymbol{\mathcal{R}_M} \, e^{+ikh}\right]^{-1} \left[\boldsymbol{\mathcal{L}_X} \, e^{-ikh} + \boldsymbol{\mathcal{C}_X} + \boldsymbol{\mathcal{R}_X} \, e^{+ikh}\right] \ , \tag{2.24}$$

is equivalent to

$$-i\frac{wh}{a} \, \vec{\zeta} = \boldsymbol{\mathcal{Z}} \, \vec{\zeta} \ . \tag{2.25}$$

In general, one is left with an eigenvalue problem with P solutions owing to the size of $\boldsymbol{\mathcal{Z}}$. The resulting eigenvalue/eigenvector pairs $(\lambda_m, \vec{v}_m)$ are related to the problem variables by

$$w_m = \frac{ia}{h}\lambda_m \ \text{ and } \ \vec{\zeta}_m \propto \vec{v}_m \ , \tag{2.26}$$

where, without losing generality, one defines $\vec{\zeta}_m = \vec{v}_m/s_m$, in which s_m is the sum of the entries of $\vec{v}_m$. The general numerical solution can readily be obtained from Eq. (2.22) since, through the right-hand side of Eq. (2.21), one has

$$\vec{\mathcal{I}}_e \, (t) = \sum_{m=0}^{P-1} Z_m \, \vec{v}_m \, \exp[i(kx_e - w_m t)] \ , \tag{2.27}$$

where the scalar coefficients Z_m are obtained from the initial condition. For instance, if $u = \exp(ikx)$ at the initial state, Eqs. (2.21) and (2.27) written at $t = 0$ yield

$$\sum_{m=0}^{P-1} Z_m \, \vec{v}_m \, \exp(ikx_e) = \vec{\zeta} \, \exp(ikx_e) \; . \tag{2.28}$$

Accordingly, $\vec{Z} = \{Z_0, \ldots, Z_{P-1}\}^T$ is given by

$$\vec{Z} = \boldsymbol{\mathcal{V}}^{-1} \vec{\zeta} \; , \tag{2.29}$$

where $\boldsymbol{\mathcal{V}} = \{\vec{v}_0, \ldots, \vec{v}_{P-1}\}$. Note that $\vec{\zeta}$ represents the elemental Galerkin projection of the complex Fourier modes $\exp(ikx)$ onto the polynomial basis, which is then projected through matrix $\boldsymbol{\mathcal{V}}^{-1}$ onto the discrete eigenbasis of the PDE being discretised.

2.2.2 The inviscid case ($\mu = 0$)

Before discussing the advection-diffusion case, it is useful to analyse CG's behaviour for pure advection. As it is customary in wave analyses, the relation $w = ak$ will be used to define a modified wavenumber k^* for each numerical angular frequency w_m, such that $w_m = ak^*_m$. The natural interpretation is that each mode (m) of the solution behaves as if governed by k^*_m instead of k. Note from Eqs. (2.24–2.26) that both w_m and k^*_m are functions of the "baseline" wavenumber k.

The dispersion and diffusion curves for polynomial orders $P = 1$ and $P = 2$ are shown in Fig. 2.3. In both cases, there is no diffusion error and thus no numerical dissipation for all wavenumbers. This was verified to hold regardless of P. The dispersion curves, however, display significant numerical error for the poorly-resolved wavenumbers ($kh/P \to \pi$). For small wavenumbers though, the linear behaviour of the exact dispersion relation ($k^* = k$) is recovered as expected. This linear region is larger for $P = 2$ due to the higher order and thus superior accuracy of the discretisation, but there is a secondary mode present which corresponds to the thin continuous branch in the bottom left plot of Fig. 2.3. The discrete bullets shown correspond to the eigencurves obtained from classical analyses, available for linear and quadratic discretisations [8] and given respectively by

$$k^*h = \frac{3\sin(kh)}{2+\cos(kh)} \quad \text{and} \quad k^*h = \frac{-4\sin(kh) \pm 2\sqrt{[\cos(kh)-1][\cos(kh)-19]}}{3-\cos(kh)} \; . \tag{2.30}$$

The role of secondary eigencurves in the context of spectral/hp methods has been interpreted in different ways in the literature. However, as pointed out in [5], generally they are simply regarded as 'spurious' and entirely neglected. A new perspective on the matter was introduced in [9], where secondary modes are interpreted as replications of the primary mode (the one that recovers $k^* = k$ as $k \to 0$). While that work focused on the discontinuous Galerkin (DG) formulation, the present work extends this interpretation to CG. As in [9], here the eigencurves were also verified to be equispaced in the (periodic) normalized $\overline{k}$ axis, where here $\overline{k} = kh/P$ rather than $kh/(P+1)$, which was the case for DG. As a result, the modified wavenumber for each mode can be obtained from

$$\overline{k^*_m}\,(\overline{k}) = \overline{k^*_0}\,(\overline{k}+2\pi m/P)\,,\ m=0,\ldots,P-1\ , \tag{2.31}$$

in which the zeroth mode was taken (without loss of generality) as the primary one. We remark that $\overline{k^*_0}$ is periodic as a function of $\overline{k}$, with period 2π, and that the above relation holds for both real and imaginary parts of $\overline{k^*_m}$.

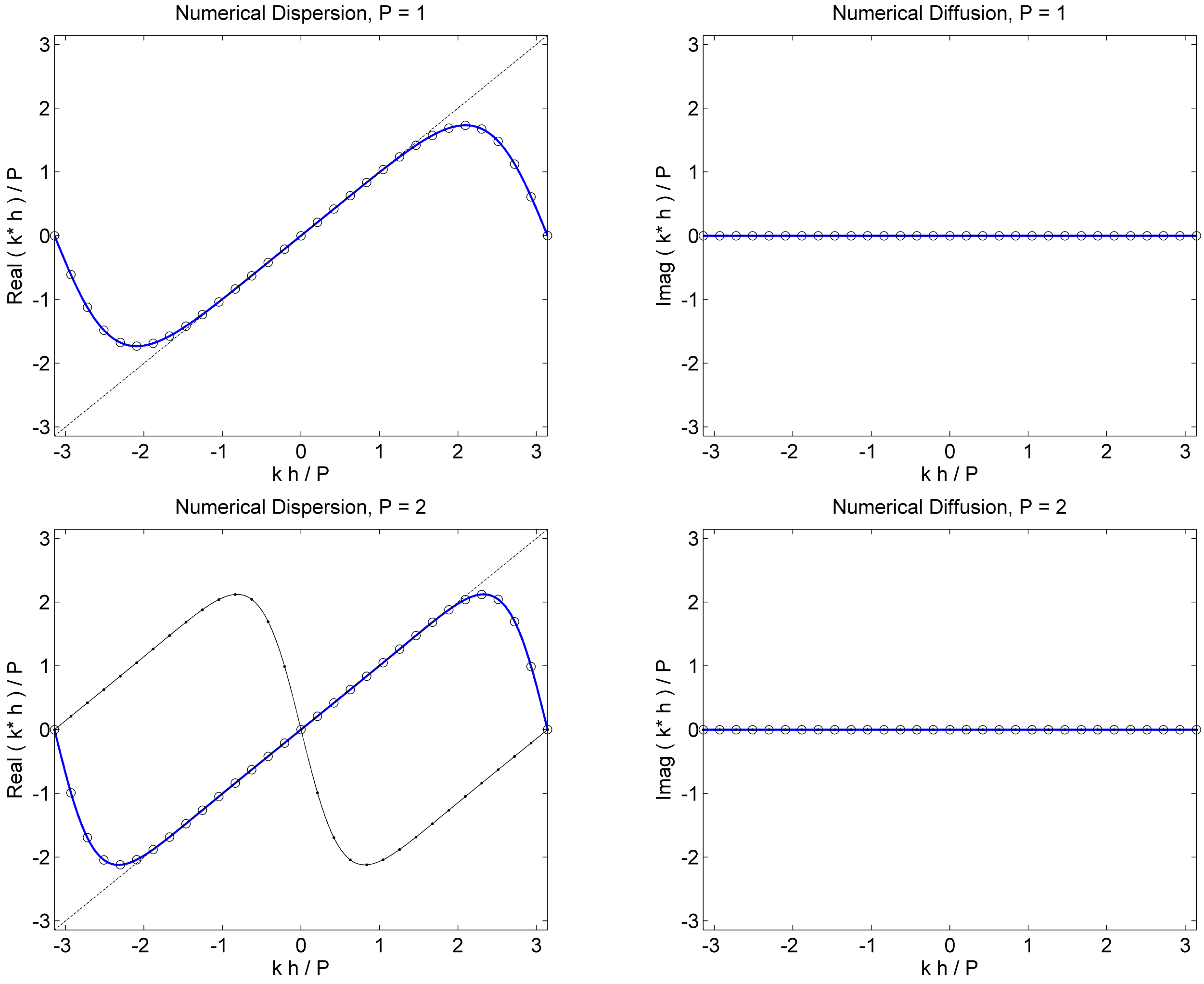

Figure 2.3: Dispersion-diffusion curves for pure advection with CG for $P = 1$ (top) and $P = 2$ (bottom). The thick branches represent the primary eigencurves, whereas dashed lines indicate the exact behaviour and discrete bullets depict the analytical results from classical analyses.

Now, upon increasing P, the imaginary part of all the eigencurves was found to remain identically zero, indicating the absence of numerical dissipation for the CG discretisation of the linear advection equation, which is consistent with analyses of classical low-order CG [8]. An unexpected behaviour was however observed for the dispersion eigencurves for the higher-order discretisations. These are depicted in Fig. 2.4 for polynomial orders varying from $P = 3$ to 6. The left column shows all the (dispersion) eigencurves while the right column shows only the primary ones, along with the exact dispersion relation $k^* = k$. The primary eigencurves for each P are also highlighted in the plots of the left column for reference. An unusual feature of these curves is their discontinuous character, which is very mild when $P = 3$, but is already quite significant for $P = 6$. These discontinuities can not be avoided since they originate from the separated (upper/lower) branches shown in the 'all-eigencurves' plots of Fig. 2.4. It should be noted that a similar behaviour, i.e. separated branches leading to discontinuities, has been observed both for DG and SV (spectral volume) methods when central fluxes are used instead of upwind ones, see e.g. Ref. [3].

The primary eigencurve has been defined as the one that recovers $k^* = k$ as $k \to 0$. Away from $k = 0$, however, the identification of the primary curve is less obvious since eigencurves can cross each other and even appear as separated branches, making the definition of the primary eigencurve somewhat arbitrary. Still, the trends observed for the lower-order discretisations (where there is less ambiguity) point out a way to define the primary curve as the polynomial order increases. More specifically, a linear region around $k = 0$ and a crossing of the horizontal axis with negative slope at $\overline{k} = \pm\pi$ are expected. When these features are taken into account, it is only natural (see Fig. 2.4) to consider the "arches" of separated branches as parts of the primary eigencurve. The resulting curve is then readily verified to obey the replication property (Eq. 2.31) since all the remaining eigencurves can be recognized as replications of the primary one. There remains to define precisely the extent of each arch, i.e. the position of the discontinuous jumps of the primary eigencurve. In this study, these positions have been defined so as to minimize the magnitude of the jumps, the minimization being performed over the relevant range of wavenumbers where distinct branches are closest. But this last definition is arbitrary and the replication property could still hold for different jump locations.

A larger number of discontinuities per curve was found for $P > 6$ (not shown) as more branches on the central section of all-eigencurves plots begin to detach as P increases, generating additional separated (upper/lower) branches. This non-smooth character might introduce potentially undesirable dispersive features on a numerical solution. Note nevertheless that the linear (central) region of the primary eigencurves approximates the exact dispersion behaviour quite accurately. Still, high-order CG discretisations may feature irregular dispersive behaviour for under-resolved simulations of pure advection when the wavenumbers involved might lie outside the linear region of the eigencurves. This should be specially true for higher-order discretisations, where the number and intensity of discontinuities is larger, as discussed above.

Regarding the fact that secondary eigencurves can be understood as replicas of a primary curve, recall Eq. (2.31), it is clear that all the information concerning numerical dispersion and diffusion characteristics can be obtained directly from the primary eigencurve. This not only simplifies subsequent analysis, but also justifies why secondary curves can be cast aside for most purposes. However, as demonstrated in [9], secondary modes should not be considered spurious since some of them can contribute to the overall accuracy of the numerical solution. The argument used in reference [9] for such demonstration can be easily adapted for the CG case and is described in the following.

Since Fourier and piecewise polynomial approximation spaces are fundamentally different, a single Fourier component given to the numerical scheme through a Galerkin projection will energize several (P) polynomial modes. However, these polynomial modes are perceived by the numerical setting as if related to different 'apparent' wavenumbers ($\overline{k} + 2\pi m/P$) as made explicit in Eq. (2.31). The CG scheme will then propagate them, as the primary eigencurve prescribes, in accordance with each of their apparent wavenumbers. As a result, those modes whose apparent wavenumbers

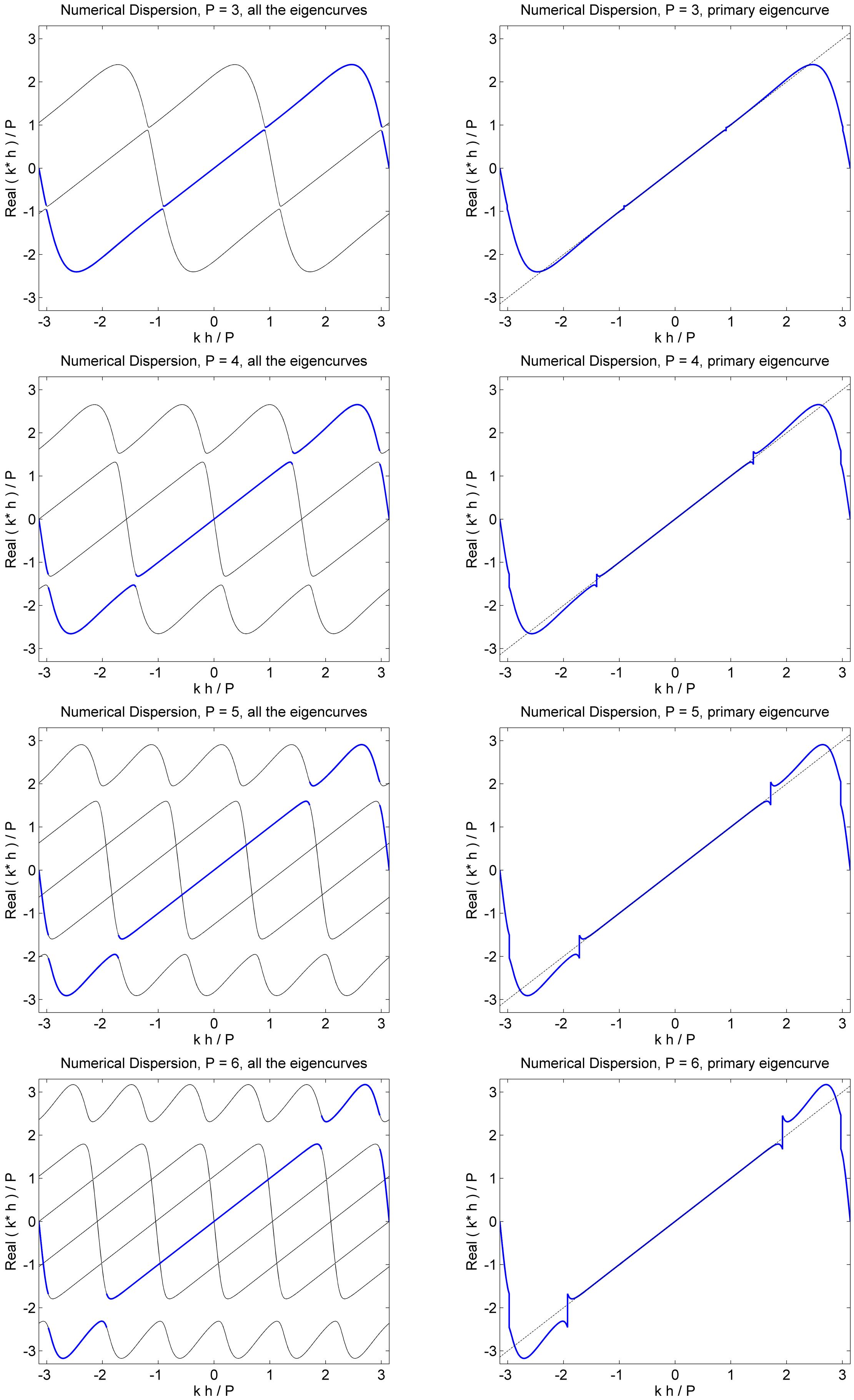

Figure 2.4: Dispersion curves for pure advection with CG for $P = 3, \ldots, 6$ (top to bottom). Left plots show all the eigencurves whereas right plots show only the primary curves (and the exact behaviour).

lie within the (approximately) linear region of the primary eigencurve will be propagated without significant dispersion or diffusion errors. These modes will hence contribute to preserve the solution at the initial state, which, coming from a Galerkin projection, constitutes the best approximation (in the L^2 sense) to the Fourier component considered initially. The remaining eigenmodes, i.e. those whose apparent wavenumbers lie outside the linear region of the primary eigencurve, will introduce dispersion and diffusion errors and thus can be regarded as unphysical. Fortunately, such unphysical modes are expected to have negligible energy if the original Fourier component is reasonably resolved by the hp setting employed.

2.2.3 The viscous case ($\mu > 0$)

The exact behaviour for the advection-diffusion problem can be derived by introducing Eq. (2.18) into Eq. (2.1), which yields $w = ak - i\mu k^2$. Since $k^* = w/a$, one has

$$\frac{k^* h}{P} = \frac{kh}{P} - i\,\frac{\mu P}{ah}\left(\frac{kh}{P}\right)^2 \;\Leftrightarrow\; k^*\overline{h} = k\overline{h} - i\,\frac{(\,k\overline{h}\,)^2}{\mathrm{Pe}^*}\;, \tag{2.32}$$

where $\mathrm{Pe}^* = a\overline{h}/\mu$ and $\overline{h} = h/P$. The relation on the right-hand side of Eq. (2.32) makes clear that the normalized dispersion-diffusion curves of the advection-diffusion problem should depend on Pe^* alone, which already takes into account the discretisation order P employed.

The eigencurves obtained for the CG discretisation of the advection-diffusion problem with $\mathrm{Pe}^* = 10$ are given in Fig. 2.5 for $P = 1$ and $P = 2$. The dispersion curves are similar to those obtained for the inviscid case (see Fig. 2.3) while the diffusion curves are obviously different. The discrete bullets shown correspond to the eigencurves obtained from classical analyses, available for linear and quadratic discretisations [8] and given respectively by

$$k^*h = \frac{3\sin(kh) + 6i[\cos(kh)-1]/\mathrm{Pe}^*}{2+\cos(kh)} \quad \text{and} \quad k^*h = \frac{-4\sin(kh) - 2i[2\cos(kh)+13]/\mathrm{Pe}^* \pm 2\sqrt{\Delta}}{3-\cos(kh)}\;, \tag{2.33}$$

where

$$\Delta = [\cos(kh)-1][\cos(kh)-19] - \frac{i\sin(kh)[7\cos(kh)-97]}{\mathrm{Pe}^*} + \frac{11\cos^2(kh) - 112\cos(kh) - 124}{(\mathrm{Pe}^*)^2}\;. \tag{2.34}$$

The exact behaviour obtained from Eq. (2.32) is depicted through the dash-dotted curves shown in Fig. 2.5. The primary eigenmodes accurately follow the correct behaviour for a reasonable range of wavenumbers. Regarding diffusion in particular, extra dissipation is introduced as numerical error for the poorly-resolved (highest) wavenumbers. This numerical diffusion becomes more significant for higher-order discretisations, as discussed below.

Cases $P = 3, \ldots, 6$, again for $\mathrm{Pe}^* = 10$, are shown in Fig. 2.6. The range of wavenumbers for which the (primary) eigencurves reproduce well the exact relation given by Eq. (2.32) increases with P. For the poorly-resolved wavenumbers, the amount of numerical error introduced also increases with the polynomial order both for dispersion and diffusion. Also, note that the discontinuities seen on the eigencurves of pure advection (Fig. 2.4) are somehow inhibited here by the viscous effects.

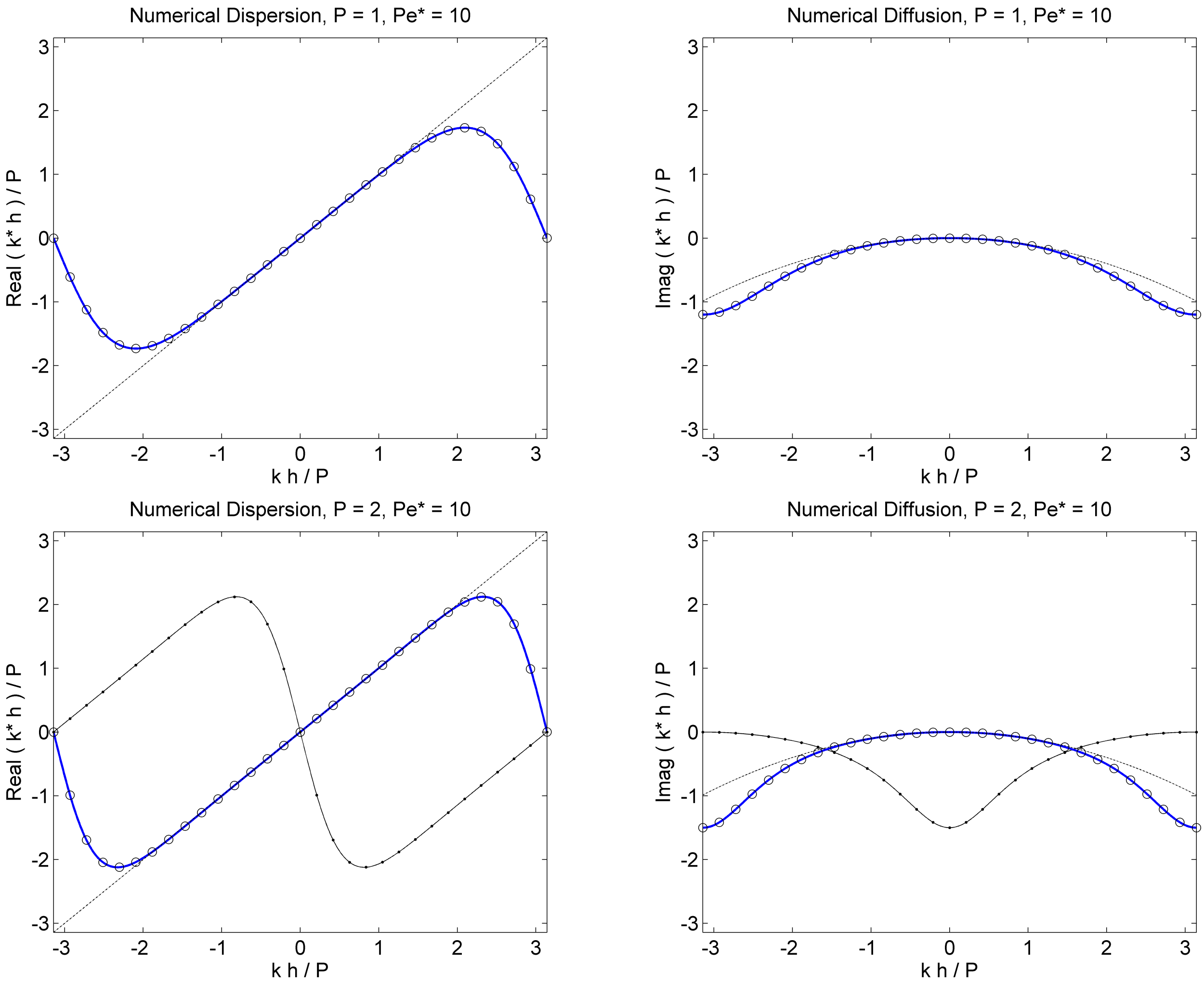

Figure 2.5: Dispersion-diffusion eigencurves for $P = 1$ (top) and $P = 2$ (bottom) for the advection-diffusion problem with $\mathrm{Pe}^* = 10$. The thick branches represent the primary eigencurves, dash-dotted curves indicate the exact behaviour and discrete bullets depict classical analytical results.

Nevertheless, for $\mathrm{Pe}^* \to \infty$ ($\mu \to 0$), not only discontinuities begin to appear on the dispersion curves, but also unusual features become apparent on the diffusion curves. This is illustrated in the plots on the upper half of Fig. 2.7, where case $P = 3$ is considered with $\mathrm{Pe}^* = 10^2$ and $\mathrm{Pe}^* = 10^3$. In addition, non-smooth behaviours are also observed when $\mathrm{Pe}^* \to 0$, i.e. for diffusion-dominated problems, as shown in the plots on the lower half of Fig. 2.7, where case $P = 3$ is considered with $\mathrm{Pe}^* = 1$ and $\mathrm{Pe}^* = 10^{-1}$. Such results raise a question on the suitability of high-order CG formulations for under-resolved simulations of problems dominated by either advection or diffusion. It is acknowledged that within the context of high-order methods, the unsuitability for under-resolved simulations is not new (schemes becoming unstable at higher orders). Moreover, due to truncation errors, there is no practical scheme free from dispersion/diffusion errors at the marginally resolved scales. Still, it is important to bear in mind the nature and extent of such errors in order to apply the numerical methods of choice in a sensible manner, regarding both accuracy and stability.

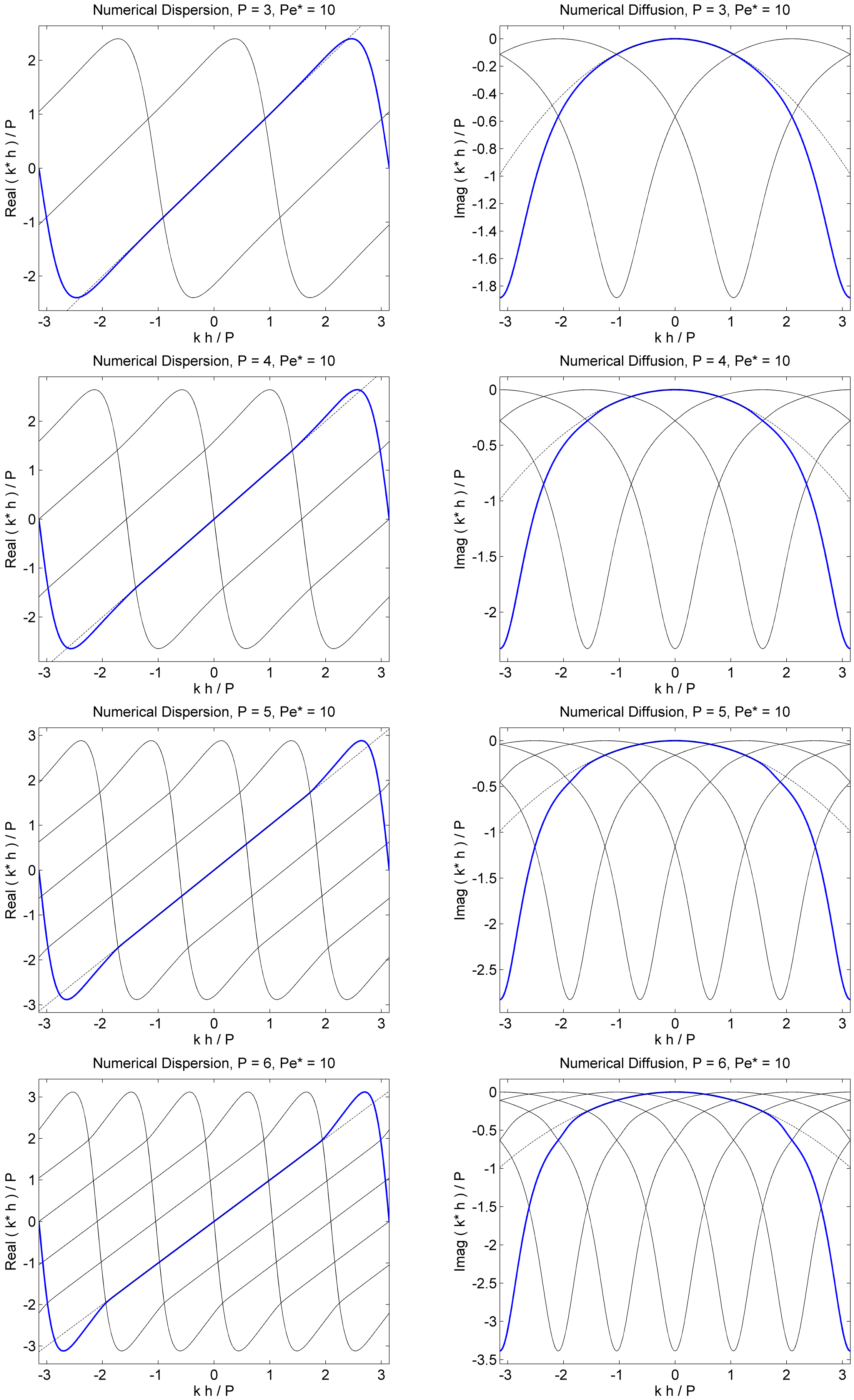

Figure 2.6: Dispersion-diffusion eigencurves for $\mathrm{Pe}^* = 10$ with $P = 3, \ldots, 6$ (top to bottom). The blue branches represent primary eigencurves while dashed curves indicate the exact behaviour.

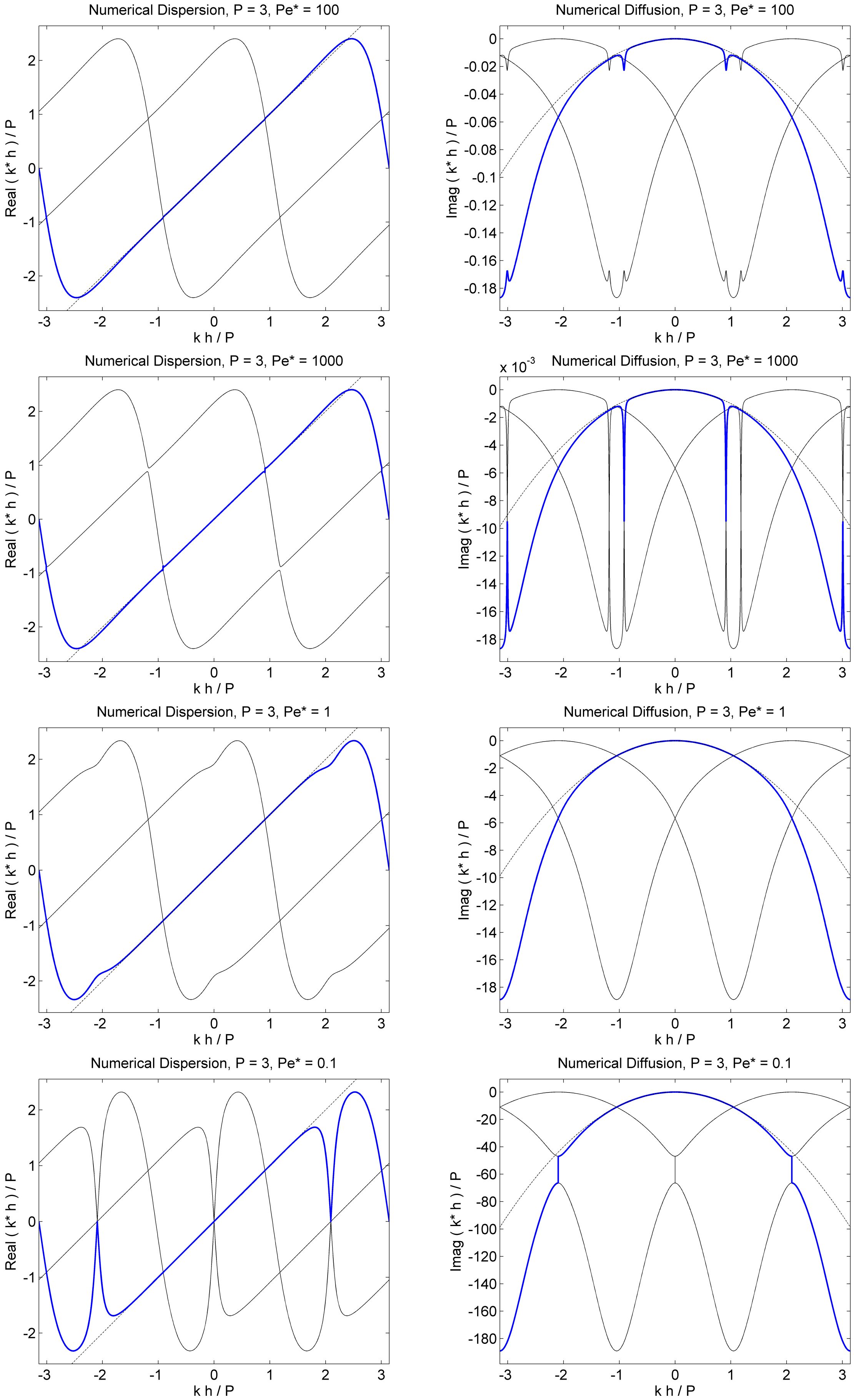
Numerical Dispersion, P = 3, Pe* = 100

Numerical Diffusion, P = 3, Pe* = 100

Numerical Dispersion, P = 3, Pe* = 1000

Numerical Diffusion, P = 3, Pe* = 1000

Numerical Dispersion, P = 3, Pe* = 1

Numerical Diffusion, P = 3, Pe* = 1

Numerical Dispersion, P = 3, Pe* = 0.1

Numerical Diffusion, P = 3, Pe* = 0.1

Figure 2.7: Dispersion-diffusion eigencurves for $P = 3$ with $\mathrm{Pe}^* = 10^2$, $\mathrm{Pe}^* = 10^3$, $\mathrm{Pe}^* = 1$ and $\mathrm{Pe}^* = 10^{-1}$ (top to bottom). Blue branches represent primary eigencurves whereas dashed curves show the exact behaviour.

2.3 Stabilized advection with CG

This section is devoted to the dispersion-diffusion analysis of the spectral/*hp* CG formulation with added spectral vanishing viscosity (SVV). The linear advection equation with SVV-based stabilization is discussed in Sec. 2.3.1, where the implementation of the standard SVV operator is also described in detail. Sec. 2.3.2 addresses potential issues of the traditional SVV operator due to its dependency on a variable Péclet number. Sec. 2.3.3 discusses how the Péclet number can be made globally constant and thus introduces a more reliable SVV approach. A new SVV kernel function is also proposed in Sec. 2.3.3 which provides a consistent increase in the range of wavenumbers not affected by SVV as the polynomial order is increased.

2.3.1 Spectral vanishing viscosity

Since the standard CG formulation provides no numerical dissipation for pure advection problems, the basic purpose of a spectral vanishing viscosity (SVV) operator is to introduce a limited amount of diffusion at higher wavenumbers in order to further stabilize the CG scheme and increase its robustness for the solution of non-linear problems dominated by advection.

The linear advection equation augmented with SVV reads

$$\frac{\partial u}{\partial t} + a\frac{\partial u}{\partial x} = \mu\frac{\partial}{\partial x}\left(\mathcal{Q}\star\frac{\partial u}{\partial x}\right) \ , \tag{2.35}$$

where μ is the base SVV magnitude and $\mathcal{Q}\star(\cdot)$ represents the (normalized) SVV operator acting on the solution derivatives. The SVV technique was first introduced for pure spectral methods [10] and its use in Fourier space can easily be implemented as a multiplication between the Fourier coefficients of the solution ($\hat{u}_k$) and those of the SVV kernel ($\hat{\mathcal{Q}}_k$), activated only at higher wavenumbers,

$$\mu\frac{\partial}{\partial x}\left(\mathcal{Q}\star\frac{\partial u}{\partial x}\right) = -\mu\sum_k k^2\,\hat{\mathcal{Q}}_k\,\hat{u}_k\,\exp(ikx) \ . \tag{2.36}$$

Originally, kernel entries were defined as $\hat{\mathcal{Q}}_k = 1$ for $k > m$ and zero otherwise [10], m being here the wavenumber threshold above which dissipation is introduced. Subsequently, discontinuous kernel variations were avoided by definitions such as $\hat{\mathcal{Q}}_k = \exp[-(k-n)^2/(k-m)^2]$ for $k > m$ and zero otherwise [20], n being the total number of Fourier modes employed.

The discretisation of Eq. (2.35) given below will follow closely that discussed in Sec. 2.2.1. Beginning from Eq. (2.35) and performing essentially the same initial steps yields

$$\int_{\Omega_e}\frac{\partial u}{\partial t}\phi_i\,dx + a\int_{\Omega_e}\frac{\partial u}{\partial x}\phi_i\,dx + \mu\int_{\Omega_e}\left(\mathcal{Q}\star\frac{\partial u}{\partial x}\right)\frac{\partial\phi_i}{\partial x}\,dx = 0 \ , \tag{2.37}$$

which should be compared with Eq. (2.7). Casting integrations into Ω_{st} gives

$$\frac{h}{2}\int_{\Omega_{st}}\phi_i\,\Sigma_j\left(\frac{\partial\ell_j}{\partial t}\phi_j\right)d\xi + a\int_{\Omega_{st}}\phi_i\,\Sigma_j\left(\ell_j\frac{\partial\phi_j}{\partial\xi}\right)d\xi = -\mu\frac{2}{h}\int_{\Omega_{st}}\frac{\partial\phi_i}{\partial\xi}\,\mathcal{Q}\star\left[\Sigma_j\left(\ell_j\frac{\partial\phi_j}{\partial\xi}\right)\right]d\xi \ . \tag{2.38}$$

The multiplication between $\hat{\mathcal{Q}}_k$ and $\hat{u}_k$ used in Fourier space, Eq. (2.36), is here accommodated as a multiplication between kernel entries and element-wise modal coefficients. Note that these are not ℓ_j, but instead the coefficients of $\Sigma_i\, \ell_i \phi'_i$, which will be called ℓ'_j and evaluated through projection, namely

$$\int_{\Omega_{st}} \left(\Sigma_i\, \ell_i \phi'_i - \Sigma_j\, \ell'_j \phi_j \right) \phi_k \, d\xi = 0 \;\;\Rightarrow\;\; \sum_{i=0}^{P} \ell_i \int_{\Omega_{st}} \phi'_i \phi_k d\xi = \sum_{j=0}^{P} \ell'_j \int_{\Omega_{st}} \phi_j \phi_k d\xi \;\;\Rightarrow\;\; \boldsymbol{A}\,\vec{\ell} = \boldsymbol{M}\,\vec{\ell'} \ , \tag{2.39}$$

so that $\vec{\ell'} = \boldsymbol{M}^{-1}\boldsymbol{A}\,\vec{\ell}$, see Eq. (2.10) for the definition of these matrices. As a result, one would have simply

$$\mathcal{Q} \star \left(\Sigma_j\, \ell_j \phi'_j \right) = \mathcal{Q} \star \left(\Sigma_j\, \ell'_j \phi_j \right) = \mathcal{Q} \star \left(\vec{\phi}^T \, \vec{\ell'} \right) = \vec{\phi}^T \, \boldsymbol{\mathcal{Q}} \, \vec{\ell'} \ , \tag{2.40}$$

where $\boldsymbol{\mathcal{Q}}$ is a diagonal matrix whose entries are the kernel components $\hat{\mathcal{Q}}_k$ associated to the operator $\mathcal{Q}$. Note that a consistent sorting must be used for the entries of $\vec{\phi}^T$ and $\vec{\ell'}$ to take into account the hierarchical nature of the basis functions employed in accordance with the kernel components.

The implementation in Eq. (2.40) was used in early applications of SVV to the CG formulation [13], but was soon recognized as not ideal because the CG set of (boundary/bubble) basis functions is not orthogonal. An alternative strategy was then employed in subsequent works [15, 21, 14] which writes the expansion $\Sigma_j\, \ell'_j \phi_j$ on a set of orthogonal basis functions, applies the SVV filtering operation (embodied in $\boldsymbol{\mathcal{Q}}$), and then rewrites the filtered expansion on its original set of basis functions. In this improved implementation, instead of Eq. (2.40), one has

$$\mathcal{Q} \star \left(\Sigma_j\, \ell_j \phi'_j \right) = \mathcal{Q} \star \left(\Sigma_j\, \ell'_j \phi_j \right) = \mathcal{Q} \star \left(\vec{\phi}^T \, \vec{\ell'} \right) = \vec{\phi}^T \, \boldsymbol{\mathcal{T}}^{-1} \boldsymbol{\mathcal{Q}} \, \boldsymbol{\mathcal{T}} \, \vec{\ell'} \ , \tag{2.41}$$

where $\boldsymbol{\mathcal{T}}$ is the transformation matrix from the CG basis employed to a suitable orthogonal basis. The orthonormal set of Legendre basis functions (popular nowadays in modal DG formulations) has been typically chosen for the process, in which case

$$\boldsymbol{\mathcal{T}}[i,j] = \int_{\Omega_{st}} \psi_i \, \phi_j \, d\xi \ , \tag{2.42}$$

where ψ_i, for $i = 0, \ldots, P$, denotes the modal DG's usual Legendre orthonormal basis functions, so that $\vec{\ell'}_{DG} = \boldsymbol{\mathcal{T}}\, \vec{\ell'}_{CG}$.

Introducing Eq. (2.41) into Eq. (2.38) yields

$$\frac{h}{2} \sum_{j=0}^{P} \frac{\partial \ell_j}{\partial t} \boldsymbol{M}[i,j] + a \sum_{j=0}^{P} \ell_j \, \boldsymbol{A}[i,j] = -\mu \frac{2}{h} \sum_{j=0}^{P} \ell_j \, \boldsymbol{D}_{\mathcal{Q}}[i,j] \ , \tag{2.43}$$

which is similar to Eq. (2.9) except for the fact that matrix $\boldsymbol{D}$ is now replaced by

$$\boldsymbol{D}_{\mathcal{Q}} = \boldsymbol{A}^T \boldsymbol{\mathcal{T}}^{-1} \boldsymbol{\mathcal{Q}} \boldsymbol{\mathcal{T}} \boldsymbol{M}^{-1} \boldsymbol{A} \ , \tag{2.44}$$

where it should be noted that $\boldsymbol{A}^T[i,j] = \int_{\Omega_{st}} \phi'_i \phi_j d\xi$ and $\vec{\ell'} = \boldsymbol{M}^{-1}\boldsymbol{A}\,\vec{\ell}$. Hence, Eq. (2.43) written in vector form becomes (assuming $a \neq 0$)

$$\frac{h}{2a}\boldsymbol{M}\,\frac{\partial\vec{\ell}}{\partial t} + \boldsymbol{A}\,\vec{\ell} = -\frac{2\mu}{ah}\,\boldsymbol{D}_{\mathcal{Q}}\,\vec{\ell}\ , \tag{2.45}$$

which is the counterpart of Eq. (2.11) with $\boldsymbol{D}_{\mathcal{Q}}$ in place of $\boldsymbol{D}$.

The rest of the discretisation process (global assembly, decoupling of reduced eigensystems, etc.) is formally identical to that conducted in Sec. 2.2.1, the only difference being that $\boldsymbol{D}_{\mathcal{Q}}$ is used instead of $\boldsymbol{D}$. Hence, the dispersion-diffusion characteristics associated to Eq. (2.45) are completely defined by the kernel entries $\hat{\mathcal{Q}}_k$, the polynomial order P and the Péclet number $\mathrm{Pe} = ah/\mu$, or, equivalently, by $\hat{\mathcal{Q}}_k$, P and $\mathrm{Pe}^* = \mathrm{Pe}/P$.

2.3.2 Analysis of traditional SVV operators

For a given Pe^*, the regular (second-order) diffusion operator is expected to provide a parabolic-like profile for the diffusion eigencurves, recall Eq. (2.32). On the other hand, SVV operators are primarily designed to introduce dissipation only at the highest (poorly-resolved) wavenumbers. Hence, SVV kernel entries $\hat{\mathcal{Q}}_k$ become non-zero only for modes above a prescribed threshold P_{SVV}. A widely used "exponential" kernel was proposed in [20], where (note that k below is a polynomial mode index)

$$\hat{\mathcal{Q}}_k = \exp\left[-\frac{(k-P)^2}{(k-P_{SVV})^2}\right]\ ,\quad \text{for } k > P_{SVV}\ . \tag{2.46}$$

The kernel's behaviour is shown in Fig. 2.8 when $\mathrm{Pe}^* = 3$ (for $P = 2$) and $\mathrm{Pe}^* = 6$ (for $P = 4$). In both cases $P_{SVV} = 0$. The parabolic profiles associated with each Pe^* are shown as thin dotted lines on the diffusion plots of Fig. 2.8. Only the primary eigencurves are depicted owing to the replication property discussed in Sec. 2.2.2.

When employing SVV, the current practice (see e.g. [13] and references therein) is to employ $\mu = \mu_0/P$, where μ is the base SVV magnitude, recall Eq. (2.35), and μ_0 a fixed parameter. Note that such practice implicitly makes $\mathrm{Pe}^* = {}^{ah}/_{\mu P}$ independent of P. This strategy will henceforth be called the "traditional" SVV approach. It should be stressed, however, that within this practice Pe^* still depends on the product ah which, in practical simulations, will vary since the advection speed and the mesh spacing are essentially independent quantities. An issue of the traditional SVV approach can be illustrated by the following reasoning. Consider a linear advection problem (i.e. given a) to be solved by CG with SVV-based stabilization. Following the traditional approach, one has $\mu \propto P^{-1}$. Given the total number of degrees of freedom (i.e. fixed h/P), consider two discretisation spaces:

(*i*) $P_1 = 2$ and $h_1 = h$, so that $\mathrm{Pe}^*_1 = {}^{ah_1}/_{\mu_1 P_1} = 3$;

(*ii*) $P_2 = 4$ and $h_2 = 2h$, so that $\mathrm{Pe}^*_2 = {}^{ah_2}/_{\mu_2 P_2} = 6$.

For these cases, the behaviour of the (exponential kernel-based) SVV operator is precisely that shown in Fig. 2.8. The diffusion plots highlight the problem with the traditional approach: SVV will have essentially different effects on a given physical problem for the same range of wavenumbers (recall that h/P is fixed). In particular, the underlying parabolic curves related to each diffusion eigencurve are different since their associated values of Pe^* are different.

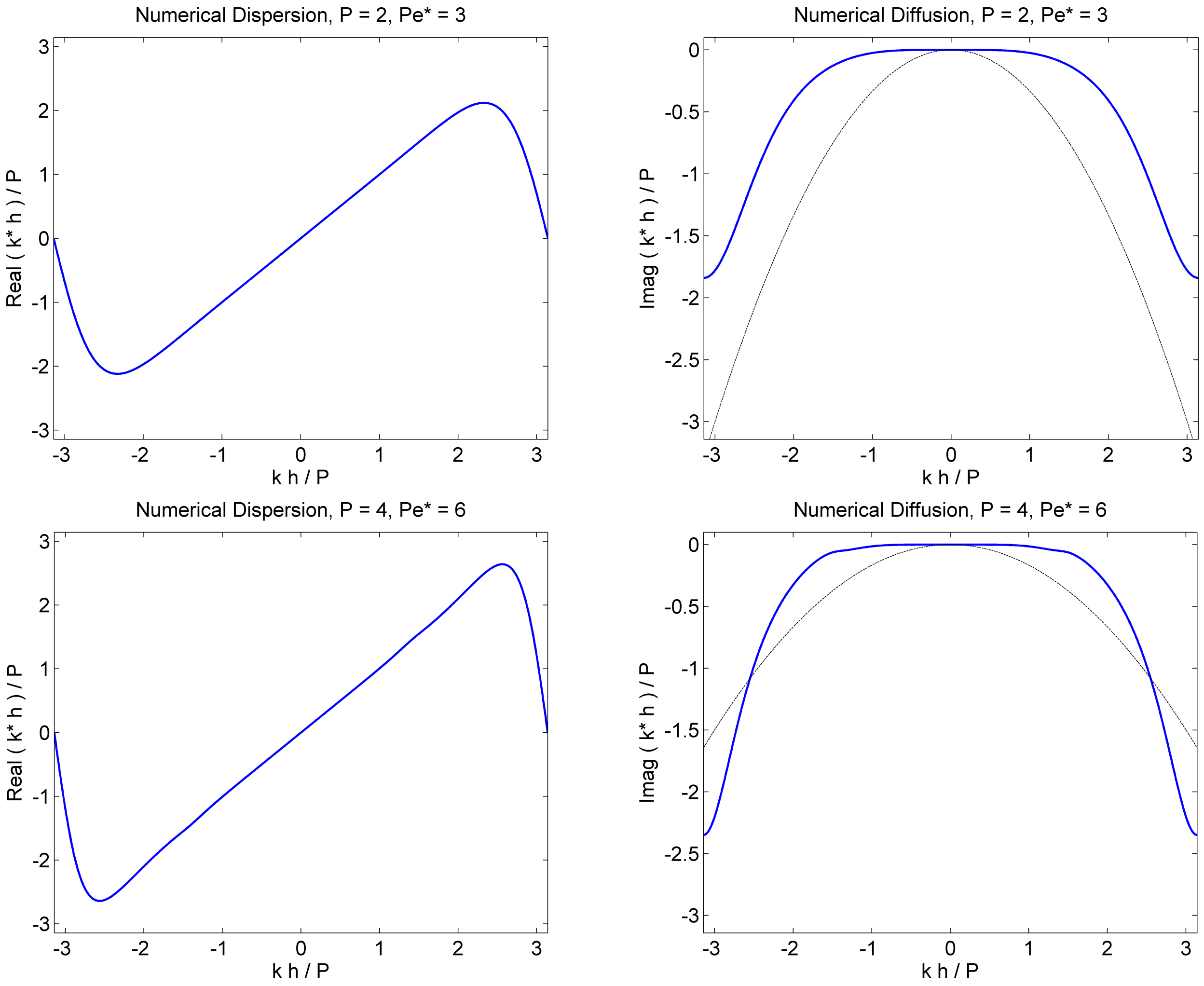

Figure 2.8: Dispersion-diffusion eigencurves for the exponential SVV kernel for $\mathrm{Pe}^* = 3$ with $P = 2$ (top) and $\mathrm{Pe}^* = 6$ with $P = 4$ (bottom). In both cases $P_{SVV} = 0$ is used. The thin dotted parabolas on the right-hand side plots show the regular (second-order) diffusion behaviour for each Pe^*.

Another inconvenience of the traditional SVV operator is that for a given discretisation order P, the eigencurves obtained with a prescribed value of Pe^* are only valid for the mesh spacing associated with such Pe^*. In other words, the mesh spacing h in the normalized horizontal axis of dispersion-diffusion plots is simply a scaling parameter, not a variable. For instance, considering a single diffusion plot, the SVV dissipation at kh/P is not the same as at $k'h'/P$ when $k'h' = kh$ but $h' \neq h$. This is because when h changes, so does Pe^*, and thus a different eigencurve must be consulted. Therefore, within the traditional SVV approach, an eigencurve obtained for a single Pe^* provides little information since the use of variable mesh spacing is unavoidable for practical applications. Furthermore, in regions of either very small or very large mesh spacing h, SVV will eventually introduce potentially undesirable non-smooth features in the solution, as happened in the case of regular diffusion when $\mathrm{Pe}^* \to 0$ or $\mathrm{Pe}^* \to \infty$, recall Fig. 2.7. In fact, CG-SVV eigencurves with irregular features have been found easily after some experimentation and this issue seems not related with SVV in itself, but with the CG formulation when it comes to the discretisation of viscous operators with either very low or very high values of Pe*.

2.3.3 Towards more reliable SVV operators

A modification to the traditional SVV operator is now proposed, that bypasses the issues discussed in the previous section and allows for the design of SVV operators that are more generally applicable. The main idea is to make the base SVV magnitude proportional to both the advection speed and mesh spacing, using $\mu = \mu_0 \, ah/P$. For general problems and discretisations, P would be the polynomial order used in each element (e.g. in case P-adaptation is employed), h would be a local mesh length, and a would be a measure of the advection speed within each element. Note that this implicitly makes $\mathrm{Pe}^* = {}^{ah}/_{\mu P}$ independent of a, h and P, more precisely a constant, $\mathrm{Pe}^* = \mu_0^{-1}$. SVV characteristics will then be solely dependent on μ_0, P, and on the kernel entries $\hat{\mathcal{Q}}_k$. This approach is advantageous if one wishes to design an SVV kernel based on a fixed value of Pe* to be used regardless of either advection speed or mesh variations.

Following the proposed approach, let us now focus on the exponential kernel-based SVV operator and discuss its suitability for high-order discretisations. The variation of the exponential kernel with its (polynomial) mode index k can be appreciated more clearly by rewriting Eq. (2.46) as

$$\hat{\mathcal{Q}}_k = \exp\left[-\frac{(\hat{k}-1)^2}{(\hat{k}-P_{SVV}/P)^2}\right] \ , \ \text{ for } \hat{k} > \frac{P_{SVV}}{P} \ , \tag{2.47}$$

where $\hat{k} = k/P$. Note that here k is a modal index rather than a wavenumber, as in Eq. (2.46). The shapes assumed by $\hat{\mathcal{Q}}_k$ for $P_{SVV} = 1$ and $P_{SVV} = \sqrt{P}$ are shown in Fig. 2.9 for different polynomial orders, $P = 2, \ldots, 7$. Both choices (fixed or variable P_{SVV}) are often used in the literature. In any case, kernel shapes can be seen to vary according the discretisation order employed and essentially introduce more dissipation as P is increased. The asymptotic shape approached as $P \to \infty$ is shown as the dotted (left-most) curves in Fig. 2.9 and is the same in both cases. This is also the kernel shape obtained for $P_{SVV} = 0$, in which case $\hat{\mathcal{Q}}_k$ becomes independent of P.

The dispersion-diffusion characteristics obtained with the exponential kernel-based SVV operator for $P_{SVV} = 0$ when $\mathrm{Pe}^* = 10$ are shown in Fig. 2.10, first for $P = 2$ and 3 and then for $P = 3$ to 8. These graphs show an undesirable feature of the exponential kernel, namely, that as P increases, “spurious” oscillations appear on the eigencurves. This behaviour is typical of the limit $\mathrm{Pe}^* \to \infty$, recall Fig. 2.7, suggesting that the overall amount of viscosity introduced by the exponential kernel should be higher. Note that $P_{SVV} = 0$ yields already the kernel shape which provides the highest levels of dissipation. Increasing P_{SVV} will only confine the viscous effects to the highest modes, thus making the situation worse. It has been verified that using $P_{SVV} \propto P$ or $P_{SVV} = \sqrt{P}$ can be equally detrimental, probably for the same reason, as expected from Fig. 2.9 (right-hand side plot).

Increasing μ_0 can delay the oscillations until higher values of P, as shown in Fig. 2.11, where $\mathrm{Pe}^* = 5$. However, another shortcoming remains: as P increases, diffusion curves are drawn inwards thus introducing more dissipation at the smaller wavenumbers. This is undesirable because SVV

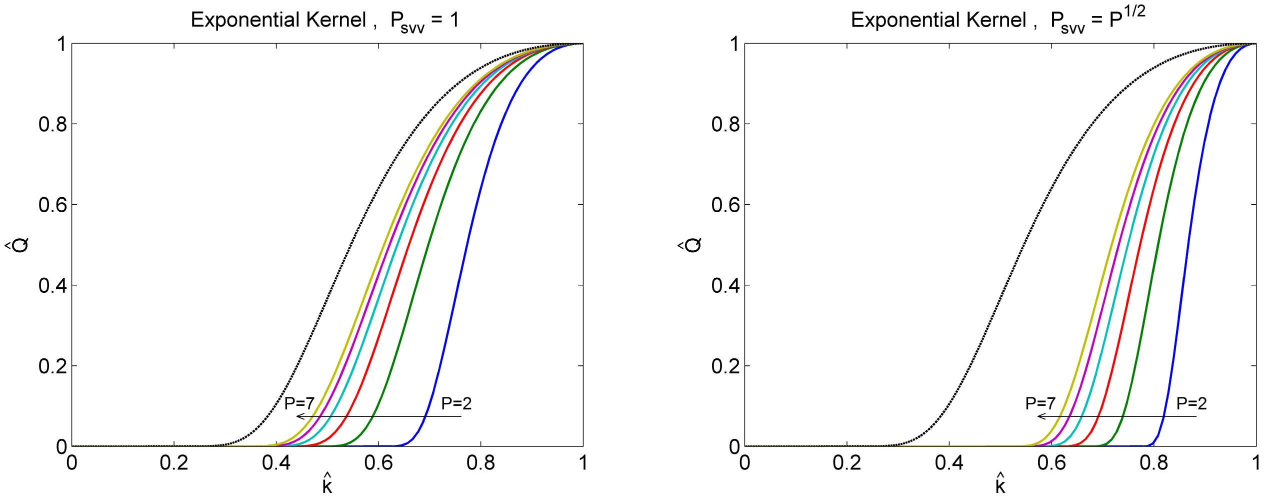

Figure 2.9: Shapes assumed by the exponential kernel $\hat{\mathcal{Q}}$ for $P_{SVV} = 1$ (left) and $P_{SVV} = \sqrt{P}$ (right) for different polynomial orders P. The asymptotic shape approached as $P \to \infty$, shown as the dotted (left-most) curves, is the same in both cases and correspond to the shape of $\hat{\mathcal{Q}}$ for $P_{SVV} = 0$.

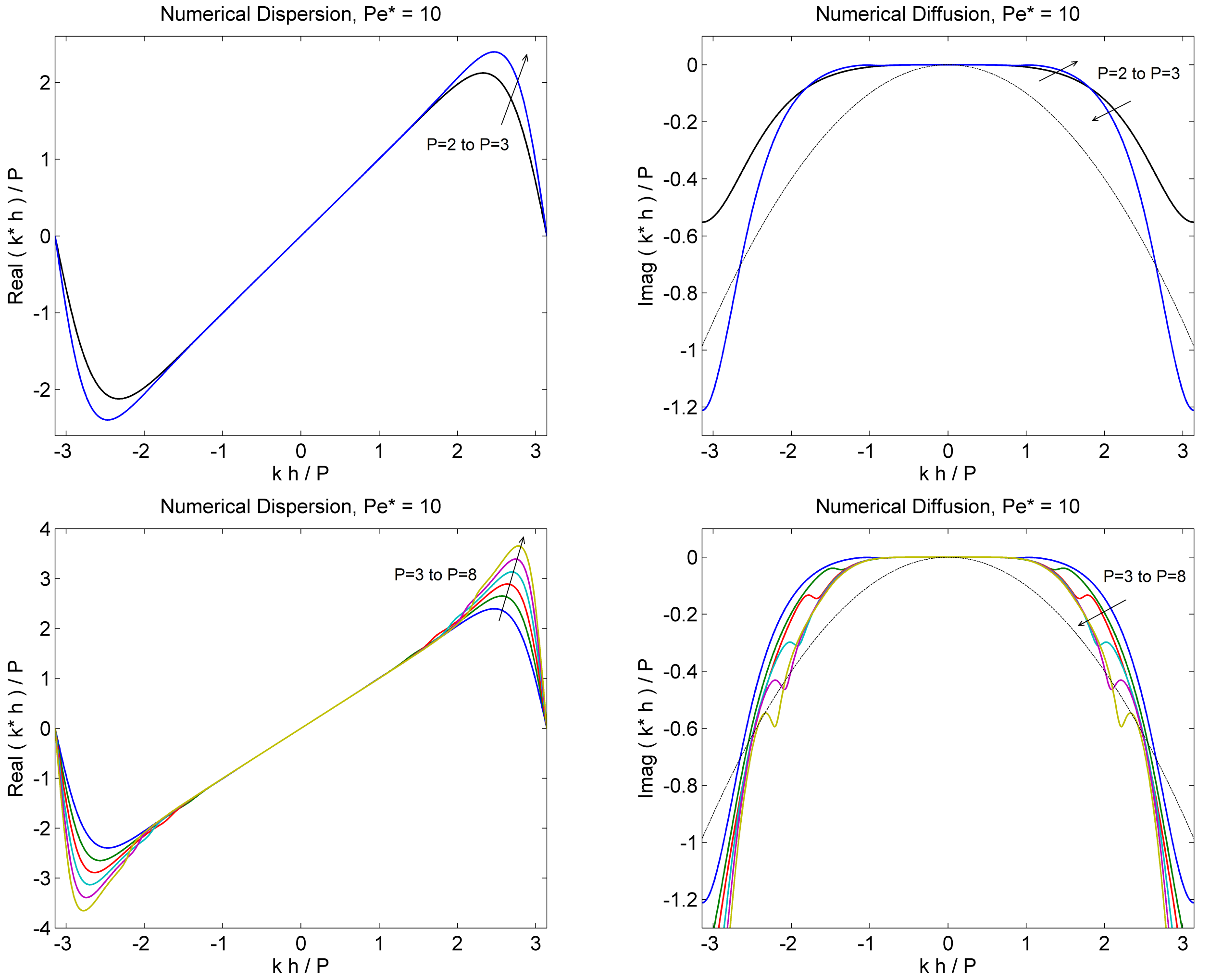

Figure 2.10: Dispersion-diffusion curves for the SVV operator based on the exponential kernel (with $P_{SVV} = 0$) when $\mathrm{Pe}^* = 10$, for $P = 2$ and 3 (top) and for $P = 3$ to 8 (bottom). Thin dotted parabolas on the diffusion plots show the regular (second-order) diffusion behaviour for $\mathrm{Pe}^* = 10$.

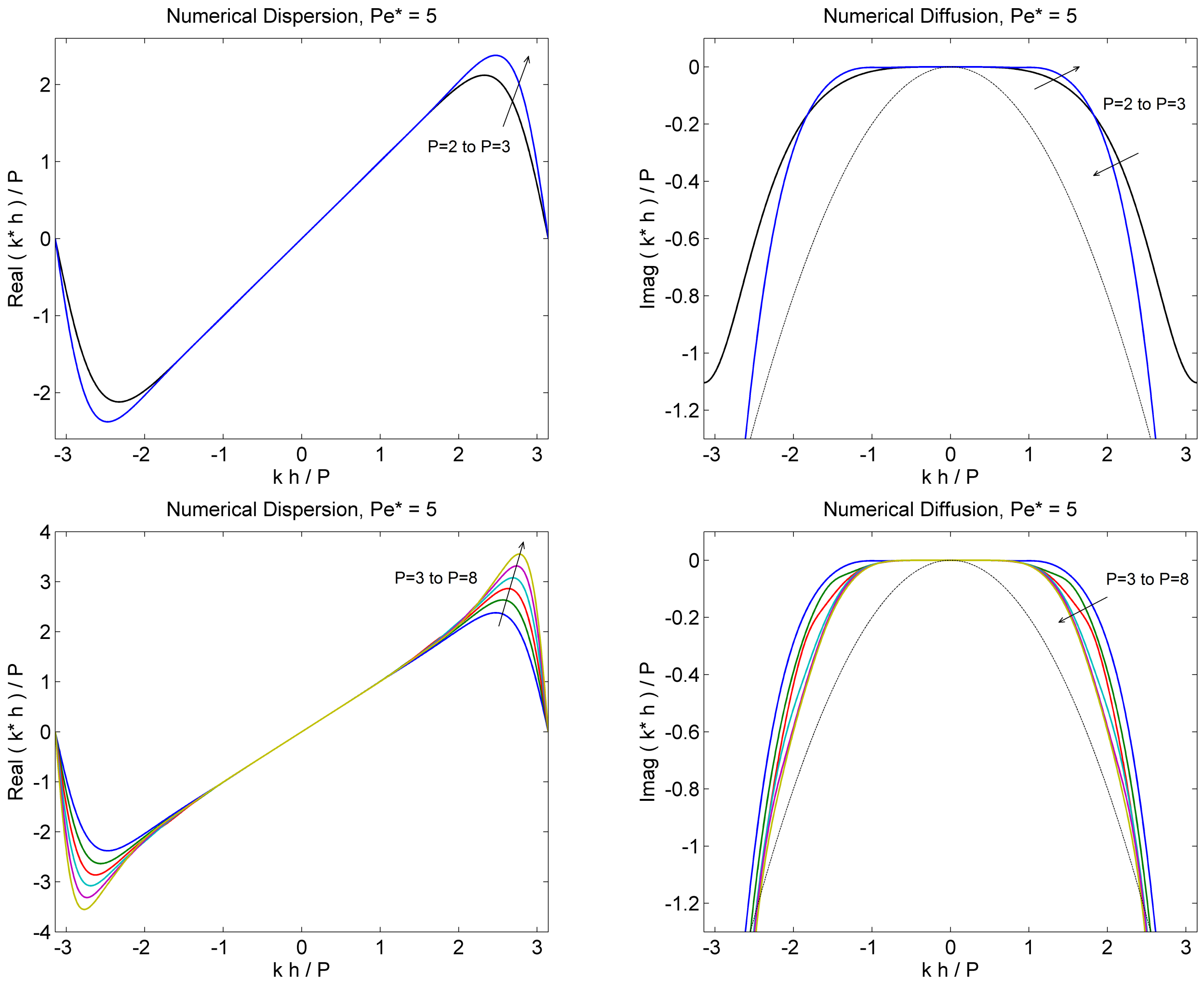

Figure 2.11: Dispersion-diffusion curves for the SVV operator based on the exponential kernel (with $P_{SVV} = 0$) when $\mathrm{Pe}^* = 5$, for $P = 2$ and 3 (top) and for $P = 3$ to 8 (bottom). Thin dotted parabolas on the diffusion plots show the regular (second-order) diffusion behaviour for $\mathrm{Pe}^* = 5$.

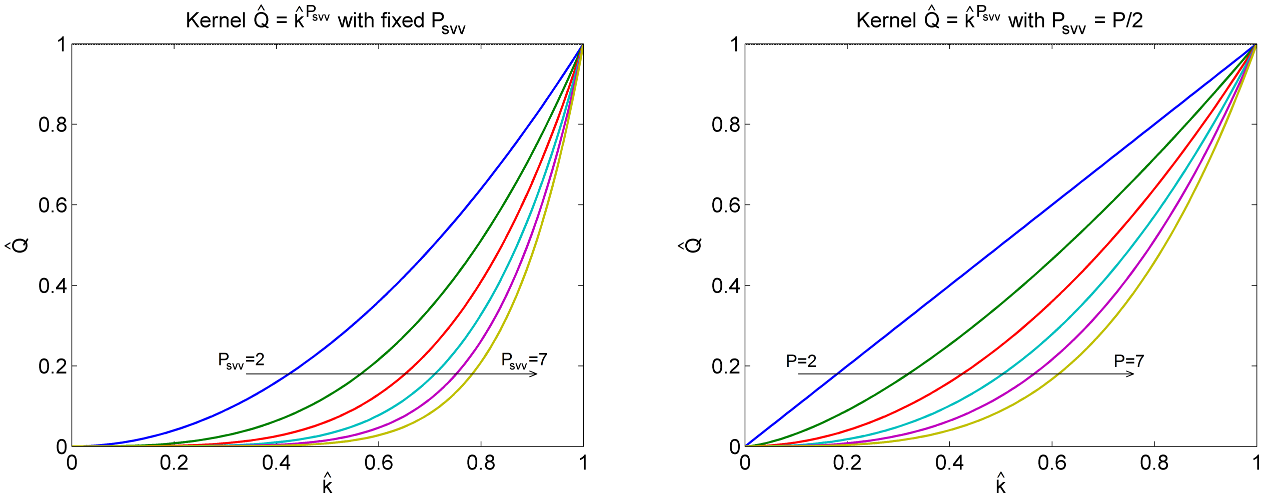

Figure 2.12: Shapes assumed by the proposed power kernel $\hat{\mathcal{Q}}_k = \hat{k}^{\,P_{SVV}}$ for increasing values of P_{SVV} (left) and for $P_{SVV} = P/2$ with increasing values of P (right).

dissipation should begin to act at increasingly higher wavenumbers as P is increased since discretisations of higher order are expected to have a superior resolution power per degree of freedom (DOF), as is the case for the DG scheme [9].

To avoid these shortcomings, a new kernel function is proposed which is given by

$$\hat{\mathcal{Q}}_k = (k/P)^{P_{SVV}} = \hat{k}^{\,P_{SVV}} \ , \ \text{for } 0 \le \hat{k} \le 1 \ . \tag{2.48}$$

Note that this "power" kernel does not depend explicitly on P, but only on $\hat{k}$ and P_{SVV}. Moreover, here P_{SVV} is not an activation threshold, but has a similar effect in terms of confining the viscous effects to the highest modes. This effect is shown in the left-hand side plot of Fig. 2.12, where the shape of the power kernel is depicted for different values of P_{SVV}.

Particularly desirable characteristics were found with the power kernel function when using $P_{SVV} \propto P$. Kernel shapes obtained with $P_{SVV} = P/2$ are shown for increasing values of P in the right-hand side graph of Fig. 2.12. By doing this, the viscous effects become increasingly confined to higher modes as P grows, contrary to what happens with the exponential kernel (see Fig. 2.9), and at the same time a non-zero (though small) amount of dissipation is always provided for the first modes. These two features are believed to be respectively the key to avoid both the "drawing inwards" behaviour and spurious oscillations. Dispersion-diffusion eigencurves obtained with the power kernel with $P_{SVV} = P/2$ when $\mathrm{Pe}^* = 2$ are shown in Fig. 2.13 for polynomial orders $P = 2, \ldots, 8$.

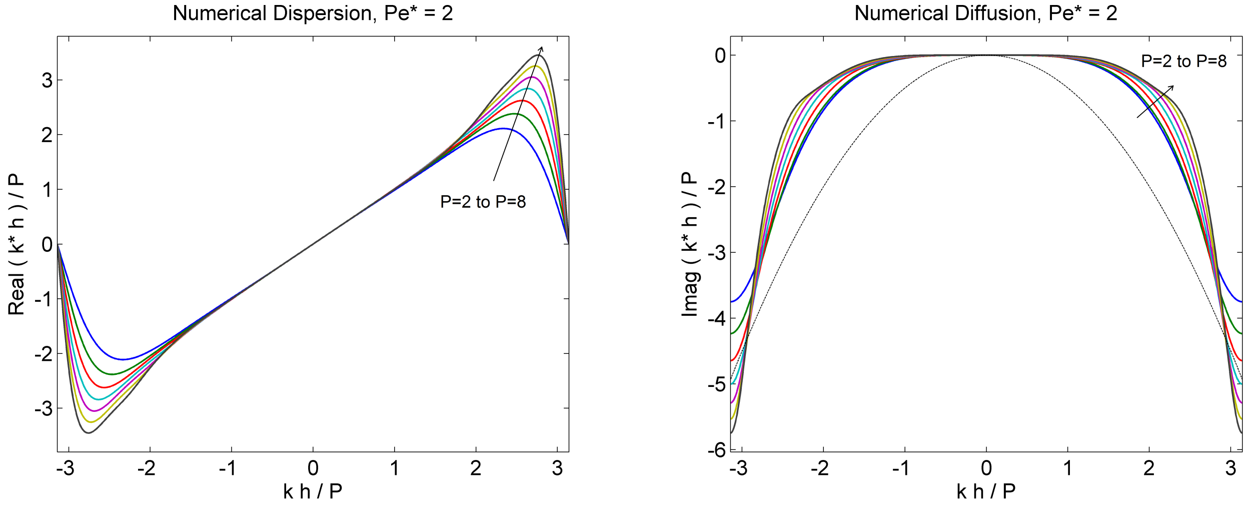
Numerical Dispersion, Pe* = 2

Numerical Diffusion, Pe* = 2

Figure 2.13: Dispersion-diffusion curves for the SVV operator based on the proposed power kernel with $P_{SVV} = P/2$ for $\mathrm{Pe}^* = 2$. The thin dotted parabola on the diffusion plot shows the regular (second-order) diffusion behaviour for $\mathrm{Pe}^* = 2$.

It is worth noting that, if applied directly in Fourier space, the power kernel would mimic the effect of hyperviscosity, see Eq. (2.36). When however applied through a polynomial (hierarchical) setting, the resulting dissipation in Fourier space follows the same trends of traditional kernel functions, as shown in Fig. 2.13. In addition, note that the power kernel function will always affect all the polynomial modes above $\hat{k} = 0$, even though this effect becomes very small for the lower-order modes when P is increased (Fig. 2.12). A detailed discussion on whether this feature might affect typical spectral properties achieved via P refinement, such as exponential convergence, is provided in this chapter's appendix. Basically, it has been found that the SVV operator based on the power kernel with fixed P_{SVV} will exhibit algebraic decay at large values of P, whereas when P_{SVV} is made proportional to P, say as $P_{SVV} = P/2$, the magnitude of the SVV operator will decay slightly faster than exponentially. The latter approach is therefore superior and preferable.

2.4 Upwinding and SVV-based stabilization

As discussed in Sec. 2.3.2, the mesh spacing h used in the normalized horizontal axis of dispersion-diffusion plots is simply a scaling parameter, not actually a variable, in the traditional SVV approach. This causes two wavenumbers at different mesh regions where the supporting number of points per wavelength is the same (i.e. $k_1h_1/P = k_2h_2/P$) to experience distinct levels of SVV dissipation due to a Péclet number difference. On the other hand, dissipation levels peculiar to spectral/hp schemes with upwind-based stabilization are observed to scale naturally with the local mesh resolution, see [3, 4, 5, 9]. As it happens, this is also achieved with the SVV approach here proposed, in which the Péclet number is held constant and so the dissipation is an actual function of kh for each P. In this sense, the dissipation characteristics of the advocated CG-SVV approach can be considered to be dimensionally equivalent to those obtained through upwinding in a DG setting, for instance.

A comparison is now carried out between the (standard) upwind DG scheme and the proposed CG-SVV formulation with the power kernel of Eq. (2.48). The main quantity compared is the extent of the wavenumber region where numerical errors are negligible. This extent is here estimated by the '1% rule' introduced in [9], summarized in the following. By expressing the modified wavenumber in the form $k^* = k^*_R + ik^*_I$, a propagating wave (of wavenumber k) can be represented as

$$u \propto \exp[i(kx - w^*t)] = \exp(ak^*_I t) \exp[i(kx - ak^*_R t)] \ , \tag{2.49}$$

where the relation $w^* = ak^*$ was used. Hence, regarding the wave's amplitude, one has

$$|u| \propto \exp(ak^*_I t) = \exp\left(k^*_I \hbar \ t/\tau\right) \ , \tag{2.50}$$

in which $\tau = \hbar/a$ and $\hbar = h/(P+1)$. Since $\hbar$ is the length measure of one DOF in both CG and DG settings, τ is the time it takes for a signal to cross a single DOF. Therefore, according to Eq. (2.50), for each $\Delta t = \tau$ passed, the magnitude of the propagating wave is scaled by $\exp(k^*_I \hbar)$, whereby this quantity can be regarded as a *damping factor per DOF crossed.* In particular, for a damping factor of 99% per DOF, the value of $k^*_I \hbar$ would be $\ln(0.99) \approx -0.01$. Although apparently arbitrary, this value was tested against one-dimensional Burgers turbulence simulations in [9] and found to be a very good measure of propagation accuracy. The 1% rule therefore consists in finding the wavenumber k for which $k^*_I \hbar = \ln(0.99)$. It is worth noting that the associated damping factor *per element crossed* is $\exp(k^*_I \hbar)^{P+1} = \exp[\ln(0.99)]^{P+1}$, which translates into $k^*_I h = (P+1)\ln(0.99)$.

Since the polynomial factor scaling $\overline{k}$ is different for CG and DG (as CG has one less *independent* DOF per element), the values of kh given by the 1% rule, named $(kh)_{1\%}$, are directly compared here for each polynomial order, as a measure of resolution power per element rather than per DOF. More specifically $(kh)_{1\%}$ is the value of kh for which $k_I^* h = (P+1)\ln(0.99)$, both for CG and DG. In the following, SVV parameters are adjusted so as to maximize the values of $(kh)_{1\%}$ for CG, given P.

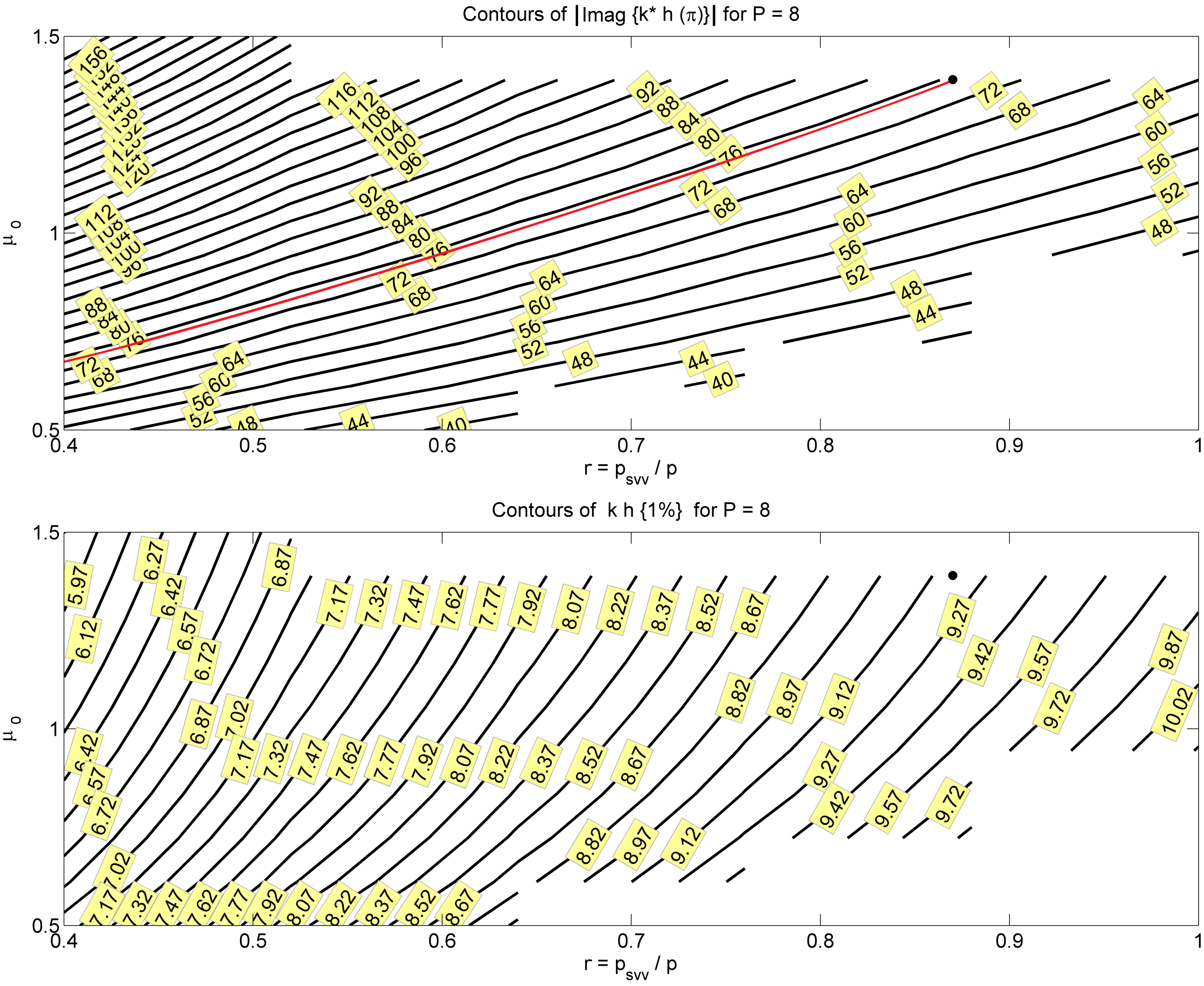

Figure 2.14: Contours of $(k_I^* h)_\pi$ (top) and $(kh)_{1\%}$ (bottom) for the proposed SVV operator and power kernel for $P = 8$ and different values of μ_0 and $r = P_{SVV}/P$. The bullet on the upper-right corner of the graphs corresponds to the maximum value of $(kh)_{1\%}$ along the curve $(k_I^* h)_\pi = (k_I^* h)_\pi^{DG}$, shown in red on the top plot.

First, note that the viscosity parameter μ_0 chosen for the SVV operator (recall that $\mu = \mu_0\, ah/P$ and so $\mathrm{Pe}^* = \mu_0^{-1}$) should not be reduced to the point of inducing very large values of $(kh)_{1\%}$ for the diffusion curves at the cost of a vanishing overall dissipation. Therefore, for a fair comparison, μ_0 is chosen so as to provide the same damping level per element, $k_I^* h$, of the full upwind DG scheme for the smallest captured scales, i.e. at $\bar{k} = \pi$. The remaining parameter of the SVV operator is the value of P_{SVV} from the power kernel, see Eq. (2.48), which is allowed to vary to maximize $(kh)_{1\%}$.

The optimization procedure described above is illustrated in Fig. 2.14 for the case $P = 8$. The top and bottom graphs display contour values of $(k_I^* h)_\pi$ and $(k\,h)_{1\%}$, respectively, within the ranges $0.5 < \mu_0 < 1.5$ and $0.4 < r < 1.0$, where $r = P_{SVV}/P$. The dot on the upper-right corner of the graphs corresponds to the maximum value of $(k\,h)_{1\%}$ along the curve $(k_I^* h)_\pi = -75.06$, which is the reference DG damping level (per element) for $P = 8$. An algorithm based on the total variation of the eigencurves was employed to avoid the irregular behaviours observed when $\mathrm{Pe}^* \to 0$ or $\mathrm{Pe}^* \to \infty$.

Table 2.1: Optimal parameters for the proposed SVV operator and kernel function

P	2	3	4	5	6	7	8
r	1.00	2.87	2.45	2.07	1.31	1.02	0.87
μ_0	1.58	13.46	7.36	4.87	2.12	1.58	1.39

The blank regions in the contour plots represent dispersion-diffusion curves with oscillation levels above a certain threshold. The procedure was carried out for $P = 2, \dots, 8$ and the values of r and μ_0 leading to the optimized values of $(k\,h)_{1\%}$ are given in Table 2.1 for each polynomial order. Note that case $P = 2$ had its value of $(k\,h)_{1\%}$ practically unchanged along the relevant dissipation curve for a wide range of values of r, and so the set of parameters $(r, \mu_0) = (1.00, 1.58)$ was arbitrarily chosen as a representative of this range.

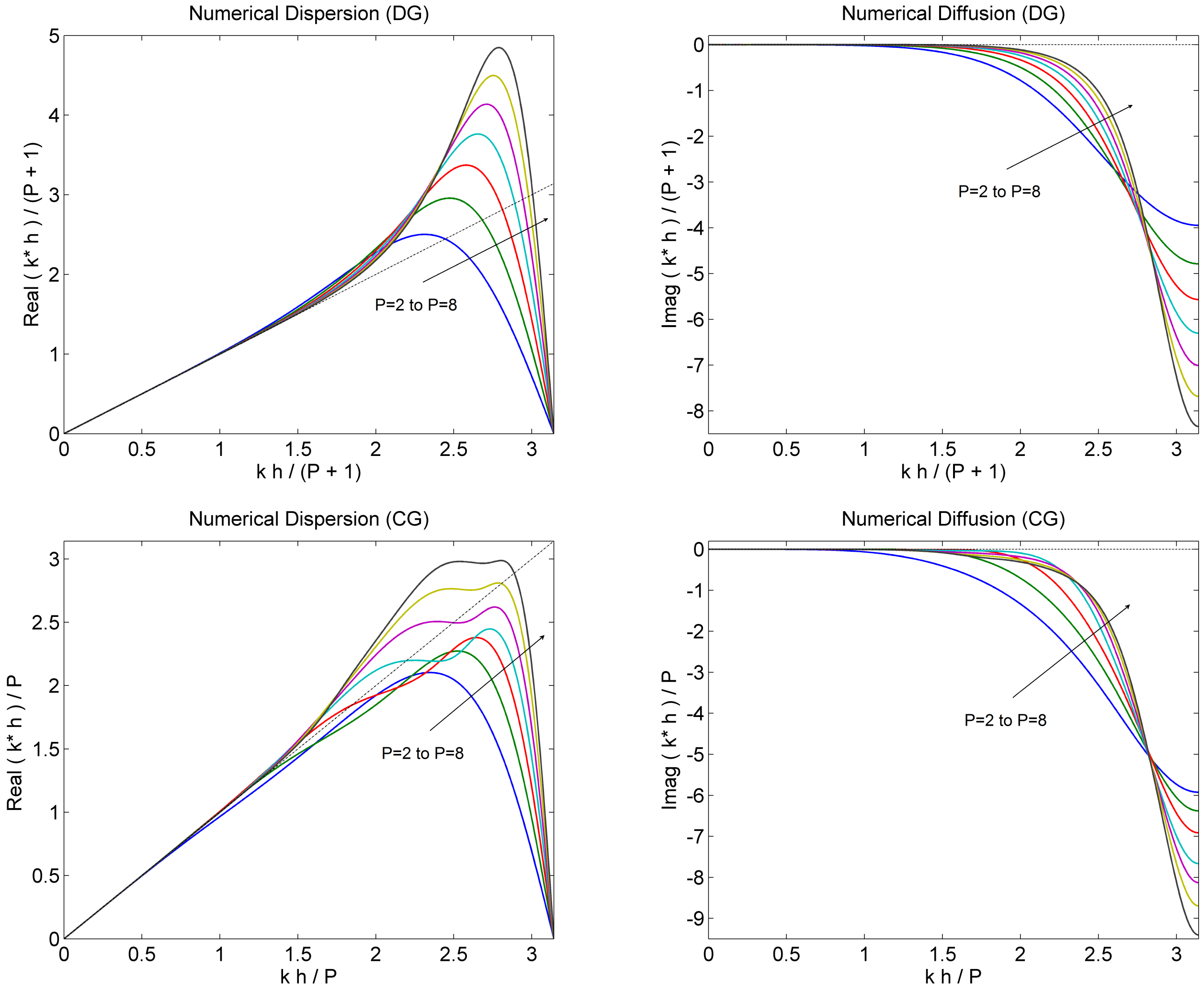

Figure 2.15: Dispersion and diffusion curves for standard upwind DG (top) and the optimized CG-SVV scheme (bottom) for $P = 2, \dots, 8$. Dotted lines show the exact behaviour for pure advection.

A graphical comparison between the eigencurves of the standard upwind DG method (from [9]) and those of the CG-SVV scheme with the parameters of Table 2.1 is shown in Fig. 2.15. Effective resolution estimates for the two discretisations are compared in Table 2.2. The second and third columns give the estimates of resolution power per element obtained from the 1% rule for each P, i.e. $(kh)_{1\%}$, from which the largest wavenumber within the range of negligible dissipation error can be evaluated. The next two columns compare the associated number of DOFs per wavelength for each scheme. Clearly, both discretisations achieve a consistent increase in resolution power per DOF for increasing polynomial orders. The last two columns respectively show the reference DG dissipation levels per element used for the SVV optimizations and the related damping factors per DOF.

Table 2.2: Effective resolution estimates for DG and CG-SVV for the same maximum dissipation

P	$(kh)^{DG}_{1\%}$	$(kh)^{CG}_{1\%}$	$2\pi/(k\hbar)^{DG}_{1\%}$	$2\pi/(k\hbar)^{CG}_{1\%}$	$\lvert k_I^*\,h\rvert_\pi$	$\exp{(k_I^*\,\hbar)_\pi}$
2	2.616	1.518	7.205	12.421	11.85	1.93×10^{-2}
3	4.330	3.142	5.804	8.000	19.16	8.31×10^{-3}
4	6.164	4.377	5.097	7.177	27.85	3.81×10^{-3}
5	8.071	5.599	4.671	6.733	37.92	1.80×10^{-3}
6	10.027	6.841	4.386	6.429	49.07	9.03×10^{-4}
7	12.018	7.989	4.183	6.292	60.80	5.00×10^{-4}
8	14.035	9.181	4.029	6.159	75.06	2.39×10^{-4}

The data summarized in Table 2.2 shows that full upwind DG and the proposed CG-SVV scheme follow the same tendency as the polynomial order is increased, but that DG has a higher resolution power per DOF. However, it should be recognized that the optimization carried out was based on the (relatively simple) power kernel suggested and that improved CG-SVV characteristics can still be pursued via different, more sophisticated kernel functions with the aid of optimization algorithms. Moreover, while DG characteristics (such as maximum dissipation) are somewhat restricted by the choice of an upwind numerical flux, the CG-SVV scheme is more flexible due to the larger number of SVV control parameters. Depending on the simulation considered and polynomial order used, DG dissipation levels are likely to be either too weak or stronger than necessary, whereas SVV could be adjusted to provide higher dissipation levels or an improved resolution power through a reduced maximum dissipation.

2.5 Conclusion

In this chapter, the spectral/*hp* continuous Galerkin (CG) formulation was assessed through the temporal eigenanalysis framework. The discretisation of the advection-diffusion equation was addressed first and the role of primary and secondary eigencurves was discussed. Those have been verified to behave in agreement with the perspective introduced in [9], by which secondary eigencurves peculiar to spectral/*hp* methods are perceived as replications of the primary one. Potentially undesirable non-smooth features have been observed on primary dispersion and diffusion curves for problems strongly dominated by either convection or diffusion. These have been found mostly at moderately high wavenumbers, indicating that high-order spectral/*hp* CG discretisations might be unsuited for under-resolved simulations of either advection or diffusion dominated problems.

Subsequently, the spectral vanishing viscosity (SVV) technique was analysed and, owing to a dependency of the traditional SVV operator on the Péclet number, the standard CG-SVV formulation was again found to feature non-smooth characteristics when convection is much stronger than dissipation or vice-versa. A new approach has been proposed where the base SVV magnitude is made locally proportional to both the advection speed and the mesh spacing. This way, the Péclet number is held constant globally and SVV effects are kept close to their design point. In addition, a "power kernel" function has been devised for the advocated SVV operator to provide a consistent increase in resolution power (per degree of freedom) when the polynomial order is increased — a feature not naturally achieved through the widely used "exponential kernel" introduced in [20]. We note however that for non-linear problems where the advection speed is solution dependent, the proposed SVV operator will also be non-linear and thus certain implementation difficulties are likely to appear. In such cases, reference values for the advection speed could be used in each element, for example.

Finally, the dissipation characteristics of the proposed SVV operator have been discussed and verified to be dimensionally equivalent to those obtained with upwind numerical fluxes. The CG formulation based on the suggested SVV operator and kernel function has been compared with the standard upwind DG scheme in terms of effective resolution power (as measured by the extent of the wavenumber range where numerical errors are negligible) according to the 1% rule introduced in [9]. The DG scheme has been found to have a moderately higher resolution power for the same dissipation levels. However, the results here obtained for CG were based on the power kernel and thus can only be regarded as "locally optimal". Improved CG-SVV characteristics can still be pursued via different kernel functions with the aid of optimization algorithms. Also, resolution power is not all that matters in under-resolved simulations. Sometimes it might be desirable to increase the overall dissipation simply to improve robustness, or to manipulate diffusion curves in order to mimic the spectral behaviour of some subgrid-scale model [13, 15, 16, 22]. Due to its larger number of control parameters, SVV can be more generally adjusted (when compared to DG) to provide the desired dissipation levels for complex problems, such as in transition and turbulence simulations.

Appendix

This section is devoted to a discussion of convergence properties of the SVV operator based on the "power" kernel proposed in Sec. 2.3.3, see Eq. (2.48). First, it should be noted that, in a pure spectral formulation, the effect of SVV can be directly analysed by inserting Eq. (2.48) into Eq. (2.36), which yields

$$\mu \frac{\partial}{\partial x}\left(\mathcal{Q} \star \frac{\partial u}{\partial x}\right) = -\mu / P^{P_{SVV}} \sum_k k^{P_{SVV}+2}\, \hat{u}_k \, \exp(ikx) \ , \tag{2.51}$$

whereby SVV formally mimics a hyperviscous operator of order $P_{SVV}+2$. Note, however, that the operator's behaviour for spectral/*hp* methods is expected to be somewhat different since spectral/*hp* discretisations are based on polynomials rather than on complex exponential functions. Nonetheless, it is expected that some of the properties (convergence properties, in particular) observed for pure spectral formulations are maintained for spectral/*hp* methods, as in fact happens with traditional SVV approaches.

From Eq. (2.51) one can estimate the magnitude of the SVV operator at a given wavenumber k as

$$|| \, \mathrm{SVV}_k \, (P) \, || \; \propto \; k^{P_{SVV}+2} / P^{P_{SVV}+1} \ , \tag{2.52}$$

since typically $\mu \propto 1/P$. As a result, for P_{SVV} fixed, one has

$$|| \, \mathrm{SVV}_k \, (P) \, || \; \propto \; 1/P^{P_{SVV}+1} \;\; \Longrightarrow \;\; \log || \, \mathrm{SVV}_k \, (P) \, || \; \propto \; -(P_{SVV}+1) \, \log P \, + \, \mathrm{const} \ , \tag{2.53}$$

and for P_{SVV} varying with P, say as $P_{SVV} = P/n$,

$$|| \, \mathrm{SVV}_k \, (P) \, || \; \propto \; k^{P/n+2} / P^{P/n+1} \;\; \Longrightarrow \;\; \log || \, \mathrm{SVV}_k \, (P) \, || \; \propto \; -(1 + P/n) \, \log(P/k) \, + \, \mathrm{const} \ . \tag{2.54}$$

The above estimates indicate that the effect of the power kernel-based SVV operator should decay algebraically via P refinement for P_{SVV} fixed, whereas for $P_{SVV} = P/n$ the decay can be faster than exponential. Furthermore, higher rates of decay could be obtained with larger values of P_{SVV} in Eq. (2.53) and smaller values of n in Eq. (2.54).

Some numerical results are now presented to substantiate the convergence estimates above. The Kovasznay flow [23] which represents a steady, laminar flow behind a two-dimensional grid was used to test how the power kernel-based SVV operator affects the spectral convergence properties of the continuous Galerkin formulation. This test case has been used in previous works [13, 14] to assess the error introduced by traditional SVV operators as applied to spectral/*hp* methods. A version of the analytical solution which is suitable for numerical tests can be found in [7] (see chapter 9) and is given by

$$\mathrm{u} = 1 - e^{\lambda x} \cos(2\pi y) \ , \ \ \mathrm{v} = \frac{\lambda}{2\pi} e^{\lambda x} \sin(2\pi y) \ , \ \ \mathrm{p} = \frac{1}{2}(1 - e^{2\lambda x}) \ , \tag{2.55}$$

where u and v represent the x and y velocity components, p is the pressure and $\lambda = (2\nu)^{-1} - [(2\nu)^{-2} + 4\pi^2]^{1/2}$, in which ν stands for the fluid's kinematic viscosity. The value $\nu = 1/400$ has been chosen here and is sufficiently small so as not to suppress the effects of SVV in the numerical solution.

From the discussions in Sec. 2.3.3, the value $\mathrm{Pe}^* = 2$ has been adopted for the tests of the power kernel (see e.g. Fig. 2.13) and the value $\mathrm{Pe}^* = 5$ has been used for the tests conducted with the exponential kernel, which will be useful for comparison. We note that these values represent a 2.5 times stronger base viscosity $\mu = a\overline{h}/\mathrm{Pe}^*$ for the power kernel-based SVV operator. Since from the analytical solution the average of u and v over the plane are respectively one and zero, the constant value $a = 1$ has been adopted globally in the test cases. The Kovasznay flow was solved in the rectangular domain $[-1/2, 3/2] \times [-1/2, 3/2]$ in an equispaced grid consisting of 16 square-shaped elements of side $h = 1/2$. Dirichlet boundary conditions based on the analytical solution have been imposed where appropriate. The incompressible Navier-Stokes solver encapsulated within spectral/*hp* element code Nektar++ [24] was used for the test cases.

Fig. 2.16 displays the convergence of the error (L^2 norm) on the y velocity component, v, which can be measured easily by comparison with the analytical solution. The convergence curves based on u or p (not shown) presented very similar trends and were just a bit more wiggly. Such results clearly support the convergence estimates given in Eqs. (2.53–2.54). In particular, they show that the power kernel with varying P_{SVV} is to be preferred over its counterpart based on a fixed P_{SVV} value, since the error introduced by this latter approach will eventually surpass the baseline error of the CG discretisation as the polynomial order is increased. Also, when using $P_{SVV} = P/2$, the comparison with the exponential kernel indicates that introducing a small amount of dissipation at the lower-order modes is not necessarily worse than introducing none, which by construction is the case for the exponential kernel tested.

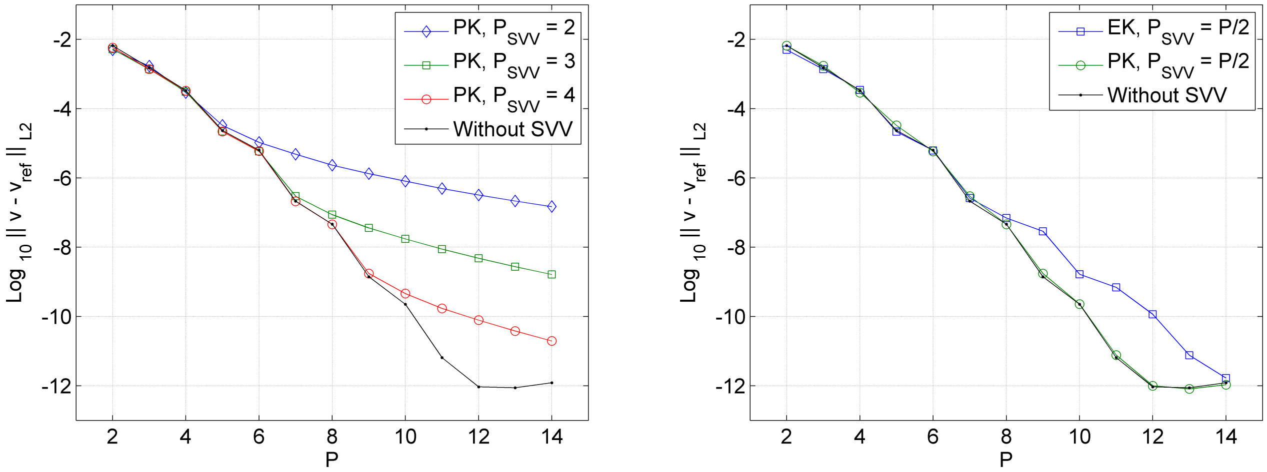

Figure 2.16: Log-linear convergence plots of the error (L^2 norm) on the y velocity component. Left: results without SVV are compared with those obtained with the power kernel (PK) for different given values of P_{SVV}. Right: results obtained with the exponential kernel (EK) are compared with those of the power kernel, both using $P_{SVV} = P/2$.

Finally, the kernel functions employed in the two-dimensional discretisation were, for the power kernel,

$$\hat{\mathcal{Q}}_{i,j} = \left(\frac{i}{P}\right)^{P_{SVV}} \left(\frac{j}{P}\right)^{P_{SVV}} \quad \text{for } 0 \leq i, j \leq P \ , \tag{2.56}$$

and, for the exponential kernel which becomes non-zero only above P_{SVV},

$$\hat{\mathcal{Q}}_{i,j} = \exp\left[-\frac{(i-P)^2}{(i-P_{SVV})^2}\right] \exp\left[-\frac{(j-P)^2}{(j-P_{SVV})^2}\right] \quad \text{for } i, j > P_{SVV} \ , \tag{2.57}$$

where i, j are used to indicate the index of the polynomial mode in a tensor-product Legendre orthogonal basis spanning the polynomial space of degree P, see [7].

References

[1] P. E. Vincent and A. Jameson. Facilitating the adoption of unstructured high-order methods amongst a wider community of fluid dynamicists. *Mathematical Modelling of Natural Phenomena*, 6(3):97–140, 2011.

[2] F. Q. Hu, M. Y. Hussaini, and P. Rasetarinera. An analysis of the discontinuous Galerkin method for wave propagation problems. *Journal of Computational Physics*, 151(2):921–946, 1999.

[3] K. Van den Abeele, T. Broeckhoven, and C. Lacor. Dispersion and dissipation properties of the 1D spectral volume method and application to a p-multigrid algorithm. *Journal of Computational Physics*, 224(2):616–636, 2007.

[4] K. Van den Abeele, C. Lacor, and Z. J. Wang. On the stability and accuracy of the spectral difference method. *Journal of Scientific Computing*, 37(2):162–188, 2008.

[5] P. E. Vincent, P. Castonguay, and A. Jameson. Insights from von Neumann analysis of high-order flux reconstruction schemes. *Journal of Computational Physics*, 230(22):8134–8154, 2011.

[6] S. J. Sherwin. Dispersion analysis of the continuous and discontinuous Galerkin formulations. In B. Cockburn, G. E. Karniadakis, and C. W. Shu, editors, *Discontinuous Galerkin Methods: Theory, Computation and Applications*, pages 425–431. Springer, 2000.

[7] G. E. Karniadakis and S. J. Sherwin. *Spectral/hp element methods for computational fluid dynamics.* Oxford University Press, 2nd edition, 2005.

[8] P. M. Gresho and R. L. Sani. *Incompressible flow and the finite element method. Volume 1: advection-diffusion.* John Wiley and Sons, 1998.

[9] R. C. Moura, S. J. Sherwin, and J. Peiró. Linear dispersion-diffusion analysis and its application to under-resolved turbulence simulations using discontinuous Galerkin spectral/*hp* methods. *Journal of Computational Physics*, 298:695–710, 2015.

[10] E. Tadmor. Convergence of spectral methods for nonlinear conservation laws. *SIAM Journal on Numerical Analysis*, 26(1):30–44, 1989.

[11] Ø. Andreassen, I. Lie, and C. E. Wasberg. The spectral viscosity method applied to simulation of waves in a stratified atmosphere. *Journal of Computational Physics*, 110(2):257–273, 1994.

[12] S. M. O. Kaber. A Legendre pseudospectral viscosity method. *Journal of Computational Physics*, 128(1):165–180, 1996.

[13] G. S. Karamanos and G. E. Karniadakis. A spectral vanishing viscosity method for large-eddy simulations. *Journal of Computational Physics*, 163(1):22–50, 2000.

[14] R. M. Kirby and S. J. Sherwin. Stabilisation of spectral/hp element methods through spectral vanishing viscosity: application to fluid mechanics modelling. *Computer Methods in Applied Mechanics and Engineering*, 195(23):3128–3144, 2006.

[15] R. M. Kirby and G. E. Karniadakis. Coarse resolution turbulence simulations with spectral vanishing viscosity–large-eddy simulations (SVV-LES). *Journal of Fluids Engineering*, 124(4):886–891, 2002.

[16] R. Pasquetti. Spectral vanishing viscosity method for LES: sensitivity to the SVV control parameters. *Journal of Turbulence*, 6(12), 2005.

[17] R. Pasquetti. Spectral vanishing viscosity method for large-eddy simulation of turbulent flows. *Journal of Scientific Computing*, 27(1-3):365–375, 2006.

[18] M. Minguez, R. Pasquetti, and E. Serre. High-order large-eddy simulation of flow over the 'Ahmed body' car model. *Physics of Fluids*, 20(9):095101, 2008.

[19] K. Koal, J. Stiller, and H. M. Blackburn. Adapting the spectral vanishing viscosity method for large-eddy simulations in cylindrical configurations. *Journal of Computational Physics*, 231(8):3389–3405, 2012.

[20] Y. Maday, S. M. O. Kaber, and E. Tadmor. Legendre pseudospectral viscosity method for nonlinear conservation laws. *SIAM Journal on Numerical Analysis*, 30(2):321–342, 1993.

[21] C. Xu and R. Pasquetti. Stabilized spectral element computations of high Reynolds number incompressible flows. *Journal of Computational Physics*, 196(2):680–704, 2004.

[22] T. Dairay, E. Lamballais, S. Laizet, and J. C. Vassilicos. Numerical dissipation vs subgrid-scale modelling for large eddy simulation. *Journal of Computational Physics*, 337:252–274, 2017.

[23] L. I. G. Kovasznay. Laminar flow behind a two-dimensional grid. In *Mathematical Proceedings of the Cambridge Philosophical Society*, volume 44, pages 58–62, 1948.

[24] C. D. Cantwell, D. Moxey, A. Comerford, A. Bolis, G. Rocco, G. Mengaldo, D. De Grazia, S. Yakovlev, J-E. Lombard, D. Ekelschot, B. Jordi, H. Xu, Y. Mohamied, C. Eskilsson, B. Nelson, P. Vos, C. Biotto, R. M. Kirby, and S. J. Sherwin. Nektar++: An open-source spectral/*hp* element framework. *Computer Physics Communications*, 192:205–219, 2015.

Chapter 3

On the performance of DG-based uDNS of free turbulence at very high Reynolds numbers

Summary [†]

This chapter presents estimates of spectral resolution power for under-resolved turbulent Euler flows obtained with the high-order discontinuous Galerkin (DG) method. The '1% rule' based on linear dispersion–diffusion analysis introduced by Moura et al. [*J. Comput. Phys.* 298 (2015) 695–710] is here adapted for 3D energy spectra and validated through the inviscid Taylor–Green vortex problem. The 1% rule estimates the wavenumber beyond which numerical diffusion induces an artificial dissipation range on turbulent spectra. As the original rule relies on standard upwinding, different Riemann solvers are tested here. Very good agreement is found for solvers which treat the different physical waves in a consistent manner. Relatively good agreement is still found for simpler solvers. The latter however displayed spurious features attributed to the inconsistent treatment of different physical waves. It is argued that, in the limit of vanishing viscosity, such features might have a significant impact on robustness and solution quality. The estimates proposed are regarded as useful guidelines for no-model DG-based simulations of free turbulence at very high Reynolds numbers.

3.1 Introduction

DG (and other discontinuous spectral element) methods have been successfully employed in eddy-resolving computations of turbulence through the so-called implicit LES approach [1, 2, 3, 4, 5], where, broadly speaking, numerical errors are expected to play the role of turbulence models. The term implicit LES has however been more traditionally connected to numerical methods whose truncation errors resemble subgrid-scale models of classical LES approaches [6, 7]. As this property has not yet been formally demonstrated for DG [8, 9], the term under-resolved DNS (uDNS) is here preferred to describe DG-based eddy-resolving simulations without added subgrid models. Linear

---

[†] This chapter is based on "R. C. Moura, G. Mengaldo, J. Peiró, S. J. Sherwin (2017) *On the eddy-resolving capability of high-order discontinuous Galerkin approaches to implicit LES / under-resolved DNS of Euler turbulence*, **Journal of Computational Physics** 330:615–623".

dispersion–diffusion analysis has suggested that DG's suitability for uDNS is due to its convenient spectral dissipation [10], which does not affect the large scales directly and is only significant at high wavenumbers / frequencies. Still, the suitability of DG-uDNS for general flows at very high Reynolds numbers is not yet fully understood (especially for wall-bounded flows). More research is therefore necessary to assess whether no-model DG (and related) approaches are capable of providing usefully accurate solutions for different types of flows when molecular viscosity is negligible.

One of the fundamental questions regarding uDNS approaches concerns their resolution power or eddy-resolving capability. A natural candidate for the effective grid size of a spectral element setting is $h/(p+1)$, h and p being the mesh spacing and the polynomial order employed. This measure relates to the number of degrees of freedom (DOFs) since $m = p + 1$ is the number of polynomial modes per element (and per dimension). However, for example when DG-based uDNS test cases of the same DOFs are compared, higher-order solutions (on coarser meshes), can outperform low-order ones (on finer grids) and follow much more closely reference DNS results [11]. The effects of h and p in terms of eddy-resolving capability have been further assessed in [10], where a simple criterion was proposed to estimate DG's effective resolution power for under-resolved computations. In [10], this criterion was named 'the 1% rule' and validated against one-dimensional Burgers turbulence. Here, the 1% rule is adapted for three-dimensional energy spectra and tested for the first time in a transitional / turbulent flow obtained through the Euler equations.

Euler (or inviscid) turbulence is often regarded as representative of real (Navier-Stokes) turbulence in the limit of very high Reynolds numbers [12, 13]. There are however at least two conditions for this to hold in any given simulation. First, vorticity has to be introduced via boundary and/or initial conditions, since the Euler equations can not generate vorticity from irrotational flows. Secondly, some artificial mechanism (e.g. numerical viscosity) is required in Euler simulations to ensure the dissipative character maintained by Navier-Stokes turbulence in the limit of vanishing viscosity [14]. For the inviscid Taylor–Green vortex [15] problem considered in the present study, vorticity is prescribed at the initial condition and upwind dissipation is relied upon for the enforcement of the entropy-consistent dissipative behaviour of the flow. The results discussed here are considered representative of DG-based uDNS of more general free flows (away from walls) at very high Reynolds numbers. Also, the results here shown for DG might be directly extendable to other discontinuous spectral element methods, in particular to certain variants of the flux reconstruction (FR) scheme, given the well established connections between DG and FR methods [16, 17, 18].

3.2 The 1% rule and its validation

The 1% rule had its origin in linear dispersion–diffusion analyses of the DG scheme [10], which showed that DG is able to resolve wave-like solution components accurately up to a certain wavenumber, beyond which numerical dissipation becomes significant. In this sense, an effective resolution power can be defined from the extent of the wavenumber region where numerical dissipation is negligible. More specifically, the 1% rule yields the wavenumber $k_{1\%}$ at which propagating waves have their amplitude scaled by 0.99 per DOF crossed, regardless of their speed — where the DOF measure is $\hbar = h/(p+1) = h/m$. Although seemingly arbitrary, this value has been tested against one-dimensional Burgers turbulence and proven to be a good measure of propagation accuracy for DG. In particular, this criterion was verified to accurately pinpoint the beginning of the (numerically induced) dissipation range on measured energy spectra.

Table 3.1: Resolution estimates (1D and 3D) for standard upwind DG

p	m	$(kh)^{1d}_{1\%}$	$2\pi/(k\hbar)^{1d}_{1\%}$	$(\Delta/h)^{1d}_{1\%}$	$(kh)^{3d}_{1\%}$	$2\pi/(k\hbar)^{3d}_{1\%}$	$(\Delta/h)^{3d}_{1\%}$
1	2	1.127	11.150	2.788	1.540	8.163	2.041
2	3	2.616	7.205	1.201	3.574	5.275	0.879
3	4	4.330	5.804	0.726	5.915	4.249	0.531
4	5	6.164	5.097	0.510	8.420	3.731	0.373
5	6	8.071	4.671	0.389	11.025	3.419	0.285
6	7	10.027	4.386	0.313	13.697	3.211	0.229
7	8	12.018	4.183	0.261	16.417	3.062	0.191
8	9	14.035	4.029	0.224	19.172	2.950	0.164

Table 3.1 provides the values of $(kh)_{1\%}$ given by the 1% rule for different discretisation orders, both for 1D and 3D Cartesian settings. The associated number of required DOFs per wavelength, $2\pi/(k\hbar)_{1\%}$, is also provided. The 1D values are the same as given in [10], whereas the 3D ones are derived in the present study (Sec. 3.4). In addition, Table 3.1 also provides measures of filter width $\Delta = \pi/k_{1\%}$ of an equivalent Gaussian filter of cutoff wavenumber $k_{1\%}$, see e.g. [19]. Note however that DG's 'implicit filter' is not exactly Gaussian as it is not isotropic in three dimensions, cf. Sec. 3.4. The estimates presented are expected to hold for full tensor-product basis functions in either modal or nodal form. In fact, while modal basis have been used in [10], nodal basis are employed in this study. Moreover, the estimates provided assume consistent integration of non-linear terms, as it seems that some resolution power may be lost otherwise [20]. Finally, note that the values in Table 3.1 are based on standard upwinding, see [10], being therefore regarded as a baseline for practical stabilized computations.

In this study, the 1% rule is validated through the Taylor–Green vortex (TGV) flow, introduced in [21] as a model problem for the analysis of transition and turbulence decay. The test case was originally proposed for the incompressible Navier-Stokes equations in a cubic domain with triply-periodic boundary conditions. As in previous works [15, 22], a modified version of the initial conditions that is suited for compressible flow solvers is adopted. The following expressions have been used at the initial state within $\Omega = [-\pi\ell_o, \pi\ell_o]^3$ respectively for the density, the three velocity components and the static pressure (note that the present DG implementation is based on conserved variables):

$$\rho = \rho_o \ , \tag{3.1}$$

$$u = V_o \sin(x/\ell_o)\cos(y/\ell_o)\cos(z/\ell_o) \ , \ \ v = -V_o\cos(x/\ell_o)\sin(y/\ell_o)\cos(z/\ell_o) \ , \ \ w = 0 \ , \tag{3.2}$$

$$p = \rho_o c_o^2/\gamma + \rho_o V_o^2 \left[\cos(2x/\ell_o) + \cos(2y/\ell_o)\right]\left[2 + \cos(2z/\ell_o)\right]/16 \ , \tag{3.3}$$

where $e = p/(\gamma-1) + \rho(u^2+v^2+w^2)/2$ is the total energy per unit volume. For the reference quantities, the values $\ell_o = \rho_o = V_o = 1$ and $c_o = 10$ have been adopted, leading to a Mach number of 0.1 and thus a quasi-incompressible test case. A non-dimensional time t is adopted based on the scale $\ell_o/V_o = 1$. A Reynolds number could be defined as $Re = \rho_o V_o \ell_o/\mu_o$, but only the inviscid problem is considered in this study, whereby the compressible Euler equations are simulated directly, with $\gamma = 1.4$. The inviscid problem has been adopted so that the effects of upwind dissipation could be directly assessed, thus allowing for a specific comparison of the performance of different Riemann fluxes in the limit of vanishing viscosity. It should be stressed that the inviscid TGV flow can be extremely demanding in terms numerical stability and may allow for the formation of singularities [23, 24, 25] if the entropy-consistent dissipative character of the flow is not enforced appropriately. As discussed in Sec. 3.3, some of the considered discretisations lacked stability/robustness.

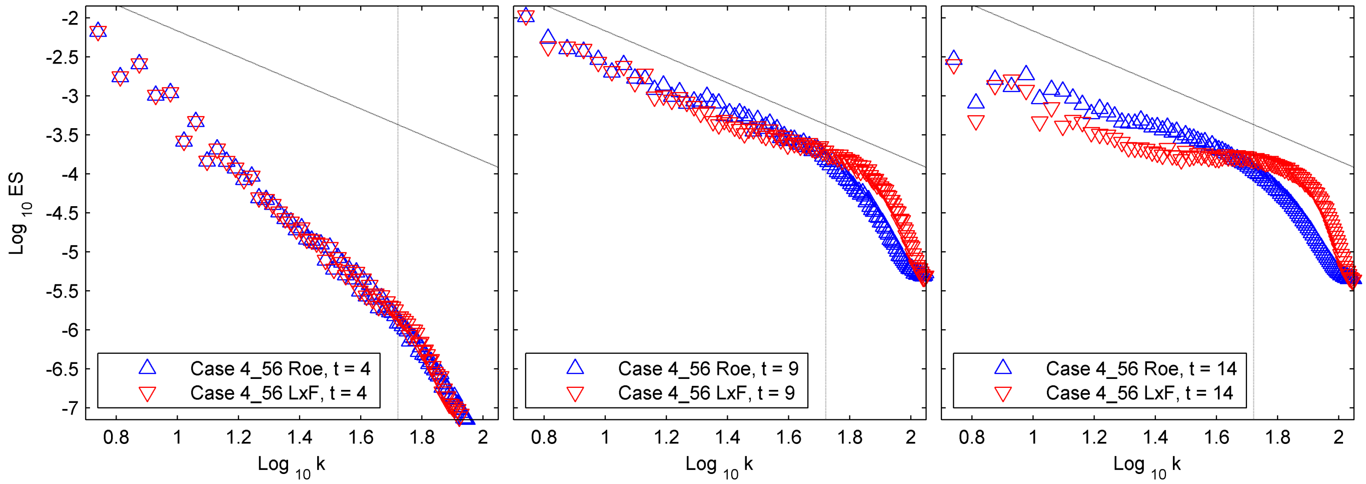

Figure 3.1: Three-dimensional energy spectra obtained with Roe (△) and Lax-Friedrichs (▽) at $t = 4$, $t = 9$ and $t = 14$ (left to right). Data obtained from simulations performed with $m = 4$ and $N_{el} = 56^3$. Vertical dashed lines correspond to $k^{3d}_{1\%}$ whereas inclined ones represent the $-5/3$ slope.

The three phases of the TGV evolution [26], namely, transition, strong dissipation and nearly-homogeneous decay are shown in Fig. 3.1. Kolmogorov's $-5/3$ slope is followed at $t \approx 9$, when a peak in overall dissipation is achieved [27]. Estimates for the start of the dissipation range (via $k^{3d}_{1\%}$) are shown as vertical lines, cf. Sec. 3.4. Two Riemann solvers are compared in Fig. 3.1, which exhibits clear differences between their behaviour at later flow phases, as discussed in the next section. These (inviscid) results have also been compared with viscous ones (not shown) at a Reynolds number of 10^6, but the energy spectra were practically indistinguishable. Only upon closer inspection one could see that the smaller scales where slightly less energetic for the viscous cases, thus supporting the claim that the inviscid solutions obtained are representative of under-resolved simulations conducted at very high Reynolds numbers.

3.3 Test cases and numerical flux performance

The base set of inviscid test cases considered relied on the Roe and Lax-Friedrichs (Rusanov) solvers, cf. e.g. [28]. This base set is shown on Table 3.2, where each column is associated to a number of polynomial modes $m = p + 1$ and each row represents a given number of DOFs, $N_{dof} = (n_{el}\, m)^3$, which is approximately constant in a row. The number of (cube-shaped) elements per direction is represented by n_{el}, whose values for each test case constitute the body of Table 3.2. Note that N_{dof} grows by a factor of $2^{3/2}$ between two adjacent rows, corresponding to a factor of $2^{1/2}$ in the number of DOFs per direction ($n_{el}\, m$). Crossed out numbers represent unstable simulations which collapsed prior to the third flow phase (nearly-homogeneous decay). Some specific cases have also been carried out with HLL, HLLC and the exact Riemann solver [28]. The energy spectra yielded by each of these solvers practically matched one of the two behaviours shown in Fig. 3.1. The latter two solvers followed Roe very closely, while the former one yielded results very similar to Lax-Friedrichs, see Fig. 3.5. This is indicated on the top row of Table 3.2 and further discussed below. All simulations have been conducted through the spectral/*hp* element code *Nektar++* [29].

Table 3.2: Summary of test cases — crossed out numbers indicate cases that crashed

	Roe (∼ HLLC, Exact)					Lax-Friedrichs (∼ HLL)				
$m = p + 1$	4	5	6	7	8	4	5	6	7	8
	28	23	19	16	14	28	23	~~19~~	~~16~~	~~14~~
n_{el}	39	32	28	23	~~19~~	39	32	~~28~~	~~23~~	~~19~~
	56	45	39	~~32~~	~~28~~	56	45	~~39~~	~~32~~	~~28~~

Table 3.2 shows that, at least for the problem considered, the Roe solver yields a more robust discretisation than Lax-Friedrichs. This is counter-intuitive since Lax-Friedrichs is traditionally regarded as more dissipative (and thus more robust) than Roe. Such differences are possibly specific to high-order DG at extremely high Reynolds numbers. In this limit, different fluxes can exhibit significant differences, see Fig. 3.1, first at the smallest resolved scales where numerical errors become noticeable (beyond $k_{1\%}$ in particular) and subsequently at larger scales owing to non-linear (triadic) interactions. Note that energy spectrum differences consistent with those found here have also been reported in recent studies involving high-Reynolds DG-based uDNS [30, 31].

All the unstable cases provided reasonable results up to the time of crash (without prior signs of instabilities), which consistently took place within the transitional phase of the TGV flow. The lack of robustness for the higher-order discretisations has been cautiously verified not to be related with time-step restrictions or polynomial aliasing errors. Typical CFL numbers (based on the acoustic wave speed) were of the order of 10^{-1} and an increased number of quadrature points ($q = 2m$ per dimension) has been employed in all the cases to ensure consistent integration of the cubic non-linearities of the compressible Euler equations. Tests conducted with particular cases to rule out these factors consistently showed the time of crash to be insensitive to time-step reductions (down to CFL $\approx 10^{-2}$) or to a further increase in the number of integration points (up to $q = 4m$). The 'global dealiasing' approach described in [32] has been employed for the interior and boundary quadratures, where over-integration is performed simply through a larger number of (Gauss-Lobatto-Legendre) quadrature points. The unstable simulations obtained highlight that DG-based uDNS approaches, even with consistent / over-integration, might in fact require additional stabilization techniques at very high Reynolds numbers so as to more strongly enforce the entropy-consistent dissipative behaviour of Navier-Stokes turbulence in the limit of zero viscosity.

Although the instabilities observed are not entirely understood at this point, one possible explanation is connected to the sharper dissipative behaviour (in Fourier space) of higher-order DG discretisations [10]. It is believed that a sharp dissipation might induce the energy-conserving character of the inviscid TGV flow to overcome the fully dissipative behaviour expected from LES-like results in the limit of vanishing viscosity. A sharper dissipation is known to induce a stronger bottleneck effect [33, 34], promoting a pile-up of energy prior to the dissipation range. DNS experiments using hyperviscosity in place of regular (second-order) viscosity have demonstrated that such 'energy bumps' grow as the hyperviscous exponent increases [35]. Complementary explanations [36, 37] showed that energy bumps emerge as the solution begins to follow an energy-conserving dynamics when only a finite number of Fourier modes are retained (consistent with the limit of increasingly sharp dissipation). While following this energy-conserving behaviour, the exact inviscid (Euler-based) evolution of the TGV flow may well develop singularities leading to the actual collapse of the solution, although this is still an open issue [23, 24, 25]. It should be stressed that the Lax-Friedrichs flux is expected to yield an even sharper spectral dissipation [9] due to its over-upwind bias for the momentum equations, especially at low Mach numbers, owing to the disparity between acoustic and convective speeds. This last point will be discussed further in Sec. 3.4, cf. Fig. 3.6.

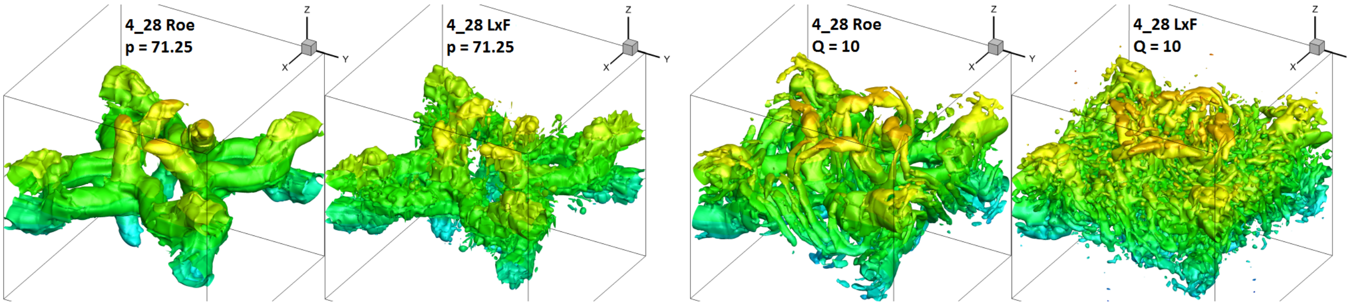

Figure 3.2: Isosurfaces of pressure (left pair) and Q-criterion (right pair) comparing simulations based on Roe (cleaner) and Lax-Friedrichs (noisier). Results obtained from test case $m = 4$, $n_{el} = 28$, at $t = 7$. Only one-eighth of the domain is shown; isosurfaces coloured by height (z-coordinate).

A complete assessment of solution quality is difficult since a DNS solution is simply out of reach for the inviscid TGV flow. Nevertheless, the energy spectra in Fig. 3.1 clearly show that the Lax-Friedrichs flux allows for an excessive accumulation of energy at the smallest captured scales, invariably connected to small non-physical structures highly contaminated by numerical errors (e.g. dispersion). This is illustrated in Fig. 3.2, where eddies of Roe-based computations are shown to be cleaner and better defined when compared to those obtained with Lax-Friedrichs. These eddies are visualized either via isosurfaces of pressure or by the Q-criterion [38]. Another feature observed at later times in the spectra of Fig. 3.1 is that the intermediate scales of Lax-Friedrichs computations are less energetic. This is likely to result from a spurious energy drain caused by the over-energetic small scales through an intense eddy viscosity-like mixing effect (as discussed in [36, 39]). In addition, near the dissipation peak ($t \approx 9$), Roe-based spectra follow Kolmogorov's $-5/3$ slope over a larger wavenumber range, see also Fig. 3.5.

Solution quality can be further assessed through the so-called QR diagrams [40, 41], cf. Fig. 3.3. These consist of joint PDFs of the second (Q) and third (R) invariants of the velocity gradient tensor for a given flow field [40] and provide a statistical description of turbulent kinematics.

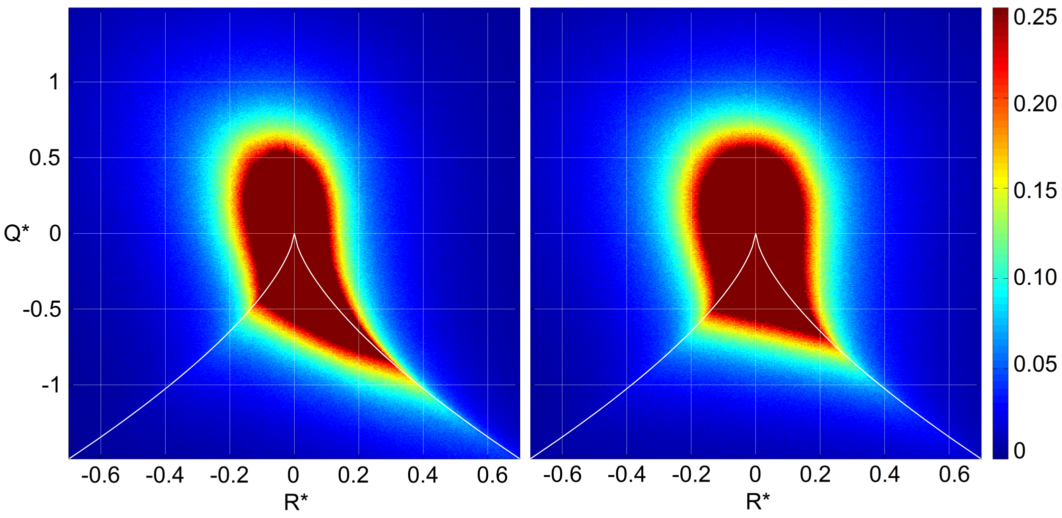

Figure 3.3: QR diagrams at $t = 9$ (dissipation peak) obtained with Roe (left) and Lax-Friedrichs (right), from case $m = 5$, $n_{el} = 23$. The dark red colour has been assigned to values above 1/4. The white curve separates rotational states (above the curve) from those without rotation (under the curve), cf. [40].

The teardrop-like profile yielded by the Roe-based case shown in Fig. 3.3 (left) is also observed in several different turbulent flows, see e.g. [42], and is regarded as one of the qualitatively universal characteristics of turbulence [41]. On the other hand, profiles obtained from Lax-Friedrichs computations yielded a more symmetrical distribution of kinematic states, typical of artificially generated Gaussian turbulence [43]. This symmetric distribution is possibly associated to the energy bump discussed previously, as bump-related scales represent a so-called thermalized state [37] where energy equipartition is favoured [36].

In any case, although a complete assessment of solution quality has not been made, the results discussed so far do not encourage the use of more simplistic Riemann solvers (such as HLL and Lax-Friedrichs) in DG-based uDNS, especially at high Reynolds and low Mach numbers.

3.4 One- and three-dimensional energy spectra

The energy spectra here considered are based on equispaced grids of $(n_{el}\, m)^3$ points, so that the number of Fourier modes extracted from a given case is consistent with its DOFs. The points inside each element are centred in order to avoid probing data at elemental interfaces. For example, element $[0, h]^3$ contains the set of points defined by the (triple) Cartesian product of coordinates $(j - 1/2)\, h/m$, for $j = 1, \ldots, m$. The grid points in the remaining elements are defined analogously. From this grid, a discrete 3D Fourier transform can directly provide the standard ‘three-dimensional energy spectrum’. It is worth recalling that the standard spectrum represents the density of kinetic energy in spectral space as distributed over spherical shells of radius $k = (\kappa_x^2 + \kappa_y^2 + \kappa_z^2)^{1/2}$, where κ_η is the wavevector component along axis η. Alternatively, a ‘one-dimensional energy spectrum’ can be defined as follows. A discrete 1D Fourier transform can be applied over each set of $(n_{el}\, m)$ points aligned with direction η to provide a single 1D energy spectrum. If an average is performed with all the $(n_{el}\, m)^2$ single 1D energy spectra aligned with η, one ends up with an averaged 1D energy spectrum for this direction. Finally, if averaged 1D spectra are obtained for the other two remaining directions and averaged again, a 'one-dimensional energy spectrum' of the TGV flow is obtained. This spectrum is shown in the chapter's appendix to represent the distribution of energy over cubic surfaces in Fourier space, where $k = |\kappa_x| = |\kappa_y| = |\kappa_z|$.

Since the 1% rule was originally devised for 1D settings [10], the validation tests regarding its application to the TGV flow initially considered the one-dimensional energy spectrum defined above. These tests showed that the values of $k_{1\%}^{1d}$ accurately pinpoint the beginning of the dissipation range for all the test cases addressed. The left plot in Fig. 3.4 compares (compensated) one-dimensional energy spectra at peak dissipation against the respective values of $k_{1\%}^{1d}$ for Roe-based cases with same DOFs and different polynomial orders (first row of cases in Table 3.2). Note that the horizontal axes in Fig. 3.4 have been normalized by the grid's Nyquist wavenumber $k_{NY} = \pi\, m/h$, which is approximately constant for the cases shown. The considered (left-hand side) plot indicates that, in Fourier space, dissipation is only significant outside the region $|\kappa_x| = |\kappa_y| = |\kappa_z| < k_{1\%}^{1d}$ and that DG's iso-dissipation surfaces seem to be cube-shaped (or nearly so) in Fourier space. This behaviour is however likely to depend on the mesh topology. These results have also been verified to be consistent with DG's dissipation characteristics for the wave equation in two dimensions [44], in that, at large wavenumbers, waves aligned with the (Cartesian) mesh suffer more dissipation than inclined (diagonal) waves.

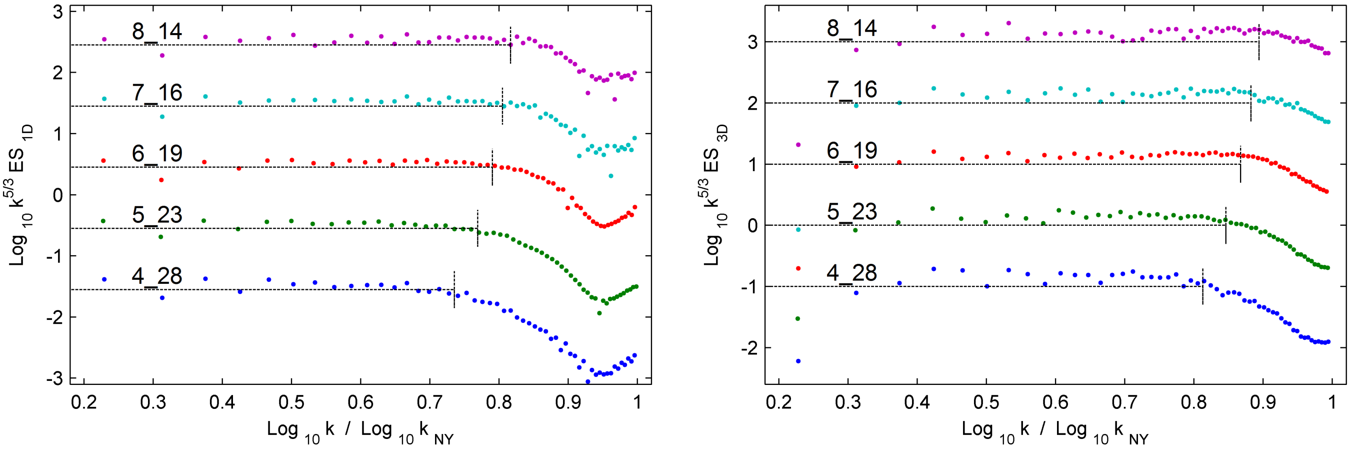

Figure 3.4: Compensated one-dimensional (left) and three-dimensional (right) energy spectra at $t = 9$ from Roe-based cases with same DOFs and different polynomial orders ($m = 4, \ldots, 8$). 1% rule estimates (1D and adapted 3D versions) mark the beginning of the dissipation range for each case. Curves have been shifted vertically for clarity, from bottom to top. The notation m_n_{el} is used in the plots to differentiate between test cases.

The one-dimensional spectra results obtained allows one to anticipate the shape of standard three-dimensional spectra as follows. When the radius k of the spherical shell in Fourier space is $k \gtrsim k_{1\%}^{1d}$, some of the surface wavevectors will begin to suffer dissipation, but the majority of them will still be within the dissipation-free cubic region delimited by $|\kappa_x| = |\kappa_y| = |\kappa_z| = k_{1\%}^{1d}$. In fact, it is not until $k \gtrsim \sqrt{3}\, k_{1\%}^{1d}$ that all the surface wavevectors will perceive significant dissipation, when the shell's diameter begins to surpass the diagonal of the dissipation-free cube. Hence, in practice, the dissipation region of three-dimensional spectra should start somewhere between $k^{1d}_{1\%}$ and $\sqrt{3}\,k^{1d}_{1\%}$. This was indeed verified to be true for all the test cases addressed. For simplicity, the 1% rule threshold for three-dimensional spectra is defined as the averaged estimate $k^{3d}_{1\%} = \frac{1}{2}(\sqrt{3}+1)\,k^{1d}_{1\%}$, whose values are those given in Table 3.2. The right-hand side plot of Fig. 3.4 shows how good this averaged estimate is for three-dimensional spectra of Roe-based computations.

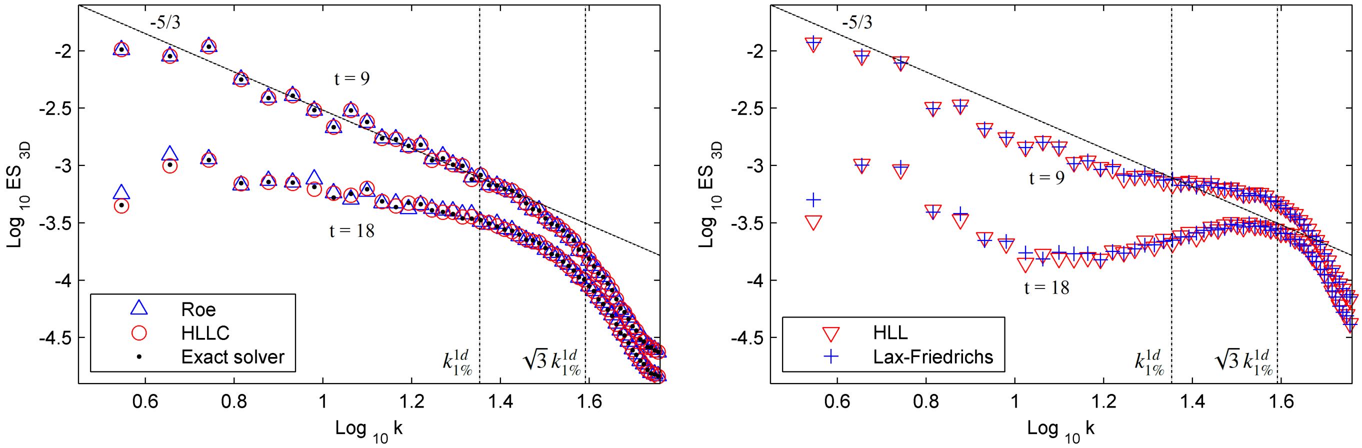

Figure 3.5: Three-dimensional energy spectra at $t = 9$ and $t = 18$ obtained with Roe, HLLC and the exact solver (left) and with HLL and Lax-Friedrichs (right), from case $m = 5$, $n_{el} = 23$. The vertical dashed lines indicate, from left to right, $k_{1\%}$ and $\sqrt{3}k_{1\%}$.

An assessment of the 1% rule for different Riemann solvers is shown in Fig. 3.5, which compares Roe, HLLC and the exact solver (left plot) against HLL and Lax-Friedrichs (right plot). Fig. 3.5 shows three-dimensional spectra obtained with $m = 5$, $n_{el} = 23$, at $t = 9$ and $t = 18$. Within each of the two graphs, different fluxes provide practically the same spectra. It is clear from the plots that dissipation begins to take place in between $k^{1d}_{1\%}$ and $\sqrt{3}\,k^{1d}_{1\%}$, especially for the more sophisticated solvers. The presence of the energy bump on the right-hand side plots can somewhat conceal the position where dissipation effectively begins in wavenumber space, see also Fig. 3.1. As discussed in Sec. 3.3, spectral bumps are believed to be caused by a sharper dissipative behaviour in Fourier space. Dissipation curves for the Lax-Friedrichs flux can be estimated from dispersion-diffusion analyses when an over-upwind factor (scaling the property jump term in the flux formula) is taken into account. Note that while the Roe solver employs the correct eigenvalues when upwinding, Lax-Friedrichs uses instead the largest one (in absolute value) alone, e.g. $|u|+c$ in one dimension. This results in over-upwinding for the momentum equations owing to the upwind factor $\beta = (|u|+c)/|u| = 1+\mathrm{Mach}^{-1}$, which tends to infinity in the incompressible limit. Fig. 3.6 illustrates DG's dissipation eigencurve for three ratios β when $m = 5$. As the Mach number decreases, a discontinuity appears on the curve. Moreover, for case $m = 5$ shown, the magnitude of the discontinuous variation increases about twelve times as Mach is reduced from 0.9 to 0.1. Since dissipation levels prior to the discontinuity also become less significant at low Mach numbers, the effective cut-off wavenumber moves towards the discontinuity. This explains why the energy bump in Fig. 3.5 (right plot) has a somewhat delayed cut-off.

For simplicity, it is better to define a 1% rule from the standard upwind condition, making it independent of the Mach number. Overall, the averaged estimate proposed is still a good choice regardless of the flux employed. It should be stressed that these estimates should only be used

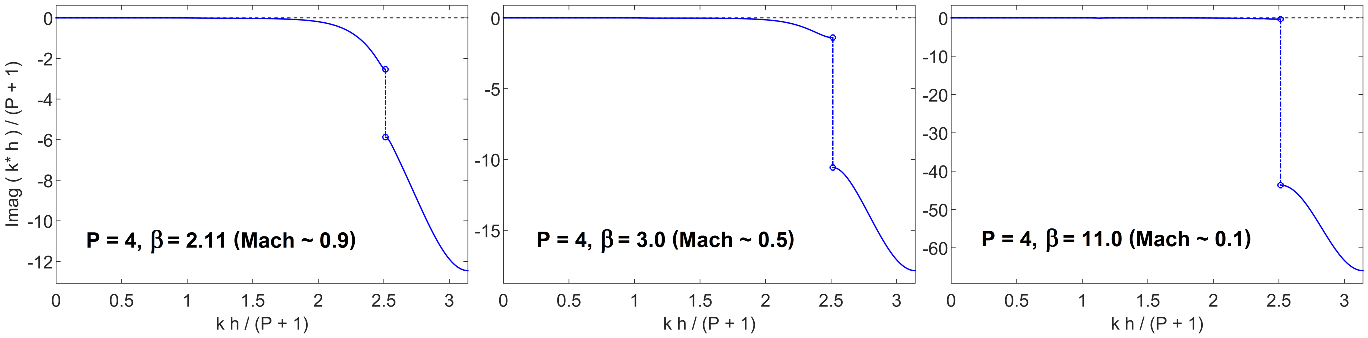

Figure 3.6: Dissipation estimates for the Lax-Friedrichs flux (for $m = 5$) as the Mach number is reduced from 0.9 to 0.1 (left to right). The plots show the imaginary part of the modified wavenumber k^* as a function of the actual wavenumber k, both scaled by h/m. Figure adapted from [9].

in connection to three-dimensional energy spectra, and that $k^{1d}_{1\%}$ is expected to be valid for 1D transforms even in 3D settings, e.g. in spanwise or streamwise spectra of turbulent channel flows. The actual dissipation threshold should however be sensitive to mesh topology as suggested in [45] and, strictly speaking, the values in Table 3.1 have only been tested in Cartesian hexahedral meshes. The application of the 1% rule to transitional and turbulent flows in complex geometries and general types of elements has yet to be addressed.

3.5 Conclusion

This study considered the adaptation of the 1% rule introduced in [10] to three-dimensional Cartesian settings. A simple adaptation has been proposed and shown to agree well with numerical experiments based on the inviscid Taylor-Green vortex (TGV) flow. Aspects of solution quality and numerical robustness have also been discussed in this large Reynolds limit. The conclusion was that moderately high polynomial orders are to be favoured along with complete Riemann solvers, which treat different physical waves in a consistent manner and conform better to the standard upwind condition. This is to avoid the sharper dissipative behaviour that induces the formation of energy bumps and associated spurious effects. These observations, together with the adapted 1% rule, can be regarded as useful guidelines for model-free DG-based simulations of free turbulence at very large Reynolds numbers.

An interesting discussion concerning the DG's localisation of numerical dissipation at the smallest captured scales deserves consideration. Kraichnan's spectral eddy viscosity theory [46] prescribes that some dissipation is induced by the small scales directly at the large ones in the form of a second-order eddy viscosity. Within this theory, the dissipation of isotropic turbulence at infinite Reynolds number is represented in Fourier space as $C(k)\,k^2$, where coefficient $C(k)$ remains approximately constant for the large and intermediate scales and rises sharply at the small ones. A plateau is therefore observed in typical plots of $C(k)$ for small and intermediate wavenumbers [47], corresponding to this second-order eddy viscosity. As DG's upwind fluxes only account for the sharp rise in dissipation at small scales, the aforementioned plateau is not being modelled. However, when a decent amount of DOFs are employed in a computation, as more scales are captured in the inertial range, the correct eddy viscosity effect will partially be reproduced due to the non-linear action of the captured turbulent scales. Also, it can be argued that this effect is of secondary importance unless turbulent decay is to be precisely reproduced. An analysis of how important this effect is for practical applications is left for future studies.

For finite Reynolds-number flows, the effects of physical dissipation (also of second-order) should only help to improve upon the accuracy and stability of computations. Although in these cases the dissipation range of the energy spectrum might begin before $k_{1\%}$ owing to the effect of molecular viscosity, the 1% rule is still expected to mark the beginning of the numerically induced dissipation range. While in classic LES approaches the explicit subgrid-scale model begins to act (ideally) on scales smaller than the filter width, DG's upwind dissipation in uDNS induces a truncation in the energy cascade beyond $k_{1\%}$. It is hoped therefore that the concept of eddy-resolving capability or resolution power as defined by the 1% rule can be regarded as an effective measure of filter width for more general DG-uDNS.

This work has also highlighted the need for stabilization techniques to improve DG's robustness while helping to enforce the entropy-consistent dissipative behaviour of turbulent flows at very high Reynolds numbers. Spectral vanishing viscosity (SVV), see e.g. [48, 49], might be a viable strategy as it introduces viscous dissipation without compromising DG's effective resolution significantly [50]. Skew-symmetric (or split form) discretisations [51, 52] are also worth pursuing as they can improve robustness significantly, although these need be further assessed with regards to their accuracy for uDNS. Nevertheless, it is believed that the inviscid TGV problem, in particular, is distinctly demanding in terms of stability, and that most DG-based computations are probably stable in practice if consistent integration is applied.

Appendix

Any quantity $Q(x,y,z)$ within the triply-periodic TGV box $\Omega = [-\pi,\pi]^3$ can be represented through a Fourier expansion as

$$Q(x,y,z) = \sum_{p,q,r} \widehat{Q}_{p,q,r} \, \exp[i(px+qy+rz)] \; , \tag{3.4}$$

where $Q \in \mathbb{R} \Leftrightarrow \widehat{Q}_{-p,-q,-r} = \widetilde{Q}_{p,q,r}$, and $\widetilde{Q}_{p,q,r}$ is the complex conjugate of $\widehat{Q}_{p,q,r}$. The Fourier components $\widehat{Q}_{p,q,r}$ can be obtained from a single 3D discrete Fourier transform based on the equispaced grid of $(n_{el}\, m)^3$ points described in the beginning of Sec. 3.4. It is advocated that using m^3 points per element for the transforms is the correct way to probe DG's piecewise continuous numerical fields, as this sets a Nyquist wavenumber $k_{\mathrm{NY}} = \pi\, m/h$ consistent with the DOFs used in the simulations. Employing more than m^3 points per element is not advised as Fourier transforms would eventually perceive interface discontinuities and feed on the energy spectra a k^{-2} signature typical of step functions.

Since the volume-averaged energy of variable Q can be expressed as

$$E_Q = \frac{1}{|\Omega|} \int_\Omega Q^2 \, d\Omega = \sum_{p,q,r} |\widehat{Q}_{p,q,r}|^2 \; , \tag{3.5}$$

where $|\widehat{Q}_{p,q,r}|^2 = \widehat{Q}_{p,q,r}\,\widetilde{Q}_{p,q,r}$ and $|\Omega| = (2\pi)^3$, the standard energy spectrum function is given by

$$\mathrm{ES}_Q^{3\mathrm{d}}(k) = \frac{1}{\Delta k}\sum_{S(k)} |\widehat{Q}_{p,q,r}|^2 \ , \tag{3.6}$$

in which $S(k)$ represents the set of Fourier components within the spherical shell of radius k and thickness Δk such that $k - \Delta k/2 < \sqrt{p^2+q^2+r^2} < k + \Delta k/2$. The (volume-averaged) kinetic energy of the TGV flow is defined from Eq. (3.5) as $K = (E_u + E_v + E_w)/2$, whose spectrum can be obtained by probing the velocity fields independently since

$$\mathrm{ES}_K^{3\mathrm{d}} = \frac{1}{2}\left(\mathrm{ES}_u^{3\mathrm{d}} + \mathrm{ES}_v^{3\mathrm{d}} + \mathrm{ES}_w^{3\mathrm{d}}\right) \ . \tag{3.7}$$

Note that Eq. (3.7) corresponds to the standard three-dimensional energy spectrum, which represents the density of kinetic energy in wavenumber space and whose integral over the range $k \geq 0$ returns the (volume-averaged) kinetic energy of the flow [19]. In the following, it is shown that the 'averaged one-dimensional energy spectrum' defined in Sec. 3.4 can be understood as an alternative spectrum, where energy is distributed over cubic shells in Fourier space.

It is useful to start by considering the one-dimensional spectrum aligned with the z direction and averaged in the x-y plane. By probing the TGV flow field at a set of points equispaced in the z direction with fixed X and Y coordinates, one is able to write

$$Q(X,Y,z) = \sum_r \widehat{Q}_r(X,Y)\exp(irz) \ , \tag{3.8}$$

whose coefficients $\widehat{Q}_r(X,Y)$ are obtained from a 1D Fourier transform. These coefficients can be related to the ones of the complete 3D Fourier transform by comparing Eq. (3.8) with Eq. (3.4) evaluated at $x = X$ and $y = Y$, which yields

$$\widehat{Q}_r(x,y) = \sum_{p,q} \widehat{Q}_{p,q,r}\ \exp[i(px+qy)] \ . \tag{3.9}$$

By expressing the averaging operation performed to obtain the averaged one-dimensional spectrum for the z direction as an integration over the x-y plane (confined to Ω), one has

$$Z\text{-}\mathrm{ES}_Q^{1\mathrm{d}}(k) = \frac{1}{(2\pi)^2}\int_{-\pi}^{+\pi}\int_{-\pi}^{+\pi}\frac{1}{\Delta k}\sum_{L(k)}|\widehat{Q}_r(x,y)|^2\,dx\,dy \ , \tag{3.10}$$

where, for a one-dimensional spectrum, the relevant set $L(k)$ of Fourier components is simply formed by the wavenumbers r such that $k - \Delta k/2 < |r| < k + \Delta k/2$. Now using Eq. (3.9), one can write

$$|\widehat{Q}_r(x,y)|^2 = \widehat{Q}_r(x,y)\,\widetilde{Q}_r(x,y) = \left[\sum_{p,q}\widehat{Q}_{p,q,r}\,e^{i(px+qy)}\right]\left[\sum_{m,n}\widehat{Q}_{-m,-n,-r}\,e^{-i(mx+ny)}\right] \ , \tag{3.11}$$

whose last term can have the signs of m and n inverted due to the symmetry of the summation (with respect to $m = n = 0$), allowing one to write

$$\int_{-\pi}^{+\pi}\int_{-\pi}^{+\pi} |\widehat{Q}_r(x,y)|^2 \, dx \, dy = \sum_{p,q,m,n} \widehat{Q}_{p,q,r} \, \widehat{Q}_{m,n,-r} \int_{-\pi}^{+\pi} e^{i(p+m)x} \, dx \int_{-\pi}^{+\pi} e^{i(q+n)y} \, dy \ , \tag{3.12}$$

which, since $\int_{-\pi}^{+\pi} \exp[i(p+m)x] \, dx$ equals 2π when $m = -p$ and zero otherwise, becomes

$$\int_{-\pi}^{+\pi}\int_{-\pi}^{+\pi} |\widehat{Q}_r(x,y)|^2 \, dx \, dy = (2\pi)^2 \sum_{p,q} \widehat{Q}_{p,q,r} \, \widehat{Q}_{-p,-q,-r} = (2\pi)^2 \sum_{p,q} |\widehat{Q}_{p,q,r}|^2 \ , \tag{3.13}$$

finally leading to

$$Z\text{-ES}_Q^{\text{1d}}(k) = \frac{1}{\Delta k} \sum_{L(k)} \sum_{p,q} |\widehat{Q}_{p,q,r}|^2 \ . \tag{3.14}$$

This can be interpreted as a summation over the set of Fourier components distributed within the two planar shells of thickness Δk which are parallel to the p-q plane and centred at $r = \pm k$. Naturally, analogous results can be obtained for the remaining directions.

At last, by averaging the contributions of each direction, one obtains the ‘averaged one-dimensional energy spectrum’ of Q as

$$\text{ES}_Q^{\text{1d}} = \frac{1}{3}\left(Z\text{-ES}_Q^{\text{1d}} + Y\text{-ES}_Q^{\text{1d}} + Z\text{-ES}_Q^{\text{1d}}\right) \ , \tag{3.15}$$

which, by taking into account the three pairs of planar shells associated to each direction, approximately represents the distribution of energy over the cubic shell of thickness Δk supported by $|p| = |q| = |r| = k$. For the kinetic energy, the averaged one-dimensional spectrum can be obtained directly from the averaged one-dimensional spectra of the velocity fields via Eq. (3.15), so that

$$\text{ES}_K^{\text{1d}} = \frac{1}{2}\left(\text{ES}_u^{\text{1d}} + \text{ES}_v^{\text{1d}} + \text{ES}_w^{\text{1d}}\right) \ . \tag{3.16}$$

References

[1] M. Parsani, G. Ghorbaniasl, C. Lacor, and E. Turkel. An implicit high-order spectral difference approach for large eddy simulation. *Journal of Computational Physics*, 229(14):5373–5393, 2010.

[2] A. Uranga, P. O. Persson, M. Drela, and J. Peraire. Implicit large eddy simulation of transition to turbulence at low Reynolds numbers using a discontinuous Galerkin method. *International Journal for Numerical Methods in Engineering*, 87(1-5):232–261, 2011.

[3] A. D. Beck, T. Bolemann, D. Flad, H. Frank, G. J. Gassner, F. Hindenlang, and C. D. Munz. High-order discontinuous Galerkin spectral element methods for transitional and turbulent flow simulations. *International Journal for Numerical Methods in Fluids*, 76(8):522–548, 2014.

[4] J. R. Bull and A. Jameson. Simulation of the Taylor–Green vortex using high-order flux reconstruction schemes. *AIAA Journal*, 53(9):2750–2761, 2015.

[5] B. C. Vermeire, S. Nadarajah, and P. G. Tucker. Implicit large eddy simulation using the high-order correction procedure via reconstruction scheme. *International Journal for Numerical Methods in Fluids*, 82(5):231–260, 2016.

[6] L. G. Margolin and W. J. Rider. A rationale for implicit turbulence modelling. *International Journal for Numerical Methods in Fluids*, 39(9):821–841, 2002.

[7] F. F. Grinstein, L. G. Margolin, and W. J. Rider. *Implicit large eddy simulation: computing turbulent fluid dynamics*. Cambridge University Press, 2007.

[8] R. C. Moura, S. J. Sherwin, and J. Peiró. Modified equation analysis for the discontinuous Galerkin formulation. In R. M. Kirby, M. Berzins, and J. S. Hesthaven, editors, *Spectral and High Order Methods for Partial Differential Equations - ICOSAHOM 2014*, pages 375–383. Springer, 2015.

[9] R.C. Moura, G. Mengaldo, J. Peiró, and S.J. Sherwin. An LES setting for DG-based implicit LES with insights on dissipation and robustness. In *Proceedings of the 11th International Conference on Spectral and High Order Methods*, Rio de Janeiro, Brazil, 2016.

[10] R. C. Moura, S. J. Sherwin, and J. Peiró. Linear dispersion-diffusion analysis and its application to under-resolved turbulence simulations using discontinuous Galerkin spectral/*hp* methods. *Journal of Computational Physics*, 298:695–710, 2015.

[11] G. J. Gassner and A. D. Beck. On the accuracy of high-order discretizations for underresolved turbulence simulations. *Theoretical and Computational Fluid Dynamics*, 27(3-4):221–237, 2013.

[12] W. J. T. Bos and J. -P. Bertoglio. Dynamics of spectrally truncated inviscid turbulence. *Physics of Fluids*, 18(7):071701, 2006.

[13] Y. Zhou, F. F. Grinstein, A. J. Wachtor, and B. M. Haines. Estimating the effective Reynolds number in implicit large-eddy simulation. *Physical Review E*, 89(1):013303, 2014.

[14] U. Frisch. *Turbulence: the legacy of A. N. Kolmogorov.* Cambridge University Press, 1995.

[15] C. W. Shu, W. S. Don, D. Gottlieb, O. Schilling, and L. Jameson. Numerical convergence study of nearly incompressible, inviscid Taylor–Green vortex flow. *Journal of Scientific Computing*, 24(1):1–27, 2005.

[16] P. E. Vincent, P. Castonguay, and A. Jameson. Insights from von Neumann analysis of high-order flux reconstruction schemes. *Journal of Computational Physics*, 230(22):8134–8154, 2011.

[17] D. De Grazia, G. Mengaldo, D. Moxey, P. E. Vincent, and S. J. Sherwin. Connections between the discontinuous Galerkin method and high-order flux reconstruction schemes. *International Journal for Numerical Methods in Fluids*, 75(12):860–877, 2014.

[18] G. Mengaldo, D. De Grazia, P. E. Vincent, and S. J. Sherwin. On the connections between discontinuous Galerkin and flux reconstruction schemes: extension to curvilinear meshes. *Journal of Scientific Computing*, 67(3):1272–1292, 2016.

[19] S. B. Pope. *Turbulent flows.* Cambridge University Press, 2000.

[20] A. D. Beck, D. G. Flad, C. Tonhäuser, G. Gassner, and C. D. Munz. On the influence of polynomial de-aliasing on subgrid scale models. *Flow, Turbulence and Combustion*, 97(2):475–511, 2016.

[21] G. I. Taylor and A. E. Green. Mechanism of the production of small eddies from large ones. *Proceedings of the Royal Society of London (A)*, 158(895):499–521, 1937.

[22] D. Drikakis, C. Fureby, F. F. Grinstein, and D. Youngs. Simulation of transition and turbulence decay in the Taylor–Green vortex. *Journal of Turbulence*, 8(20), 2007.

[23] M. E. Brachet, M. Meneguzzi, A. Vincent, H. Politano, and P. L. Sulem. Numerical evidence of smooth self-similar dynamics and possibility of subsequent collapse for three-dimensional ideal flows. *Physics of Fluids A: Fluid Dynamics (1989-1993)*, 4(12):2845–2854, 1992.

[24] C. Cichowlas and M.-E. Brachet. Evolution of complex singularities in Kida–Pelz and Taylor–Green inviscid flows. *Fluid Dynamics Research*, 36(4):239–248, 2005.

[25] T. Y. Hou and R. Li. Blowup or no blowup? The interplay between theory and numerics. *Physica D: Nonlinear Phenomena*, 237(14):1937–1944, 2008.

[26] M. E. Brachet, D. I. Meiron, S. A. Orszag, B. G. Nickel, R. H. Morf, and U. Frisch. Small-scale structure of the Taylor–Green vortex. *Journal of Fluid Mechanics*, 130:411–452, 1983.

[27] M. E. Brachet. Direct simulation of three-dimensional turbulence in the Taylor–Green vortex. *Fluid Dynamics Research*, 8(1):1–8, 1991.

[28] E. F. Toro. *Riemann solvers and numerical methods for fluid dynamics.* Springer, 1999.

[29] C. D. Cantwell, D. Moxey, A. Comerford, A. Bolis, G. Rocco, G. Mengaldo, D. De Grazia, S. Yakovlev, J-E. Lombard, D. Ekelschot, B. Jordi, H. Xu, Y. Mohamied, C. Eskilsson, B. Nelson, P. Vos, C. Biotto, R. M. Kirby, and S. J. Sherwin. Nektar++: An open-source spectral/*hp* element framework. *Computer Physics Communications*, 192:205–219, 2015.

[30] L. Diosady and S. Murman. Higher-order methods for compressible turbulent flows using entropy variables. In *Proceedings of the 53rd AIAA Aerospace Sciences Meeting (AIAA Paper 2015-0294)*, Kissimmee, USA, 2015.

[31] C. Carton Wiart, K. Hillewaert, L. Bricteux, and G. Winckelmans. Implicit LES of free and wall-bounded turbulent flows based on the discontinuous Galerkin/symmetric interior penalty method. *International Journal for Numerical Methods in Fluids*, 78(6):335–354, 2015.

[32] G. Mengaldo, D. De Grazia, D. Moxey, P. E. Vincent, and S. J. Sherwin. Dealiasing techniques for high-order spectral element methods on regular and irregular grids. *Journal of Computational Physics*, 299:56–81, 2015.

[33] G. Falkovich. Bottleneck phenomenon in developed turbulence. *Physics of Fluids*, 6(4):1411, 1994.

[34] M. Coantic and J. Lasserre. On pre-dissipative 'bumps' and a Reynolds-number-dependent spectral parameterization of turbulence. *European Journal of Mechanics-B/Fluids*, 18(6):1027–1047, 1999.

[35] A. G. Lamorgese, D. A. Caughey, and S. B. Pope. Direct numerical simulation of homogeneous turbulence with hyperviscosity. *Physics of Fluids*, 17(1):015106, 2005.

[36] U. Frisch, S. Kurien, R. Pandit, W. Pauls, S. S. Ray, A. Wirth, and J. Z. Zhu. Hyperviscosity, Galerkin truncation, and bottlenecks in turbulence. *Physical Review Letters*, 101(14):144501, 2008.

[37] D. Banerjee and S. S. Ray. Transition from dissipative to conservative dynamics in equations of hydrodynamics. *Physical Review E*, 90(4):041001, 2014.

[38] Y. Dubief and F. Delcayre. On coherent-vortex identification in turbulence. *Journal of Turbulence*, 1(11), 2000.

[39] C. Cichowlas, P. Bonaïti, F. Debbasch, and M. Brachet. Effective dissipation and turbulence in spectrally truncated Euler flows. *Physical Review Letters*, 95(26):264502, 2005.

[40] M. S. Chong, A. E. Perry, and B. J. Cantwell. A general classification of three-dimensional flow fields. *Physics of Fluids A: Fluid Dynamics (1989-1993)*, 2(5):765–777, 1990.

[41] A. Tsinober. *An informal conceptual introduction to turbulence.* Springer, 2nd edition, 2009.

[42] S. Laizet, J. Nedić, and C. Vassilicos. Influence of the spatial resolution on fine-scale features in DNS of turbulence generated by a single square grid. *International Journal of Computational Fluid Dynamics*, 29(3-5):286–302, 2015.

[43] M. Chertkov, A. Pumir, and B. I. Shraiman. Lagrangian tetrad dynamics and the phenomenology of turbulence. *Physics of Fluids*, 11(8):2394–2410, 1999.

[44] F. Q. Hu, M. Y. Hussaini, and P. Rasetarinera. An analysis of the discontinuous Galerkin method for wave propagation problems. *Journal of Computational Physics*, 151(2):921–946, 1999.

[45] C. Carton de Wiart, K. Hillewaert, M. Duponcheel, and G. Winckelmans. Assessment of a discontinuous Galerkin method for the simulation of vortical flows at high Reynolds number. *International Journal for Numerical Methods in Fluids*, 74(7):469–493, 2014.

[46] M. Lesieur. *Turbulence in fluids*. Springer, 4th edition, 2008.

[47] S. Cerutti, C. Meneveau, and O. M. Knio. Spectral and hyper eddy viscosity in high-Reynolds-number turbulence. *Journal of Fluid Mechanics*, 421:307–338, 2000.

[48] M. Minguez, R. Pasquetti, and E. Serre. High-order large-eddy simulation of flow over the 'Ahmed body' car model. *Physics of Fluids*, 20(9):095101, 2008.

[49] J.-E. W. Lombard, D. Moxey, S. J. Sherwin, J. F. A. Hoessler, S. Dhandapani, and M. J. Taylor. Implicit large–eddy simulation of a wingtip vortex. *AIAA Journal*, 54(2):506–518, 2016.

[50] R. C. Moura, S. J. Sherwin, and J. Peiró. Eigensolution analysis of spectral/*hp* continuous Galerkin approximations to advection-diffusion problems: insights into spectral vanishing viscosity. *Journal of Computational Physics*, 307:401–422, 2016.

[51] J. Malm, P. Schlatter, P. F. Fischer, and D. S. Henningson. Stabilization of the spectral element method in convection dominated flows by recovery of skew-symmetry. *Journal of Scientific Computing*, 57(2):254–277, 2013.

[52] G. J. Gassner, A. R. Winters, and D. A. Kopriva. Split form nodal discontinuous Galerkin schemes with summation-by-parts property for the compressible Euler equations. *Journal of Computational Physics*, 327:39–66, 2016.

Chapter 4

On the performance of CG-based uDNS of non-trivial turbulent boundary layers

Summary †

This chapter presents a preliminary investigation into the suitability of spectral/hp continuous Galerkin (CG) schemes for model-free under-resolved simulations of non-trivial turbulent boundary layer flows. A model problem is considered that features a rotating free-stream velocity condition and admits a statistically asymptotic solution with significant cross-flow effects. This test case is substantially more complex than typical turbulent boundary layer canonical problems owing to its unsteadiness and enhanced small-scale anisotropy. Reported LES-based solutions to this problem are known to require sophisticated modelling and relatively fine grids to achieve meaningful results, with traditional models (e.g. standard or dynamic Smagorinsky) exhibiting poor performance. The model-free CG-based approach advocated, on the other hand, yields surprisingly good results with considerably less degrees of freedom for higher-order discretisations. Usefully accurate results for the mean flow quantities can be even obtained with half as many degrees of freedom per direction (in comparison to reference LES solutions), leading to substantial reduction in computational cost. Despite the preliminary character of the study, usage of high-order spectral element methods (CG in particular) is strongly motivated for wall-bounded turbulence simulations via under-resolved DNS / implicit LES approaches.

4.1 Introduction

Although still widely used in industry, Reynolds-averaged Navier-Stokes (RANS) approaches are known to become less reliable for wall-bounded turbulent flows involving richer physical scenarios such as non-standard transition, relaminarization, strong curvature effects, separation, rotation, etc [1]. While high-fidelity LES approaches are the obvious alternative in such situations, these become prohibitively expensive even at moderately high Reynolds numbers as the boundary layer thickness

---

† This chapter is based on "R. C. Moura, S. J. Sherwin, J. Peiró (2017) *On the suitability of CG for non-trivial wall-bounded turbulent flows*, **Research Report** (doi:10.13140/RG.2.2.30744.70407)".

decreases rapidly with it. Even a wall-modelled LES, see e.g. [2, 3], when properly performed, can be orders of magnitude more expensive than RANS, not to mention it is still unreliable for detached flows or under strong non-equilibrium effects [4]. If a wall-resolved LES is required, the near-wall structures need to be captured as they are the relevant "large eddies" in turbulent boundary layers and cannot be accounted for by subgrid-scale models [5]. In this case, a very fine grid is required also along planes parallel to the wall, and the cost becomes comparable to that of a DNS. In fact, the cost of effectively capturing wall-bounded turbulence has been estimated [6] to scale with the Reynolds number as $\mathrm{Re}^{1.9}$ for an LES and $\mathrm{Re}^{2.6}$ for a DNS. Nevertheless, there are practical fields of applications for which a wall-resolved LES is currently achievable for low to moderate Reynolds numbers, e.g. turbomachinery, UAVs, wind turbines, impellers (mixing tanks and pumps), small propellers, etc.

The use of spectral element methods (SEM) for model-free computations of wall-bounded turbulence via under-resolved DNS (or wall-resolved implicit LES) approaches exhibited a promising potential for different schemes in various studies. Spectral/*hp* continuous Galerkin (CG) methods, sometimes mixed with Fourier expansions along homogeneous directions, are among the first SEM used in such approaches [7, 8, 9, 10, 11], with results on LES-sized grids typically agreeing with DNS and/or experiments. At large Reynolds numbers, high-order CG methods usually rely on spectral vanishing viscosity (SVV) for stabilization [12], whose parameters can influence solution quality depending on how its filter kernel is designed to damp higher-order polynomial modes [13, 14]. Discontinuous Galerkin (DG) methods have also demonstrated very good capability for model-free computations of wall-bounded turbulent flows, both in canonical and practical test cases [15, 16, 17, 18, 19, 20, 21, 22]. Unlike CG, DG schemes rely primarily on the upwind dissipation introduced by interface Riemann fluxes for small-scale regularization at high Reynolds numbers [23, 24]. Already in the early investigation reported in [15], DG was recognized as able to successfully predict low-order statistics with fewer degrees of freedom than traditional numerical methods by the use of higher polynomial orders near the wall. The benefits of this strategy have also been emphasized subsequently in [19], where the connection between *hp* refinement within the boundary layer and well-known efficient zonal strategies [25, 26] is made clear. Other discontinuous SEM approaches have been used with success for the field in question, notably flux reconstruction and spectral difference schemes, see e.g. [27, 28].

Advances have also been made in SEM-based (explicit) LES approaches, with good performance demonstrated for wall-bounded flows, again for different numerical schemes [29, 30, 31, 32, 33]. In particular, studies considering wall-modelled approaches with a minimum of modelling away from the wall, namely wall-modelled under-resolved DNS / implicit LES, are very important in furthering the industrialisation of high-order spectral element methods. Recent examples of such studies are [32], in which a RANS-like eddy viscosity confined to the viscous and buffer layers is introduced, and [33], where the novel free-slip / penetration wall boundary condition proposed in [34] is employed without any additional modelling. These strategies are especially promising because they have the potential to reduce considerably the cost of wall-bounded turbulence computations while minimizing the effects of modelling assumptions on the captured scales. The latter point is important due to our limited knowledge about the complex physics of turbulent boundary layers, which becomes obvious as new studies are made available every so often, see e.g. [35, 36, 37, 38, 39]. Nevertheless, such approaches still need development and further testing, as [32] assumes a (perhaps too restrictive) zero pressure gradient RANS-type parametrisation and [33] still presents numerical stability issues in certain test cases. So long as the obstacles currently faced by wall-modelled strategies remain unsolved, wall-resolved approaches are likely to maintain their position as the sole alternatives to DNS that can be expected to provide reliable results for all types of (affordable) wall-bounded flows.

This study presents a preliminary assessment into the performance of CG-based model-free under-resolved computations for a non-trivial turbulent boundary layer test case. This model problem was proposed by Spalart in [40] and has since been used in the assessment of different LES approaches [41, 42]. As explained in Sec. 4.2, the test problem involves rotating free-stream velocity and pressure gradient conditions, but admits a statistically permanent solution in the rotating frame, featuring a cross-flow velocity profile. Its inherent unsteadiness and small-scale anisotropy leads to a misalignment between mean-flow shear and Reynolds stresses at the wall. All this makes the model problem in question considerably more complex than wall-bounded test cases typically used in the assessment of SEM-based under-resolved DNS / implicit LES approaches, see e.g. [43, 44]. This complexity causes traditional subgrid-scale models, including classic and dynamic Smagorinsky formulations, to perform poorly. Accurate LES results tend to require novel modelling and relatively fine grids. In Sec. 4.3, the CG solutions of interest are shown to reproduce the quality of sophisticated LES models with considerably less degrees of freedom without any added model or even SVV. This however requires moderately high polynomial orders, e.g. fifth-order discretisations, in which case usefully accurate results for the mean flow quantities can even be obtained with half as many grid points per direction. This performance is attributed to the lack of modelling assumptions combined with the increased resolution power per degree of freedom delivered by CG at higher polynomial orders. Despite the preliminary character of the investigation, the results presented strongly motivate the adoption of high-order CG (and possibly other SEM) for under-resolved computations of non-trivial wall turbulence.

4.2 The rotating boundary layer problem

The rotating boundary layer test case proposed in [40] is defined as follows. A flat plate rests at the bottom of the domain ($y = 0$) while the wind blows parallel to it at infinity ($y = y_\infty$). This free-stream wind has fixed magnitude V_o, but rotates at a constant angular frequency f, so that, at $y = y_\infty$,

$$u(x,z,t) = V_o \cos\phi \ , \ w(x,z,t) = V_o \sin\phi \ , \ \phi = ft \ . \tag{4.1}$$

Laterally, the physical domain also extends to infinity, whereby periodic boundary conditions should be used at the lateral boundaries of a computational domain.

A rotating pressure gradient is also necessary to allow for an asymptotic solution to this flow, namely,

$$\frac{\partial p}{\partial x} = f\rho_o V_o \sin\phi \ , \ \frac{\partial p}{\partial z} = -f\rho_o V_o \cos\phi \ , \tag{4.2}$$

where ρ_o is the free-stream density. Incompressible flow conditions are however assumed as in [40]. The pressure gradient above is always normal to the free-stream velocity and should be applied within the whole domain, thereby generating a crossflow velocity profile (pointing towards $-\nabla p$), which is particularly noticeable close to the wall, cf. Fig. 4.1.

The problem considered admits an asymptotic solution which is either laminar or turbulent depending on the Reynolds number, as discussed below. This solution is homogeneous in planes parallel to the wall and statistically stationary from the perspective of a reference frame that rotates aligned to the free-stream velocity. The rotating, asymptotic solution is sketched in Fig. 4.1, which also illustrates the axis notation adopted. As can be seen, different reference frames are required. Frame $\widetilde{x} \times \widetilde{z}$ rotates with the free-stream velocity, with $\widetilde{x}$ aligned to V_o. Frame $\overline{\overline{x}} \times \overline{\overline{z}}$ rotates with the (averaged) wall shear stress vector, with $\overline{\overline{x}}$ aligned to it. Finally, $\widehat{x} \times \widehat{z}$ rotates with the (averaged) Reynolds stress vector at the wall, with $\widehat{x}$ aligned to it. Angles α and ϕ^* denote the misalignment between the pairs $\overline{\overline{x}}$–$\widetilde{x}$ and $\widehat{x}$–$\widetilde{x}$, respectively.

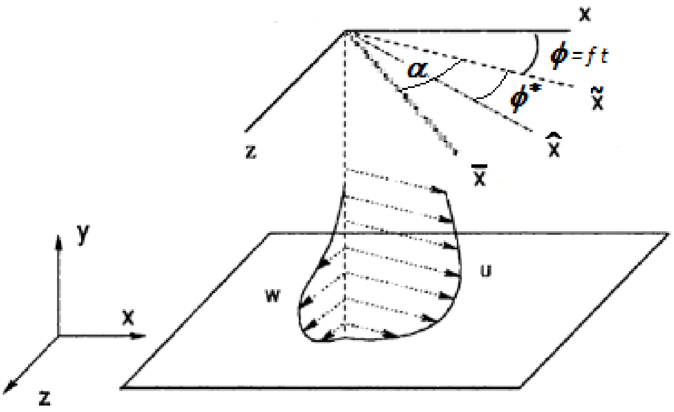

Figure 4.1: Schematics of the rotating boundary layer problem. Adapted from [42].

The velocity components for the different reference frames are defined in the usual way, e.g.

$$\widetilde{u} = u \cos\phi + w \sin\phi \ , \quad \widetilde{w} = w \cos\phi - u \sin\phi \ , \tag{4.3}$$

which are the velocity components in the frame rotating with V_o. As an example, note that angle α is such that

$$\tan(\alpha) = [\, \partial_y \langle \widetilde{w} \rangle \,/\, \partial_y \langle \widetilde{u} \rangle \,]_{\text{wall}} \tag{4.4}$$

where $\langle \cdot \rangle$ denotes statistical averaging over a plane and/or time.

The laminar solution is available in analytic form [40], namely

$$u/V_o = \cos\phi - \exp(-y/\delta_\ell)\cos(\phi - y/\delta_\ell) \ , \ w/V_o = \sin\phi - \exp(-y/\delta_\ell)\sin(\phi - y/\delta_\ell) \ , \tag{4.5}$$

in which $\phi = ft$ and δ_ℓ is the laminar boundary layer thickness, given by

$$\delta_\ell = \sqrt{2\nu/f} \ , \tag{4.6}$$

where ν is the fluid's kinematic viscosity. A laminar Reynolds number can therefore be defined as

$$R_\ell = \frac{V_o\,\delta_\ell}{\nu} = \frac{2\,V_o}{f\,\delta_\ell}\ . \tag{4.7}$$

Note that $R_\ell = 500$ is approximately the lowest Reynolds number at which a self-sustaining turbulent solution exists. As mentioned in [40], the transitional scenario for this case is probably sub-critical and therefore a finite perturbation is usually required to trigger transition. A random noise of about 10–20% in magnitude is sufficient to that end.

For turbulent solutions, additional length scales need be introduced. For instance, near the wall, the viscous length scale δ_* is typically employed to normalize distances (e.g. $y^+ = y/\delta_*$), namely

$$\delta_* = \nu/V_*\ , \tag{4.8}$$

where V_* is the so-called friction velocity, defined as

$$V_* = \left[\nu\,\partial_y\sqrt{u^2+w^2}\right]^{1/2}_{\text{wall}}\ , \tag{4.9}$$

in which the statistical averaging $\langle\sqrt{u^2+w^2}\,\rangle$ is implied.

The relevant length for the large turbulent scales, δ_τ, which is also taken to be the turbulent boundary layer thickness in this case [40], is given by

$$\delta_\tau = V_*/f = \nu\,(\delta_* f)^{-1}\ , \tag{4.10}$$

and is used directly in the definition of a turbulent Reynolds number R_τ for the flow, namely

$$R_\tau = \frac{V_*\,\delta_\tau}{\nu} = \frac{1}{2}\left(\frac{V_*}{V_o}R_\ell\right)^2\ , \tag{4.11}$$

which is analogous to the friction Reynolds number used in canonical turbulent boundary layer flows [5]. According to [40], angle ϕ^* can be estimated from α as (radian values are assumed)

$$\phi^* \approx\ \alpha - 52/R_\tau\ . \tag{4.12}$$

Additionally, for the sake of reference, an "engineering" turbulent Reynolds number Re based on the free-stream velocity can also be defined,

$$Re = \frac{V_o\,\delta_\tau}{\nu} = R_\ell\,\frac{\delta_\tau}{\delta_\ell}\ . \tag{4.13}$$

In Table 4.1, a summary of the different Reynolds numbers and length scales relevant to the model problem in question are provided, based on computations conducted in [40, 41, 42]. Only the highest Reynolds number case shown in Table 4.1 is considered in the present study.

Additional relations might be useful when dealing with the boundary layer flow under consideration, e.g.

$$\frac{\delta_\tau}{\delta_\ell} = \frac{R_\tau}{R_\ell}\frac{V_o}{V_*} = \frac{R_\tau}{R_\ell}\frac{R_\ell}{\sqrt{2R_\tau}} = \sqrt{\frac{R_\tau}{2}} \ , \tag{4.14}$$

in which relation $(V_*/V_o)^2 = 2R_\tau/R_\ell^2$ was used from Eq. (4.11); furthermore,

$$\frac{\delta_\ell}{\delta_*} = \frac{\delta_\ell}{(\nu/V_o)(V_o/V_*)} = R_\ell \frac{V_*}{V_o} \ , \tag{4.15}$$

where values of V_*/V_o can be obtained from DNS solutions and are available in Table 4.1 below; lastly, multiplying Eqs. (4.14) and (4.15) yields

$$\frac{\delta_\tau}{\delta_*} = \sqrt{\frac{R_\tau}{2}}\, R_\ell \frac{V_*}{V_o} = R_\tau \ , \tag{4.16}$$

in which relation $(V_*/V_o)^2 = 2R_\tau/R_\ell^2$ was used again.

Table 4.1: Summary of Reynolds numbers and length scales of relevant tests cases

R_ℓ	R_τ	Re	δ_τ/δ_ℓ	V_*/V_o	δ_*/δ_ℓ	$\alpha\,(^\circ)$	$\phi^*\,(^\circ)$
500	466	7632	15.3	0.0610	0.0328	26.24	19.88
620	653	11203	18.1	0.0583	0.0277	23.20	18.62
767	914	16397	21.4	0.0561	0.0232	20.91	17.70

4.3 Discussion of preliminary results

It is useful to start by summarizing the relevant DNS and LES results available in the literature, as those are used as reference in the performance assessment of CG-based under-resolved DNS (uDNS) results. The more interesting test case conducted at $R_\ell = 767$, cf. Table 4.1, is considered here since it is shared by all the relevant previous studies. DNS results for this case are available from Spalart's original work [40]. Wall-resolved LES solutions obtained with both traditional and sophisticated modelling approaches are reported in [41, 42]. Table 4.2 summarizes the discretisation details adopted in these previous works. Although various LES models are considered in each of these two later studies, only the most prominent strategies advocated by them are included in Table 4.2. The subgrid-scale models referred to as DA and ML correspond respectively to a dynamic anisotropic model described in [45, 46] and to a mixed Lagrangian model that combines elements from [47] and [48]. Also, for all the cases considered in this study, the condition $y^+ = 1$ was met at the wall.

Table 4.2: Summary of different computational settings used at $R_\ell = 767$

Approach	Model	Discretisation	L_x , L_z	L_y	Mesh points	Δx^+, Δz^+
DNS [40]	—	Spectral method [49]	$2\,\delta_t$	?	$256^2 \cdot 80$	7
LES [41]	ML	2^{nd} order central FD	$1.6\,\delta_t$	$1.6\,\delta_t$	65^3	23
LES [42]	DA	2^{nd} order central FD	$1.6\,\delta_t$	$1.6\,\delta_t$	66^3	22

The DNS solution was obtained through a spectral method described in [49], with a relatively large domain and very fine grid, as required to capture the smallest flow scales. The vertical domain size used for the DNS in question is not described, but the two LES results mentioned above used a cubic domain of matching vertical and lateral sizes. These had however 20% smaller lateral extensions compared to the DNS. The effects of this reduced domain on solution quality were found to be negligible. Both LES approaches were conducted numerically with a second-order finite difference (FD) method with the same number of grid points used across each direction of the domain. However, while equispaced grids were used along wall-parallel planes, wall-normal stretching was applied in the vertical direction in order for the mean flow gradients to be better captured. The number of points in the lateral directions was sufficient to guarantee a normalised mesh spacing $\Delta x^+ = \Delta z^+$ in the range $12 - 30$, which is typically the range required in wall-resolved LES for the cross-flow direction [50]. Note that the latter is four to five times more stringent than the usual stream-wise spacing range, but is here necessary along both wall-parallel directions due to the rotating character of the model problem under consideration. The number of points required in the vertical direction also adds to the cost of the computations, being two to three times larger than the number of points typically employed in the wall-normal direction of "traditional" turbulent boundary layers [3, 51].

Regarding wall-normal spacing, although only [49] mentions that "there were at least ten grid points within ten wall units of the wall" in the DNS, visual inspection of the plots shown in [40, 41, 42] indicates that all the discretisations considered in Table 4.2 employed ten *equispaced* grid points within $y^+ \leq 10$ and a *constant geometric stretching* throughout the rest of the turbulent boundary layer, in which the first layer above $y^+ = 10$ matches the constant spacing used under it. With this information, it is possible to generate a grid very similar to the ones used in the LES approaches of Table 4.2. However, due to the fact that preliminary CG-uDNS results obtained on much coarser grids yielded already LES-like quality, meshes similar to those used in [41, 42] have not been considered. In fact, the discretisations employed here have only half as many degrees of freedom (DOFs) per direction, and thus eight times less DOFs in total. Two polynomial orders are investigated, representing both low- and high-order CG strategies. The first uses linear element-wise approximations, i.e. polynomial order $P = 1$, which is formally second-order accurate and equivalent to a standard finite element discretisation. The second relies on fourth-order polynomials, i.e. $P = 4$, and is formally fifth-order accurate. The grids used in these two strategies have respectively 32^3 and 8^3 elements, and their corresponding test cases are hereafter denoted as $32p1$ and $8p4$. These have exactly the same number of approximating DOFs, namely $32 \times 1 = 8 \times 4$ per direction. Note that although $P + 1$ polynomial modes per element (and per direction) are employed in each case, interface modes are shared by neighbouring elements due to the fact that CG strongly imposes C^0 continuity at elemental boundaries [52]. Hence, each polynomial boundary mode counts only as half a DOF for those elements sharing it, whereby each element has effectively P *independent* polynomial modes (per direction).

In the wall-normal direction, the meshes used for the test cases $32p1$ and $8p4$ had eight DOFs within $y^+ \leq 10$ (in contrast to the 10 grid points used in previous LES cases), which translates into 8 and 2 equispaced elements, respectively. The remaining elemental layers are distributed with a constant geometric stretching in between $y^+ = 10$ and $y = 1.6\,\delta_\tau$, with the first vertical spacing above

$y^+ = 10$ matching the spacing used below it. This translates respectively into 24 and 6 elements along the region of constant geometric stretching (in contrast to about 54 grid points used in the previous LES cases). It should be mentioned that a third (equispaced) grid region has been used in the CG computations for $1.6\,\delta_\tau < y < 4.8\,\delta_\tau$. Although a longer vertical extension of the domain had no significant effect on solution quality, it allowed for dummy elemental layers to be introduced in order to better fit the total number of elements to the available (highly parallel) computational resources. The lateral domain sizes however matched that of previous LES.

All simulations have been conducted with the incompressible flow solver of spectral/*hp* element code *Nektar++* [53]. No-slip boundary conditions are employed at the wall, with a zero Dirichlet specification for the velocity components ($u = v = w = 0$) and a zero Neumann condition for the pressure ($\partial_y p = 0$). The latter is applied through a high-order technique typically employed within the velocity correction scheme [54, 55] used in the CG-based incompressible flow solver of *Nektar++*. On the top boundary of the domain, free-stream values are applied as time-dependent Dirichlet conditions, namely $u = V_o \cos(ft)$, $v = 0$, $w = V_o \sin(ft)$ and $p = 0$. Periodic boundary conditions are specified over the two pairs of opposite lateral boundaries. Polynomial dealiasing is employed via consistent/over-integration, as described in [56, 57]. This is required both for accuracy and numerical stability of high-order CG spectral element discretisations. No SVV is however used in the simulations considered here. The set-up parameters of the test cases have been defined as follows. First, the reference laminar boundary layer thickness is set to $\delta_\ell = 1$. Numerical values for the turbulent boundary layer thickness δ_τ can then be obtained through the ratio δ_τ/δ_ℓ available in Table 4.2, from which the domain extension is also evaluated. Next, the free-stream velocity magnitude is set to $V_o = \pi$. This causes the rotation period of the test case to match numerically the laminar Reynolds number adopted, $R_\ell = 767$, cf. Eq. (4.7). At this point, the rotating frequency f and the fluid's kinematic viscosity are readily available, completing the set of parameters needed for the simulations set-up. Initial conditions are prescribed from the laminar solution at the same Reynolds, cf. Eq. (4.5), with a small random noise added. Flow statistics can be gathered over one inertial cycle ($2\pi/f$) after an asymptotic solution state is reached, which takes about ten cycles [41] to happen.

The statistics obtained from test case $32p1$ are shown in Fig. 4.2, where CG-uDNS results are compared with the reference DNS data from [40]. Mean velocity profiles, turbulent intensities and Reynolds stresses are shown respectively from top to bottom. Results obtained with the dynamic Smagorinsky model (on a finer grid of 65^3 DOFs) are available from [41] for the mean velocity profiles, which are also included in Fig. 4.2. Note that all velocities are normalised by the (averaged) wall friction velocity V_*, estimated via Eq. (4.9). For this case, V_* was underestimated by about 3% when compared to its reference value in Table 4.1, which is a very slight mismatch taking into account that statistical averaging periods are hardly ideal. All quantities shown are written with respect to the reference frame $\widehat{x} \times \widehat{z}$ which rotates with the (averaged) Reynolds stress vector, with $\widehat{x}$ aligned to it, cf. Fig. 4.1. This projection requires the evaluation of angles α and ϕ^*, which is done through the relations in Eqs. (4.4) and (4.12). The comparison of mean velocity profiles in the top plot of Fig. 4.2 indicates overestimation of the stream-wise velocity component over the whole inertial log layer. This trend is also observed in the results yielded by the dynamic Smagorinsky model on a finer

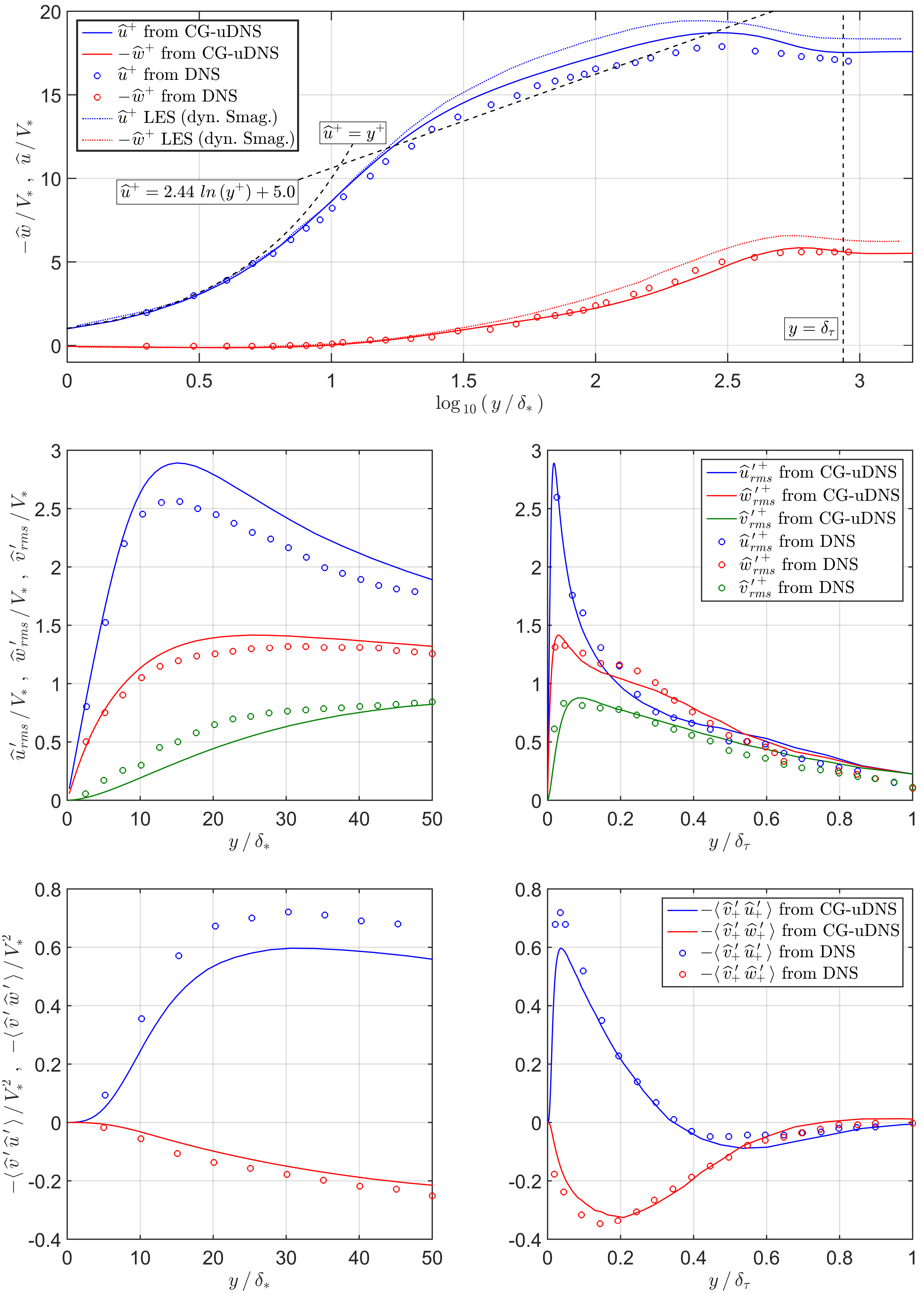

Figure 4.2: CG-uDNS results of case $32p1$ (solid lines) plotted against DNS (circles) and relevant fine-grid LES (dashed lines) from [41]. From top to bottom, mean velocity profiles, turbulent intensities and Reynolds stresses are compared.

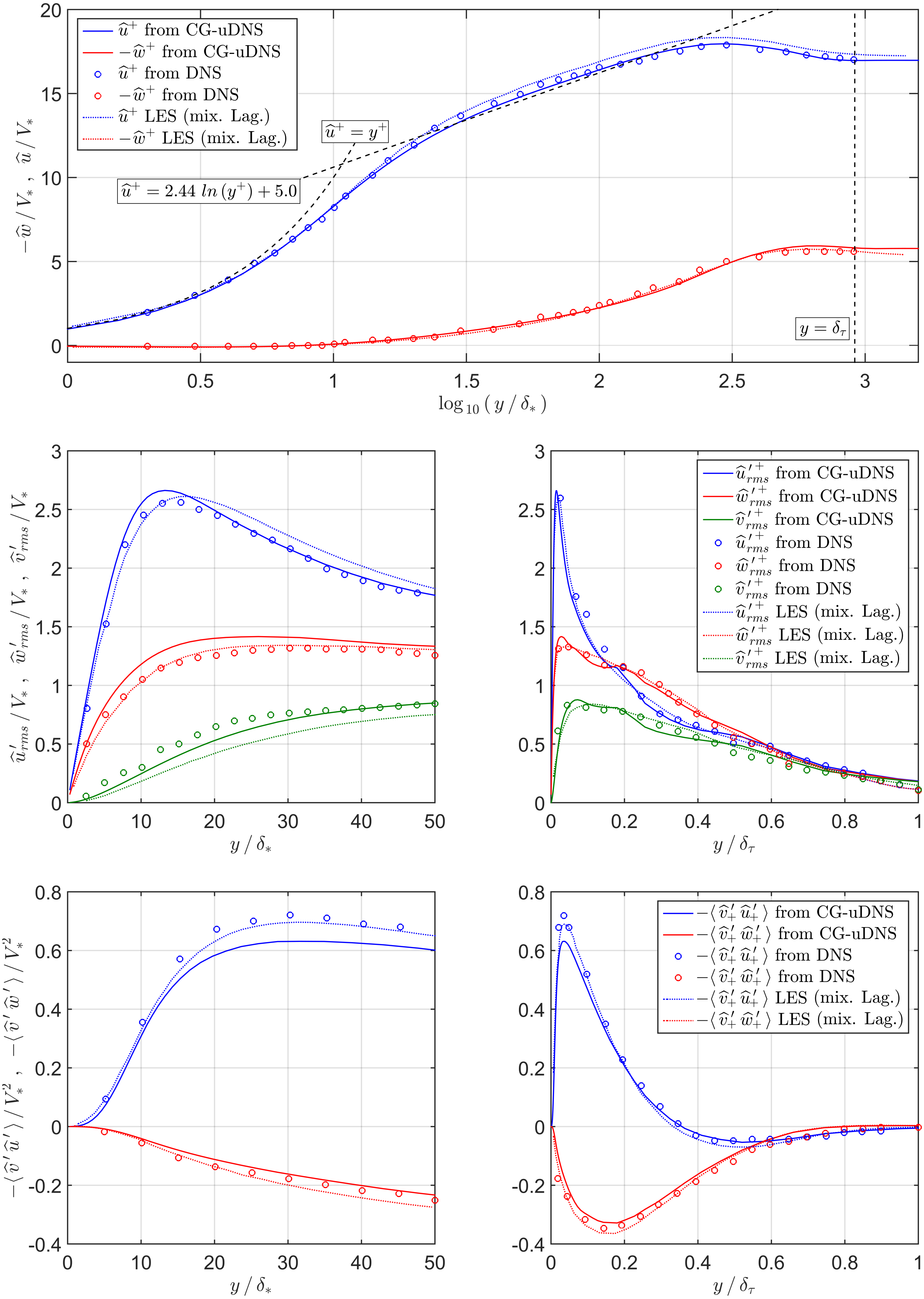

Figure 4.3: CG-uDNS results of case $8p4$ (solid lines) plotted against DNS (circles) and relevant fine-grid LES (dashed lines) from [41]. From top to bottom, mean velocity profiles, turbulent intensities and Reynolds stresses are compared.

grid of 65^3 DOFs, however the overestimation of CG-based case $32p1$ is less intense. Additionally, the cross-flow velocity profile is captured quite well here, whereas the Smagorinsky model also tends to overestimate it. The centre plots of Fig. 4.2 indicate an overestimation of the stream-wise turbulence intensity profile near the wall, by about 15% of the reference peak value. The cross-flow turbulence intensity profile is slightly less overestimated, whereas the wall-normal values are underestimated. These trends are also typically observed in subgrid-scale parametrisations [41, 42], but the error percentages become considerably less intense with sophisticated modelling (on finer grids of 65^3 or 66^3 DOFs). Finally, the bottom plots of Fig. 4.2 show that the magnitude of the Reynolds stresses is somewhat underestimated by case $32p1$. Nevertheless, overall, the results yielded by this low-order test case are of surprisingly good quality, taking into account the significantly reduced number of DOFs employed and the complete absence of (explicit) modelling.

The results obtained with the high-order test case $8p4$ are shown in Fig. 4.3. Clearly, these are much closer to the reference DNS data. Here, the value of V_* was underestimated by less than 1%. Solution quality is in fact comparable to that obtained on finer grids of 65^3 and 66^3 DOFs respectively with the sophisticated mixed Lagrangian and dynamic anisotropic models used in [41, 42]. The results obtained with the former model are included in Fig. 4.3 for comparison (dashed lines). Note that although the Reynold stresses' stream-wise component is still slightly underestimated by case $8p4$, the turbulence intensity of the wall-normal velocity component is better captured here than in Ref. [41], for example. All this is very surprising given that case $8p4$ has only 32^3 DOFs, i.e. eight times less DOFs than the cases considered in [41, 42]. This is attributed to the superior resolution power per DOF achieved by high-order spectral element methods [23, 14], which explains why case $8p4$ yielded much better results than case $32p1$. Note also that the latter, as a second-order finite element discretisation, has a superior resolution power than a second-order finite difference formulation on the same grid [58]. It is believed that capturing more of the governing equations' behaviour through an increased resolution power is eventually more effective than what subgrid-scale models can deliver, especially in complex flow scenarios with enhanced small-scale anisotropy.

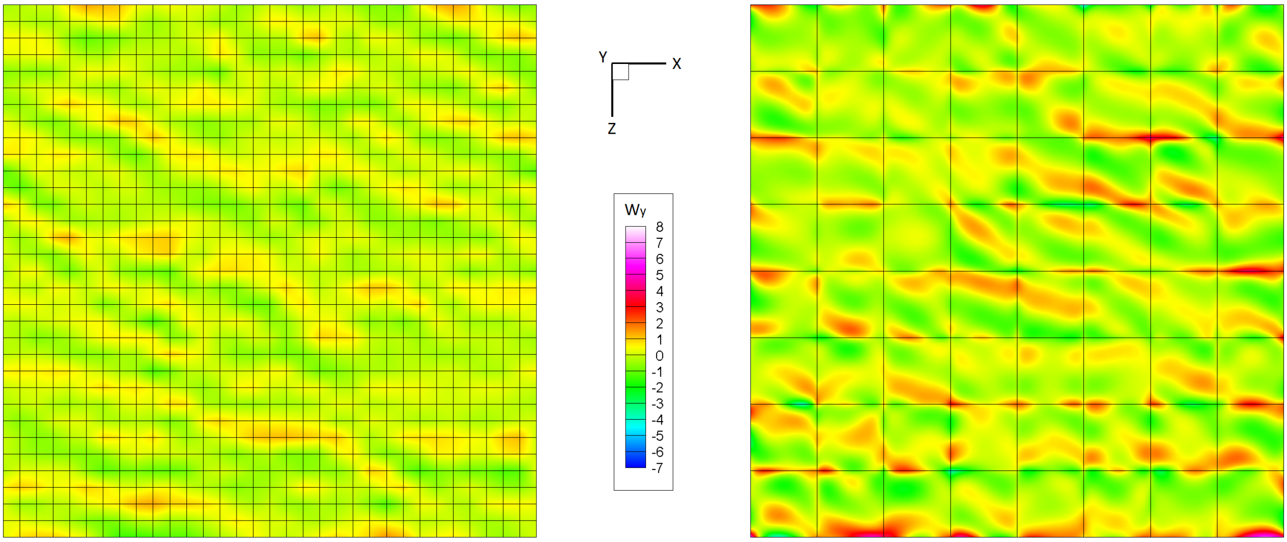

Figure 4.4: Contours of wall-normal vorticity over wall-parallel plane $y^+ = 10$ for CG-uDNS cases $32p1$ (left) and $8p4$ (right).

Another comparison can be made to assess the eddy-resolving capability of low- and high-order discretisations. In Fig. 4.4, contours of wall-normal vorticity at $y^+ = 10$ are shown for cases $32p1$ and $8p4$. These plots are representative of the asymptotic solution reached beyond approximately ten rotations. It is clear that a larger number of high-speed streaks are captured in the higher order solution, even though the grid is four times coarser. A similar comparison has been done in [28] for turbulent channel flows, and the same trend is observed when the polynomial order is increased in a fixed-DOF setting. Here, however, the near-wall streaks are not aligned with the free-stream velocity (which is aligned to axis x after an integer number of rotations), but is tilted towards positive values of z due to the influence of the cross-flow velocity profile, cf. Fig. 4.1.

Finally, it is important to highlight that both CG test cases addressed exhibited a subtle issue not observed in previous LES results, namely, an increased turbulence intensity near the boundary layer edge, which can be seen in the centre plots (right-hand side) of Figs. 4.2 and 4.3. It is still unclear what is causing this, but tests are being conducted to investigate the issue. Possibly, a longer integration time might help to dissipate these outer oscillations which apparently originate during the transient phase of the flow and are subsequently merely convected across the periodic domain directions, since the average vertical velocity of the model problem is practically zero.

4.4 Conclusion

This study considered the suitability of under-resolved DNS (uDNS) approaches based on spectral/hp continuous Galerkin (CG) methods for the simulation of non-trivial wall-bounded turbulent flows. Specifically, a model problem has been investigated that features rotating free-stream velocity and pressure gradient conditions, while admitting an asymptotic solution in the rotating reference frame. Owing to its unsteadiness and enhanced small-scale anisotropy, the adopted test case is considered to be substantially more complex than typical turbulent boundary layer canonical problems. In fact, reported LES solutions to the considered model flow required sophisticated modelling and relatively fine grids to yield meaningful results. On the other hand, the CG-based model-free approach assessed here has been shown capable of producing usefully accurate solutions with significantly less DOFs, especially at high polynomial orders. The surprising quality of the CG-uDNS results obtained is attributed to the superior resolution power of high-order CG schemes and to the absence of (often restrictive) modelling assumptions.

Despite the preliminary character of the present investigation, the results shown strongly motivate the adoption of high-order CG (and possibly other spectral element methods) for under-resolved computations of non-trivial wall turbulence. The study of variable polynomial orders (zonal wall adaptation) [25, 26] across the boundary layer is left for future studies, in which case the reduction in the number of DOFs required for meaningful results is expected to be even more significant, especially at high Reynolds numbers. The addition of SVV and its effect on energy spectra and vortical structures might also be considered.

References

[1] M. Leschziner. *Statistical turbulence modelling for fluid dynamics — demystified: an introductory text for graduate engineering students*. World Scientific, 2015.

[2] U. Piomelli and E. Balaras. Wall-layer models for large-eddy simulations. *Annual Review of Fluid Mechanics*, 34(1):349–374, 2002.

[3] U. Piomelli. Wall-layer models for large-eddy simulations. *Progress in Aerospace Sciences*, 44(6):437–446, 2008.

[4] J. Larsson, S. Kawai, J. Bodart, and I. Bermejo-Moreno. Large eddy simulation with modeled wall-stress: recent progress and future directions. *Mechanical Engineering Reviews*, 3(1):15–00418, 2016.

[5] S. B. Pope. *Turbulent flows*. Cambridge University Press, 2000.

[6] H. Choi and P. Moin. Grid-point requirements for large eddy simulation: Chapmans estimates revisited. *Physics of Fluids*, 24(1):011702, 2012.

[7] G. S. Karamanos and G. E. Karniadakis. A spectral vanishing viscosity method for large-eddy simulations. *Journal of Computational Physics*, 163(1):22–50, 2000.

[8] R. M. Kirby and G. E. Karniadakis. Coarse resolution turbulence simulations with spectral vanishing viscosity–large-eddy simulations (SVV-LES). *Journal of Fluids Engineering*, 124(4):886–891, 2002.

[9] E. Séverac and E. Serre. A spectral vanishing viscosity for the LES of turbulent flows within rotating cavities. *Journal of Computational Physics*, 226(2):1234–1255, 2007.

[10] J. Ohlsson, P. Schlatter, P. F. Fischer, and D. S. Henningson. Large-eddy simulation of turbulent flow in a plane asymmetric diffuser by the spectral-element method. In V. Armenio, B. Geurts, and J. Frhlich, editors, *Direct and Large-Eddy Simulation VII*, pages 193–199. Springer, 2010.

[11] J.-E. W. Lombard, D. Moxey, S. J. Sherwin, J. F. A. Hoessler, S. Dhandapani, and M. J. Taylor. Implicit large–eddy simulation of a wingtip vortex. *AIAA Journal*, 54(2):506–518, 2016.

[12] R. M. Kirby and S. J. Sherwin. Stabilisation of spectral/hp element methods through spectral vanishing viscosity: application to fluid mechanics modelling. *Computer Methods in Applied Mechanics and Engineering*, 195(23):3128–3144, 2006.

[13] R. Pasquetti. Spectral vanishing viscosity method for LES: sensitivity to the SVV control parameters. *Journal of Turbulence*, 6(12), 2005.

[14] R. C. Moura, S. J. Sherwin, and J. Peiró. Eigensolution analysis of spectral/*hp* continuous Galerkin approximations to advection-diffusion problems: insights into spectral vanishing viscosity. *Journal of Computational Physics*, 307:401–422, 2016.

[15] S. S. Collis. Discontinuous Galerkin methods for turbulence simulation. In *Proceedings of the 2002 Center for Turbulence Research Summer Program*, pages 155–167, 2002.

[16] A. Uranga, P. O. Persson, M. Drela, and J. Peraire. Implicit large eddy simulation of transition to turbulence at low Reynolds numbers using a discontinuous Galerkin method. *International Journal for Numerical Methods in Engineering*, 87(1-5):232–261, 2011.

[17] L. Wei and A. Pollard. Direct numerical simulation of compressible turbulent channel flows using the discontinuous Galerkin method. *Computers & Fluids*, 47(1):85–100, 2011.

[18] A. D. Beck, T. Bolemann, D. Flad, H. Frank, G. J. Gassner, F. Hindenlang, and C. D. Munz. High-order discontinuous Galerkin spectral element methods for transitional and turbulent flow simulations. *International Journal for Numerical Methods in Fluids*, 76(8):522–548, 2014.

[19] J. B. Chapelier, M. de la Llave Plata, F. Renac, and E. Lamballais. Evaluation of a high-order discontinuous Galerkin method for the DNS of turbulent flows. *Computers & Fluids*, 95:210–226, 2014.

[20] C. Carton de Wiart, K. Hillewaert, L. Bricteux, and G. Winckelmans. Implicit LES of free and wall-bounded turbulent flows based on the discontinuous Galerkin/symmetric interior penalty method. *International Journal for Numerical Methods in Fluids*, 78(6):335–354, 2015.

[21] C. Carton de Wiart and K. Hillewaert. A discontinuous Galerkin method for implicit LES of moderate Reynolds number flows. In *Proceedings of the 53rd AIAA Aerospace Sciences Meeting (AIAA Paper 2015-0055)*, Kissimmee, USA, 2015.

[22] A. Frére, N. N. Sørensen, K. Hillewaert, and G. Winckelmans. Discontinuous Galerkin methodology for large-eddy simulations of wind turbine airfoils. *Journal of Physics: Conference Series*, 753(2):022037, 2016.

[23] R. C. Moura, S. J. Sherwin, and J. Peiró. Linear dispersion-diffusion analysis and its application to under-resolved turbulence simulations using discontinuous Galerkin spectral/*hp* methods. *Journal of Computational Physics*, 298:695–710, 2015.

[24] R. C. Moura, G. Mengaldo, J. Peiró, and S. J. Sherwin. On the eddy-resolving capability of high-order discontinuous Galerkin approaches to implicit LES / under-resolved DNS of Euler turbulence. *Journal of Computational Physics*, 330:615–623, 2017.

[25] A. G. Kravchenko, P. Moin, and R. Moser. Zonal embedded grids for numerical simulations of wall-bounded turbulent flows. *Journal of Computational Physics*, 127(2):412–423, 1996.

[26] M. Manhart. A zonal grid algorithm for DNS of turbulent boundary layers. *Computers & Fluids*, 33(3):435–461, 2004.

[27] B. C. Vermeire, S. Nadarajah, and P. G. Tucker. Implicit large eddy simulation using the high-order correction procedure via reconstruction scheme. *International Journal for Numerical Methods in Fluids*, 82(5):231–260, 2016.

[28] J. B. Chapelier, G. Lodato, and A. Jameson. A study on the numerical dissipation of the spectral difference method for freely decaying and wall-bounded turbulence. *Computers & Fluids*, 139:261–280, 2016.

[29] H. M. Blackburn and S. Schmidt. Spectral element filtering techniques for large eddy simulation with dynamic estimation. *Journal of Computational Physics*, 186(2):610–629, 2003.

[30] G. Lodato, P. Castonguay, and A. Jameson. Structural wall-modeled LES using a high-order spectral difference scheme for unstructured meshes. *Flow, Turbulence and Combustion*, 92(1):579–606, 2014.

[31] J. B. Chapelier and G. Lodato. A spectral-element dynamic model for the large-eddy simulation of turbulent flows. *Journal of Computational Physics*, 321:279–302, 2016.

[32] H. Zhu, S. Fu, L. Shi, and Z. J. Wang. Implicit large-eddy simulation for the high-order flux reconstruction method. *AIAA Journal*, pages 2721–2733, 2016.

[33] C. Carton de Wiart and S. M. Murman. Assessment of wall-modeled LES strategies within a discontinuous-Galerkin spectral-element framework. In *Proceedings of the 55th AIAA Aerospace Sciences Meeting (AIAA Paper 2017-1223)*, Grapevine, USA, 2017.

[34] S. T. Bose and P. Moin. A dynamic slip boundary condition for wall-modeled large-eddy simulation. *Physics of Fluids*, 26(1):015104, 2014.

[35] W. K. George. Recent advancements toward the understanding of turbulent boundary layers. *AIAA Journal*, 44(11):2435–2449, 2006.

[36] M. H. Buschmann and M. Gad-el Hak. Turbulent boundary layers: reality and myth. *International Journal of Computing Science and Mathematics*, 1(2-4):159–176, 2007.

[37] I. Marusic, B. J. McKeon, P. A. Monkewitz, H. M. Nagib, A. J. Smits, and K. R. Sreenivasan. Wall-bounded turbulent flows at high Reynolds numbers: recent advances and key issues. *Physics of Fluids*, 22(6):065103, 2010.

[38] F. Karimpour and S. K. Venayagamoorthy. Some insights for the prediction of near-wall turbulence. *Journal of Fluid Mechanics*, 723:126–139, 2013.

[39] A. Cimarelli, E. De Angelis, J. Jimenez, and C. M. Casciola. Cascades and wall-normal fluxes in turbulent channel flows. *Journal of Fluid Mechanics*, 796:417–436, 2016.

[40] Philippe R Spalart. Theoretical and numerical study of a three-dimensional turbulent boundary layer. *Journal of Fluid Mechanics*, 205:319–340, 1989.

[41] X. Wu and K. D. Squires. Large eddy simulation of an equilibrium three-dimensional turbulent boundary layer. *AIAA Journal*, 35(1):67–74, 1997.

[42] A. Abbà, C. Cercignani, G. Picarella, and L. Valdettaro. A 3D turbulent boundary layer test for LES models. In N. Satofuka, editor, *Computational Fluid Dynamics 2000: Proceedings of the 1st International Conference on Computational Fluid Dynamics - ICCFD1*, pages 485–490. Springer, 2001.

[43] B. C. Vermeire, S. Nadarajah, and P. G. Tucker. Canonical test cases for high-order unstructured implicit large eddy simulation. In *Proceedings of the 52nd AIAA Aerospace Sciences Meeting (AIAA Paper 2014-0935)*, National Harbour, USA, 2014.

[44] J. B. Chapelier, M. de la Llave Plata, F. Renac, and E. Lamballais. DNS of canonical turbulent flows using the modal discontinuous Galerkin method. In J. Frhlich, H. Kuerten, B. Geurts, and V. Armenio, editors, *Direct and Large-Eddy Simulation IX*, pages 91–96. Springer, 2015.

[45] A. Abbà, C. Cercignani, and L. Valdettaro. Anisotropy effects in LES simulation of turbulent flows. In *Annual GAMM meeting*, Regensburg, Germany, 1997.

[46] A. Abbà, C. Cercignani, and L. Valdettaro. High Rayleigh number convection with LES models. In K. D. Papailiou, D. Tsahalis, J. Priaux, and D. Knrzer, editors, *Computational Fluid Dynamics '98: Proceedings of the 4th ECCOMAS Computational Fluid Dynamics Conference*, volume 2, pages 280–285. Wiley, 1998.

[47] B. Vreman, B. Geurts, and H. Kuerten. On the formulation of the dynamic mixed subgrid-scale model. *Physics of Fluids*, 6(12):4057–4059, 1994.

[48] C. Meneveau, T. S. Lund, and W. H. Cabot. A Lagrangian dynamic subgrid-scale model of turbulence. *Journal of Fluid Mechanics*, 319:353–385, 1996.

[49] P. R. Spalart. Numerical simulation of boundary layers — Part I: weak formulation and numerical method. Technical Report TM 88222, NASA, 1986.

[50] P. Sagaut. *Large eddy simulation for incompressible flows: an introduction*. Springer Science & Business Media, 2006.

[51] N. J. Georgiadis, D. P. Rizzetta, and C. Fureby. Large-eddy simulation: current capabilities, recommended practices, and future research. *AIAA Journal*, 48(8):1772–1784, 2010.

[52] G. E. Karniadakis and S. J. Sherwin. *Spectral/hp element methods for computational fluid dynamics*. Oxford University Press, 2nd edition, 2005.

[53] C. D. Cantwell, D. Moxey, A. Comerford, A. Bolis, G. Rocco, G. Mengaldo, D. De Grazia, S. Yakovlev, J-E. Lombard, D. Ekelschot, B. Jordi, H. Xu, Y. Mohamied, C. Eskilsson, B. Nelson, P. Vos, C. Biotto, R. M. Kirby, and S. J. Sherwin. Nektar++: An open-source spectral/*hp* element framework. *Computer Physics Communications*, 192:205–219, 2015.

[54] J. L. Guermond and J. Shen. Velocity-correction projection methods for incompressible flows. *SIAM Journal on Numerical Analysis*, 41(1):112–134, 2003.

[55] G. E. Karniadakis, M. Israeli, and S. A. Orszag. High-order splitting methods for the incompressible Navier-Stokes equations. *Journal of Computational Physics*, 97(2):414–443, 1991.

[56] R. M. Kirby and G. E. Karniadakis. De-aliasing on non-uniform grids: algorithms and applications. *Journal of Computational Physics*, 191(1):249–264, 2003.

[57] G. Mengaldo, D. De Grazia, D. Moxey, P. E. Vincent, and S. J. Sherwin. Dealiasing techniques for high-order spectral element methods on regular and irregular grids. *Journal of Computational Physics*, 299:56–81, 2015.

[58] P. M. Gresho and R. L. Sani. *Incompressible flow and the finite element method. Volume 1: advection-diffusion.* John Wiley and Sons, 1998.

Chapter 5

Spatial eigenanalysis of DG and its importance for under-resolved computations of spatially developing flows at high Reynolds numbers

Summary [†]

This chapter is devoted to the spatial eigensolution analysis of discontinuous Galerkin (DG) schemes. The analysis focuses on the numerical dispersion and diffusion characteristics of spatially developing problems dominated by convection. These are of particular importance when dealing with under-resolved computations, as they affect both numerical stability and solution quality. The spatial eigenanalysis considered here complements previous studies based on the temporal analysis, which are more commonly found in the literature. While the latter assumes periodic boundary conditions, the spatial approach assumes inflow/outflow type boundary conditions and is therefore better suited for the investigation of open flows typical of aerodynamics. DG's propagation characteristics are discussed in detail for various polynomial orders. The influence of spurious/reflected eigenmodes is also assessed with regards to the amount of upwind dissipation introduced by Riemann solvers. This provides insights into DG's accuracy and robustness for eddy-resolving computations of high Reynolds-number flows, including under-resolved direct numerical simulation (uDNS) / implicit large-eddy simulation (iLES) approaches. The knowledge obtained from the spatial eigenanalysis is verified via two-dimensional compressible Euler simulations that mimic (spatially developing) grid turbulence.

5.1 Introduction

High-order methods are known to offer numerical benefits over traditional low-order schemes especially when small-scale flow features need to be captured and propagated correctly over long distances [1, 2, 3], as typical in fields such as acoustics, turbulence and transition. Over the last few decades, the

---

[†] This chapter is based on "G. Mengaldo, R. C. Moura, B. Giralda, J. Peiró, S. J. Sherwin (2017) *Spatial eigensolution analysis of discontinuous Galerkin schemes with practical insights for under-resolved computations and implicit LES*, **Computer & Fluids** (accepted for publication)".

so-called spectral element methods [4, 5, 6], in particular, have been drawing the attention of several researchers and practitioners interested in the fields mentioned before [7, 8, 9, 10, 11, 12, 13, 14, 15]. It is therefore of fundamental importance to better understand the numerical characteristics of these methods regarding wave-like solution components. The present study investigates the dispersion and diffusion/dissipation properties of the discontinuous Galerkin (DG) spectral element method, see e.g. [16], through the spatial eigensolution analysis framework.

The application of eigensolution analysis to spectral element methods is not new [17, 18, 19, 20, 21, 22, 23]. Still, most of the dedicated literature covers only the *temporal* eigenanalysis approach, which (strictly speaking) is valid specifically for periodic problems. When however inflow/outflow type boundary conditions are present, a *spatial* approach is to be preferred, this being the relevant analysis for numerical propagation in open flows. While the former approach focuses on the temporal evolution of spatially-coherent signals, the latter focuses on their spatial evolution and assumes temporal coherence only. The two approaches complement each other and are equally important for a comprehensive understanding of any discretisation technique suited for advection-diffusion problems. However, while many works covering DG's temporal eigenanalysis are available in the literature, only two are devoted to its spatial analysis, namely Refs. [18] and [24]. Besides, the latter focuses mainly on the super-convergence properties of well-resolved computations, hence being of lesser interest for more complex, practical applications. While revisiting the results presented in [18], the present work addresses DG's spatial eigenanalysis with a particular interest in under-resolved simulations.

The results discussed are expected to be of especial interest to direct computations of turbulent flows. This no-model eddy-resolving approach becomes too expensive at high Reynolds numbers if all the turbulent scales are to be resolved (DNS). If the discretisation is robust enough, the straightforward alternative is to simply employ a reduced number of DOFs (as in LES) and hope for reasonably accurate solutions — which, surprisingly, can be obtained sometimes even at infinite Reynolds number [25]. This approach, which is basically an under-resolved DNS strategy, is often regarded as an implicit LES (iLES) approach [10, 13, 14]. However, the latter terminology has originally been coined [26, 27] to describe numerical schemes whose truncation errors resemble typical subgrid-scale models employed in classical LES. As this resemblance has not yet been formally demonstrated for DG, see e.g. [28, 29], the term under-resolved DNS (uDNS) is here preferred. Since no (explicit) model is used in the uDNS strategy, numerical error (dissipation in particular) acts as the primary mechanism for regularization at small scales. The detailed analysis of numerical diffusion is therefore of crucial importance to sensible uDNS practice.

While focusing on the relevance of DG's spatial eigenanalysis to uDNS, this study is complementary to [22], which focused on the temporal approach. Owing to the particular interest in high Reynolds-number flows, only the linear advection equation is considered. Numerical diffusion is however present due to the upwind fluxes employed in the DG discretisation. One of the main topics to be addressed is the presence (or absence) of a secondary eigenmode usually related to spurious reflections that appear, for instance, due to variations in mesh spacing [18]. As will be pointed out opportunely, unless especial care is taken, spurious eigenmodes may have a significant effect e.g. on the accuracy of acoustics-related simulations or, in extreme cases, on the numerical stability of under-resolved turbulence computations.

This study is organized as follows. In Sec. 5.2, the spatial eigensolution analysis framework is presented and it's application to DG is discussed. Sec. 5.3 addresses the spatial dispersion and dissipation characteristics for various discretisation orders and also discusses in detail the effects of under/over-upwinding. In Sec. 5.4, numerical experiments are conducted to assess how the results from the spatial eigenanalysis translate into under-resolved simulations. Sec. 5.5 gathers concluding remarks and presents guidelines for subsequent studies.

5.2 DG's spatial eigenanalysis framework

To begin with, the one-dimensional linear advection equation is considered in a semi-infinite domain,

$$\frac{\partial u}{\partial t} + a\,\frac{\partial u}{\partial x} = 0 \ , \text{ for } x > 0 \ , \ t > 0 \ , \tag{5.1}$$

where $a > 0$ is the advection velocity. The relevant solutions are wave-like components such as

$$u \propto \exp\left[i(\kappa x - \omega t)\right] \ , \tag{5.2}$$

κ and ω being the component's wavenumber and (angular) frequency, respectively. Accordingly, boundary conditions at $x = 0$ are assumed in the form

$$u_0(t) \propto \exp(-i\omega t) \ . \tag{5.3}$$

Inserting Eq. (5.2) into Eq. (5.1) yields the analytical dispersion relation $\kappa = \varpi$, where $\varpi = \omega/a$. In the spatial eigenanalysis, one is interested in the evolution of wave-like components of given frequency as they move from the inlet boundary into the domain. Due to numerical error, the effective dispersion relation observed in computations can be expressed as

$$\kappa^* = \kappa^*(\varpi) \ , \tag{5.4}$$

in which κ^* is the (possibly complex) modified wavenumber obtained numerically from a prescribed (real) inlet frequency. It is easy to see from Eq. (5.2) that the real part of κ^* will define the numerical wavelength of the considered wave, whereas its imaginary part will induce exponential growth or decay (as a direct function of space travelled), which are not present in the analytical solution. For sufficiently well resolved simulations, a consistent scheme should yield $\kappa^* = \varpi$.

For DG's eigenanalysis, a formulation similar to that discussed in [22] is followed closely. In fact, the only difference is that here a generalized interface flux is allowed through an upwind parameter β that scales the property-jump term in DG's numerical flux formula, namely

$$\tilde{u}\left(u_\ominus, u_\oplus\right) = \frac{u_\ominus + u_\oplus}{2} + \beta\frac{u_\ominus - u_\oplus}{2} \ , \tag{5.5}$$

where $\ominus$ and $\oplus$ denote respectively the left and right solution states adjacent to the considered interface. By varying β, one can recover, in particular, standard upwind ($\beta = 1$) and fully central

($\beta = 0$) discretisations. This flexibility also allows for the investigation of over-upwinding effects.

From Eq. (5.5), DG's semi-discrete advection problem can be written in vector form as

$$\frac{h}{2a}\frac{\partial \vec{u}}{\partial t} = \boldsymbol{\mathcal{L}}^{\beta}\,\vec{u}_L + \boldsymbol{\mathcal{C}}^{\beta}\,\vec{u} + \boldsymbol{\mathcal{R}}^{\beta}\,\vec{u}_R\ , \tag{5.6}$$

where h is the mesh spacing adopted and $\vec{u} = \{u_0, \ldots, u_P\}^T$ is the vector of element-wise coefficients approximating the numerical solution at a given element, whereas $\vec{u}_L$ and $\vec{u}_R$ denote the analogous coefficients' array of its left and right neighbours, respectively. It is worth noting that while Legendre orthonormal polynomials $\phi_k(\xi)$ are assumed here, see e.g. [4], DG's numerical dispersion and diffusion characteristics are independent of the set of basis functions adopted, provided that exact integrations are relied upon in the discretisation process. Finally, the matrices appearing in Eq. (5.6) are given by

$$\boldsymbol{\mathcal{C}}^{\beta}_{i,j} \ = \ \mu_{i,j} \ + \ \frac{1}{2}(1-\beta)\phi_i(-1)\phi_j(-1) \ - \ \frac{1}{2}(1+\beta)\phi_i(+1)\phi_j(+1)\ , \tag{5.7}$$

$$\boldsymbol{\mathcal{L}}^{\beta}_{i,j} \ = \ \frac{1}{2}(1+\beta)\phi_i(-1)\phi_j(+1)\ , \quad \boldsymbol{\mathcal{R}}^{\beta}_{i,j} \ = \ \frac{1}{2}(1-\beta)\phi_i(+1)\phi_j(-1)\ , \tag{5.8}$$

in which $\mu_{i,j} = \int_{-1}^{+1} \phi_i'\,\phi_j\,d\xi$.

When Eq. (5.6) is rearranged by taking into account Eq. (5.2), it leads to the eigenvalue problem

$$-i\frac{\varpi h}{2}\,\vec{u} = \left[\boldsymbol{\mathcal{L}}^{\beta}\,e^{-i\kappa h} + \boldsymbol{\mathcal{C}}^{\beta} + \boldsymbol{\mathcal{R}}^{\beta}\,e^{+i\kappa h}\right]\,\vec{u}\ , \tag{5.9}$$

in which the asterisk in the numerical wavenumber κ^* has been omitted to simplify notation. In order to solve for the product $\kappa h = \kappa h\,(\varpi h)$, one can introduce variable $z = \exp(i\kappa h)$ and solve for z the corresponding determinant problem

$$\det\left[\left(z^{-1}\boldsymbol{\mathcal{L}}^{\beta} + \boldsymbol{\mathcal{C}}^{\beta} + z\,\boldsymbol{\mathcal{R}}^{\beta}\right) + i\frac{\varpi h}{2}\,\mathcal{I}\right] = 0\ , \tag{5.10}$$

where $\mathcal{I}$ is the identity matrix of the required size. As discussed in [18], this determinant problem admits at most two distinct solutions $z = z(\varpi h)$, regardless of DG's discretisation order. Whereas one of them is the physical solution which approximately obeys the exact dispersion/diffusion relation for sufficiently resolved simulations, the other one is unphysical and propagates contrary to the sign of the advection velocity. This unphysical eigenmode is typically triggered by spurious reflections emanating from outflow boundaries or at element interfaces where mesh spacing is changed. Although Eq. (5.10) can be solved analytically via algebra manipulation packages (strategy adopted in [18]), it can also be solved numerically through a root-finding algorithm. This latter approach is followed here as it is probably more easily extensible to other spectral element methods and to more general problems, e.g. advection-diffusion equation.

MATLAB's function *newtzero* has been chosen for the solution of Eq. (5.10). This root-finding algorithm benefits from a reasonable guess for the root's location, but it is always possible to try random guesses for z until a desired solution is obtained. It is important to note that *newtzero* typically returns the physical and spurious solutions for z altogether for each given ϖh. To avoid scrambling the two roots, it is useful to track them separately. This can be done by noting that physical and spurious solution components are expected to have opposite amplification behaviours, as will be discussed in Sec. 5.3. Fortunately, the amplification behaviour is encapsulated in the absolute value of $z = \exp(i\kappa h)$, as

$$z = \exp\left[i\,\Re(\kappa h)\right]\exp\left[-\Im(\kappa h)\right] \;\therefore\; \Im(\kappa h) \gtrless 0 \Leftrightarrow |z| \lessgtr 1 \;, \tag{5.11}$$

where $\Re(\cdot)$ and $\Im(\cdot)$ stand for the real and imaginary parts of a complex number. Employing the above is useful because it bypasses the numerical difficulties of inverting the complex exponential function in order to access the imaginary component of κh. One can be sure that a physical root has been found by checking whether $|z| < 1$. A random guess for a physical solution can be of course $z = r_1 \exp(2\pi i r_2)$, where r_1 and r_2 are real numbers within $(0, 1)$. These criteria can also be used for a spurious root if one considers Eq. (5.10) with an inverted definition for z, i.e. $z = 1/\exp(i\kappa h) = \exp(-i\kappa h)$. Such sign change guarantees that the spurious root found through this strategy will have an absolute value smaller than unity. This spurious root will obviously have to be inverted subsequently if one is to store the actual spurious root of Eq. (5.10) for a given ϖh.

Once the (two) sequences of complex z values are obtained for the chosen range of ϖh, dispersion and diffusion curves can be generated by plotting $\Re(\kappa h)$ and $\Im(\kappa h)$ versus ϖh. However, while the latter can be readily obtained as $\Im(\kappa h) = -\ln|z|$, the former invariably requires using a (multi-valued) complex logarithm function, as $\Re(\kappa h) = -i \ln(z/|z|)$. It is therefore advisable that dispersion curves are carefully adjusted so as to avoid mistakes in complex phase estimates (usually seen as discontinuities on dispersion curves). Note that admissible corrections in $\Re(\kappa h)$ have to be a multiple of π. To verify whether any correction is in fact justifiable, it is worth checking the derivative of κh with respect to ϖh, which can be evaluated without ambiguity. This can be done by noting that

$$z = \exp(i\kappa h) \;\Rightarrow\; \frac{dz}{d(\varpi h)} = i\,\frac{d(\kappa h)}{d(\varpi h)}\,z \;\Rightarrow\; \frac{d(\kappa h)}{d(\varpi h)} = -\frac{i}{z}\frac{dz}{d(\varpi h)} \;, \tag{5.12}$$

where the rightmost derivative can be approximated numerically for a physical or spurious root z as

$$\frac{dz}{d(\varpi h)} \approx \frac{z|_{\varpi h+\epsilon} - z|_{\varpi h-\epsilon}}{2\epsilon} \;, \tag{5.13}$$

in which ϵ is a sufficiently small variation in ϖh. In particular, the real part of $d(\kappa h)/d(\varpi h)$ will indicate whether the slopes of dispersion curves have been evaluated correctly. With the above guidelines, fully continuous dispersion and diffusion curves have been obtained for physical and spurious modes. These are discussed in the following section.

5.3 Eigencurves and upwinding effects

It is useful to start by illustrating the eigencurves obtained for DG-based linear advection with standard upwinding ($\beta = 1$). Such results are given in Fig. 5.1, which shows dispersion and dissipation curves for various polynomial orders, namely $P = 0, \dots, 8$. The numerical wavenumbers are denoted in the plots as κ^*. Each axis is normalized by the number of polynomial degrees of freedom per element, $m(\mathrm{DG}) = P+1$. Note that positive dissipation is here represented by $\Im(\kappa^* h) > 0$, contrary to temporal eigenanalysis [22], since κ and ω have opposite signs in Eq. (5.2). Note that in the spatial analysis framework one actually evaluates κ^* instead of ϖ, the latter being merely interpreted as κ^* in a temporal framework. Regarding the range of $\varpi\hbar = \varpi h/m$ adopted in the plots, it is worth mentioning that there is no natural limit for this range (contrary to the periodicity limit of $\kappa\hbar = \pi$ observed in temporal eigenanalysis). However, from a practical standpoint, higher frequency values will eventually require infeasibly small CFL values to be resolved in a computation. Therefore, we here adopt $\varpi\hbar = 4$ as limit, which leaves a margin beyond the corresponding temporal framework limit of π. Lastly, it should be stressed that for compressible Navier-Stokes and Euler simulations, Roe's original Riemann flux [30] is the one that more naturally represents the standing upwind discretisation, as the penalty (property jump) term, cf. Eq. (5.5), in its flux formula is multiplied by the unmodified eigenvalues of the system of equations.

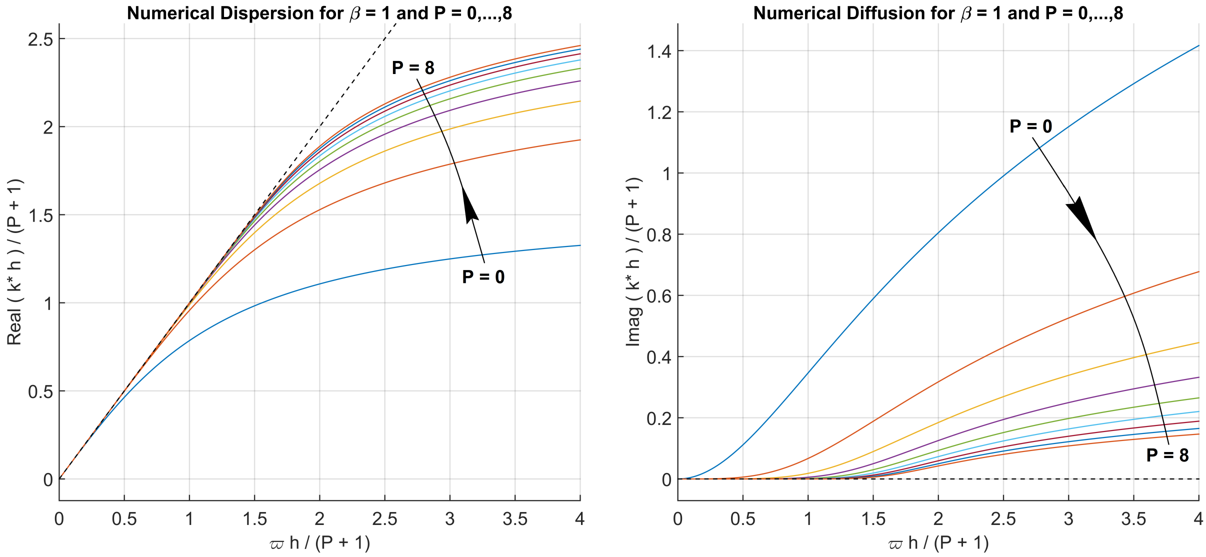

Figure 5.1: Numerical dispersion (left) and dissipation (right) curves for DG-based linear advection with standard upwind ($\beta = 1$) for various polynomial orders ($P = 0, \ldots, 8$). Dashed lines indicate the exact linear advection behaviour.

The element-wise constant discretisation ($P = 0$) is particularly inaccurate and strongly diffusive, which is not surprising. As the order is increased, the frequency range around $\varpi\hbar = 0$ where dispersion and dissipation errors are negligible also increases. The accuracy on a basis of total degrees of freedom employed (DOF $\propto m/h$) improves significantly as P is increased from lower orders, but this improvement becomes less significant at higher orders (say, above $P = 4$). These trends are similar to those observed in temporal eigenanalysis, but marked differences can be noted for the dissipation curves. Firstly, these eigencurves rise much more slowly here as the frequency increases. In temporal analysis, this rise is much sharper, especially at higher polynomial orders. Secondly, overall dissipation levels are notably smaller here. The maximum values of $\Im(\kappa^* h)$ scale approximately as $(P+1)^2$ in the temporal framework [22], whereas here the dissipation at large frequencies decreases with P. Regarding the frequency range of negligible dissipative effects, the values of $\varpi\hbar_{1\%}$ marking a dissipation threshold of 1% damping factor per DOF crossed (named "the 1% rule" in previous studies [22, 25]) has been found to be remarkably close to the corresponding values of $\kappa\hbar_{1\%}$ defined from temporal analysis. Nevertheless, owing to the two differences mentioned above, in it is unlikely that the 1% rule remains as effective in spatially evolving flows with regards to marking a cutoff-like wavenumber/frequency beyond which the inertial range in the energy spectrum of under-resolved turbulence computations is curtailed.

Attention is now given to the effects of non-standard upwinding on dispersion and dissipation characteristics. It should be noted that a spurious (reflected) mode exists in addition to the physical mode depicted in Fig. 5.1 whenever $\beta \neq 1$, as first pointed out by [18]. Fig. 5.2 shows the eigencurves obtained when nearly central fluxes ($\beta = 0.01$) are employed, for various polynomial orders $P = 1, \ldots, 5$, where physical eigencurves are shown in blue and spurious ones in red. Spurious eigenmodes are known to propagate contrary to the advection velocity and typically originate from interfaces where mesh spacing is changed and also at outflow boundaries under certain circumstances, cf. Sec. 5.4. The opposite signs of dispersion/dissipation curves of physical and spurious modes can be understood directly from Eq. (5.2), which can be rewritten as

$$u \,\propto\, \exp\left[\,-\Im(\kappa)\,x\,\right]\,\exp\left\{i\left[\,\Re(\kappa)\,x - \omega\,t\,\right]\right\}. \tag{5.14}$$

Hence, a positive sign of $\Im(\kappa^*)$ for the physical modes indicates that those are damped as they propagate forwards. Also, a negative sign of $\Im(\kappa^*)$ for the spurious modes indicates that these are damped as they propagate backwards ($\Delta x < 0$). Regarding $\Re(\kappa^*)$, the positive sign observed for the physical modes (and the correct asymptotic slope) are only consistent with the analytical dispersion relation. On the other hand, the negative sign of $\Re(\kappa^*)$ for the spurious modes is somewhat inconsequential in practice as it merely affects their phase and shape in space. It is important to mention that some of the dispersion curves of spurious modes shown in [18] started at $\Re(\kappa^* h) = \pi$ instead of at the origin. It so happens that both results are valid solutions of the determinant problem in Eq. (5.10) owing to the periodic nature of the complex logarithm function, as discussed at the end of Sec. 5.2. However, it can be argued that, on the grounds of consistency, a steady interface condition ($\varpi \to 0$) should not generate a spatially varying wave ($\Re(\kappa^*) \neq 0$) into the domain, physical or otherwise. Therefore, in the present study, dispersion curves of spurious modes are assumed to start at the origin of the plots. In any case, as explained above, the value of $\Re(\kappa^*)$ for the spurious modes is irrelevant in practice.

The dispersion eigencurves of the physical modes shown in Fig. 5.2 become more accurate on a per DOF basis as the polynomial order increases, as expected. The behaviour of dissipation curves is however more involved. The frequency range of nearly zero dissipation does not increase monotonically with the polynomial order owing to the appearance of “bubbles” in these curves. If bubbles can be tracked across different P values, a given bubble seem to grow and to move away from the origin as the polynomial order is increased. Particularly large low-dissipation frequency ranges are obtained with $P = 1$, $P = 4$ and perhaps $P = 5$, if the bubble of the latter is deemed negligible. It should be pointed out that dissipation levels really decrease to zero (except near bubbles) as $\beta \to 0$, which can be seen clearly when dissipation is plotted in a logarithmic scale (not shown). This is in contrast with the low dissipation levels observed in the case of standard upwinding within

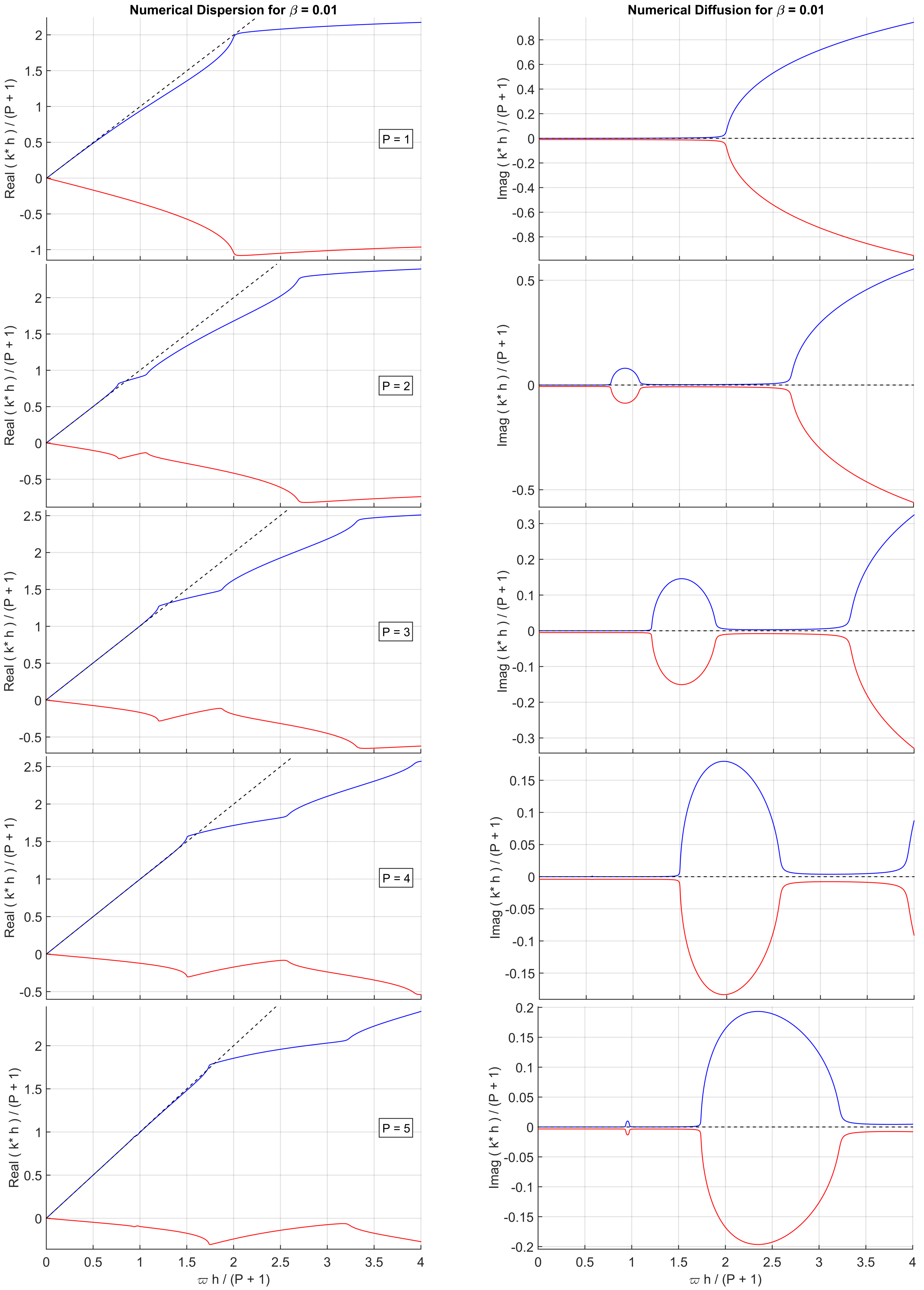

Figure 5.2: DG's dispersion (left) and dissipation (right) eigencurves for $\beta = 0.01$ and $P = 1, \ldots, 5$ (top to bottom).

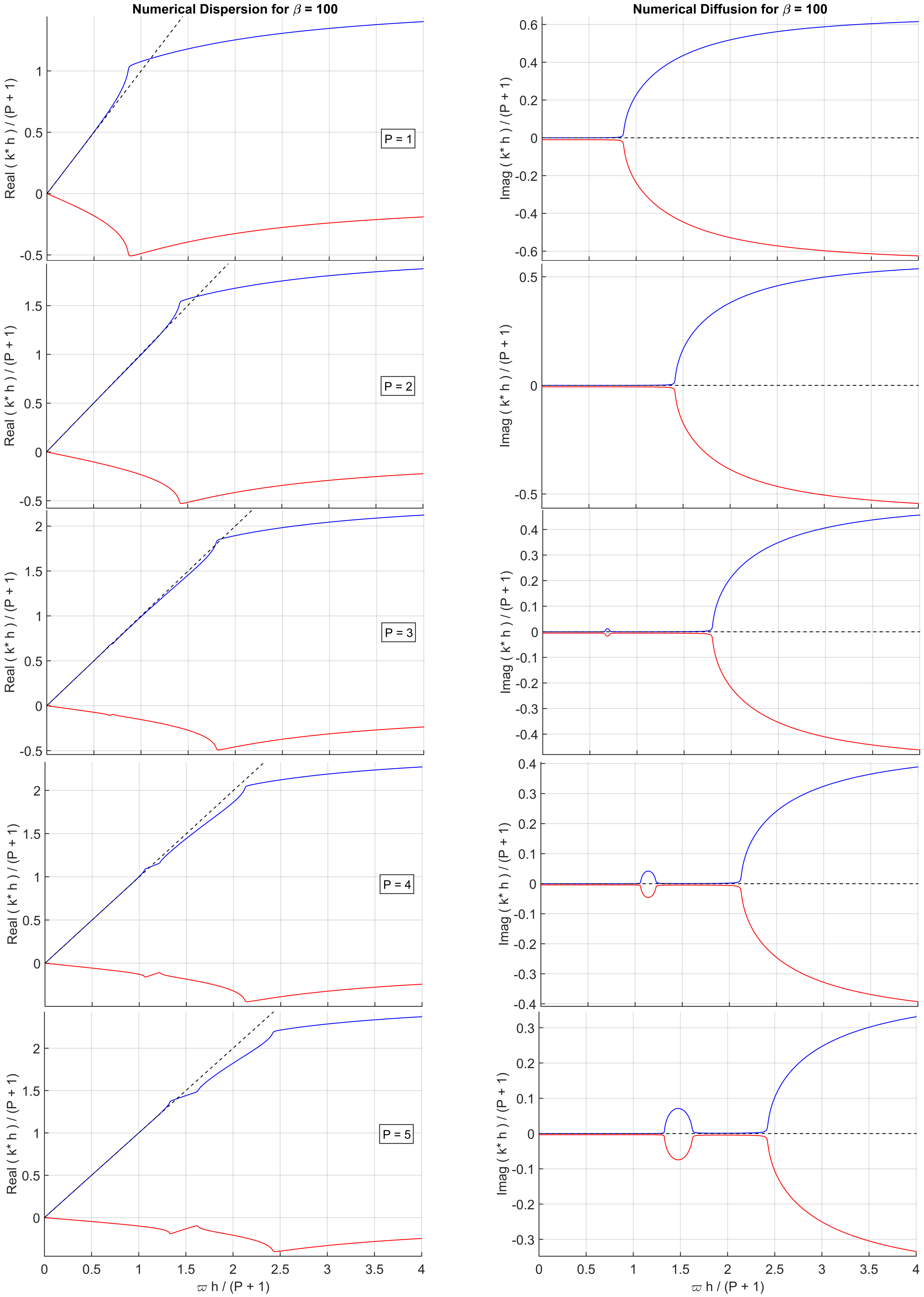

Figure 5.3: DG's dispersion (left) and dissipation (right) eigencurves for $\beta = 100$ and $P = 1, \ldots, 5$ (top to bottom).

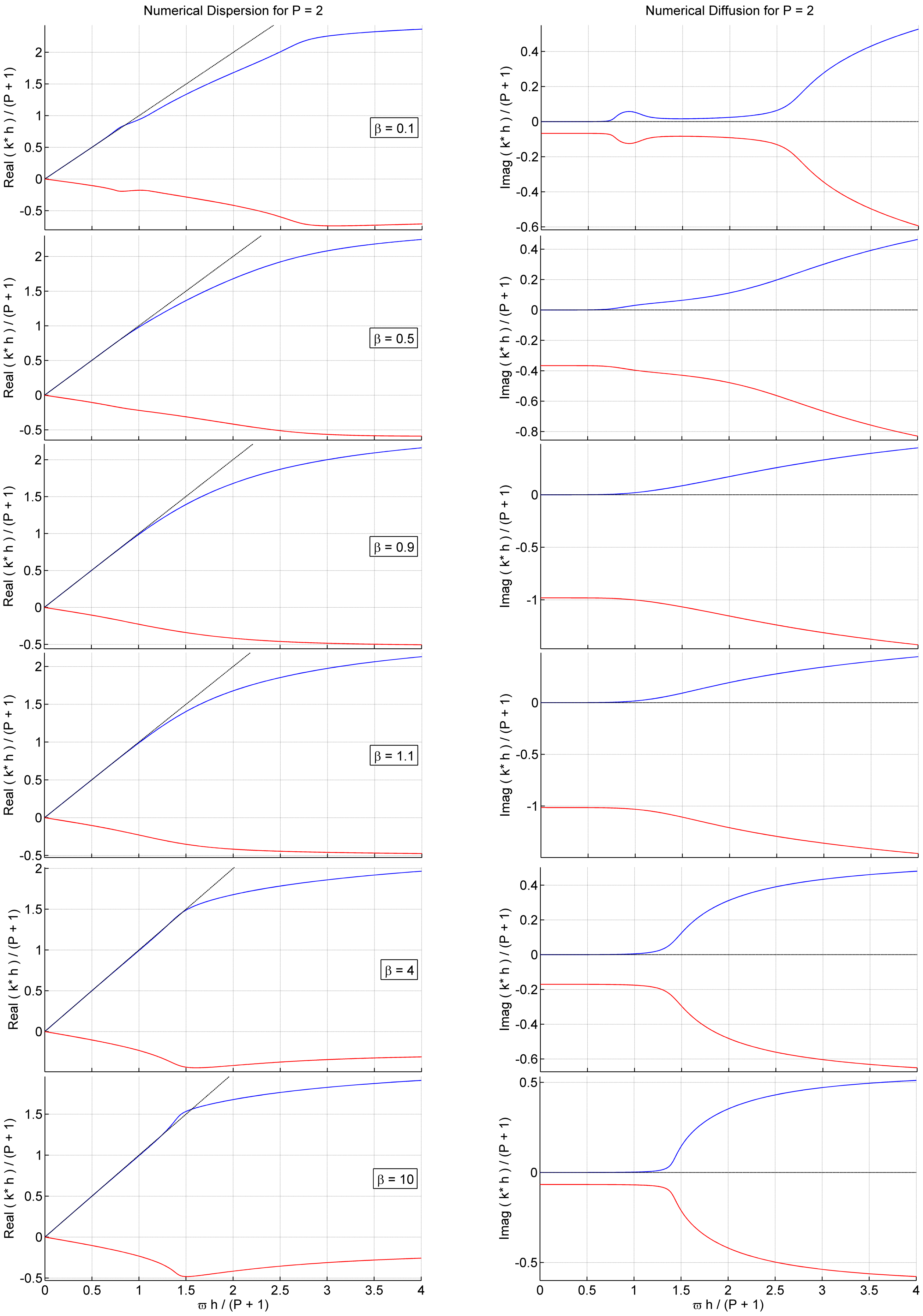

Figure 5.4: DG's dispersion (left) and dissipation (right) eigencurves for $P = 2$ and $\beta = 0.1, \ldots, 10$ (increasing from top to bottom).

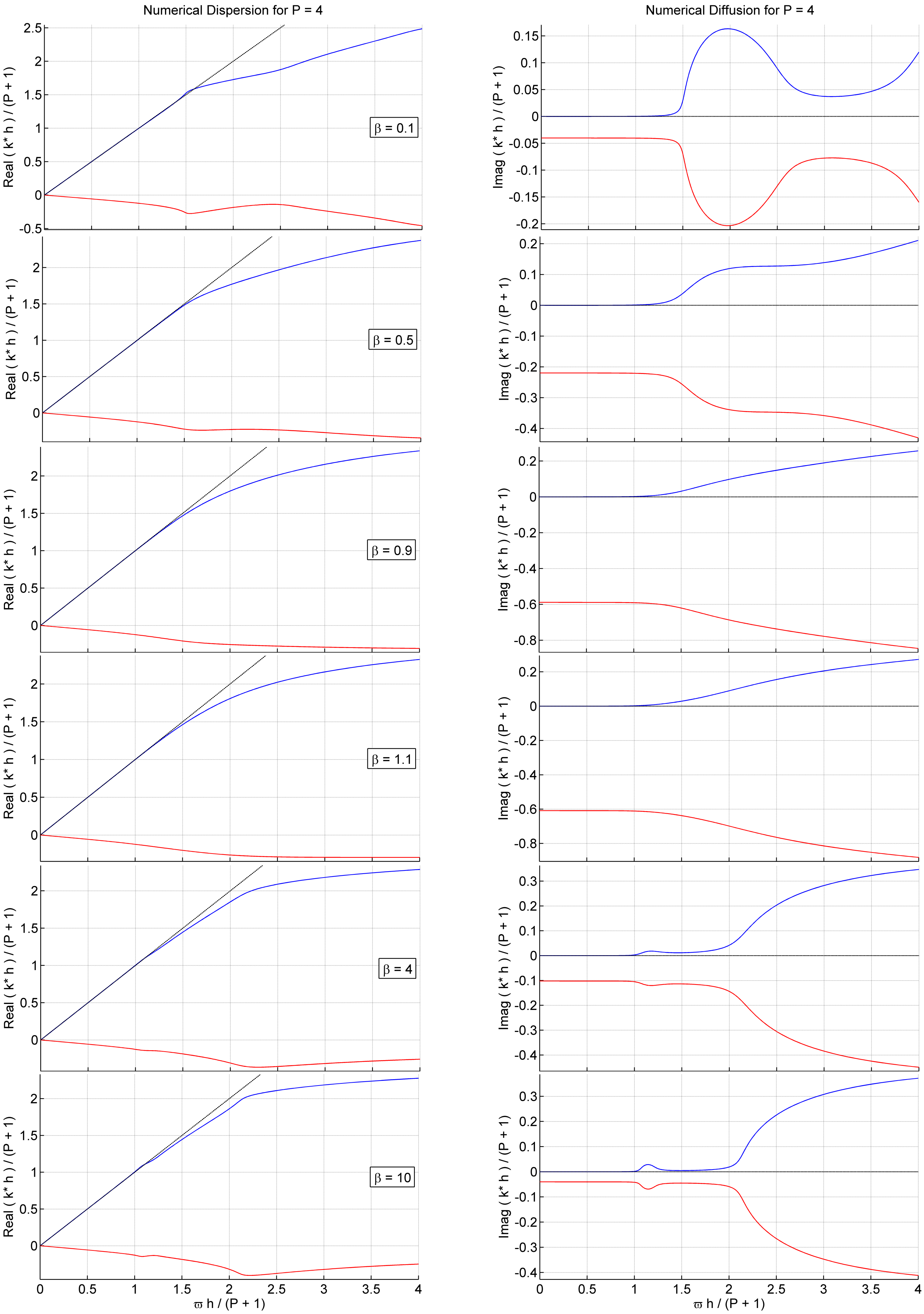

Figure 5.5: DG's dispersion (left) and dissipation (right) eigencurves for $P = 4$ and $\beta = 0.1, \ldots, 10$ (increasing from top to bottom).

a range around $\varpi\hbar = 0$, especially at higher polynomial orders, cf. Fig. 5.1. It is likely that such small (but finite) dissipation levels help to promote the superior numerical stability/robustness of standard upwind DG discretisations over those based on central (or nearly so) fluxes. Also, note that the exact dispersion characteristics are better represented by the standard upwind discretisation.

It is worth stressing that, at the dissipative bubbles mentioned above, finite dissipation levels are indeed obtained with central fluxes — contrary to what is found in temporal eigenanalysis, where central fluxes yield zero dissipation for all wavenumbers. This is a surprising result and means that, for DG simulations of spatially developing flows, central fluxes can effectively yield non-zero dissipation at certain frequency ranges. Such information is particularly relevant for computations that involve a broad range of frequencies. The presence of dissipative bubbles might induce potentially undesirable non-smooth features in such simulations. Employing a central (or nearly so) flux would otherwise seem reasonable, for example, in a DNS where one wishes to avoid upwind dissipation and rely solely on viscous diffusion, as done e.g. in [31]. Also, some Riemann solver corrections aimed at low Mach number applications can effectively reduce them to nearly central fluxes around low-speed flow regions, cf. [32]. Such strategies may also be problematic due to the vanishing dissipation levels associated to the spurious eigenmodes as $\beta \to 0$. In the central flux limit, physical and spurious modes feature a pair of opposite dissipation eigencurves, which apparently are symmetrical reflections of each other about the horizontal axis. This implies that spurious reflected waves will also be subjected to negligible damping over a considerable range of frequencies. In simulations of acoustics, for example, spurious modes reflected far downstream of a region of interest could return and corrupt the solution significantly. Also, in a turbulent wake, coarsening the mesh could cause spurious reflections to interact with incoming turbulent structures and affect not only solution quality, but also numerical stability, in case coarsening is sufficiently abrupt.

The limit of very large β values, named "hyper-upwinding" hereinafter, is now considered. This limit is relevant e.g. to low Mach number DG simulations of spatially developing flows performed with the local Lax-Friedrichs (LLF) solver, also known as the Rusanov flux [33]. For compressible Navier-Stokes or Euler computations, the LLF Riemann solver essentially replaces $|u|$ with $|u| + c$ in the momentum equations, where u is the relevant component of the convection velocity and c is the speed of sound. This effectively amounts to an over-upwind factor $\beta = (|u| + c)/|u|$, which scales as $1 + \text{Mach}^{-1}$ and hence increases without bound when Mach $\to 0$. The effects of LLF-induced hyper-upwinding in turbulence computations have been first discussed in [25, 34]. Fig. 5.3 shows the eigencurves obtained with $\beta = 100$ for various polynomial orders $P = 1, \ldots, 5$. Although this value of β is particularly representative of Mach ≈ 0.01, the eigencurves shown do not change noticeably as β is further increased. Interestingly, the eigencurves' behaviour in the limit of hyper-upwinding is not very different than that observed for central fluxes. One of the conclusions of the above is that LLF-based acoustics simulations at low Mach numbers should suffer from spurious modes reflected throughout the domain as mesh spacing is varied. Potentially undesirable non-smooth features may also be expected due to dissipative bubbles in simulations involving a broad range of frequencies. It is worth noting that polynomial orders $P = 2$ and $P = 3$ yield particularly large frequency ranges of low-dissipation, as well as good dispersion characteristics — at higher frequencies, superior to what is achieved with $P = 4$ or $P = 5$.

The eigencurves' behaviour in between the two upwinding limits considered so far is discussed next. Figs. 5.4 and 5.5 show, respectively for cases $P = 2$ and $P = 4$, how dispersion and dissipation curves change as the amount of upwinding employed varies from $\beta \ll 1$ to $\beta \gg 1$. Away from these two limits, the curves exhibit a more monotonic behaviour, without bubbles or kinks, both for physical and spurious modes. It is also interesting to see how the dissipation curves of spurious modes tend to become the symmetrical pairs of their physical counterparts in both limits. Additionally, as the standard upwind discretisation is approached, spurious modes become increasingly damped. In fact, when $\beta \to 1$, their dissipation curves tend to minus infinity (not shown) and spurious modes cease to exist, cf. Fig. 5.1. By putting together all the plots considered in this section, a fairly complete picture of the qualitative behaviour of different DG discretisations of linear advection can be visualized.

The results shown here indicate that any departure from the standard upwind condition is to be considered with caution, especially in the case of under-resolved simulations involving a broad range of frequencies, where a considerable $\varpi\hbar$ range is energised. Note that Roe's flux is not the only representative of the standard upwind condition. In fact, any "complete" Riemann solver [35], i.e. any solver that takes into account all the physical wave speeds consistently, should behave like Roe's flux with regards to the amount of upwinding they employ. This is supported by e.g. the under-resolved transitional/turbulent flow simulations conducted in [25] with different Riemann solvers.

5.4 Numerical experiments in under-resolved vortical flows

This section is devoted to the assessment of DG's propagation characteristics in actual numerical experiments of spatially developing flows. Particular emphasis will be given to spurious reflections associated to the unphysical eigenmodes discussed in Sec. 5.3. The model problem considered is a two-dimensional flow governed by the compressible Euler equations with a set of boundary conditions designed to replicate a grid turbulence scenario at very high Reynolds numbers, cf. Fig. 5.6. Note that in DG-based uDNS of Navier-Stokes turbulence, sufficiently high Reynolds numbers will eventually cause numerical dissipation to overcome molecular diffusion. In this context, solutions will be essentially governed by the Euler equations regularized by numerical dissipation. This scenario is typical of traditional LES at very high Reynolds numbers (away from walls), when the effects of molecular viscosity are negligible in comparison to those of the subgrid-scale model.

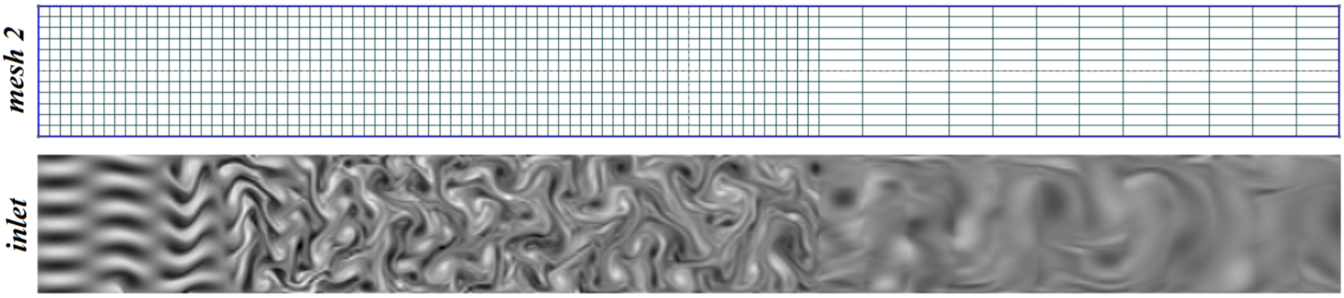

Figure 5.6: Example of mesh and flow configuration adopted. Inlet boundary conditions are applied so as to mimic a physical screen generating eddies that propagate into the domain and downstream.

In the model problem adopted, the inlet boundary condition is set to mimic a passive generator of eddies, which is the role of e.g. a physical screen in producing the initial vorticity in real grid turbulence. Free-slip walls are used to confine the flow in order to prevent the occurrence of what seemed to be a physical instability due to vortex pairing in the cross-flow direction. These have been observed in some of the simulations (depending on the inflow shedding frequency) when periodic boundary conditions were first applied in the cross-flow direction. Simplistic outflow boundary conditions are used at the domain's outlet. Although the two-dimensional character of the model problem prevents the formation of three-dimensional eddy structures typical of real turbulence, small-scale vorticity is still generated. This is sufficient for the purposes of the present study since the broad range of scales generated allows for the investigation of DG's propagation characteristics in an under-resolved numerical scenario.

The domain size for the model problem is of 2π (cross-flow) vs. 20π (streamwise) length units. The element-wise polynomial order was chosen as $P = 5$ for all the test cases, which gives a nominal order of accuracy of $P + 1 = 6$. Two meshes have been used in the test cases considered. The first mesh, referred to as *mesh 1*, is a uniform grid of square-shaped elements, composed of 12 (cross-flow) vs. 120 (streamwise) high-order elements. The second mesh, referred to as *mesh 2*, is composed of two sections of different streamwise grid spacing, as shown in Fig. 5.6. One of the sections constitutes the first 60% of the domain (upstream portion) and matches exactly the corresponding part of *mesh 1*. The other part constitutes the remaining 40% of the physical domain (downstream portion) and has four times less elements when compared the corresponding part of *mesh 1*. The change across the two sections is in streamwise spacing only and amounts to an abrupt factor of 4x increase in mesh spacing in the direction of propagation. In summary, *mesh 2* is composed of 12 (cross-flow) vs. 72 plus 12 (streamwise) elements, respectively in the first and second sections of the grid. The interface between these two sections, namely station 60%, is a potential point of origin of unphysical reflections associated to spurious eigenmodes, as discussed in Sec. 5.3. Spurious reflections can also originate from the outflow boundary in certain cases, as will become clear further on.

The free-slip wall boundaries confining the flow are implemented as mirror symmetry conditions at $y = \pm\pi$. Inflow boundary conditions are set through the outer state considered by the Riemann solvers at the faces of the elements adjacent to the inlet. The following conditions are prescribed respectively for the density, the momentum components in the streamwise and cross-flow directions, and the total energy per unit volume:

$$\rho = \rho_\infty \ , \tag{5.15}$$

$$\rho u = \rho_\infty u_\infty \left[\, 1 + A \, \sin(Ky) \, \sin(\varOmega\, t) \,\right] \ , \quad \rho v = 0 \ , \tag{5.16}$$

$$E = p_\infty/(\gamma - 1) + \rho_\infty u_\infty^2/2 \ , \tag{5.17}$$

where $\rho_\infty = 1$, $u_\infty = 1$ are the free-stream density and mean flow velocity, while $p_\infty = \rho_\infty c_\infty^2/\gamma$ is the free-stream static pressure which is used to define the flow's reference Mach number through the speed of sound $c_\infty = u_\infty \, \mathrm{Mach}^{-1}$. Moreover, the fluid's ratio of specific heats is set to $\gamma = 7/5$ and the parameters defining the inflow perturbations are given by $A = 1/2$, $K = 5$ and $\varOmega = 1$. For the outflow boundary, the simplest possible conditions were employed, in order to highlight that strong spurious reflections can be obtained with some Riemann solvers and entirely suppressed with others, as discussed below. More specifically, constant far-field conditions were used as outside states for the numerical fluxes evaluated at the outlet interfaces, i.e. $\rho = \rho_\infty$, $\rho u = \rho_\infty u_\infty$, $\rho v = 0$ and $E = p_\infty/(\gamma - 1) + \rho_\infty u_\infty^2/2$. These same conditions were used for the whole domain at $t = 0$, except that a small cross-flow momentum component ($\rho v = 0.1$) was used to facilitate the onset of the turbulent-like flow state of interest. After approximately 20π time units, the numerical solution reaches a chaotic state which then becomes permanent in time. The results discussed in this section are of solutions obtained after 100 time units.

Integration in time is performed with a second-order Runge-Kutta scheme at a sufficiently small time step to ensure negligible errors from the temporal discretisation. Note that the semi-discrete DG scheme is considered in the eigenanalysis of Sec. 5.3, for which integration in time is assumed to be exact. Two Riemann solvers are considered for the test cases, namely, Roe's original solver [30] and the local Lax-Friedrichs (LLF) flux, also known as the Rusanov solver [33]. These are arguably the most common inviscid fluxes used in DG simulations. Although these two solvers are known to display comparable performance for most well-resolved DG computations, especially at higher polynomial orders, their behaviour can be drastically different for under-resolved computations. This has been shown for temporally evolving flows in [25] and is demonstrated here for spatially developing ones. Finally, two Mach numbers are tested in the simulations, namely, 0.3 and 0.03. The latter is relied upon to illustrate the effects of hyper-upwinding induced by the Lax-Friedrichs solver, as discussed in Sec. 5.3. By taking into account the two grids considered, eight test cases are evaluated in total. All simulations have been conducted with spectral/*hp* element code *Nektar++* [36]. It is important to note that an increased number of quadrature points ($q = 2m$ per element, per dimension) has been employed in all test cases to ensure consistent integration of the cubic non-linearities of the compressible Euler equations, see e.g. [4]. This should suppress polynomial aliasing errors caused by insufficient integration accuracy [37].

It is useful to begin by assessing the cases of moderate Mach number (Mach = 0.3) illustrated in Fig. 5.7, which shows contour fields of vorticity $\boldsymbol{\omega}_z = \partial v/\partial x - \partial u/\partial y$. The upper two plots refer to results obtained with LLF for both *mesh 1* and *mesh 2*. The lower two plots show analogous fields extracted from Roe-based solutions. Strong reflections can be seen at the outlet of case LLF–*mesh 1*, which then rapidly decay towards the interior of the domain. This is expected from the exponential damping of spurious eigenmodes during backwards propagation. The initial magnitude of spurious waves is defined by how abruptly solution values are changing across the interface of interest [18]. As a constant far-field state is prescribed outside of the outlet boundary, strong reflections can be anticipated. On the other hand, case Roe–*mesh 1* shows no reflections whatsoever. This is also expected because Roe's solver employs standard upwinding, in which case spurious modes are simply non-existent. Outlet reflections are also significantly reduced in case LLF–*mesh 2*. This is because the downstream section present in *mesh 2* acts as a buffer zone by strongly diffusing small-scale vorticity. As a result, the solution arriving at the outflow is much closer to the constant state prescribed outside of the outlet boundary. Since the change in solution values across the outflow interface is not so abrupt in this case, weaker reflections are only natural.

Although outlet reflections in case LLF–*mesh 2* are arguably mild, their presence can still be noted on the sharper streamwise discontinuities observed at element interfaces on the downstream portion of the mesh. These in fact strongly demarcate the underlying grid spacing adopted, cf. Fig. 5.6, which is characteristic of spurious waves. Note that a similar demarcation occurs near the outlet in case LLF–*mesh 1*. This is because spurious eigenmodes typically assume highly oscillatory shapes, especially near element-wise boundaries [18]. Roe-based cases, on the other hand, exhibit much milder demarcation effects which are only consistent with the piecewise continuous DG approximation. Finally, reflections originating from station 60% can be noted on case LLF–*mesh 2*, but not on case Roe–*mesh 1*. The former are moderate when compared to the outlet reflections observed on case LLF–*mesh 1*, owing to the different intensity in solution change across the respective interfaces. Nevertheless, reflections from station 60% of case LLF–*mesh 2* seem to decay first and subsequently grow towards the region of more intense vorticity. This subsequent growth is believed to be a non-linear effect caused by an interaction between small-scale eddies and spurious waves. A similar effect also takes place (to a lesser extent) in case LLF–*mesh 1*. It should be stressed that the exponential decay character of spurious waves produces a stronger initial damping followed by gradually weaker decay rates, whereby spurious waves are never actually totally dissipated. This accounts for the larger distance between the outlet of case LLF–*mesh 1* and the region of more intense vorticity which is closer to the inlet boundary.

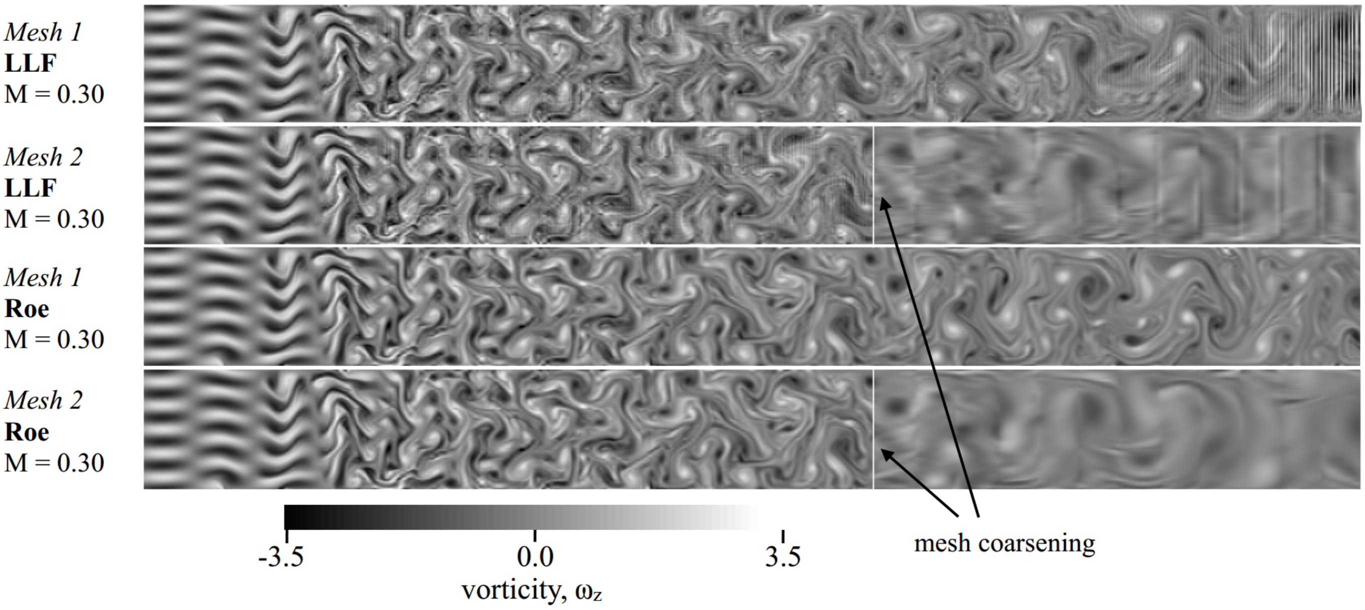

Figure 5.7: Comparison of the vorticity fields $\boldsymbol{\omega}_z$ from Lax-Friedrichs and Roe-based simulations performed at Mach = 0.3, both for *mesh 1* and *mesh 2*. Station 60% is highlighted as the interface where streamwise grid spacing is varied abruptly on *mesh 2*.

It remains to assess the nearly incompressible test cases (Mach = 0.03) considered. Their results are given in Fig. 5.8, which is the exact counterpart of Fig. 5.7 for the lower Mach number cases. It is interesting to see that the variation in Mach number had a negligible effect in the transitional part of the flow, but it did change slightly its spatial evolution, whereby differences can be clearly noted between cases Roe–*mesh 1* in Figs. 5.7 and 5.8, especially at downstream regions. However, the most notable difference between the cases shown in these two figures concerns the spurious reflections in LLF-based cases. Lowering the Mach number exacerbates the effects of hyper-upwinding expected at the incompressible limit. In particular, the amount of damping to which spurious modes are subjected to becomes much weaker. As a result, reflections are allowed to propagate much longer and are perceived even at the "laminar" transitional region near the inlet. Moreover, as the magnitude of spurious waves is still considerable in the upstream regions of the domain, a stronger nonlinear interaction is expected between them and small-scale vortical eddies which are stronger right after transition. This interaction is strong to the point of clearly demarcating both streamwise and cross-flow elemental boundaries. The resulting flow field of LLF-based computations is considerably noisier than those obtained with Roe's solver.

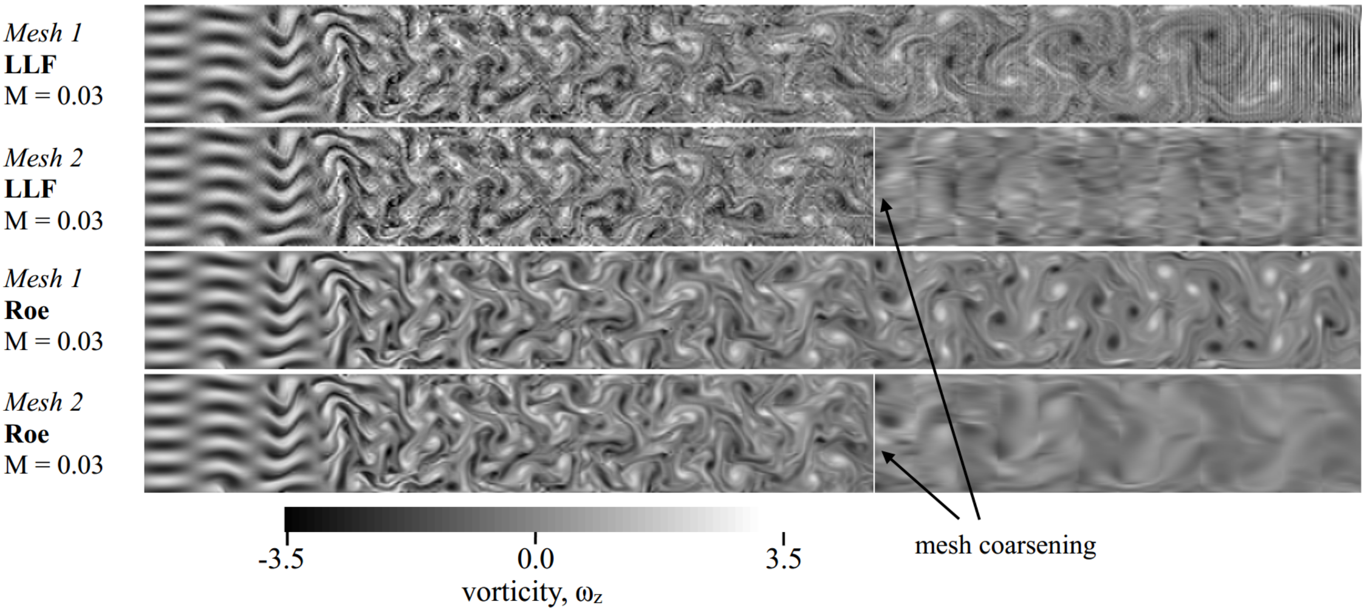

Figure 5.8: Comparison of the vorticity fields $\boldsymbol{\omega}_z$ from Lax-Friedrichs and Roe-based simulations performed at Mach = 0.03, both for *mesh 1* and *mesh 2*. Station 60% is highlighted as the interface where streamwise grid spacing is varied abruptly on *mesh 2*.

Interestingly, this last feature (LLF-induced spurious noise) has also been observed in temporally evolving under-resolved turbulence computations at infinite Reynolds number [25], although for different reasons. The main suggestion for practitioners is therefore to simply favour Roe-type (or complete) Riemann solvers over more simplistic and cheaper flux formulas, especially at low Mach numbers. Regarding flows with a spatially developing character, avoiding spurious reflections is fundamental for solution quality. For example, in simulations of acoustics, the presence of unphysical modes generated by variable mesh spacing have the potential to affect post-processing significantly. Moreover, in under-resolved flow computations featuring turbulent wakes, for example, where mesh coarsening is typically applied, spurious reflections might affect not only solution quality, but also numerical stability. This has been observed in simulations performed with the continuous Galerkin (CG) method for a model problem very similar to the one considered here [38], which crashed at high Reynolds numbers due to a build-up of small-scale energy prior to an interface of sudden mesh coarsening. It is possible that DG and other spectral element methods might lack numerical stability in similar scenarios provided that turbulence intensity and mesh coarsening is sufficiently intense. The simple adoption of complete Riemann solvers should suffice in suppressing such types of numerical instabilities.

5.5 Conclusion

This study addressed the spatial eigenanalysis of the discontinuous Galerkin (DG) method as applied to the linear advection equation. The results first presented in [18] have been revisited and additional analyses have been performed. These included an assessment on the effects of different upwinding levels and the discussion of eigenanalysis results which are relevant to computations that involve a broad range of frequencies. Subsequently, numerical experiments based on a two-dimensional model problem that mimicked spatially evolving grid turbulence have been explored to verify and complement DG's propagation characteristics obtained from the linear eigenanalysis. This aligns with various recent works that investigate the suitability of spectral element methods for model-free eddy-resolving approaches to transitional and turbulent flow problems, namely under-resolved DNS (uDNS) / implicit LES (iLES) strategies [10, 39, 12, 22, 29, 40, 25, 15].

The main novel results obtained from the spatial eigenanalysis conducted are the following. For DG discretisations based on central (or nearly so) inviscid fluxes, dissipative bubbles of finite dissipation levels have been observed for certain frequency ranges for polynomial orders $P = 2$ and above. These might induce potentially undesirable non-smooth features on under-resolved computations of spatially developing flows with non-negligible high-frequency energy content. Qualitatively similar characteristics have been found for DG discretisations in the limit of strong over-upwinding (named hyper-upwinding), including the presence of dissipative bubbles for $P = 3$ and above, although the bubble observed for $P = 3$ is arguably very small. Another feature found in the limits of both zero- and hyper-upwinding is that the damping levels associated to unphysical eigenmodes become vanishingly small. This results in spurious reflections that are propagated over long distances and that can interact nonlinearly with small-scale flow structures producing oscillations (noise) and degrading solution quality and numerical stability. Spurious reflections can originate at interfaces where streamwise mesh spacing changes or at outflow boundaries, provided that Riemann solvers based on non-standard upwinding are employed. This can be the case when e.g. certain corrected flux formulas are used, such as those incorporating entropy fixes [41] or low-Mach scaling corrections [32]. In addition, more simplistic fluxes such as the local Lax-Friedrichs solver, also known as Rusanov's flux [33], will induce over-upwinding effects at low Mach numbers due to their unphysical eigenvalue scaling. The adoption of complete Riemann fluxes that account for all wave speeds in a consistent manner, such as Roe's original solver [30], are expected to avoid all of the aforementioned issues due to their standard upwinding character.

The numerical experiments conducted with the model problem proposed basically confirmed the eigenanalysis' results and illustrated them in a more physical context. From the insights gathered in this study, the following guidelines are advised for uDNS/iLES:

1. *Favour Roe-type (or complete) solvers over more simplistic flux formulas.* This should help to suppress spurious reflections and small-scale noise, especially at low Mach numbers.

2. *Avoid sharp mesh coarsening for simulations of spatially developing flows.* Although Roe-type fluxes have suppressed reflections in all cases investigated here, this benefit is likely to be somewhat reduced for irregular meshes typical of more complex flow problems.

3. *Favour moderately high polynomial orders, such as $P = 5$.* Lower discretisation orders yield a reduced spectral resolution power per degree of freedom employed, whereas much higher polynomial orders might require additional stabilization techniques at very high Reynolds numbers due to their inherently low dissipation levels.

Subsequent studies may extend the investigation conducted here for different spectral element methods. A natural candidate is the so-called Flux Reconstruction (FR) scheme, also known as Correction Procedure via Reconstruction (CPR) methods. These have the flexibility to recover various discontinuous spectral element methods, including some versions of DG [42, 43, 44]. Another candidate scheme is the spectral/*hp* continuous Galerkin (CG) method [4], which lacks numerical dissipation for convection-dominated flows, but can be stabilized by added Spectral Vanishing Viscosity (SVV), see e.g. [45, 23]. CG schemes with SVV-based stabilization have also been used in several works for uDNS/iLES [46, 47, 13, 48]. Other than investigating different methods, there are aspects of the DG discretisation that still deserve consideration. For instance, the effect of different mesh topologies and types of elements should be addressed, in order to understand how effective Roe-type solvers are in suppressing spurious reflections for complex meshes (including curved elements). Finally, a systematic study regarding which strategy of gradual mesh coarsening is more appropriate to minimize reflections and improve robustness in different scenarios would also be important for various applications.

References

[1] J. A. Ekaterinaris. High-order accurate, low numerical diffusion methods for aerodynamics. *Progress in Aerospace Sciences*, 41(3):192–300, 2005.

[2] Z. J. Wang. High-order methods for the Euler and Navier-Stokes equations on unstructured grids. *Progress in Aerospace Sciences*, 43(1):1–41, 2007.

[3] P. E. Vincent and A. Jameson. Facilitating the adoption of unstructured high-order methods amongst a wider community of fluid dynamicists. *Mathematical Modelling of Natural Phenomena*, 6(3):97–140, 2011.

[4] G. E. Karniadakis and S. J. Sherwin. *Spectral/hp element methods for computational fluid dynamics*. Oxford University Press, 2nd edition, 2005.

[5] C. Canuto, M. Y. Hussaini, A. Quarteroni, and T. A. Zang. *Spectral methods: evolution to complex geometries and applications to fluid dynamics*. Springer Science & Business Media, 2007.

[6] D. A. Kopriva. *Implementing spectral methods for partial differential equations: algorithms for scientists and engineers*. Springer Science & Business Media, 2009.

[7] P. Delorme, P. Mazet, C. Peyret, and Y. Ventribout. Computational aeroacoustics applications based on a discontinuous Galerkin method. *Comptes Rendus Mécanique*, 333(9):676–682, 2005.

[8] M. Minguez, R. Pasquetti, and E. Serre. High-order large-eddy simulation of flow over the 'Ahmed body' car model. *Physics of Fluids*, 20(9):095101, 2008.

[9] N. Castel, G. Cohen, and M. Duruflé. Application of discontinuous Galerkin spectral method on hexahedral elements for aeroacoustic. *Journal of Computational Acoustics*, 17(02):175–196, 2009.

[10] A. Uranga, P. O. Persson, M. Drela, and J. Peraire. Implicit large eddy simulation of transition to turbulence at low Reynolds numbers using a discontinuous Galerkin method. *International Journal for Numerical Methods in Engineering*, 87(1-5):232–261, 2011.

[11] R. D. R. Rinaldi, A. Iob, and R. Arina. An efficient discontinuous Galerkin method for aeroacoustic propagation. *International Journal for Numerical Methods in Fluids*, 69(9):1473–1495, 2012.

[12] A. D. Beck, T. Bolemann, D. Flad, H. Frank, G. J. Gassner, F. Hindenlang, and C. D. Munz. High-order discontinuous Galerkin spectral element methods for transitional and turbulent flow simulations. *International Journal for Numerical Methods in Fluids*, 76(8):522–548, 2014.

[13] J.-E. W. Lombard, D. Moxey, S. J. Sherwin, J. F. A. Hoessler, S. Dhandapani, and M. J. Taylor. Implicit large–eddy simulation of a wingtip vortex. *AIAA Journal*, 54(2):506–518, 2016.

[14] H. Zhu, S. Fu, L. Shi, and Z. J. Wang. Implicit large-eddy simulation for the high-order flux reconstruction method. *AIAA Journal*, pages 2721–2733, 2016.

[15] P. Fernandez, N. C. Nguyen, and J. Peraire. The hybridized Discontinuous Galerkin method for Implicit Large-Eddy Simulation of transitional turbulent flows. *Journal of Computational Physics*, 336:308–329, 2017.

[16] J. S. Hesthaven and T. Warburton. *Nodal discontinuous Galerkin methods: algorithms, analysis, and applications*. Springer, 2007.

[17] F. Q. Hu, M. Y. Hussaini, and P. Rasetarinera. An analysis of the discontinuous Galerkin method for wave propagation problems. *Journal of Computational Physics*, 151(2):921–946, 1999.

[18] F. Q. Hu and H. L. Atkins. Eigensolution analysis of the discontinuous Galerkin method with nonuniform grids: I. one space dimension. *Journal of Computational Physics*, 182(2):516–545, 2002.

[19] K. Van den Abeele, T. Broeckhoven, and C. Lacor. Dispersion and dissipation properties of the 1D spectral volume method and application to a p-multigrid algorithm. *Journal of Computational Physics*, 224(2):616–636, 2007.

[20] K. Van den Abeele, C. Lacor, and Z. J. Wang. On the stability and accuracy of the spectral difference method. *Journal of Scientific Computing*, 37(2):162–188, 2008.

[21] P. E. Vincent, P. Castonguay, and A. Jameson. Insights from von Neumann analysis of high-order flux reconstruction schemes. *Journal of Computational Physics*, 230(22):8134–8154, 2011.

[22] R. C. Moura, S. J. Sherwin, and J. Peiró. Linear dispersion-diffusion analysis and its application to under-resolved turbulence simulations using discontinuous Galerkin spectral/*hp* methods. *Journal of Computational Physics*, 298:695–710, 2015.

[23] R. C. Moura, S. J. Sherwin, and J. Peiró. Eigensolution analysis of spectral/*hp* continuous Galerkin approximations to advection-diffusion problems: insights into spectral vanishing viscosity. *Journal of Computational Physics*, 307:401–422, 2016.

[24] M. Ainsworth. Dispersive and dissipative behaviour of high order discontinuous Galerkin finite element methods. *Journal of Computational Physics*, 198(1):106–130, 2004.

[25] R. C. Moura, G. Mengaldo, J. Peiró, and S. J. Sherwin. On the eddy-resolving capability of high-order discontinuous Galerkin approaches to implicit LES / under-resolved DNS of Euler turbulence. *Journal of Computational Physics*, 330:615–623, 2017.

[26] L. G. Margolin and W. J. Rider. A rationale for implicit turbulence modelling. *International Journal for Numerical Methods in Fluids*, 39(9):821–841, 2002.

[27] F. F. Grinstein, L. G. Margolin, and W. J. Rider. *Implicit large eddy simulation: computing turbulent fluid dynamics*. Cambridge University Press, 2007.

[28] R. C. Moura, S. J. Sherwin, and J. Peiró. Modified equation analysis for the discontinuous Galerkin formulation. In *Proceedings of the 10th International Conference on Spectral and High Order Methods (ICOSAHOM)*, Salt Lake City, USA, 2014.

[29] R. C. Moura, G. Mengaldo, J. Peiró, and S. J. Sherwin. An LES setting for DG-based implicit LES with insights on dissipation and robustness. In *Proceedings of the 11th International Conference on Spectral and High Order Methods*, Rio de Janeiro, Brazil, 2016.

[30] P. L. Roe. Approximate Riemann solvers, parameter vectors, and difference schemes. *Journal of Computational Physics*, 43(2):357–372, 1981.

[31] L. Wei and A. Pollard. Direct numerical simulation of compressible turbulent channel flows using the discontinuous Galerkin method. *Computers & Fluids*, 47(1):85–100, 2011.

[32] K. Oßwald, A. Siegmund, P. Birken, V. Hannemann, and A. Meister. L^{2}Roe: a low dissipation version of Roe's approximate Riemann solver for low Mach numbers. *International Journal for Numerical Methods in Fluids*, 81(2):71–86, 2015.

[33] V. V. Rusanov. Calculation of interaction of non-steady shock waves with obstacles. *USSR Journal of Computational and Mathematical Physics*, 1:267–279, 1961.

[34] A. R. Winters, R. C. Moura, G. Mengaldo, G. J. Gassner, S. Walch, J. Peiró, and S. J. Sherwin. A comparative study on polynomial dealiasing and split form discontinuous Galerkin schemes for under-resolved turbulence computations. *Journal of Computational Physics (under revision)*, 2017.

[35] E. F. Toro. *Riemann solvers and numerical methods for fluid dynamics*. Springer, 1999.

[36] C. D. Cantwell, D. Moxey, A. Comerford, A. Bolis, G. Rocco, G. Mengaldo, D. De Grazia, S. Yakovlev, J-E. Lombard, D. Ekelschot, B. Jordi, H. Xu, Y. Mohamied, C. Eskilsson, B. Nelson, P. Vos, C. Biotto, R. M. Kirby, and S. J. Sherwin. Nektar++: An open-source spectral/*hp* element framework. *Computer Physics Communications*, 192:205–219, 2015.

[37] G. Mengaldo, D. De Grazia, D. Moxey, P. E. Vincent, and S. J. Sherwin. Dealiasing techniques for high-order spectral element methods on regular and irregular grids. *Journal of Computational Physics*, 299:56–81, 2015.

[38] R. C. Moura, J. Peiró, and S. J. Sherwin. On the accuracy and robustness of under-resolved DNS approaches based on spectral element methods. In *Proceedings of the 10th International Symposium on Turbulence and Shear Flow Phenomena (TSFP-10)*, Chicago, USA, 2017.

[39] G. J. Gassner and A. D. Beck. On the accuracy of high-order discretizations for underresolved turbulence simulations. *Theoretical and Computational Fluid Dynamics*, 27(3-4):221–237, 2013.

[40] B. C. Vermeire, S. Nadarajah, and P. G. Tucker. Implicit large eddy simulation using the high-order correction procedure via reconstruction scheme. *International Journal for Numerical Methods in Fluids*, 82(5):231–260, 2016.

[41] A. Harten. High resolution schemes for hyperbolic conservation laws. *Journal of Computational Physics*, 49(3):357–393, 1983.

[42] H. T. Huynh. A flux reconstruction approach to high-order schemes including discontinuous Galerkin methods. In *Proceedings of the 18th AIAA Computational Fluid Dynamics Conference (AIAA Paper 2007-4079)*, Miami, USA, 2007.

[43] D. De Grazia, G. Mengaldo, D. Moxey, P. E. Vincent, and S. J. Sherwin. Connections between the discontinuous Galerkin method and high-order flux reconstruction schemes. *International Journal for Numerical Methods in Fluids*, 75(12):860–877, 2014.

[44] G. Mengaldo, D. De Grazia, P. E. Vincent, and S. J. Sherwin. On the connections between discontinuous Galerkin and flux reconstruction schemes: extension to curvilinear meshes. *Journal of Scientific Computing*, 67(3):1272–1292, 2016.

[45] R. M. Kirby and S. J. Sherwin. Stabilisation of spectral/hp element methods through spectral vanishing viscosity: application to fluid mechanics modelling. *Computer Methods in Applied Mechanics and Engineering*, 195(23):3128–3144, 2006.

[46] G. S. Karamanos and G. E. Karniadakis. A spectral vanishing viscosity method for large-eddy simulations. *Journal of Computational Physics*, 163(1):22–50, 2000.

[47] R. M. Kirby and G. E. Karniadakis. Coarse resolution turbulence simulations with spectral vanishing viscosity–large-eddy simulations (SVV-LES). *Journal of Fluids Engineering*, 124(4):886–891, 2002.

[48] D. Serson, J. R. Meneghini, and S. J. Sherwin. Direct numerical simulations of the flow around wings with spanwise waviness. *Journal of Fluid Mechanics*, 826:714–731, 2017.

Chapter 6

Spatial eigenanalysis of CG and its stabilization via SVV in the high Reynolds number limit

Summary [†]

This chapter is devoted to the spatial eigensolution analysis of spectral/*hp* continuous Galerkin (CG) schemes, complementing a recent work [1] that addressed CG's temporal analysis. While the latter assumed periodic boundary conditions, the spatial approach presumes inflow/outflow type conditions and therefore provides insights for a different class of problems. The linear advection-diffusion problem is here considered for a wide range of Péclet numbers, whereby viscous effects are assessed at different intensities. The inviscid (linear advection) case received particular attention owing to the manifestation of peculiar characteristics previously observed for discontinuous Galerkin (DG) schemes in the limit of strong over-upwinding. These are discussed in detail due to their potential to negatively affect the solution quality and numerical stability of under-resolved simulations at high Reynolds numbers. The spectral vanishing viscosity (SVV) technique is subsequently considered as a natural stabilization strategy for CG. An optimization procedure is employed to match SVV diffusion levels to those of DG at appropriate polynomial orders. The resulting CG-SVV discretisations are tested against under-resolved computations of spatially developing vortex-dominated flows and display excellent robustness at high Reynolds numbers along with superior eddy-resolving characteristics at higher polynomial orders. This highlights the importance of appropriate stabilization techniques to improve the potential of spectral/*hp* CG methods for high-fidelity simulations of transitional and turbulent flows, including implicit LES / under-resolved DNS approaches.

6.1 Introduction

Assessing the dispersive and diffusive behaviour of any numerical scheme is a fundamental step towards the understanding of its accuracy and stability characteristics. This is particularly true for high-order methods, where the trade-off between low dissipation and numerical robustness is of

---

[†] This chapter is partially based on "R. C. Moura, S. J. Sherwin, J. Peiró (2017) *Spatial eigenanalysis of CG and DG methods with insights on solution quality and stability*, **Research Report** (doi:10.13140/RG.2.2.33310.13129)".

critical importance [2, 3]. As a result, dispersion-diffusion analyses have been conducted for different high-order schemes [4, 5], and more recently for various spectral element methods [6, 7, 8, 9, 10]. The present work considers the spatial eigenanalysis of spectral/*hp* continuous Galerkin (CG) scheme [11] as applied to the (one-dimensional) linear advection-diffusion equation and the linear advection equation augmented with spectral vanishing viscosity (SVV), see e.g. [12, 13].

The spatial analysis addressed here is to be contrasted with the temporal analysis which is much more often find in the literature. While the latter assumes periodic boundary conditions, the former presumes inflow/outflow type conditions and is therefore concerned with a different class of problems. This study can be seen as a continuation of a previous work which considered CG's temporal eigenanalysis [1]. The present investigation has also been motivated by a recent spatial analysis conducted for the discontinuous Galerkin (DG) method [14] that focused on the insights that eigenanalysis can provide for more complex applications, such as turbulence simulations. Hence, SVV is here considered as a natural stabilization strategy given its usage in model-free eddy-resolving computations of turbulent flows [15, 16, 17, 18, 19].

The SVV technique is essentially embodied in a modified diffusion operator that is designed to affect only higher order polynomial components, as a high-order viscosity (or hyperviscosity) would act. Note that higher order CG discretisations tend to reach negligible dissipation levels at high Reynolds numbers [1], whereby added stabilization techniques are required. However, the inviscid limit observed from the spatial analysis framework is more involved and in fact reproduces undesirable characteristics typical of DG in the limit of strong over-upwinding [14]. In particular, diffusion eigencurves feature "dissipation bubbles" at certain frequency ranges and the amount of damping affecting spurious reflected eigenmodes becomes negligible in the high Reynolds limit. As these issues have the potential to negatively affect solution quality and numerical robustness, candidate SVV operators must be able to help minimise them. The strategy followed here was to match SVV dissipation levels to those of DG at appropriate polynomial orders. This was achieved with the aid of optimization algorithms, as first suggested by [1], and proved to be a successful strategy in the suppression of the aforementioned issues. The advocated approach is tested in the context of vortex-dominated flows through a two-dimensional model problem that mimics (spatially developing) grid turbulence, originally proposed in [14].

DG dissipation levels were chosen as reference for the SVV because of the good balance DG is known to offer between numerical robustness and low dissipation at higher polynomial orders. Note that using a CG scheme with DG-like dissipation characteristics instead of DG itself can sometimes be advantageous in terms of computational cost. First of all, DG is more naturally suited to hyperbolic conservation laws typical of compressible flows, even though nowadays there are DG formulations adapted for incompressible flows as well. In any case, for incompressible flow problems, CG solvers have been available for longer and rely on mature and arguably more efficient algorithms. Moreover, at low Mach numbers, solving the incompressible Navier-Stokes equations is usually less expensive than dealing with their compressible counterpart, which are more complex and involve additional flow variables. Another important point concerns the time-stepping restrictions associated to turbulent boundary layers. Note that incompressible formulations are required to take time steps defined by the small fluid velocities aligned with relatively (locally) large streamwise mesh spacing inside the boundary layer. On the other hand, compressible solvers are restricted by the much more stringent condition of large acoustic velocities perpendicular to very small wall-normal mesh spacing. This typically makes CG-based incompressible solvers much more inexpensive than DG-based compressible ones for wall-bounded turbulent flows, especially at low Mach numbers.

This study is organized as follows. In Sec. 6.2, the spatial eigensolution analysis framework is presented and its application to CG is discussed. Sec. 6.3 addresses the spatial dispersion and diffusion characteristics for various discretisation orders and also discusses in detail the inviscid limit case. Sec. 6.4 is devoted to the design of appropriate SVV operators and describes the optimization strategy adopted. In Sec. 6.5, numerical experiments are conducted to illustrate how the spatial eigenanalysis' results appear in under-resolved simulations and to demonstrate the performance of optimized SVV operators. Sec. 6.5 summarizes the study's findings and gathers concluding remarks.

6.2 CG's spatial eigenanalysis framework

The model problem considered here is the one-dimensional linear advection-diffusion equation in a semi-infinite domain,

$$\frac{\partial u}{\partial t} + a\,\frac{\partial u}{\partial x} = \mu\,\frac{\partial^2 u}{\partial x^2} \text{ , for } x > 0 \text{ , } t > 0 \text{ ,} \tag{6.1}$$

where $a > 0$ is the advection velocity and $\mu > 0$ is the viscosity. The relevant solutions are wave-like components such as

$$u \propto \exp\left[i(\kappa x - \omega t)\right] \text{ ,} \tag{6.2}$$

κ and ω being the component's wavenumber and (angular) frequency, respectively. Accordingly, boundary conditions at $x = 0$ are assumed in the form

$$u_0(t) \propto \exp(-i\omega t) \text{ .} \tag{6.3}$$

This problem has been discussed in detail in [20], which considered solutions compatible with time-periodic boundary conditions.

Inserting Eq. (6.2) into Eq. (6.1) yields

$$-i\varpi + i\kappa = -\kappa^2/r \text{ ,} \tag{6.4}$$

where variables $\varpi = \omega/a$ and $r = a/\mu$ have been introduced. In general, both ϖ and κ can be complex, but the more interesting analyses are carried out assuming that one of them is real. From Eq. (6.4), one can define $\varpi = \varpi(\kappa)$, which is perhaps a more well known relation, but it is also possible to define $\kappa = \kappa(\varpi)$, whereby two dispersion relations can be obtained, namely

$$\varpi = \kappa - i\kappa^2/r \text{ ,} \tag{6.5}$$

and

$$\kappa = \left(-1 + \sqrt{1 - 4i\varpi/r}\right) ir/2 \text{ .} \tag{6.6}$$

While the relation in Eq. (6.5) with κ real is the basis of temporal analyses, taking Eq. (6.6) with ϖ real is the practice in spatial analyses. Note that the positive root sign in Eq. (6.6) has been adopted as it gives the relevant physical solution here. The negative root sign is associated to a "viscous" wave that propagates contrary to the sign of a and is infinitely damped as μ approaches zero. In fact, this wave is simply non-existent in the case of pure advection. Moreover, this alternative solution is unbounded at $x \to \infty$ and is generally considered inadmissible in the solution of the model problem in question [20]. As this alternative solution also does not appear in the numerical results discussed in the present study, it will be disregarded hereinafter.

Although the real and imaginary parts of Eq. (6.6) can be obtained analytically [20], these can be easily evaluated numerically from the formula above. It is also worth mentioning that the advection/diffusion characteristics of temporal waves, i.e. Eq. (6.2) with Eq. (6.5), and spatial waves, i.e. Eq. (6.2) with Eq. (6.6), are generally different. This is because, for complex-valued functions like $\varpi = \varpi(\kappa)$ and $\kappa = \kappa(\varpi)$, the difference between their real/imaginary parts does not amount to a simple swap of Cartesian axes. Some relations can nevertheless be drawn between these two, see e.g. [21].

Regarding CG's eigenanalysis, it is useful to start from the eigenvalue relation corresponding to the semi-discrete advection-diffusion problem in one dimension, which has been derived in [1] and reads

$$-i\varpi h\,\vec{u} = \boldsymbol{\Gamma}(\kappa h)\,\vec{u}\ , \tag{6.7}$$

where h is the (constant) mesh spacing employed and $\boldsymbol{\Gamma}$ is a square matrix of size $m(\mathrm{CG}) = P$, which is the number of (independent) element-wise degrees of freedom, P being the polynomial order. In the temporal approach, for each real κh given, m complex values for ϖh are obtained directly through the eigenvalues of $\boldsymbol{\Gamma}$. In the spatial approach, however, obtaining complex-valued κh from a given real ϖh requires the solution of a determinant problem, such as

$$\det\left[\,\boldsymbol{\Gamma}(\kappa h) + i\varpi h\,\mathcal{I}\,\right] = 0\ , \tag{6.8}$$

in which $\mathcal{I}$ is the identity matrix of the required size. A slight restructuring of the above has been found to help with the numerical evaluation of its roots, as follows. Matrix $\boldsymbol{\Gamma} = \boldsymbol{\Gamma}(\kappa h)$ is defined in Eq. (24) of Ref. [1] as

$$\boldsymbol{\Gamma} = 2\left[\boldsymbol{\mathcal{L}_M}\,e^{-i\kappa h} + \boldsymbol{\mathcal{C}_M} + \boldsymbol{\mathcal{R}_M}\,e^{+i\kappa h}\right]^{-1}\left[\boldsymbol{\mathcal{L}_X}\,e^{-i\kappa h} + \boldsymbol{\mathcal{C}_X} + \boldsymbol{\mathcal{R}_X}\,e^{+i\kappa h}\right]\ , \tag{6.9}$$

where matrices $\boldsymbol{\mathcal{L}}_{(\cdot)}$, $\boldsymbol{\mathcal{C}}_{(\cdot)}$ and $\boldsymbol{\mathcal{R}}_{(\cdot)}$ above stem either from the mass matrix $\boldsymbol{M}$ or from matrix $\boldsymbol{X}$, which incorporates advection/diffusion effects and depend on the Péclet number $\mathrm{Pe} = ah/\mu = hr$, see [1] for details. Inserting Eq. (6.9) into Eq. (6.8) and rearranging yields

$$\det\left[\left(z^{-1}\boldsymbol{\mathcal{L}_X} + \boldsymbol{\mathcal{C}_X} + z\,\boldsymbol{\mathcal{R}_X}\right) + i\frac{\varpi h}{2}\left(z^{-1}\boldsymbol{\mathcal{L}_M} + \boldsymbol{\mathcal{C}_M} + z\,\boldsymbol{\mathcal{R}_M}\right)\right] = 0\ , \tag{6.10}$$

where $z = \exp(i\kappa h)$. The above has been solved numerically for complex-valued z through MATLAB's function *newtzero*. No more than two roots have been found for each real ϖh, corresponding to: (i) the physical component that matches Eq. (6.6) for small ϖh, and (ii) a spurious component associated to e.g. variations in mesh spacing. Similar results have been found for DG schemes, as reported in [22, 14].

At this point, it is convenient to mention that Eq. (6.9) can also account for an SVV term which is introduced in the formulation as a modified diffusion operator. This is done by a simple adaptation in matrix $\boldsymbol{X}$, which consequently affects matrices $\boldsymbol{\mathcal{L}_X}$, $\boldsymbol{\mathcal{C}_X}$, and $\boldsymbol{\mathcal{R}_X}$, see Sec. 3 of Ref. [1] for details. This adaptation basically incorporates SVV's (normalized) kernel entries. These define the relative intensity in which SVV affects different polynomial modes (when written in a suitable hierarchical basis). While unit kernel entries recover the regular second-order diffusion operator, SVV kernels are designed to affect mainly the higher order modes. This usually amounts to kernel entries increasing from zero to one, so that higher order modes are more strongly damped. These entries are then scaled by SVV's base viscosity μ_{SVV}, from which a Péclet number $\mathrm{Pe} = ah/\mu_{SVV}$ is also defined. The spatial eigenanalysis of linear advection with added SVV will be discussed in Sec. 6.4.

The root-finding algorithm employed in the solution of Eq. (6.10) benefits from a reasonable guess for the root's location. Nevertheless, it is always possible to try random guesses for z until the desired solution is obtained. It is important to note that MATLAB's function *newtzero*, for instance, typically returns the physical and spurious solutions for z altogether for each given ϖh. To avoid scrambling these two solutions, it is useful to track them separately. This can be done by realising that physical and spurious solution components are expected to have opposite amplification behaviours, as will become clear in Sec. 6.3. Fortunately, this information is encapsulated in the absolute value of $z = \exp(i\kappa h)$, as

$$z = \exp\left[i\,\Re(\kappa h)\right]\exp\left[-\Im(\kappa h)\right] \;\therefore\; \Im(\kappa h) \gtrless 0 \;\Leftrightarrow\; |z| \lessgtr 1 \;, \tag{6.11}$$

where $\Re(\cdot)$ and $\Im(\cdot)$ stand for the real and imaginary parts of a complex number. Employing the above is useful because it bypasses the numerical difficulties of inverting the complex exponential function in order to access the imaginary component of κh. One can be sure that a physical root has been found by checking whether $|z| < 1$. Random guesses for a physical solution can be generated, for instance, through the expression $z = r_1 \exp(2\pi i r_2)$, where r_1 and r_2 are real numbers within $(0, 1)$. These same criteria can be used for the spurious roots if one considers Eq. (6.10) with an inverted definition for z, i.e. $z = 1/\exp(i\kappa h) = \exp(-i\kappa h)$. Such sign change guarantees that the spurious root found through this strategy will have an absolute value smaller than unity. This spurious root will obviously have to be inverted subsequently if one is to store the actual spurious root of Eq. (6.10) for a given ϖh.

Once the (two) sequences of complex z values are obtained for the chosen range of ϖh, dispersion-diffusion curves can be generated by plotting $\Re(\kappa h)$ and $\Im(\kappa h)$ versus ϖh. However, while the latter can be readily obtained as $\Im(\kappa h) = -\ln|z|$, the former invariably requires using a (multi-valued) complex logarithm function, as $\Re(\kappa h) = -i\ln(z/|z|)$. It is therefore advisable that dispersion curves are carefully adjusted so as to avoid mistakes in complex phase estimates (usually seen as discontinuities on dispersion curves). Note that admissible corrections in $\Re(\kappa h)$ have to be a multiple of π. To verify whether any correction is in fact justifiable, it is worth checking the derivative of κh

with respect to ϖh, which can be evaluated without ambiguity. This can be done by noting that

$$z = \exp(i\kappa h) \;\Rightarrow\; \frac{dz}{d(\varpi h)} = i\,\frac{d(\kappa h)}{d(\varpi h)}\,z \;\Rightarrow\; \frac{d(\kappa h)}{d(\varpi h)} = -\frac{i}{z}\frac{dz}{d(\varpi h)}\ , \tag{6.12}$$

where the rightmost derivative can be approximated numerically for a physical or spurious root z as

$$\frac{dz}{d(\varpi h)} \approx \frac{z|_{\varpi h+\epsilon} - z|_{\varpi h-\epsilon}}{2\epsilon}\ , \tag{6.13}$$

in which ϵ is a sufficiently small variation in ϖh. In particular, the real part of $d(\kappa h)/d(\varpi h)$ will indicate whether the slopes of dispersion curves have been evaluated correctly. With the above guidelines, fully continuous dispersion-diffusion curves have been obtained for physical and spurious modes. These are discussed in the following two sections.

6.3 Eigencurves for linear advection-diffusion

This section addresses the spatial eigencurves of the continuous Galerkin method for the linear advection-diffusion problem. The Péclet number $\text{Pe} = ah/\mu$ mentioned in Sec. 6.2 is the main parameter to be varied. It represents the ratio between advective and diffusive effects and can be thought of as a local Reynolds number based on the mesh spacing h. As the eigencurves considered here are defined uniquely by P and Pe, it is useful to follow [1] and work instead with the equivalent pair of variables P and $\text{Pe}^* = a\hbar/\mu$, the latter being the Péclet number based on a DOF length scale ($\hbar = h/m(\text{CG}) = h/P$). This will allow for a fair comparison between eigencurves with usual DOF-based normalization.

To begin with, case $\text{Pe}^* = 10$ can be considered, as it represents an intermediate Péclet number such that neither advective or diffusive effects alone dominate the character of the problem [1]. Fig. 6.1 shows the corresponding dispersion and diffusion curves for $P = 1, \ldots, 5$, with physical modes shown in blue and spurious ones in red. Due to viscous effects, the reference results (dashed curves) are not straight lines, but are given by the real and imaginary parts of Eq. (6.6). It is worth stressing the presence of a spurious reflected mode whose diffusion levels decrease slowly as the polynomial order is increased. It is interesting to see that the overall accuracy of the results (on a per DOF basis) do not change significantly with P, which contrasts with results obtained e.g. for DG [22, 14]. Nevertheless, it is clear that the frequency range of say, negligible diffusion error, is larger for $P = 5$ than for $P = 1$. The diffusion curve of case $P = 2$ seems to benefit from the fact that, as the eigencurve begins to leave its expected low-error frequency range (say, beyond $\varpi\hbar \approx 1.5$), it fortuitously "deviates" to the correct direction and ends up extending the frequency range of negligible diffusion error until about $\varpi\hbar \approx 2.5$, therefore surpassing what is achieved with higher orders (on a per DOF basis). This fortuitous behaviour of discretisation $P = 2$ changes, however, with the Péclet number and does not hold anymore at, e.g. $\text{Pe}^* = 5$ or $\text{Pe}^* = 20$ (not shown).

The limit of negligible viscosity is considered in Fig. 6.2, which shows case $\text{Pe}^* = 1000$ for $P = 1, \ldots, 5$. This figure bears a striking resemblance with Fig. 3 of Ref. [14], which shows DG's linear advection eigencurves in the limit of hyper-upwinding (i.e. strong over-upwinding). Interestingly,

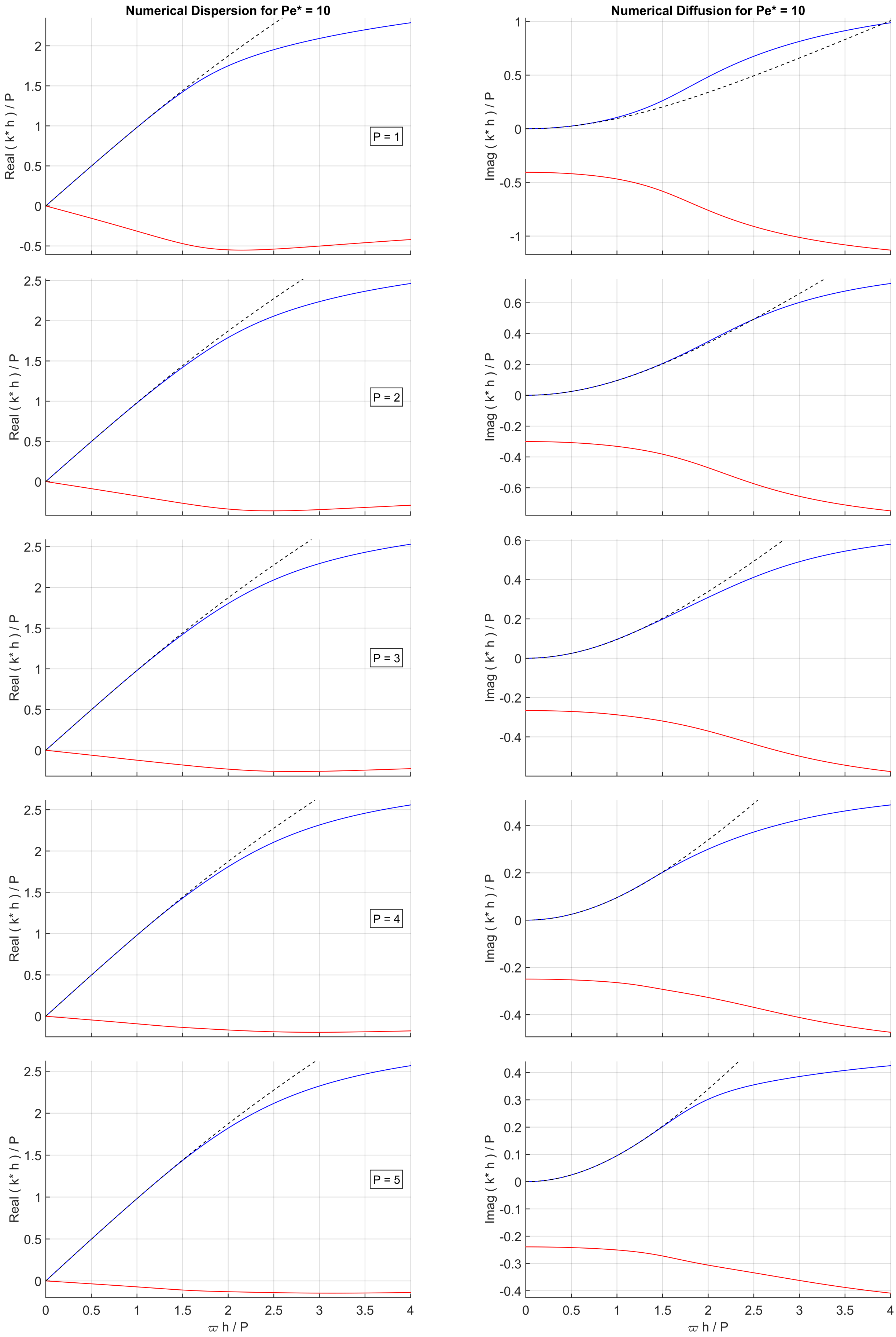

Figure 6.1: Numerical dispersion (left) and diffusion (right) curves for CG-based linear advection-diffusion with $\mathrm{Pe}^* = 10$ and $P = 1, \ldots, 5$ (top to bottom). Dashed curves show the exact advection-diffusion behaviour at this Pe^*.

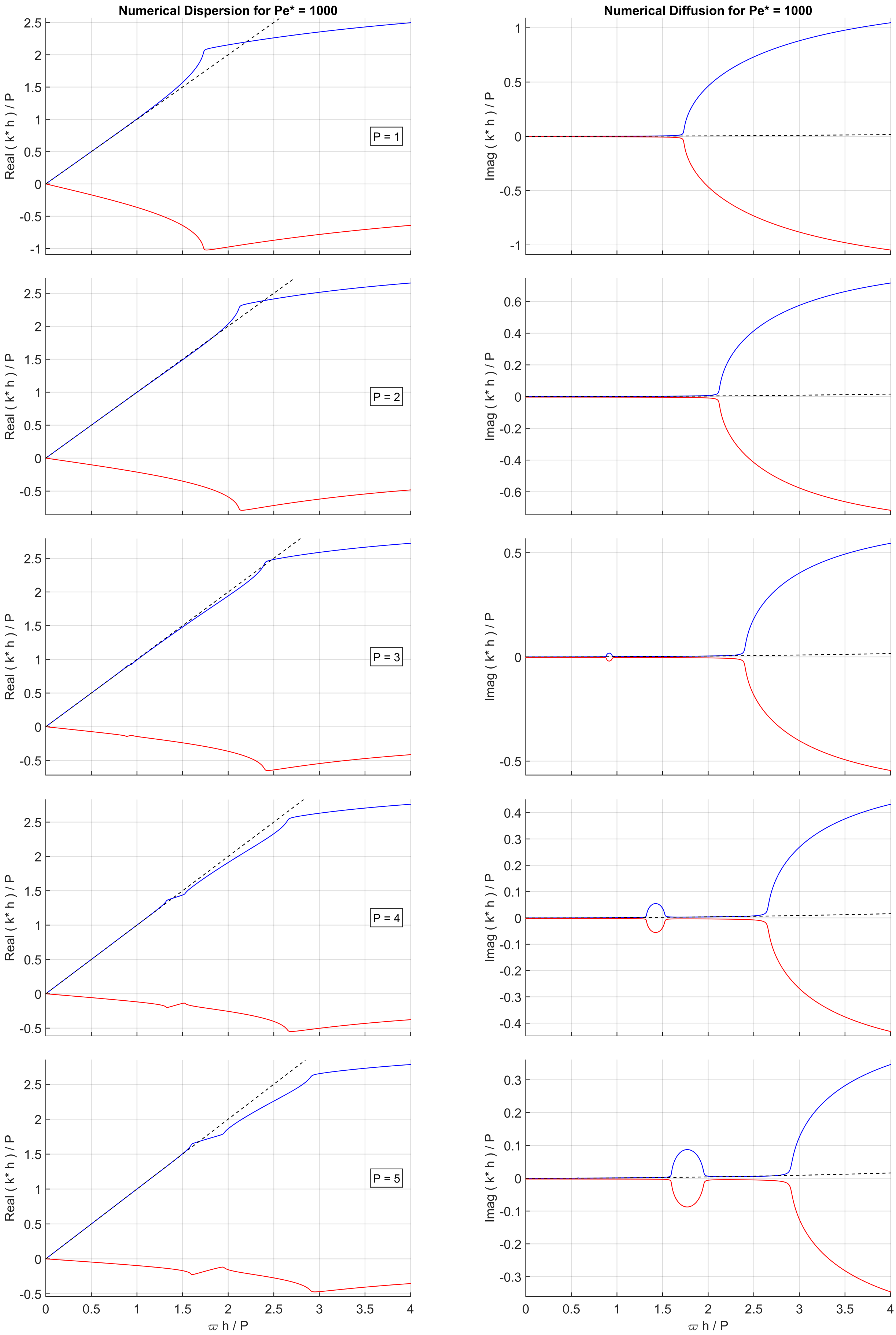

Figure 6.2: Numerical dispersion (left) and diffusion (right) curves for CG-based linear advection-diffusion with $\mathrm{Pe}^* = 1000$ and $P = 1, \ldots, 5$ (top to bottom). Dashed curves show the exact advection-diffusion behaviour at this Pe^*.

this has been found to be more than mere resemblance. In fact, these figures have been verified to match exactly upon superposition (not shown) of the real and imaginary parts of $\kappa^{*}h$ vs. ϖh, i.e. when the normalizing factors $m(\mathrm{CG}) = P$ and $m(\mathrm{DG}) = P + 1$ are dropped. This implies that the dispersive/dissipative behaviour of inviscid CG matches that of hyper-upwind DG for the same mesh and polynomial order — for linear advection. This equivalence of behaviours makes clear that the interface continuity condition enforced in CG does not always corresponds to a fully central discretisation and can even introduce numerical dissipation. One should stress, however, that the inviscid CG limit is in fact similar to a dissipation-free central discretisation in the setting of temporal eigenanalysis [1]. This fundamental difference highlights that spatial and temporal frameworks concern essentially different types of physical problems. For spatially developing flows, it seems that CG's interface solution is much more strongly influenced by upstream conditions (upwind character).

While still in Fig. 6.2, note that case $P = 2$ exhibits again particularly accurate characteristics for its physical mode, with a significant frequency range of negligible numerical error. However, CG's inviscid limit, as DG's hyper-upwind limit, features spurious reflected modes subjected to very small damping. This is useful information for CG-based under-resolved turbulence computations (of spatially developing flows) at high Reynolds numbers, as it suggests that spurious reflections around regions of variable mesh spacing might interact with incoming turbulent structures, affecting solution quality and numerical robustness, as will be discussed in Sec. 6.5. Another feature observed in CG's inviscid limit is the presence of dissipation bubbles (for $P > 2$) that are likely to induce non-smooth dissipative features in under-resolved computations. For example, a sufficiently strong dissipation bubble might cause a "dissipative valley" in the (streamwise) energy spectrum of spatially developing turbulent flows. The effect of a dissipation bubble is illustrated next in a simple numerical example.

A one-dimensional simulation conducted on a mesh with two grid blocks is now considered. The first block covers the initial portion of the domain ($0 \leq x \leq 0.36$) and is composed of elements of size $h_1 = 0.01$. The second block covers the remainder of the domain and consists of a coarser grid with $h_2 = 0.04$. Advection velocity and viscosity values are set to $a = 1$ and $\mu = 10^{-5}$, respectively. The polynomial order is chosen to be $P = 4$, leading to $\mathrm{Pe}^{*} = 10^{3}$ in the second block of the domain. The relevant eigencurves for this polynomial order and Péclet number can be found in Fig. 6.2 and feature a dissipation bubble around $\varpi\hbar \approx 1.4$. Finally, three frequency values are considered for the boundary condition at $x = 0$, defined as $u_0 = 1 + \sin(\omega t)$. The adopted frequencies lead to $\varpi\hbar$ values of 1.2, 1.42 and 1.6 (for the second grid block), corresponding to three test cases named (a), (b) and (c), respectively. These are illustrated in Fig. 6.3, which shows the three cases marked on the relevant diffusion eigencurve (top-left plot) and the associated solutions after a long integration time (after transient effects). In the solution plots, a vertical red line indicates the station after which grid spacing becomes coarser. Case (b), although of intermediate frequency, has the strongest damping factor for the transmitted wave owing to the effect of the dissipative bubble. Spurious reflections can also be seen very clearly for case (b). Note that the first mesh block features a different Péclet value (and different $\varpi\hbar$ values) due to its finer mesh spacing. Added SVV can help to suppress dissipative bubble effects and also increases the damping of spurious modes, as will be discussed in Sec. 6.4.

The scenario where viscosity dominates is now discussed. This high-viscosity limit is considered

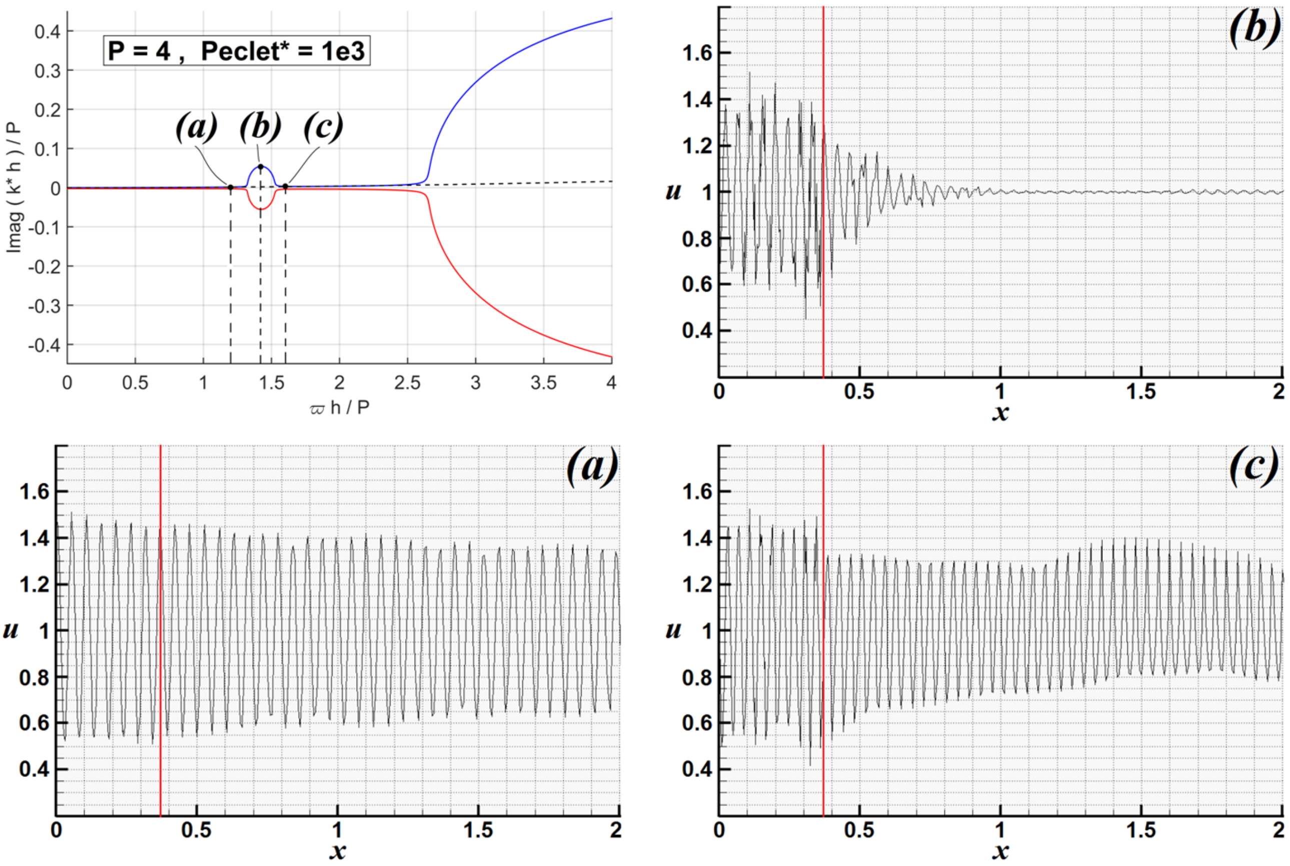

Figure 6.3: Numerical experiment demonstrating the effect of dissipative bubbles for $P = 4$. Three inlet frequencies are tested, corresponding to cases (a), (b) and (c) as shown in the top-left plot. The intermediate frequency case (b) has the strongest damping factor for the transmitted wave.

in Fig. 6.4, which shows case $\mathrm{Pe}^* = 0.1$ for $P = 1$ and $P = 5$. The results of intermediate orders are omitted because the eigencurves change very little as P is varied. Also, eigencurves remain practically unchanged as Pe^* is further reduced, indicating that the limit of viscous-dominated propagation has already been reached. Although curves in Fig. 6.4 might appear to be somewhat dull, it is important to note that both dispersion and diffusion eigencurves are practically exact regardless of the polynomial order. This may be useful information for CG-based computations of (spatially developing) turbulent boundary layers when the viscous sub-layer is to be resolved. As Fig. 6.4 indicates, there is negligible gain in employing higher-order discretisations and therefore one might benefit from using a lower order very close to the wall if the algorithms employed are more efficient computationally at lower orders. This would of course require more elements for a given number of DOFs. Further away from the wall, one is however likely to benefit from higher-order discretisations due to their improved resolution power per DOF (larger range of scales with low numerical error). Therefore, more efficient strategies for this type of flows would most likely require use of variable polynomial order across the domain.

Finally, it is useful to consider how the inviscid and the high-viscosity limits are connected through intermediate Péclet numbers. Fig. 6.5 illustrates how the eigencurves of case $P = 2$ change as Pe^* grows from 0.5 to 0.99 (top plot), then from 1.01 to 2 (centre plot) and finally from 3 to 100 (bottom plot). We note that the first ($\mathrm{Pe}^* = 0.5$) and last ($\mathrm{Pe}^* = 100$) eigencurves shown in

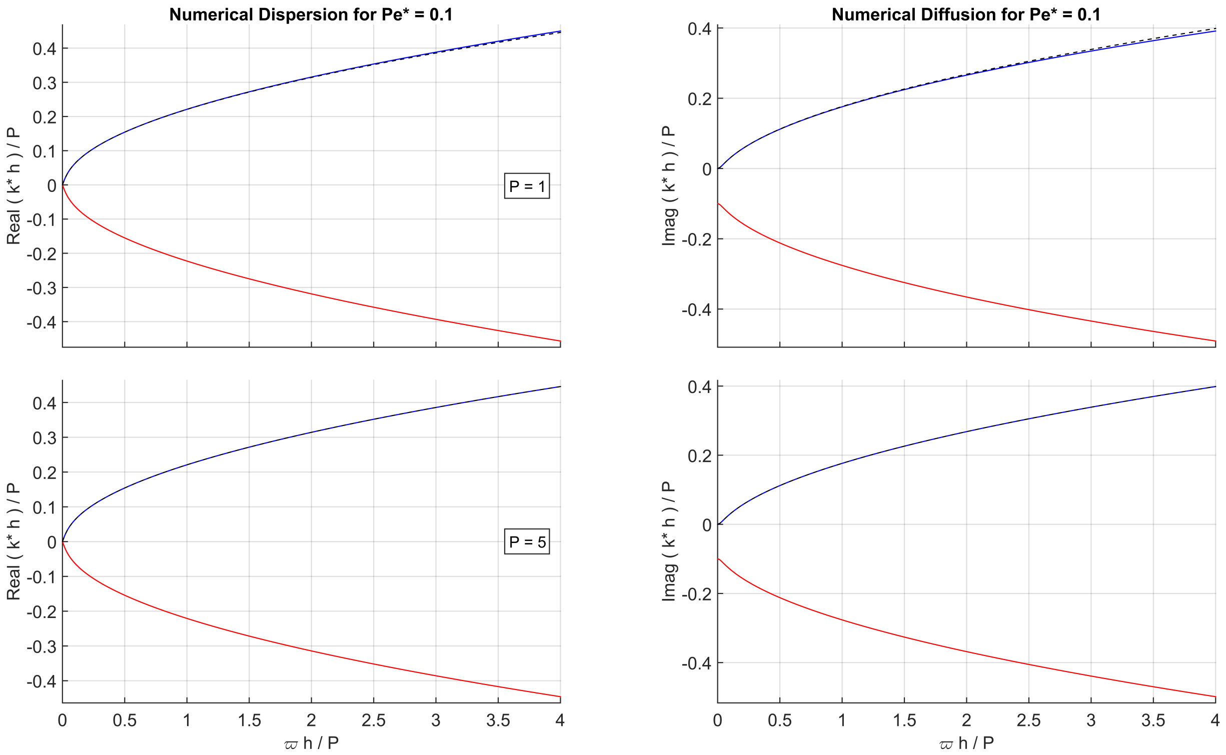

Figure 6.4: Numerical dispersion (left) and diffusion (right) curves for CG-based linear advection-diffusion with $\mathrm{Pe}^* = 0.1$ for $P = 1$ (top) and $P = 5$ (bottom). The dashed curves indicate the exact advection-diffusion behaviour at this Pe^*.

Fig. 6.5 can be compared respectively to those shown in Figs. 6.4 and 6.2 for $P = 2$. The variation of the physical mode, shown in blue in Fig. 6.5, is somewhat straightforward. Its dispersion curves essentially bend upwards as Pe^* grows. The diffusion curves initially shift upwards (top plot), then start to change this trend (centre plot) and finally bend downwards (bottom plot).

The behaviour of the spurious mode, shown in red in Fig. 6.5, is more involved. Its dispersion curve starts to bend downwards at higher frequencies (top plot) and forms a steep negative slope around $\varpi\hbar \approx \sqrt{5}$ (discussed further ahead) as Pe^* approaches unity from below. Eigencurves are generated with greater difficulty near $\mathrm{Pe}^* = 1$ as the roots of the associated characteristic polynomial are more difficult to track. Nevertheless, soon after this "barrier", dispersion curves are found to flip upwards (centre plot) and reach positive values of $\Re(\kappa^* h)$. The abrupt slope variations do not result from a mistake in complex phase estimate as has been carefully verified through the strategy discussed at the end of Sec. 6.2. As Pe^* is further increased, dispersion curves become flatter and the frequency range for which $\Re(\kappa^* h) > 0$ is enlarged, eventually reaching the origin. The diffusion curves remain always negative and form a cusp-like profile (top and centre plots) as case $\mathrm{Pe}^* = 1$ is approached. In the limit, the cusp reaches increasingly stronger diffusion levels (not shown) and waves of frequency around $\varpi\hbar \approx \sqrt{5}$ are infinitely damped, i.e. the spurious mode ceases to exist around this frequency. As Pe^* is further increased (bottom plot), dispersion curves bend downwards and become negative again for all frequencies. The associated diffusion curves shift upwards, indicating weaker damping of the reflected spurious mode, as expect from CG's inviscid limit.

The results obtained for $P = 2$ could have been obtained analytically as the relevant eigenmatri-

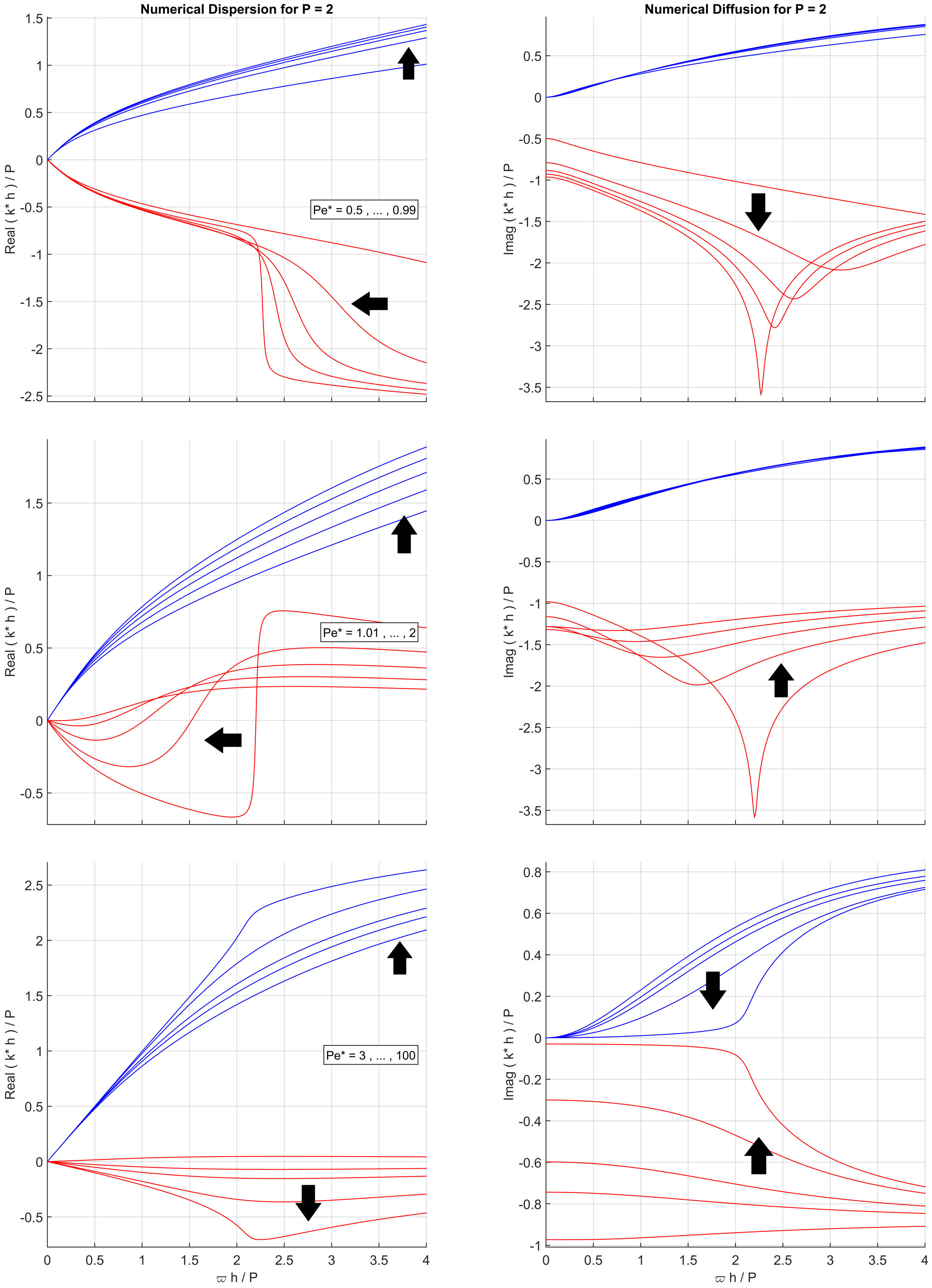

Figure 6.5: Numerical dispersion (left) and diffusion (right) curves for CG-based linear advection-diffusion with $P = 2$ and Pe^* varying from 0.5 to 0.99 (top), 1.01 to 2 (centre) and 3 to 100 (bottom). Arrows are used to indicate the direction of increasing Pe^* for each set of curves.

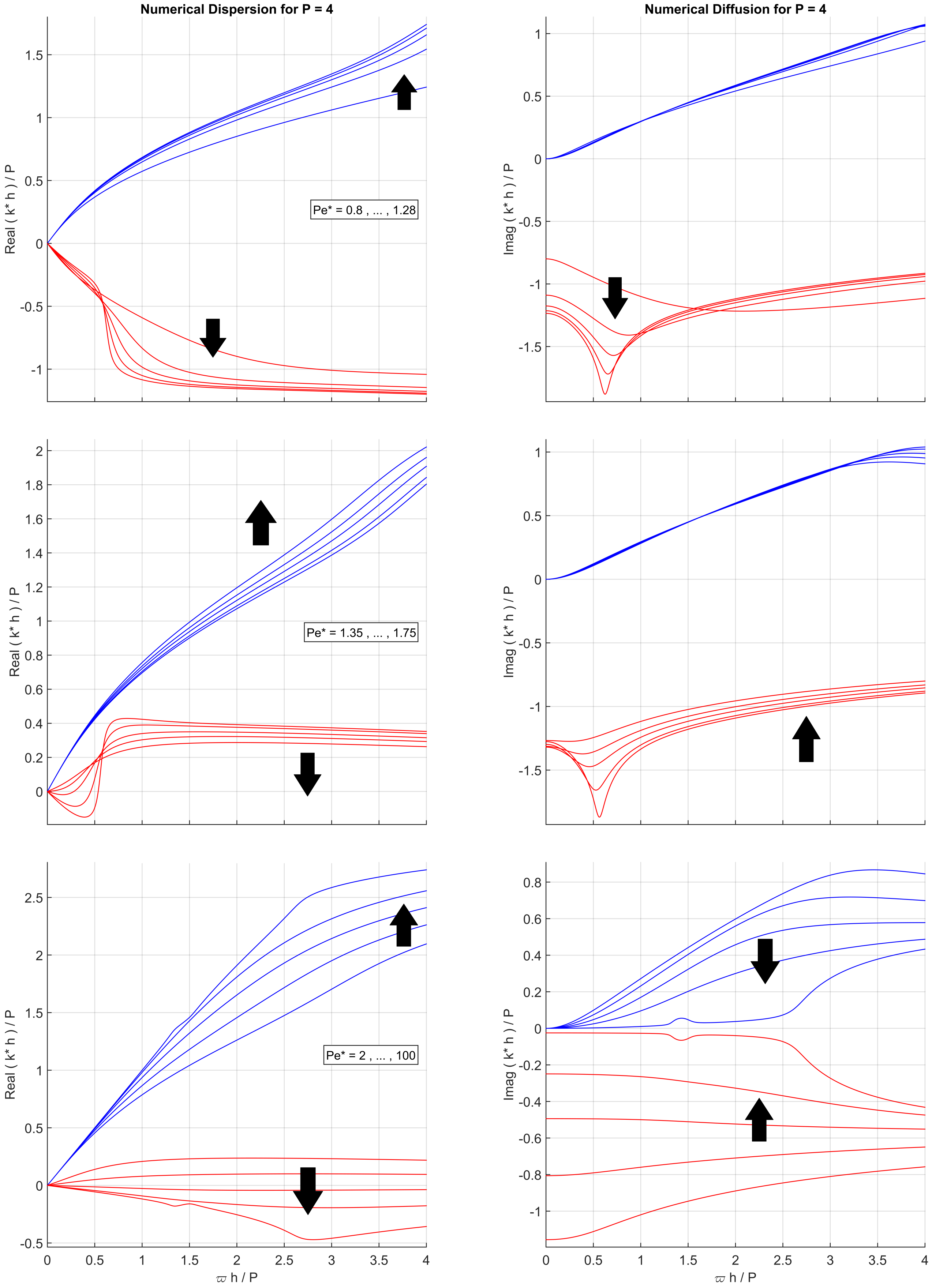

Figure 6.6: Numerical dispersion (left) and diffusion (right) curves for CG-based linear advection-diffusion with $P = 4$ and Pe^* varying from 0.8 to 1.28 (top), 1.35 to 1.75 (centre) and 2 to 100 (bottom). Arrows are used to indicate the direction of increasing Pe^* for each set of curves.

ces, cf. Sec. 6.2, are of size 2 × 2. In particular, case $\mathrm{Pe}^* = 1$ can be handled without computational algebra packages due to certain symmetries of the associated characteristic polynomial. The analytical solution found for $P = 2$ and $\mathrm{Pe}^* = 1$ is given by

$$z = \frac{3\,(\varpi h)^2 + 52i\,(\varpi h) - 80 \pm \sqrt{8\left[(\varpi h)^4 + 41i\,(\varpi h)^3 - 378\,(\varpi h)^2 - 1080i\,(\varpi h) + 450\right]}}{(\varpi h)^2 - 20}\,, \quad (6.14)$$

where $z = \exp(i\kappa h)$. The relation above makes clear that the abrupt slope variation discussed previously happens at $\varpi h = \sqrt{20}$, or equivalently, at $\varpi\hbar = \sqrt{5}$. The plots generated from this analytical solution (not shown) confirmed that the diffusion eigencurve of the spurious mode in fact tends to minus infinity at $\varpi\hbar = \sqrt{5}$, but is otherwise similar to the cusp-like profile shown in Fig. 6.5 for $\mathrm{Pe}^* = 0.99$ or $\mathrm{Pe}^* = 1.01$. Interestingly, the corresponding dispersion curve, although not defined at $\varpi\hbar = \sqrt{5}$, shows no abrupt slope variation and resembles an "average" between the dispersion profiles of cases $\mathrm{Pe}^* = 0.99$ or $\mathrm{Pe}^* = 1.01$, following after $\varpi\hbar = \sqrt{5}$ the trend expected since the beginning of the curve, as if there was effectively nothing especial about this point.

The trends observed in Fig. 6.5 are not restricted to $P = 2$. In fact, very similar trends have been found for $P = 4$, as shown in Fig. 6.6. The main difference is that the "critical" Péclet number across which dispersion curves flip from negative to positive values is $\mathrm{Pe}^* \approx 1.32$, while the frequency at which this happens is $\varpi\hbar \approx 0.6$. The behaviours observed for odd polynomial orders (not shown) is similar except for the fact that dispersion eigencurves flip at the origin, instead of at a finite frequency value — this has been verified for $P = 1, 3$ and 5. For these cases, once the flip occurs, positive values of $\Re(\kappa^* h)$ will exist for all frequencies. Nevertheless, as Pe^* is further increased, dispersion curves eventually change sign again. The critical Péclet numbers at which the dispersion flip takes place have been found to be, for $P = 1, 3$ and 5, respectively $\mathrm{Pe}^* \approx 2, 1.55$ and 1.46.

Despite the more involved behaviour of the dispersion curves of spurious modes, changes in $\Re(\kappa^* h)$ are somewhat inconsequential in practice. Originally, positive $\Re(\kappa^* h)$ values for the spurious mode were thought to indicate transmitted (instead of reflected) waves. In that case, negative $\Im(\kappa^* h)$ values for a transmitted spurious mode would mean amplification in space, i.e. a convectively unstable spurious wave. However, after some experimentation, those have not been found in practice. It seems that spurious modes correspond always to reflected waves, the sign of $\Re(\kappa^* h)$ only affecting their phase and shape in space. This can be understood directly from Eq. (6.2), which can be rewritten as

$$u \propto \exp\left[\,-\Im(\kappa)\,x\,\right]\,\exp\left\{i\left[\,\Re(\kappa)\,x - \omega\,t\,\right]\right\}. \quad (6.15)$$

Note that, for example, when $\Re(\kappa^* h)$ is approximately zero (see e.g. in Fig. 6.5 the spurious dispersion curve of case $P = 2$ for $\mathrm{Pe}^* \gtrsim 3$), the reflected wave is expected to decay monotonically in space, oscillating only in time. Such wave would however be strongly damped (note the large dissipation of the spurious mode at the referred Pe^* value), making its observation difficult in practice. On the other hand, positive or negative values of $\Re(\kappa^* h)$ for the spurious mode are only expected to affect its phase and its oscillatory character in space.

6.4 The inviscid limit and SVV stabilization

This section addresses the issues encountered with CG's eigencurves in the limit of very high Péclet (or Reynolds) numbers, namely, dissipative bubbles and the vanishing dissipation of spurious modes. The linear advection equation will be considered with SVV-based stabilization, which has the potential to suppress the aforementioned issues. As in Sec. 6.3, the parameters defining the eigencurves are the polynomial order P and the Péclet number (now based on SVV's base magnitude), $\mathrm{Pe}^* = a\hbar/\mu_{SVV}$. In addition, here the normalized kernel entries defining the SVV operator also impact the eigencurves, as explained in Sec. 6.2. It is important to stress that the constant Péclet SVV approach proposed in [1] is adopted here. This approach basically prescribes that SVV's base magnitude μ_{SVV} is to be made proportional to $a\hbar$ in order to keep SVV's reference Péclet number fixed. More specifically, one is to set $\mu_{SVV} = \mu_0 a\hbar$, whereby $\mathrm{Pe}^* = \mu_0^{-1}$ is kept constant throughout the computational domain. This reference Péclet number is set to one (hence $\mu_0 = 1$) in this section, and thus SVV's kernel entries are the only remaining parameters defining the eigencurves for each polynomial order.

The question of how much artificial viscosity is to be added in general is a difficult one because a given test case might require low diffusion levels for accuracy reasons whereas another case might be prone to instabilities and require stronger stabilization. As a result, the SVV operator designed here takes the dissipation levels of DG as reference, since, among many high-order schemes, DG is arguably robust and yet weakly dissipative at higher orders. The possibility of using optimization algorithms to match SVV's dissipation to that of DG has been explored in [1] in the context of temporal eigenanalysis. Here, an optimization is conducted for the spatial analysis and complements the results discussed in [1]. Originally, the optimizations performed in this study aimed at matching DG's dissipation curves using regular plots of $\Im(\kappa^* h)$ vs. ϖh, having in mind the different polynomial normalizing factors used for CG and DG, namely $m(\mathrm{CG}) = P$ and $m(\mathrm{DG}) = P + 1$. In addition, relying on log-log scales for the plots proved to be very important. This is because the low dissipation levels observed at small ϖh would otherwise lack appropriate weight in the optimization process. Matching these low dissipation values turned out to be critical for the accuracy of spatially developing flows involving physical instabilities and transition, as those discussed in Sec. 6.5.

Matching DG dissipation levels proved to be difficult due to the fact that CG's dissipative bubbles, which become much more prominent in log-log scale plots, overlap the relevant DG curves. This can be seen in Fig. 6.7, which shows dissipation curves for CG-based advection-diffusion (without SVV) at $\mathrm{Pe}^* = 10^{10}$ with $P = 3$ (left) and $P = 7$ (right) compared against DG's standard upwinding dissipation curves for P, $P - 1$ and $P - 2$ (colour). As the bubbles shown do not vanish as viscosity is reduced to zero, it is clear that adding SVV will not remove them. Hence, Fig. 6.7 essentially demonstrates that it is not possible to match same-order dissipation curves exactly. Another difficulty originated from the fact that SVV diffusion levels obtained in the optimization process were not steep enough to match same-order DG curves. It is possible that the slopes achieved by DG in Fig. 6.7, related to DG's super-convergent scaling of $\Im(\kappa^* h) \propto (\varpi h)^{2P+2}$ for small ϖh [23], are simply too steep to be matched by SVV.

The alternative adopted here was to match the dissipation curves of CG with SVV stabilization of order P to those of DG of order $P - 2$. This was not only achievable through the optimization

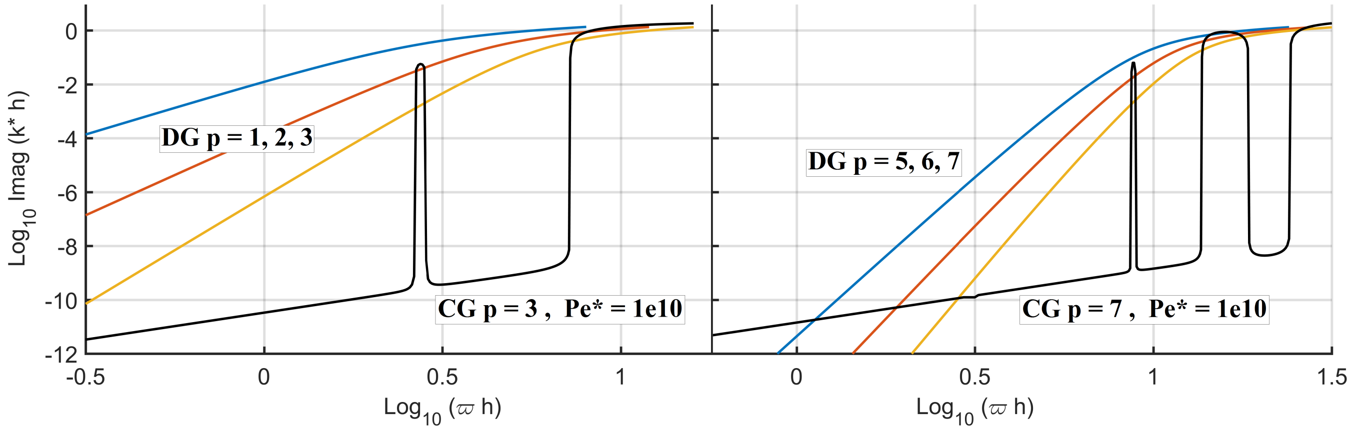

Figure 6.7: Dissipation curves in log-log scale for CG-based advection-diffusion at $\mathrm{Pe}^* = 10^{10}$ with $P = 3$ (left) and $P = 7$ (right) compared to DG dissipation for P, $P-1$ and $P-2$ (colour).

procedure, but also solved the issue of CG's dissipative bubbles. The latter were naturally covered by the dissipation levels typical of DG at order $P-2$, as can be anticipated from Fig. 6.7. The kernel entries obtained from the optimization process for different polynomial orders are given below. The corresponding optimized dissipation curves are shown in Fig. 6.8. Note that focus is given to higher-order discretisations ($P > 2$), which are the ones requiring more stabilization.

- $P = 3 :\ 0, 0.70546, 0.078836, 1$
- $P = 4 :\ 0, 0, 0.49411, 0.072394, 1$
- $P = 5 :\ 0, 0, 0.0000735, 0.40506, 0.094122, 1$
- $P = 6 :\ 0, 0, 0, 0.0001422, 0.36863, 0.11815, 1$
- $P = 7 :\ 0, 0, 0, 0, 0.00019497, 0.41397, 0.16927, 1$
- $P = 8 :\ 0, 0, 0, 0, 0, 0.0009762, 0.12747, 0.13763, 1$
- $P = 9 :\ 0, 0, 0, 0, 0, 0, 0.0023592, 0.23683, 0.17196, 1$
- $P = 10 :\ 0, 0, 0, 0, 0, 0, 0, 0.0026055, 0.28682, 0.22473, 1$

A first point deserving some comments is the non-monotonic behaviour of the kernel entries above, as intuition indicates that this should also yield non-monotonic dissipation curves. Although it is not clear at this point why this is not the case here, a possible explanation is that SVV needs only to provide a dissipation distribution to fill the gap between the (monotonic) DG curve of order $P-2$ and that of inviscid CG of order P, which features (non-monotonic) bubbles. Another important point is that matching was performed mostly for the regions of constant slope in log-log plots, as will be described below. This caused the dissipation levels that are more evident in linear scale plots (right-hand side of Fig. 6.8) to be basically a by-product of the optimization process. However, the matching at higher frequencies does not need to be perfect, and the fact the CG dissipation levels in this range were typically stronger than expected is actually good for robustness.

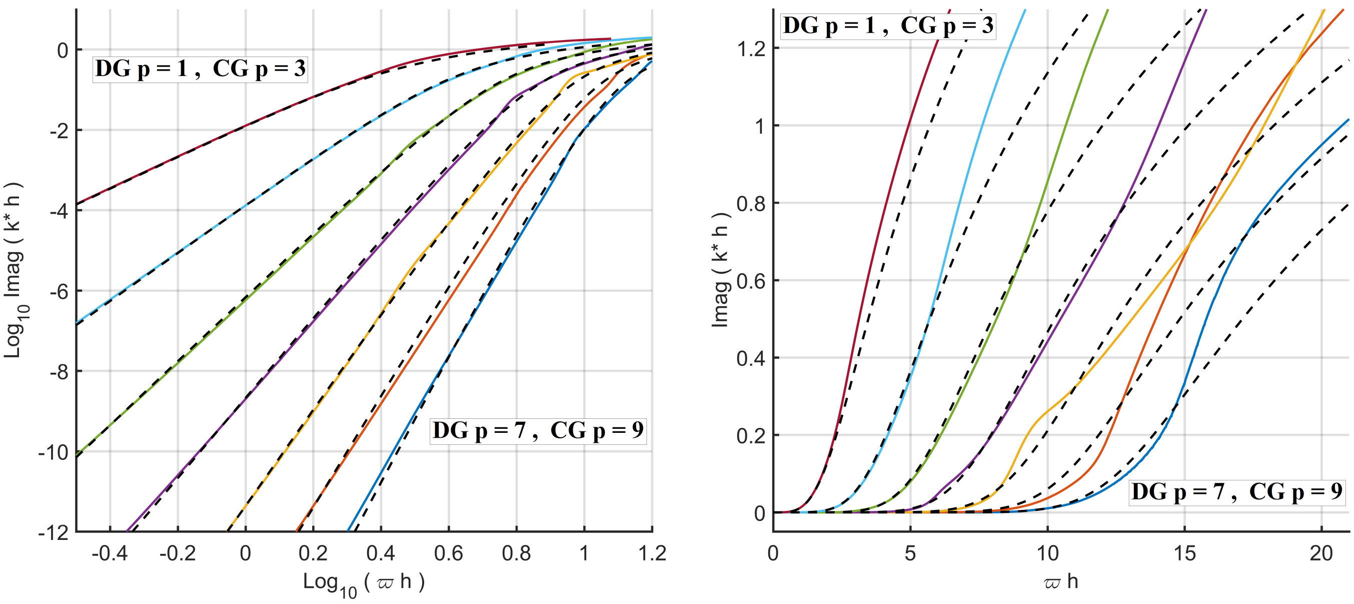

Figure 6.8: Comparison between optimized CG-SVV dissipation (colour) for $P_{CG} = 3, \ldots, 9$ and their reference DG curves (dashed) for $P_{DG} = 1, \ldots, 7$. The polynomial order of the curves increases from left to right in both the log-log (left) and bilinear (right) plot.

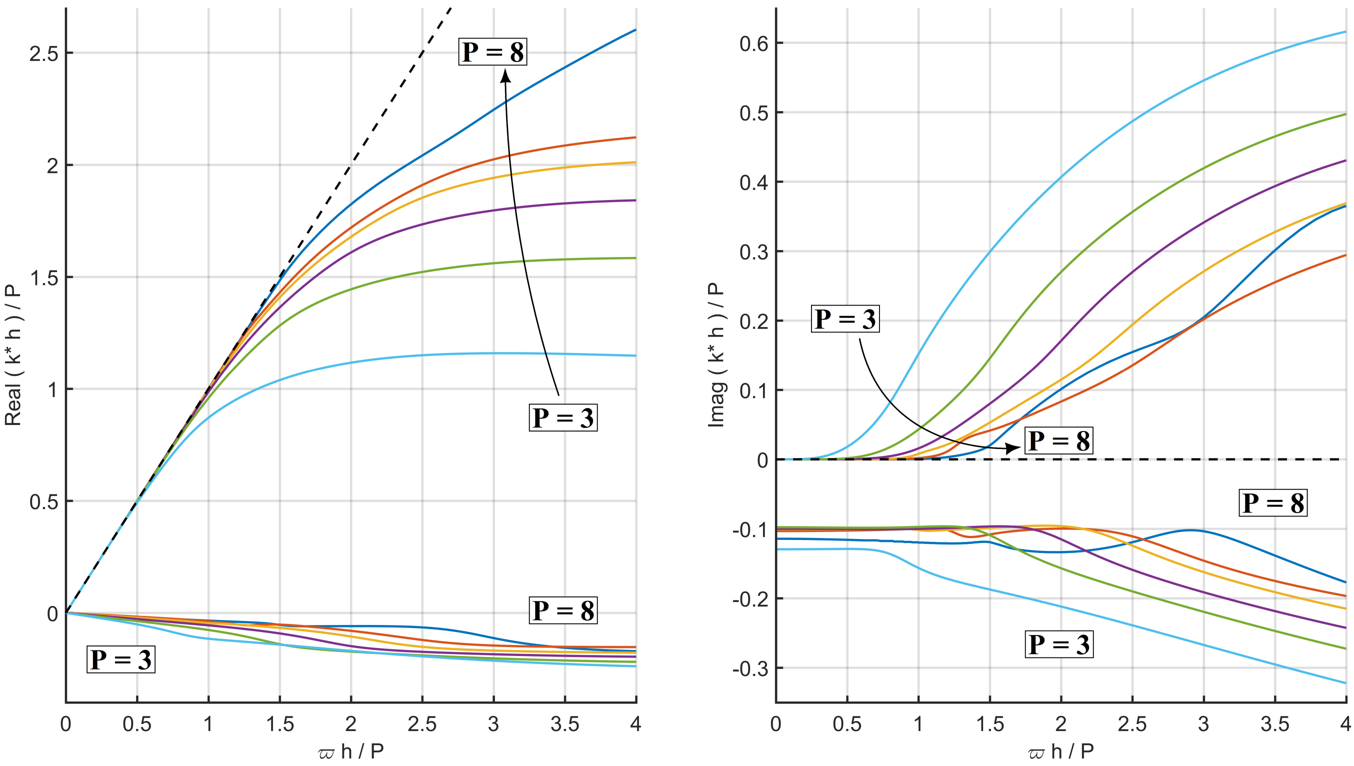

Figure 6.9: Numerical dispersion (left) and diffusion (right) characteristics of the CG-SVV approach proposed for $P = 3, \ldots, 8$. Results are shown on the usual DOF-based plots and indicate superior resolution power per DOF at higher polynomial orders (arrows).

The optimization procedure conducted consisted essentially in minimizing the distance between a reference DG curve and that yielded by a trial SVV kernel at a set of equispaced points along the DG curve. Their position covered mostly the region of constant slope (in log-log plots) for each DG curve. The number of points was chosen to be twice the number of free kernel entries for each case. Note that the first entry is always zero for a proper SVV operator, whereas the last one is a (unit) dummy entry that actually does not affect the eigencurves [1]. Hence, the CG discretisation with $P = 3$, for example, had only two free kernel entries to be adjusted. Optimization was performed via MATLAB's global optimization toolbox. Different algorithms have been tested, but the best results were achieved with the so-called particle swarm approach, see e.g. [24], through MATLAB's function *particleswarm*. At this point, it is worth explaining why the unit Péclet number ($\mathrm{Pe}^* = \mu_0^{-1} = 1$) was chosen for the SVV operators considered in this study. It happens that the SVV characteristics are actually defined by the product between μ_0 and the kernel entries. However, the optimal entries found were observed to be inversely proportional to whichever value of μ_0 was set for the optimization. For example, when optimizations were performed with $\mu_0 = 10$, the optimal kernel entries obtained were exactly ten times smaller than the ones tabulated previously, resulting in the same dissipation curves. Hence, the reference Péclet value adopted for the SVV is not important in itself, and the unit value has only been chosen here for simplicity.

The optimized SVV operators obtained with the proposed approach were found to improve discretisation robustness significantly, as will be discussed in Sec. 6.5. The accuracy at moderate orders was however not so good due to the fact that DG dissipation curves of order $P - 2$ were used as reference. For example, CG at $P = 3$ had the dissipation levels of DG order $P = 1$, which are know to be too large e.g. for under-resolved turbulence computations [10, 25]. Nevertheless, at higher polynomial orders, much smaller dissipation levels are achieved and the CG-SVV approach proposed becomes suitable for high-fidelity simulations.

Finally, the dispersion/diffusion eigencurves obtained with the optimized SVV operators are shown in Fig. 6.9 with the usual DOF-based plots. These indicate that a superior resolution power (based on the extent of the frequency range of negligible error) is achieved on a per DOF basis as the polynomial order is increased, for both dispersion and diffusion. An additional condition used in the optimization process was the penalization of eigencurves whose dissipation values of the spurious mode were too small. More specifically, a requirement of $\Im(\kappa^* \hbar) < -0.1$ was set for the spurious modes. This of course made more difficult the attainment of low dissipation levels for the physical modes. The threshold of -0.1 was considered sufficiently strong to damp reflected waves over a short distance, based on the experiments conducted in connection with Fig. 6.3. The optimized SVV operators are tested against more physical test cases in the next section.

6.5 Numerical experiments in under-resolved vortical flows

This section is devoted to the simulation of spatially developing vortex-dominated flows as a means to assess the fidelity and robustness of high-order CG discretisations with and without SVV. This is a preliminary step towards the assessment of CG-based computations of transitional and turbulent flows and should provide some insight into the scheme's behaviour for under-resolved computations. A model problem is considered that mimics to a certain degree a grid turbulence flow evolving inside a duct in a two-dimensional setting. This test case was originally proposed for DG in Ref. [14] and consists of a rectangular domain with inflow/outflow boundary conditions on the sides and free-slip wall conditions on the top and bottom boundaries. All simulations have been conducted with the incompressible Navier-Stokes solver of spectral/*hp* element code *Nektar++* [26].

The adopted model problem relies on inlet boundary conditions that mimic a passive generator of eddies. This produces large-scale vorticity that propagates into and along the domain. Inflow conditions for the streamwise and cross-flow velocity components and for the pressure are set respectively as $u = 1 + 0.5\,\sin(5y)\,\sin(t)$, $v = 0$ and $\partial p/\partial x = 0$, where x and y denote the Cartesian coordinates in the streamwise and cross-flow directions and t stands for the time. The domain top and bottom boundaries are situated at $y = \pm\pi$ and are assigned the conditions $\partial u/\partial y = 0$, $v = 0$ and $\partial p/\partial y = 0$. Finally, the outlet is placed 20π length units apart from the inlet and is subjected to the conditions $\partial u/\partial x = 0$, $\partial v/\partial x = 0$ and $p = 0$. All the results shown here correspond to solutions obtained after a temporal span of one hundred time units, allowing for the (unit) mean velocity of the flow to sweep the streamwise extension of the domain approximately 1.5 times.

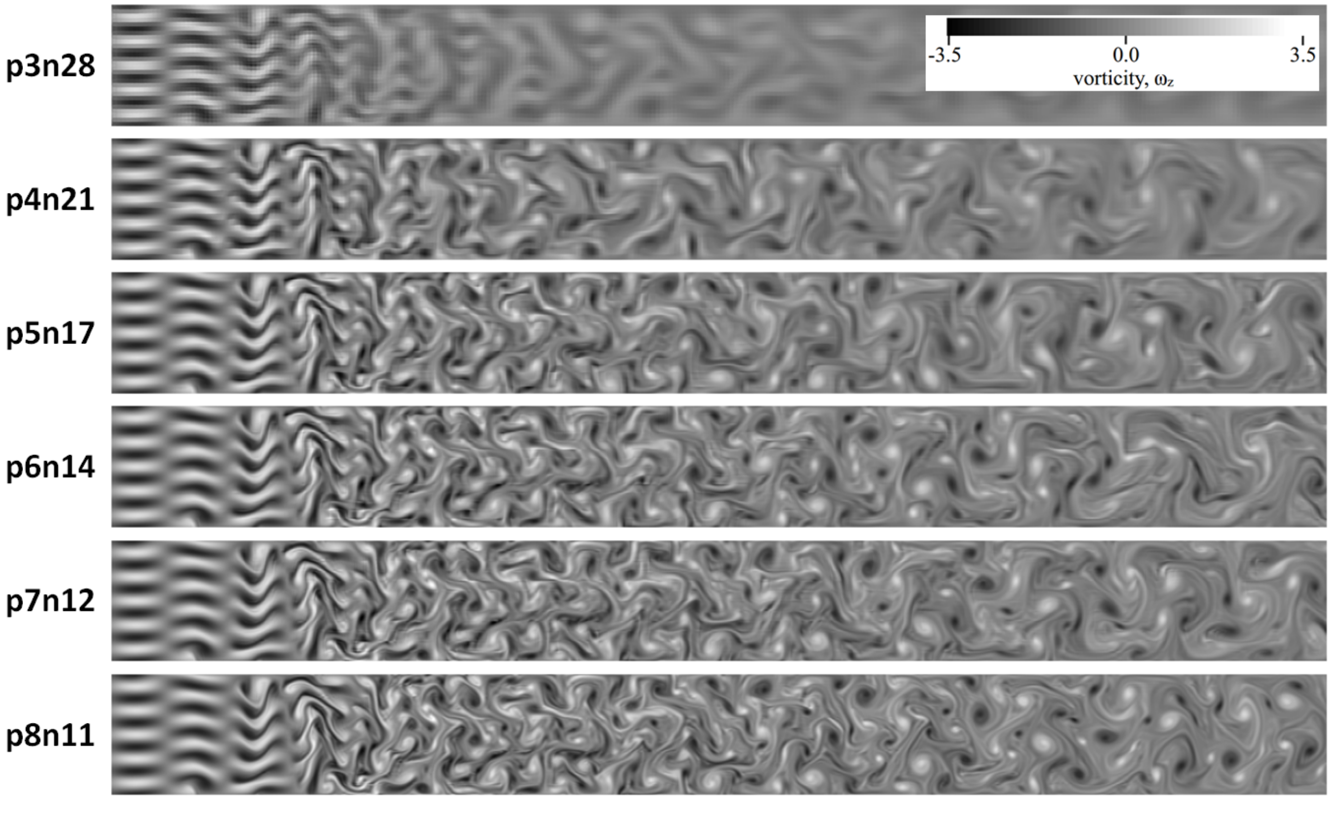

Figure 6.10: Vorticity contours of same-DOF test cases for uniform meshes with various polynomial orders ($P = 3, \ldots, 8$) at Re $= 1.5 \times 10^4$. Increased resolution is achieved with higher orders.

The SVV implementation adopted the optimized kernel entries discussed in Sec. 6.4, although the reference Péclet number was kept only approximately constant as the streamwise velocity was assumed to be the same (and equal to its unit mean value) throughout the flow. More specifically, SVV's base magnitude was set to $\mu_{SVV} = h/P$, where h is the local grid spacing in the streamwise direction. This was done to avoid a non-linear SVV operator of more complex implementation in this initial stage of testing. The base set of test cases consisted of uniform (equispaced) meshes of square-shaped elements, although cases of variable grid spacing have also been considered, as discussed further below. Test cases of polynomial order P with N elements in the cross-flow direction (hence 10 N elements in the streamwise direction) are denoted as "pPnN". The Reynolds number of the test cases was defined based on the (unit) flow mean velocity, the length scale $\pi/5$ representing the size of the inlet eddies, and the fluid's viscosity. The latter is varied to control the Reynolds number in the simulations.

All the test cases conducted without SVV lacked numerical stability and crashed as the Reynolds number was increased. In contrast, when SVV was introduced, all test cases became stable regardless of the Reynolds number. This is not surprising given the robust dissipation characteristics of DG reproduced by the optimized SVV operators. Obviously, for each given case, the solution at sufficiently high Reynolds "saturates" and remains practically unchanged as the fluid's viscosity is further decreased. This is because SVV dissipation effects eventually become more significant than those of molecular viscosity. This scenario resembles that of e.g. under-resolved DG computations in the limit of vanishing viscosity, where upwind dissipation remains alone to provide small-scale regularization [10, 27, 14]. In case of saturation, higher fidelity results will require an increased number of elements or a higher polynomial order. It should be stressed that, for a given number of DOFs, discretisations of higher order (and fewer elements) are to be preferred. This has been confirmed for a set of test cases with (approximately) the same number of DOFs for $P = 3, \dots, 8$, as shown in Fig. 6.10. These cases are conducted at a Reynolds number of $\mathrm{Re} = 1.5 \times 10^4$ and are nearly saturated considering the reduced number of DOFs employed. Increased resolution power is clearly achieved with higher orders thanks to the optimized SVV operators, cf. Fig. 6.9. It should be stressed that, without SVV, higher-order cases crashed at Reynolds numbers as low as 1500 due to instabilities developed around the "transitional" flow region near the inlet. Similar instabilities occurred for the lower order cases, although those took longer distances to form inside the domain. Case p3n28, for example, crashed slightly after $\mathrm{Re} = 5000$.

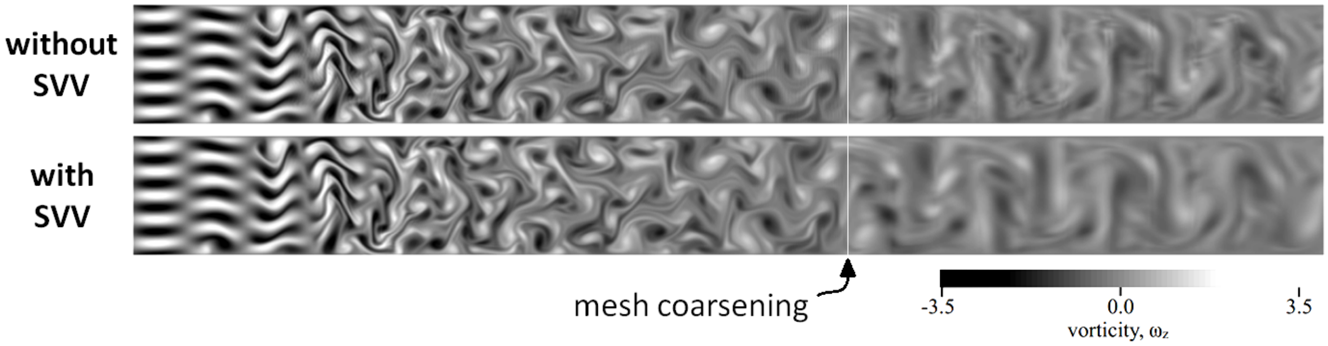

Figure 6.11: Vorticity contours of case p8n11 at $\mathrm{Re} = 1000$ with and without SVV when a four times larger streamwise spacing is used after the first 60% of the domain. Closer examination reveals that SVV is able to suppress spurious reflections from the interface of mesh spacing discontinuity.

Test cases conducted with mesh coarsening beyond a certain station of the domain have also been considered. It was difficult to find numerical instabilities specifically related to spurious reflections because the test cases without SVV are already unstable at low Reynolds numbers, when the damping of spurious modes is not negligible. Note that, for cases without SVV, the (mean) local Péclet value for uniform mesh regions (square-shaped elements) can be expressed as $\mathrm{Pe}^* = \mathrm{Re}/P$. Vorticity contours of case p8n11 at Re = 1000 with and without SVV are shown in Fig. 6.11 when mesh coarsening is applied after the first 60% of the domain. For this case, streamwise spacing becomes four times larger for the domain's second block, whereas cross-flow spacing remains unchanged. Without SVV, reflections are very mild due to the low Reynolds number and can hardly be noticed even in vorticity contours, which rely on velocity gradients and hence tend to highlight numerical oscillations. Nevertheless, a closer look reveals the positive effect of SVV in suppressing spurious reflections without significantly affecting solution quality. Note that case p8n11 is unstable without SVV beyond the considered Reynolds number.

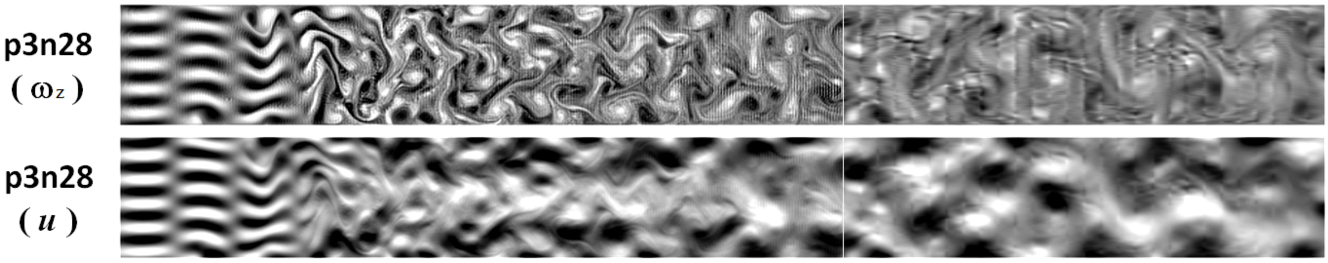

Figure 6.12: Contours of vorticity and streamwise velocity for case p3n28 at Re = 5000 without SVV. Mesh coarsening is applied after station 60%. Colour bars are the same of Fig. 6.11, except that for the velocity contours its values range from 0.5 (black) to 1.5 (white).

Case p3n28 is stable without SVV at a higher Reynolds and is now considered with the same type of mesh coarsening mentioned above to demonstrate how reflections become more prominent as molecular viscosity is further reduced. Contours of vorticity and streamwise velocity for case p3n28 at Re = 5000 (without SVV) are given in Fig. 6.12. These clearly highlight the adverse effect of spurious reflections on solution quality at higher Reynolds numbers. Adding SVV does suppress reflections, but also damps most of the relevant flow scales due to the lower order in question, as can be anticipated from Fig. 6.10. The sensible approach to high-fidelity under-resolved computations at high Reynolds is therefore to employ higher polynomial orders along with moderately coarse grids, so as to avoid spurious waves while retaining a superior resolution power.

6.6 Conclusion

This study addressed the spatial eigenanalysis of spectral/*hp* continuous Galerkin (CG) methods as applied to the linear advection-diffusion equation and to the advection equation with added spectral vanishing viscosity (SVV). The work was motivated by two previous studies, namely, one that considered CG's temporal eigenanalysis [1] and another that addressed the spatial analysis of DG schemes [14]. Here, the influence of viscous effects have been assessed through the variation of the so-called Péclet number, which can be regarded as a numerical Reynolds number based on the local mesh size. A spurious wave mode associated to unphysical reflections was found to exist no matter the Péclet number and was discussed in detail. The stabilization of CG at large Péclet numbers was also discussed, and a novel SVV strategy was proposed for spatially developing flows. This strategy was tested on a two-dimensional vortex-dominated model problem designed to approximate the behaviour of a grid turbulence flow. The test cases addressed supported the excellent potential of the proposed approach, especially at higher polynomial orders, for under-resolved computations of transitional and turbulent flows.

In the spatial eigenanalysis, the inviscid (large Péclet) limit received particular attention due to residual dissipative effects with peculiar characteristics found to exist in this limit. More specifically, “dissipation bubbles” were observed for certain frequency ranges. Those are expected to induce undesirable non-smooth diffusion features on CG-based under-resolved simulations of spatially developing flows at high Reynolds numbers. Moreover, the damping of spurious reflected eigenmodes was found to become negligible in the inviscid limit for a large range of frequencies. As these also have the potential to negatively affect solution quality, an SVV-based stabilization approach was sought that could suppress the adverse effects of dissipative bubbles and spurious reflections. This lead to an optimization strategy that matched SVV diffusion levels to those of (standard upwind) DG at a lower order. Due to the fact that DG dissipation curves were too steep (in log-log scale) owing to DG’s super-convergent behaviour [23], the optimization process employed was not able to match dissipation levels of same polynomial order. The achievable alternative was to match CG-SVV diffusion levels at order P to those of DG at order $P-2$. This however naturally solved the issue of dissipative bubbles, given that the optimized SVV diffusion levels were sufficient to overcome those of the bubbles, resulting in smooth dissipation curves for the proposed CG-SVV discretisation.

The optimized SVV operator was tested in the final part of the study, which addressed CG’s performance for spatially developing under-resolved vortical flows. While test cases without SVV lacked numerical stability even at low Reynolds numbers, those relying on SVV remained stable even in the limit of vanishing viscosity. Although discretisations of lower order (e.g. third polynomial order) were found to be excessively diffusive, higher order results displayed excellent performance. In fact, increasing the polynomial order rapidly recovered the superior resolution capabilities of high-order DG [10, 27, 14], while at the same time suppressing unphysical features such as spurious reflections. This highlighted the strong numerical potential that appropriately stabilized spectral/*hp* CG methods have for high-fidelity simulations of transitional and turbulent flows at high Reynolds numbers. The analysis of how physical under-resolved CG numerical solutions can be (as a function of the DOFs used) with the proposed SVV operator is left for future studies, where test problems such as those considered in Refs. [28, 29] might be employed.

References

[1] R. C. Moura, S. J. Sherwin, and J. Peiró. Eigensolution analysis of spectral/*hp* continuous Galerkin approximations to advection-diffusion problems: insights into spectral vanishing viscosity. *Journal of Computational Physics*, 307:401–422, 2016.

[2] J. A. Ekaterinaris. High-order accurate, low numerical diffusion methods for aerodynamics. *Progress in Aerospace Sciences*, 41(3):192–300, 2005.

[3] Z. J. Wang. High-order methods for the Euler and Navier-Stokes equations on unstructured grids. *Progress in Aerospace Sciences*, 43(1):1–41, 2007.

[4] S. K. Lele. Compact finite difference schemes with spectral-like resolution. *Journal of Computational Physics*, 103(1):16–42, 1992.

[5] C. Bogey and C. Bailly. A family of low dispersive and low dissipative explicit schemes for flow and noise computations. *Journal of Computational Physics*, 194(1):194–214, 2004.

[6] F. Q. Hu, M. Y. Hussaini, and P. Rasetarinera. An analysis of the discontinuous Galerkin method for wave propagation problems. *Journal of Computational Physics*, 151(2):921–946, 1999.

[7] K. Van den Abeele, T. Broeckhoven, and C. Lacor. Dispersion and dissipation properties of the 1D spectral volume method and application to a p-multigrid algorithm. *Journal of Computational Physics*, 224(2):616–636, 2007.

[8] K. Van den Abeele, C. Lacor, and Z. J. Wang. On the stability and accuracy of the spectral difference method. *Journal of Scientific Computing*, 37(2):162–188, 2008.

[9] P. E. Vincent, P. Castonguay, and A. Jameson. Insights from von Neumann analysis of high-order flux reconstruction schemes. *Journal of Computational Physics*, 230(22):8134–8154, 2011.

[10] R. C. Moura, S. J. Sherwin, and J. Peiró. Linear dispersion-diffusion analysis and its application to under-resolved turbulence simulations using discontinuous Galerkin spectral/*hp* methods. *Journal of Computational Physics*, 298:695–710, 2015.

[11] G. E. Karniadakis and S. J. Sherwin. *Spectral/hp element methods for computational fluid dynamics*. Oxford University Press, 2nd edition, 2005.

[12] E. Tadmor. Convergence of spectral methods for nonlinear conservation laws. *SIAM Journal on Numerical Analysis*, 26(1):30–44, 1989.

[13] R. M. Kirby and S. J. Sherwin. Stabilisation of spectral/hp element methods through spectral vanishing viscosity: application to fluid mechanics modelling. *Computer Methods in Applied Mechanics and Engineering*, 195(23):3128–3144, 2006.

[14] G. Mengaldo, R. C. Moura, B. Giralda, J. Peiró, and S. J. Sherwin. Spatial eigensolution analysis of discontinuous Galerkin schemes with practical insights for under-resolved computations and implicit LES. *Computers & Fluids*, 2017 (under review).

[15] G. S. Karamanos and G. E. Karniadakis. A spectral vanishing viscosity method for large-eddy simulations. *Journal of Computational Physics*, 163(1):22–50, 2000.

[16] R. M. Kirby and G. E. Karniadakis. Coarse resolution turbulence simulations with spectral vanishing viscosity–large-eddy simulations (SVV-LES). *Journal of Fluids Engineering*, 124(4):886–891, 2002.

[17] R. Pasquetti. Spectral vanishing viscosity method for LES: sensitivity to the SVV control parameters. *Journal of Turbulence*, 6(12), 2005.

[18] M. Minguez, R. Pasquetti, and E. Serre. High-order large-eddy simulation of flow over the 'Ahmed body' car model. *Physics of Fluids*, 20(9):095101, 2008.

[19] J.-E. W. Lombard, D. Moxey, S. J. Sherwin, J. F. A. Hoessler, S. Dhandapani, and M. J. Taylor. Implicit large–eddy simulation of a wingtip vortex. *AIAA Journal*, 54(2):506–518, 2016.

[20] J. D. Logan and V. Zlotnik. The convection-diffusion equation with periodic boundary conditions. *Applied Mathematics Letters*, 8(3):55–61, 1995.

[21] M. Gaster. A note on the relation between temporally-increasing and spatially-increasing disturbances in hydrodynamic stability. *Journal of Fluid Mechanics*, 14(02):222–224, 1962.

[22] F. Q. Hu and H. L. Atkins. Eigensolution analysis of the discontinuous Galerkin method with nonuniform grids: I. one space dimension. *Journal of Computational Physics*, 182(2):516–545, 2002.

[23] M. Ainsworth. Dispersive and dissipative behaviour of high order discontinuous Galerkin finite element methods. *Journal of Computational Physics*, 198(1):106–130, 2004.

[24] G. Venter and J. S. Sobieski. Particle swarm optimization. *AIAA Journal*, 41(8):1583–1589, 2003.

[25] G. J. Gassner and A. D. Beck. On the accuracy of high-order discretizations for underresolved turbulence simulations. *Theoretical and Computational Fluid Dynamics*, 27(3-4):221–237, 2013.

[26] C. D. Cantwell, D. Moxey, A. Comerford, A. Bolis, G. Rocco, G. Mengaldo, D. De Grazia, S. Yakovlev, J-E. Lombard, D. Ekelschot, B. Jordi, H. Xu, Y. Mohamied, C. Eskilsson, B. Nelson, P. Vos, C. Biotto, R. M. Kirby, and S. J. Sherwin. Nektar++: An open-source spectral/*hp* element framework. *Computer Physics Communications*, 192:205–219, 2015.

[27] R. C. Moura, G. Mengaldo, J. Peiró, and S. J. Sherwin. On the eddy-resolving capability of high-order discontinuous Galerkin approaches to implicit LES / under-resolved DNS of Euler turbulence. *Journal of Computational Physics*, 330:615–623, 2017.

[28] T. A. Zang and S. E. Krist. Numerical experiments on stability and transition in plane channel flow. *Theoretical and Computational Fluid Dynamics*, 1(1):41–64, 1989.

[29] M. F. Schatz, R. P. Tagg, H. L. Swinney, P. F. Fischer, and A. T. Patera. Supercritical transition in plane channel flow with spatially periodic perturbations. *Physical Review Letters*, 66(12):1579, 1991.

Conclusions

The main question motivating this study concerns the surprising possibility of achieving accurate results in the simulation of transitional and turbulent flows via *model-free* under-resolved computations based on spectral element methods. Given the history of (explicit) large-eddy simulations and their subgrid-scale models based on turbulence physics, it is unsettling that any model-free approach should yield results of similar or even superior quality for the same number of degrees of freedom. As there can be no magic involved, the key to this question must lie on the truncation errors peculiar to spectral element methods. In particular, the behaviour of numerical diffusion / dissipation is the most important aspect that need be investigated, as it defines small-scale regularisation at large Reynolds numbers while also dictating numerical robustness.

Although no-model eddy-resolving approaches to turbulence are not so recent, these originally relied on *low-order* schemes whose truncation errors (typically non-linear second-order diffusion terms) have been shown to resemble subgrid-scale models used in classic large-eddy simulation (LES) strategies. The term implicit LES (iLES) has been coined to describe those approaches in which numerical errors implicitly work as a turbulence model. Despite the fact that this terminology is currently also employed to describe model-free turbulence computations conducted with *high-order* spectral element methods (SEM), the term under-resolved direct numerical simulation (uDNS) is preferred here. This is partially to highlight that no correspondence is anticipated between subgrid-scale models and the truncation errors of SEM, and also because, from a numerical perspective, the term 'under-resolved DNS' describes precisely what model-free SEM-based approaches are. Still, it is difficult to compete with the widespread use of the older terminology 'implicit LES', whereby both terms (uDNS / iLES) are used throughout the thesis so that the relevant community might identify with this work.

The rationale offered for uDNS / iLES approaches based on SEM is the following. Higher-order SEM are know to achieve spectral-like resolution, i.e. a superior eddy-resolving capability similar to that offered by spectral methods. This allows them to take much better advantage of the available degrees of freedom (DOF) when compared to the low-order methods typically used in practical LES applications. Also, their numerical diffusion is introduced by appropriate stabilisation techniques, e.g. spectral vanishing viscosity (SVV) or upwind dissipation, whose effect is only significant at the smallest captured scales which could not be resolved accurately by the DOFs employed. Therefore, when properly stabilised SEM are applied to turbulent flows, a wider wavenumber / frequency range is captured and meaningful results can be expected if a considerable portion of their energy spectrum is resolved. The question as to whether it is better to solve more of the governing equations with a numerically (rather than physically) motivated dissipation or to solve less scales and have a physics-based turbulence model has been answered by numerical experiments. Various comparisons currently available in the literature indicate that high-order SEM-based uDNS / iLES approaches can provide results comparable to those obtained with traditional low-order LES strategies for the same number of DOFs. In some cases, even better results are obtained, e.g. in transitional flows which benefit from very small dissipation levels at the large / intermediate flow scales, or in more complex scenarios of less small-scale homogeneity.

What remains to be established is whether SEM approaches can offer even better results with added subgrid-scale models. So far, this question has received but little consideration by the community, perhaps because the performance of model-free SEM strategies is already very good. While it might seem obvious that added models can only improve upon model-free approaches, it is worth remembering that turbulence models are based on assumptions which are sometimes too restrictive for more complex flow scenarios. Moreover, results obtained with sophisticated modelling based on less restrictive assumptions have to be compared with those yielded by the corresponding model-free approach on a finer mesh, so that the cost of these two computations is the same. In either case, the investigation of *how* to apply model-free SEM-based strategies in order to achieve the best possible results is clearly a priority. This has also been a strong motivation behind this work, which addressed the extent to which solution quality and robustness is affected by the various discretisation variables peculiar to SEM approaches, namely: polynomial order, appropriate mesh spacing, Riemann solvers, SVV design, dealiasing strategies, etc. A summary of such investigations is given below.

Summary of work

Chapter 1 considered the temporal eigensolution analysis of the discontinuous Galerkin (DG) method for the one-dimensional linear advection equation. This allowed for the assessment of dispersion and diffusion errors in a scenario that assumes periodic boundary conditions in space (temporal approach). The linear advection equation is the simplest model problem one can use to investigate the behaviour of numerical schemes in the absence of physical viscosity, which arguably represents the limit of very large Reynolds numbers. A novel interpretation of the eigenanalysis' results was proposed as follows. First, the role of multiple solution eigenmodes (peculiar to high-order SEM) was discussed and a new perspective on the matter was suggested. While previous studies often considered one of the modes as physical and the remaining ones as spurious, the new perspective revealed that all "secondary" modes actually just replicate the numerical characteristics of the primary one, but for a shifted range of wavenumbers. This formally allows one to focus on the dispersive and diffusive behaviour of the primary mode in the assessment of DG and potentially other SEM. Secondly, the numerical diffusion introduced by DG's standard upwinding was appraised and its effect over the poorly-resolved scales was quantified. A simple criterion was then proposed to estimate DG's effective resolution power in terms of the largest wavenumber that can accurately be resolved given mesh spacing and polynomial order. This criterion, named "the 1% rule", relies on the fact that DG's numerical dissipation rises sharply after a certain wavenumber, especially at higher polynomial orders. The 1% rule essentially defines the wavenumber $k_{1\%}$ as that at which propagating waves are scaled by a factor of 0.99

per DOF crossed, thereby separating wavenumber regions of negligible and significant damping. Tests conducted with inviscid Burgers turbulence simulations (in one dimension) confirmed that $k_{1\%}$ closely corresponds to the wavenumber after which a numerically induced dissipation range appears in the simulations' energy spectra. The criterion and its validation tests also showed that improved resolution power is achieved on a per-DOF basis at higher polynomial orders.

Chapter 2 addressed the temporal eigenanalysis of spectral/*hp* continuous Galerkin (CG) methods for the linear advection-diffusion equation in one dimension. The pure advection case was also considered with added spectral vanishing viscosity (SVV), so that the behaviour of CG (with proper stabilisation) could be assessed in the limit of very large Reynolds numbers. The actual parameter representing the ratio between convective and diffusive effects was however the Péclet number, which can be thought of as a Reynolds number based on the local grid spacing. The analysis presented was in fact the first to be offered for high-order CG methods, with the differentiation between primary and secondary eigenmodes (as discussed in Chapter 1) proving to be of fundamental importance. For the advection-diffusion case, the agreement between exact and numerical dispersion / diffusion curves was found to hold over a larger wavenumber range at higher polynomial orders (for a fixed number of DOFs). This is consistent with the superior resolution power achieved by high-order DG schemes on a per-DOF basis. However, in the limits of very large or small Péclet numbers, CG's eigencurves were found to exhibit potentially undesirable non-smooth features such as kinks and discontinuous variations. The former limit is particularly important as it represents high Reynolds numbers. SVV was then added to the linear advection equation and its effects on the issues above were considered. Traditional SVV operators were assessed and shown to display similar issues depending on the local advection velocity and mesh spacing. A novel SVV approach was then suggested based on a fixed Péclet number, so as to avoid the aforementioned issues even in convection-dominated flows. Within this approach, a new SVV kernel function was proposed that guarantees a consistent growth in resolution power per DOF as the polynomial order is increased. An optimisation algorithm was finally used to tune the new SVV parameters in order to match its dissipation levels to those of DG. This indicated that high-order CG schemes, with appropriate SVV stabilisation, have the potential to perform comparably to DG with regards to uDNS / iLES capabilities.

Chapter 3 dealt with DG computations of the inviscid Taylor-Green vortex (TGV) flow, which is a model problem proposed by Taylor and Green in the late 1930's for the analysis of transition to turbulence and subsequent turbulence decay. The inviscid case was chosen for the assessment of DG's performance in the limit of infinite Reynolds number, while also allowing for a direct comparison of various Riemann solvers. The inviscid TGV is however extremely demanding in terms of numerical stability and it's been long conjectured that its exact (Euler-based) energy conserving solution might develop finite-time singularities leading to actual solution collapse. However, DG's upwind dissipation is expected to enforce the entropy-consistent behaviour maintained by the Navier-Stokes equations in the limit of vanishing viscosity, where dissipation remains finite and the possibility of singularities is practically ruled out. In other words, for the inviscid TGV flow, DG-based uDNS / iLES approaches are expected to behave as an LES strategy at very high Reynolds numbers, where molecular viscosity becomes negligible, but the dissipative effect of a subgrid-scale model remains. An extensive set of test cases was considered, with some exhibiting very good performance, others displaying spurious features, and yet others lacking stability and crashing during the transitional flow phase. The latter demonstrated that DG-based uDNS / iLES approaches, even with consistent/over-integration (used in all test cases), might require additional stabilisation at very high Reynolds numbers.

TGV solutions based on complete Riemann solvers achieved better quality (typical energy spectra, physical QR diagrams, etc.) and robustness (crashed less often). Simpler Riemann fluxes induced however a spurious pile-up of small-scale energy in the form of a spectral energy bump, which contaminates solution quality with unphysical noise and also enhances damping at intermediate scales through an intense eddy-viscosity effect. This energy bump was recognised as a strong manifestation of the bottleneck phenomenon, caused by the sharper dissipative behaviour (in wavenumber space) of simplistic Riemann solvers at low Mach numbers. As energy bumps induced by a sharp dissipation have previously been associated with the emergence of an energy-conserving flow character, one can argue that the lack of stability observed for some of the cases might be related to the singularities conjectured for the exact inviscid TGV flow. As crashes occurred only at higher order discretisations, for which dissipation is sharper, finite-time singularities may well be related to the crashes observed, although a deeper investigation is still needed. Finally, the 1% rule (from Chapter 1) was also found to hold in the (stable) TGV solutions simulated, accurately pinpointing the beginning of the dissipation range on measured energy spectra. Agreement was however better for the complete Riemann solvers, which treat different waves consistently and therefore are closer to the standard upwind assumption behind the 1% rule. A simple adaptation was also necessary for three-dimensional spectra, which consisted in multiplying $k_{1\%}$ by $(\sqrt{3}+1)/2$. In summary, this chapter demonstrated the usefulness of one-dimensional linear dispersion / diffusion analysis for three-dimensional turbulent flows. It also showed that, at very large Reynolds numbers, complete Riemann solvers and moderately high polynomial orders (e.g. sixth order discretisations) tend to deliver the best results in terms of solution quality and numerical robustness, assuming consistent integration is used.

Chapter 4 considered CG-based computations of a non-trivial turbulent boundary layer model problem introduced by Spalart in the late 1980's. This problem features rotating free-stream velocity conditions and significant cross-flow effects, while admitting a statistically stationary solution in the rotating frame of reference aligned with the free-stream velocity. Owing to its inherent unsteadiness and reduced small-scale homogeneity, meaningful LES solutions are known to require sophisticated modelling and relatively fine grids. CG-based uDNS / iLES approaches, on the other hand, showed excellent potential for complex wall-bounded turbulent flows by delivering high-quality results with fewer DOFs and even without SVV. A second-order CG discretisation on 32^3 DOFs yielded results similar to those given by a second-order finite difference LES approach with a dynamic Smagorinsky parametrisation on 64^3 DOFs. When more sophisticated models are used in this LES, results close to that of a DNS are achieved. Nevertheless, a similarly improved quality was also obtained with a fifth-order CG discretisation on the same 32^3 DOFs. This performance is attributed to the superior resolution power of high-order CG methods for a given number of DOFs, and also to the lack of modelling assumptions which are sometimes too restrictive for complex flow scenarios. The relatively low Reynolds number of the computations is possibly the reason why stable results were achieved without SVV, although polynomial dealiasing was necessary. Despite the fact that only a few CG test cases were conducted, the excellent potential of CG-based uDNS / iLES approaches for complex wall-bounded turbulent flows was successfully demonstrated. Even better results for a given number of DOFs can be expected via zonal strategies with increased polynomial order near the wall. Although spectral/*hp* CG formulations offer full support to such strategies, this possibility was not explored here and is left for future studies.

Chapters 5 addressed DG's spatial eigensolution analysis for the linear advection equation in one dimension. The spatial framework assumes inflow / outflow type boundary conditions and is therefore complementary to eigenanalyses based on the temporal approach, which assumes periodicity in space. Although the latter is more often found in the literature, both types of analyses are important in the assessment of numerical dispersion and diffusion characteristics. DG's standard upwind discretisation produced well-behaved eigencurves, whose resolution power per DOF increased with the polynomial order. For each of the orders considered, the frequency beyond which a damping factor larger than 1% per DOF crossed sets in was found to practically match the equivalent $k_{1\%}$ value obtained from the temporal analysis. Nevertheless, the rise in dissipation values after this threshold was observed to be much milder and less sharp for the spatial eigencurves, especially at higher polynomial orders. This suggested that the 1% rule is likely to be less effective for high-order DG-based under-resolved computations of spatially developing flows at very high Reynolds numbers, although this necessitates further confirmation. Discretisations of different upwinding levels were also considered, in which case spurious eigenmodes typically associated with unphysical reflections are known to exist. These are likely to affect the solution quality of under-resolved simulations (including simulations of acoustics) based on Riemann solvers that depart from standard upwinding. The limits of vanishing upwind bias (central fluxes) and strong over-upwinding (induced by incomplete Riemann solvers) were shown to feature dissipation bubbles related to non-smooth dissipative characteristics. Also, in both limits, the damping of the spurious mode was found to tend to zero over large frequency ranges, allowing for their unphysical effects to manifest more freely. Finally, numerical experiments were conducted with a two-dimensional model problem proposed to reproduce a (spatially developing) grid turbulence scenario. Different Riemann solvers were tested and localised mesh coarsening was employed to highlight the undesirable effects of spurious reflected modes. These tests confirmed the predictions of the spatial analysis and substantiated the claims that complete Riemann solvers should be favoured along with moderately high polynomial orders for DG-based uDNS / iLES at very high Reynolds numbers.

At last, chapter 6 dealt with the spatial eigenanalysis of CG for the linear advection-diffusion equation in one dimension. CG's behaviour was discussed for various polynomial orders and different Péclet number values, with spurious modes found to exist in all cases. The inviscid (pure advection) limit exhibited dissipation bubbles in the eigencurves of high-order discretisations, which were shown to induce potentially undesirable non-smooth dissipative characteristics. The case of pure advection was also considered with added SVV, whose dissipation levels were tuned via optimisation algorithms to match those of (standard upwind) DG. However, same-order matching proved impossible owing to the presence of dissipative bubbles and also because of the very steep (super-convergent) dissipation slopes achieved by DG. The viable alternative was to match the dissipation curves of CG at order P to those of DG at order $P-2$. This yielded well-behaved eigencurves whose resolution power per DOF increased with the polynomial order (as happens with DG). The damping of spurious modes was also adjusted through the optimisation process to maintain a reasonably strong intensity. Numerical experiments were conducted with the two-dimensional (grid turbulence) test case introduced in chapter 5. Without SVV, these lacked stability even at relatively low Reynolds numbers. With the optimised SVV, however, all simulations were stabilised even at extremely large Reynolds. Excellent eddy-resolving capability was demonstrated at higher polynomial orders, along with the suppression of spurious reflections. This indicated that high-order CG, with appropriate stabilisation, can achieve very good potential for uDNS / iLES of spatially developing flows at large Reynolds numbers.

Future research directions

The theme of the present study is undoubtedly a complex one. It is simply impossible to cover all of its relevant aspects in the timespan of a single doctoral research. The following items compose a list of important topics that need be addressed in the future to further the current understanding about the performance and applicability of SEM-based uDNS / iLES approaches.

- More tests are required in those situations where (explicit) LES strategies are known to perform well, e.g. in the scenarios for which traditional subgrid-scale models have been calibrated. For example, in the very simple case of decaying isotropic turbulence in a triply-periodic box, most works indicated good performance of model-free SEM, but a few others showed poor agreement against reference data. Do SEM-based uDNS / iLES approaches always adapt their dissipation to account for whatever energy transfer is produced by the large scales? Similarly, does the energy spectrum maintain its shape during decay? If yes, why and how? If not, what can be done to correct this? These questions, although very fundamental, still need clarification.

- As the upwind dissipation typically found in discontinuous SEM damps propagating waves on a basis of distance travelled rather than time passed, one can argue that implicit SEM models lack Galilean invariance. The implications of this fact have yet to be investigated. A possible test would be the evolution (both temporal and spatial) of isotropic turbulence in the presence of a background advective stream. Larger advection velocities are likely to induce a stronger damping at all scales, whose impact on solution quality necessitates evaluation.

- Further testing is also required in complex situations for which classical LES models are known to offer an inferior performance. Possible scenarios involve flows featuring non-trivial transition routes and relaminarisation, significant non-equilibrium and massive separation, heat transfer and strong compressibility effects. In these cases, the influence of discretisation variables such as polynomial order, Riemann solvers or SVV design on solution quality has to be investigated in detail. If good results are consistently reproduced and clear guidelines can be offered regarding which discretisation choices are better, dissemination of SEM-based uDNS / iLES will be much facilitated.

- Strategies that improve the robustness of model-free SEM approaches also need further testing. Novel skew-symmetric discretisations and alternative formulations based on entropy variables have been proposed, but their results have yet to be compared in detail against those obtained with consistent / over-integration, both in terms of accuracy and computational cost. Note that the inviscid Taylor-Green vortex problem considered in chapter 3 was an extreme case, as the vast majority of cases are likely to be stabilized by proper dealiasing. Moreover, the activation and extent of over-integration can be made adaptive with the aid of under-resolution sensors. This could reduce considerably the cost of polynomial dealiasing in practical applications.

- For compressible flows involving shocks, specific techniques such as filtering, artificial viscosity or limiters are needed. These have also been developed for high-order SEM, but in the presence of turbulence, additional care is necessary. This is because the techniques in question should not affect the turbulent scales significantly. So far, very few studies have considered this topic. Since SVV can also be added to compressible solvers, one could certainly consider its application in a type of hyperviscosity-based shock capturing strategy (which is not unheard of).
- As in solutions featuring shocks, turbulent flow computations also benefit from adaptive mesh refinement. Output-based refinement strategies can be developed for those situations in which the extent of turbulent regions is not know a priori (e.g. separated flows). These could rely on element-wise estimators since high-order elements gather significant information. For instance, the ratio between numerical and physical (molecular) dissipation within each element could be estimated so that refinement is applied to regions of large ratios, until these are maintained below a given threshold over the whole turbulent domain. Alternatively, a dynamic polynomial order adaptation procedure could be employed throughout the domain in those cases of strong unsteadiness.
- For complex applications, hexahedral elements are less often used. Prisms are usually employed in near-wall regions and tetrahedra are used elsewhere. Only a few studies have considered the impact of mesh topology on the accuracy of SEM-based uDNS / iLES approaches. This is a very important topic if the methods in question are to be applied to complex problems of industrial interest. Further investigation is required, for example, to estimate how much resolution power can be achieved with different types of elements.
- Due to the elevated cost of turbulence computations, practitioners are often tempted to use the largest time step allowed by the stability constraints of the temporal discretisation. However, the truncation errors of the discrete time-stepping process affect the numerical dispersion and diffusion characteristics of SEM (not to mention stability). Although these can be estimated via fully discrete eigenanalyses, this topic has received little attention so far, despite its relevance to the field.
- Wall-turbulence computations, very important to engineering and atmospheric sciences, should benefit from near-wall zonal refinement strategies. In the context of high-order SEM, these can be implemented by using layers of higher-order elements close to the wall. Away from the wall, but still within the boundary layer, lower-order elements can be employed so as to reduce the number of DOFs along wall-parallel planes. Only a few studies have considered this possibility for SEM-based uDNS / iLES. This technique is estimated to produce significant computational

savings, especially at large Reynolds numbers, by reducing the total number of DOFs for wall-bounded turbulent flows.

- Finally, due to the considerable cost of wall-resolved computations of turbulent boundary layers, wall-modelling strategies compatible with the character of SEM-based uDNS / iLES approaches need be developed. Techniques with less restrictive modelling assumptions and that only affect the innermost portions of the boundary layer are to be preferred. Although promising advances have been made recently, improvements and more extensive testing are still required. This is a very important step to further the application of model-free SEM approaches to wall-bounded turbulent flows of industrial interest.